Measurements of the Top Quark Pair Production Cross Section and an Estimate of the DØ Silicon Detector Lifetime

by

Sara Strandberg

Department of Physics
Stockholm University
2007

Doctoral Dissertation 2007
Fysikum
Stockholm University
Roslagstullsbacken 21
106 91 Stockholm

Abstract

This thesis presents two measurements of the top quark pair production cross section at $\sqrt{s} = 1.96$ TeV using data from the DØ experiment. Both measurements are performed in the dilepton final state and make use of secondary vertex b-tagging. With 158 pb^{-1} of data in the $e\mu$ final state, the measured cross section is:

$$\sigma_{t\bar{t}} = 11.1\ ^{+5.8}_{-4.3}\ (\mathrm{stat}) \pm 1.4\ (\mathrm{syst})\ \pm 0.7\ (\mathrm{lumi})\ \mathrm{pb}.$$

With 425 pb^{-1} of data in the $e+$track and $\mu+$track final states, the measured cross section is:

$$\sigma_{t\bar{t}} = 6.3\ ^{+2.1}_{-1.8}\ (\mathrm{stat})\ ^{+1.1}_{-1.1}\ (\mathrm{syst})\ \pm 0.4\ (\mathrm{lumi})\ \mathrm{pb}.$$

Both measurements are in agreement with the prediction from perturbative QCD calculations.

In addition, an estimate of the DØ silicon detector lifetime is presented. The radiation damage is determined by studying the depletion voltage of the silicon sensors as a function of time. Based on this data the silicon detector is estimated to remain operational up to delivered luminosities of 6-8 fb^{-1}.

ISBN 91-7155-386-X
Printed by Universitetsservice US AB, Stockholm 2007

Cover image courtesy of Fermilab Visual Media Services, the DØ Collaboration and Jan-Henrik Andersen.

The work presented in this thesis is published in the following papers:

I *Measurement of the $t\bar{t}$ Production Cross Section in $p\bar{p}$ Collisions Using Dilepton Events*

The DØ Collaboration

To be submitted to Phys. Rev. D, currently in DØ editorial board review

II *Measurement of the $t\bar{t}$ production cross-section at $\sqrt{s} = 1.96$ TeV in the combined lepton+track and $e\mu$ channel using 370 pb^{-1} of DØ data*

Sara Lager for the DØ Collaboration

hep-ex/0605059, FERMILAB-CONF-06-117-E

Presented at the 41st Rencontres de Moriond on Electroweak Interactions and Unified Theories, La Thuile, Aosta Valley, Italy, 11-18 March 2006

III *D0 silicon microstrip tracker*

Sergey Burdin for the DØ Collaboration

physics/0511173, FERMILAB-CONF-05-515-E

Presented at the 2005 IEEE Nuclear Science Symposium and Medical Imaging Conference, El Conquistador Resort, Puerto Rico, 23-29 Oct 2005

IV *Measurement of the $t\bar{t}$ Production Cross-section at $\sqrt{s} = 1.96$ TeV in the $e\mu$ Channel Using Secondary Vertex b-tagging*

The DØ Collaboration

DØ Note 4528-CONF

Contents

Acknowledgments

This thesis builds on the work of many people and would not have been written without the endless efforts made by everyone in the DØ Collaboration. Thank you all for devoting days and nights to keeping DØ running.

I am a very fortunate graduate student to have two excellent advisors. Barbro Åsman, who came up with the idea to join DØ and worked hard to make sure her students got the opportunity to do analysis with real data. Your knowledge of the field of physics and your female intuition have made sure we were always in the right place at the right time. It meant a lot to me that you were always on my side, having confidence that I would pull it all together. And Christophe Clément, my constant source of information. Thank you for never looking impatient no matter how many questions I asked. I am proud to have been your first student. Without your guidance and advice I would never have made it.

The DØ top group has taught me how to be a particle physicist. A special thanks to Elizaveta Shabalina for your constant support and for always having the right answers. To Aurelio Juste for your never-ending enthusiasm and for teaching me to pay attention to the details. To Flera Rizatdinova for getting me introduced to the world of vertexing and for taking much of your precious time listening to my lepton+track status reports.

Many people have worked with me along the way. Thank you Kirti Ranjan for getting the lepton+track analysis going. Stefan Anderson for working so hard on the dilepton combination and for putting the PRD draft together. Sergey Burdin for getting me involved in the radiation damage study and for making sure it got finished by doing the lion's share of the work. Andrei Nomerotski for sharing with me his vast silicon knowledge. Prolay Mal and Daniel Whiteson for laying the foundations for the $e\mu$ analysis.

It would not have been as fun without: Nils Gollub, Per Hansson and Yann Coadou, my ever smiling and always helpful partners in the Swedish Consortium. My office mates Thomas Burgess, Christin Burgess and Henrik Johansson as well as the rest of the particle physics group who always made me feel welcome when coming back to Stockholm.

Thank you Ellen, Leon, Minx, Sunny and Tobi for getting me out of the office, showing me all the beautiful corners of Fermilab. For green tea, red wine and for making me feel at home.

To Mom and Dad for raising me and loving me. For teaching me to be curious and making me understand that anything is possible but that you have to work hard to get there. To my big sister for being the best of role models.

To Jonas, for sharing my life. For slowing me down when I am going to fast and motivating me when I am going to slow. For making me happy, for keeping me sane. I love you.

About This Thesis

This thesis includes an estimate of the DØ silicon detector lifetime as well as two measurements of the top quark pair production cross section. The thesis is divided into four parts. Part I gives a brief overview of the theory of elementary particle physics, focusing on the top quark. It also introduces the Tevatron accelerator complex and the DØ detector. Part II describes the effects of radiation damage in silicon and presents an estimate of the DØ silicon tracker lifetime. Part III describes two measurements of the top quark pair production cross section using events in the dilepton final states. The last part of the thesis, Part IV, contains a summary and outlook, followed by an informal summary in Swedish.

Author's Contributions

I started as a graduate student in the DØ experiment in the summer of 2002. During my first year I focused on the development and testing of the readout electronics for the Run IIb silicon upgrade. A lot of my effort went into establishing procedures to evaluate the performance of the SVX4 chip [1], which was then in a pre-production phase.

In the summer of 2003 I shifted to more software-oriented tasks. During the summer I worked with the implementation of a more realistic description of the silicon detector noise in the simulation of the DØ detector response. In the fall of 2003 I helped in certifying a new primary vertex algorithm, work which is documented in an internal DØ Note [2].

In 2004 I started developing a top quark pair production cross section measurement in the $t\bar{t} \rightarrow e\mu$ channel using secondary vertex b-tagging. This work was communicated at several conferences during 2004 and is documented in Paper IV. It is also included as a part of this thesis.

To further increase the sensitivity in the dilepton sector, where the statistical uncertainties are dominant due to the small branching ratio for a pair of top quarks to decay into the dilepton final state, I started to design a new cross section analysis using lepton+track final states. Loosening the kinematic selections, and suppressing the background using b-tagging, is found to increase the sensitivity in the dilepton sector. The first feasibility studies were made in January 2005 and a preliminary result, documented in Paper II, was communicated at conferences in 2006. The conference result includes a combination of the lepton+track result and another measurement from DØ which is performed in the $e\mu$ channel and does not use b-tagging. During 2006 I worked on refining the lepton+track analysis, and the updated version of the analysis is included in this thesis. A combination of the lepton+track result and measurements in other dilepton final states is documented in Paper I, which is under review by the DØ Collaboration and intended to be submitted to Phys. Rev. D.

Within the top physics working group I have also helped in group-wide efforts such as deriving data-to-simulation correction factors and estimating the flavor composition of jets produced in conjunction with a W boson. The latter is an important component in b-tagging based analyses where the dominant source of background originates from W+jets events.

During 2005 and 2006 I worked on the development and implementation of new calibration algorithms for the DØ silicon tracker, which are used to adjust the online pedestal and threshold settings. Compared to the previous calibration code, the new algorithms also include information about the expected occupancy for a given threshold setting. This type of information is important for sensors where the noise does not follow a Gaussian distribution.

The lifetime of the silicon tracker is limited by radiation damage caused by the Tevatron beam. I have worked on the development of a method which uses the noise on the n-side of the silicon sensors to estimate the depletion voltage and thus the radiation damage. The study, which was finished in 2005 and presented in Paper III, shows that the innermost layer of the silicon is less affected by radiation than predicted by irradiation tests performed before the start of Run II.

Part I

Introduction

Particle physics is concerned with the fundamental building blocks of matter and their interactions. At present the subatomic world is best described by a theory called the standard model (SM) of particle physics. It represents the world in terms of twelve fundamental spin-1/2 fermions (and twelve antifermions[1]), which are the building blocks of matter, and three forces mediated by the exchange of spin-1 bosons or force carriers. The particles included in the SM are shown in Fig. 1. The twelve fermions are subdivided into six leptons and six quarks, and at the same time divided into three generations, each containing two leptons and two quarks. Among the force carriers the massless photon is responsible for the electromagnetic interaction, the massive Z and W bosons mediate the weak interactions and the gluons are the carriers of the strong interaction.

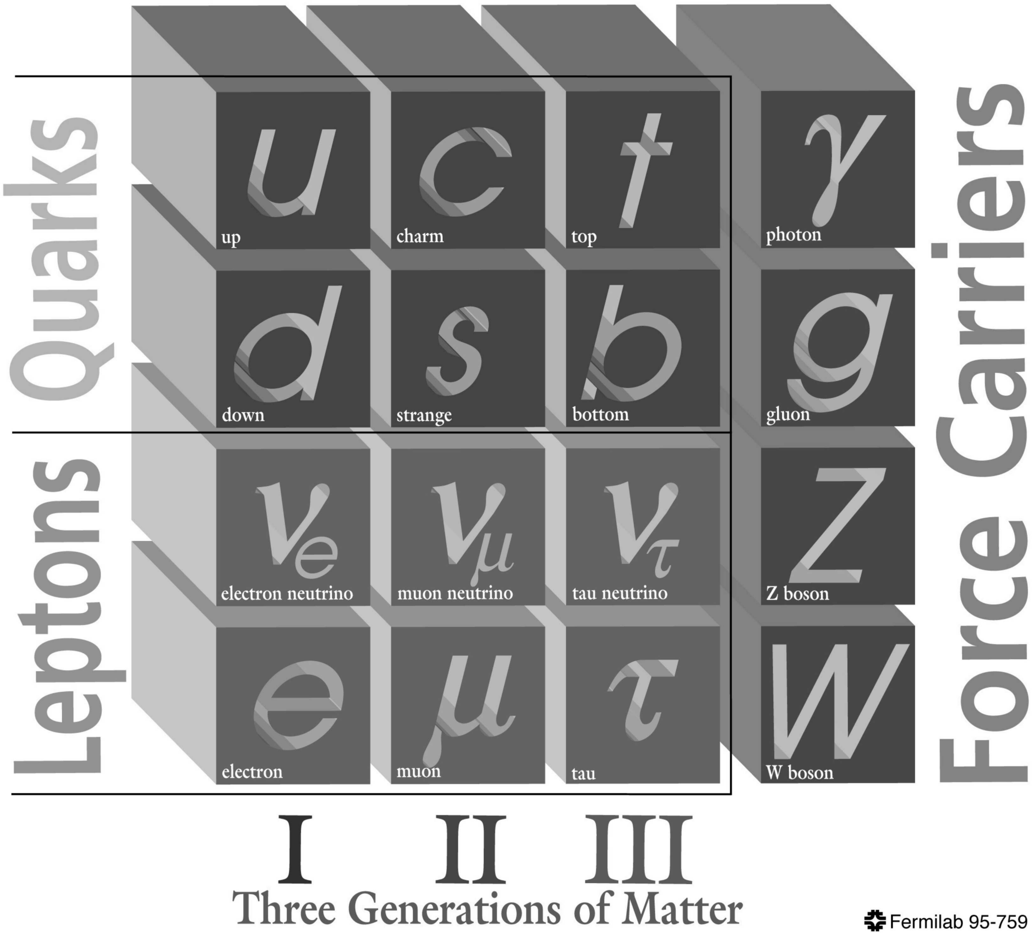

Figure 1: The elementary particles included in the SM.

---

[1] Unless explicitly stated otherwise, a reference to a particle species also refers to its antiparticle.

A probe with momentum p can only resolve structures which are larger than its corresponding wavelength $\lambda = h/p$. Studying objects at small scales therefore requires high energies. To access these high energies, large particle colliders have been built at which particles are accelerated and brought to collide at certain interaction points. Around these interaction points, detectors are installed to record the particles created in the high energy collisions.

The Tevatron collider located at Fermilab near Chicago is the highest energy collider currently operating in the world. It collides protons with antiprotons at a center-of-mass energy of 1.96 TeV. The Tevatron has a radius of 1 km and the protons and antiprotons are kept in their circular orbit by a 4.2 T magnetic field. The two experiments recording the Tevatron collisions are CDF and DØ, both operated by large international collaborations. The DØ Collaboration currently consists of 633 physicists from 81 institutions. The first data taking period, known as Run I, lasted from 1992 to 1996. During this period the Tevatron operated at a center-of-mass energy of 1.8 TeV. Many interesting physics results were obtained in Run I, the most spectacular of which being the long-awaited discovery of the top quark in 1995 [3,4]. Between 1996 and 2001, the Tevatron was upgraded to increase its instantaneous luminosity as well as the center-of-mass energy. At the same time both experiments were upgraded in order to take full advantage of the upgraded accelerator complex.

The Tevatron is still the only accelerator in the world with enough energy to create top quarks. Studying the top quark properties, production and decay is an important part of the Tevatron physics program. The large top quark mass provides a unique environment for tests of the SM and searches for new physics.

1 Theoretical Overview

1.1 The Standard Model of Particle Physics

The standard model is the theoretical framework which describes all the known elementary particles as well as three of the four fundamental forces of nature. The SM incorporates the theory of electroweak interaction and the theory of strong interaction (quantum chromodynamics or QCD). The gravitational force is not included in the SM. This force is very weak at distances and energies currently available in particle physics experiments and will be so for the foreseeable future. Although the large scale behavior of gravity is accurately described by the theory of general relativity, little is known about the quantum nature of the force.

The standard model has been extensively tested by many experiments, and has been found to accurately predict a vast range of phenomena. A review of the SM and a summary of the experimental tests of its predictions can be found in Ref. [5].

1.1.1 Quarks, Leptons and Bosons

In the SM, the particles which are the building blocks of matter are spin-1/2 fermions. They are divided into six leptons and six quarks. The leptons and quarks are furthermore grouped into three generations. Each generation contains one electrically charged and one neutral lepton, plus an up-type and a down-type quark. Only the first generation of charged leptons and quarks are stable as the heavier fermions quickly decay into lighter ones.

The forces in the SM are mediated by spin-1 bosons. The exchange particle for the electromagnetic force is the photon γ. The weak force is mediated by the W^+, W^- and Z^0 bosons. The strong force is mediated by the eight gluons $g_1, \ldots, g_8$. The fermions and bosons in the SM are summarized in Tab. 1.1 together with the year of their discovery.

1.1.2 The Electroweak Interaction

The theory of quantum electrodynamics (QED) describes interactions between electrically charged particles. Invariance of the Lagrangian under local (i.e. space-time dependent) transformations generated by the $\mathrm{U}(1)_{\mathrm{EM}}$ group is the founding principle of QED. This so called gauge invariance requires an interaction field where the asso-

	Generation		
	I	II	III
Leptons	ν_e (1953) [6]	ν_μ (1962) [7]	ν_τ (2000) [8]
	e (1897) [9]	μ (1936) [10]	τ (1975) [11]
Quarks	u (1964) [12]	c (1974) [13,14]	t (1995) [3,4]
	d (1964) [12]	s (1964) [12]	b (1977) [15]
Bosons		γ (1900) [16,17]	
		$W^{\pm}, Z$ (1983) [18–21]	
		$g_1, \ldots, g_8$ (1979) [22]	
		H (Not discovered)	

Table 1.1: The particles in the SM and their year of discovery. The Higgs boson H has not yet been discovered.

ciated gauge boson, the photon, is massless. From the invariance of the Lagrangian under global gauge transformations follows the conservation of electric charge.

The form of the weak interaction is partly derived from the invariance of the Lagrangian under SU(2) gauge transformations. It leads to interactions where charged $W^{\pm}$ bosons or neutral W^0 bosons are exchanged. The charged states give rise to charged current interactions in agreement with observations. The W^0 boson implies a neutral current process with the same strength as the charged current process, something which is not in agreement with observations.

To arrive at the correct form of neutral current weak interactions the electromagnetic and the weak force need to be unified. The task was achieved in 1968 [23–25]. The combined symmetry group for the electroweak interactions is $\mathrm{SU}(2)_L \times \mathrm{U}(1)_Y$ where the subscript L indicates that the weak force only acts on left-handed particles. Invariance of the Lagrangian under $\mathrm{SU}(2)_L$ transformations leads to the conservation of so called weak isospin I, whereas invariance under $\mathrm{U}(1)_Y$ transformations leads to conservation of the weak hypercharge Y. The photon and the Z^0 boson can be defined as linear combinations of the W^0 boson and the boson B^0 associated with the $\mathrm{U}(1)_Y$ group:

$$\gamma = B^0 \cos\theta_W + W^0 \sin\theta_W \tag{1.1}$$

$$Z = -B^0 \sin\theta_W + W^0 \cos\theta_W \tag{1.2}$$

where $\cos\theta_W = m_W/m_Z$ is the weak mixing angle. The coupling constants g_Z, g_W and e which occur in electroweak interactions are not independent, but are related through the unification condition

$$e = g_W \sin\theta_W = g_Z \cos\theta_W. \tag{1.3}$$

After electroweak unification one problem still remains. In any unbroken gauge field theory, the gauge bosons are required to be massless. Explicit mass terms for the bosons in the Lagrangian are not invariant under gauge transformations. But according to experiments, both the $W^{\pm}$ and the Z^0 bosons are heavy particles. This problem is solved through the mechanism of spontaneous symmetry breaking, described in Sec. 1.1.3

The weak interaction is maximally parity violating, coupling only to left-handed fermions (and right-handed antifermions). The left-handed quarks and leptons are members of $I = 1/2$ isospin doublets while right-handed quarks and charged leptons are $I = 0$ isospin singlets. The electroweak eigenstates of the fermions in the SM together with their weak quantum numbers are summarized in Tab. 1.2. The $W^{\pm}$ bosons are assigned an isospin value of 1 which allows them to mediate transitions between the left-handed leptons and quarks. The Z^0 boson is an isospin 0 particle, and does not mediate transitions between different generations.

		I_3	Y	Q
Leptons				
Doublet	$\begin{pmatrix} \nu_e \\ e \end{pmatrix}_L \begin{pmatrix} \nu_\mu \\ \mu \end{pmatrix}_L \begin{pmatrix} \nu_\tau \\ \tau \end{pmatrix}_L$	1/2	−1	0
		−1/2	−1	−1
Singlet	e_R μ_R τ_R	0	−2	−1
Quarks				
Doublet	$\begin{pmatrix} u \\ d' \end{pmatrix}_L \begin{pmatrix} c \\ s' \end{pmatrix}_L \begin{pmatrix} t \\ b' \end{pmatrix}_L$	1/2	1/3	2/3
		−1/2	1/3	−1/3
Singlet	u_R c_R t_R	0	4/3	2/3
Singlet	d'_R s'_R b'_R	0	−2/3	−1/3

Table 1.2: The electroweak eigenstates of the fermions in the SM together with their third weak isospin component I_3, hypercharge Y and electric charge $Q = I_3 + Y/2$ in units of e. The subscripts L and R indicates if a state is left- or right-handed.

If the electroweak eigenstates listed in Tab. 1.2 were also the mass eigenstates, weak transitions would only be observed within each generation. This is true for the charged leptons. The same was thought to be true for the neutrinos until recently when neutrino oscillations were observed [26, 27]. For the quarks, the mass eigenstates differ from the weak eigenstates which allows for the weak interaction to mediate transitions between different generations. The weak eigenstates of the down-type quarks (d', s', b') can be written as a linear combination of the three down-type quark mass eigenstates (d, s, b) with the coefficients given by the 3×3

Cabibbo-Kobayashi-Maskawa (CKM) matrix [28]:

$$\begin{pmatrix} d' \\ s' \\ b' \end{pmatrix} = \begin{pmatrix} V_{ud} & V_{us} & V_{ub} \\ V_{cd} & V_{cs} & V_{cb} \\ V_{td} & V_{ts} & V_{tb} \end{pmatrix}_{CKM} \begin{pmatrix} d \\ s \\ b \end{pmatrix}$$

Each matrix element squared $|V_{ij}|^2$ is proportional to the coupling at the quark-W-quark vertex, describing the transition from quark i to quark j. Since the neutrinos have been observed to oscillate, a similar matrix must also exist for the mixing in the neutrino sector.

1.1.3 Electroweak Symmetry Breaking

The non-zero mass of the weak gauge bosons implies that the local $\mathrm{SU}(2)_L\times\ \mathrm{U}(1)_Y$ symmetry of the electroweak Lagrangian is not an exact symmetry. However, the Lagrangian should still be invariant under $\mathrm{U}(1)_{\mathrm{EM}}$ transformations since the photon is observed to be massless.

In the SM, $\mathrm{SU}(2)_L\times\ \mathrm{U}(1)_Y$ is broken down to $\mathrm{U}(1)_{\mathrm{EM}}$ while maintaining the initial gauge invariance of the Lagrangian by the formalism of spontaneous symmetry breaking. A symmetry is said to be spontaneously broken if the theory's Lagrangian is invariant under this symmetry but its vacuum state is not.

In the Higgs mechanism [29–31] the spontaneous symmetry breaking is introduced by a new electroweak doublet of complex scalar fields. These fields interact through a potential with an assumed shape illustrated in Fig. 1.1. The key feature of this potential is that at least one of the components of the complex Higgs fields must be non-zero in order for it to reach its minimum.

To predict the particle spectrum of the theory in the Higgs and gauge boson sectors, the Lagrangian is evaluated in the vicinity of a specific vacuum state. In order to obtain an electrically neutral vacuum, the non-zero component is chosen to be along the real axis of the neutral Higgs field. The process of selecting a specific vacuum state breaks the initial $\mathrm{SU}(2)_L\times\ \mathrm{U}(1)_Y$ symmetry, and the real component of the neutral Higgs field acquires a non-vanishing vacuum expectation value v. When expanding the Lagrangian around its vacuum state, effective mass terms for the electroweak gauge bosons $W^\pm$ and Z appear. Three of the initial four degrees of freedom of the Higgs fields are transformed into the longitudinal components of the weak gauge bosons $W^\pm$ and Z. The remaining degree of freedom gives rise to a new physical state, the Higgs boson, with charge and spin 0.

In the standard model, the masses of the weak gauge bosons at tree level are related to the vacuum expectation value v of the Higgs field through

$$m_W = \sqrt{2} g_W v \tag{1.4}$$

$$m_Z = \frac{\sqrt{2} g_W v}{\cos\theta_W} = \frac{m_W}{\cos\theta_W} \tag{1.5}$$

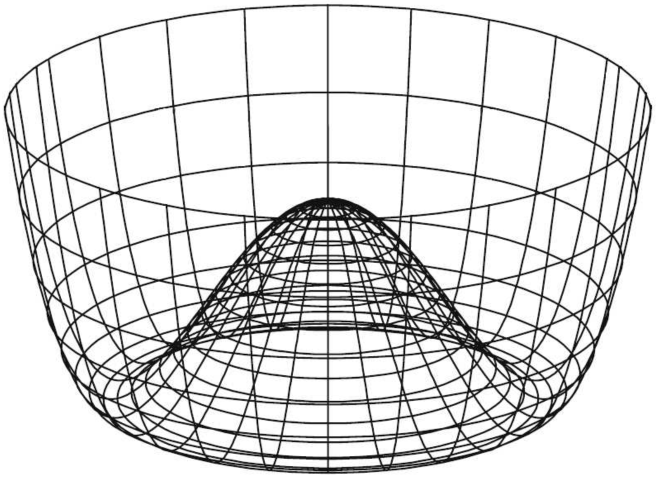

Figure 1.1: The Higgs potential as a function of two of its four degrees of freedom. The neutral component of the Higgs field acquires a vacuum expectation value on the circle of minima in the Higgs-field space.

The parameter ρ_0, defined as

$$\rho_0 = \frac{m_W^2}{m_Z^2 \cos^2 \theta_W}, \tag{1.6}$$

is predicted to be unity which is in very good agreement with the observed value [28]. This result represents one of the great achievements of the SM and imposes strict limits on possible new theories or extensions of the SM.

The vacuum expectation value of the Higgs field can be determined from

$$v = (\sqrt{2} G_F)^{-1/2} \approx 246 \text{ GeV} \tag{1.7}$$

where $G_F = 1.166 \cdot 10^{-5}$ GeV^{-2} [28] is the Fermi weak interaction coupling constant. The mass of the Higgs boson (m_H) remains a free parameter in the model and must be determined experimentally. The search for the Higgs boson has become one of the most pressing topics in high energy physics. To date, no Higgs boson has been observed. The most stringent direct search limit comes from the LEP II experiments. They exclude a SM Higgs boson lighter than 114.4 GeV/c^2 at the 95% confidence level [34].

1.1.4 The Strong Interaction

The strong force is modeled by the theory of QCD [12, 32, 33]. The complicated spectrum of mesons and baryons was successfully described in the 1960s as originating from bound states of quarks. To avoid violation of the Pauli principle, a new quantum number called color had to be introduced. Color appears in three states, commonly referred to as red, green and blue.

All hadrons are postulated to be color singlets. Mesons consist of a quark-antiquark pair in a color-anticolor state. Baryons consist of three quarks, with each quark carrying a different color in order to make the baryon colorless. Besides the two or three so called valence quarks, there exists a sea of virtual quarks and gluons within each hadron which also contribute to its total energy and momentum.

The strong interaction between quarks and gluons is derived from invariance of the Lagrangian under SU(3) rotations in color space. Local invariance can only be achieved by introducing eight new gauge fields into the Lagrangian, corresponding to the eight gluons which mediate the strong force. The gluons themselves carry color-anticolor charge, giving rise to gluon self-interactions. The strength of the strong interaction is described by $\alpha_s = g_s^2/(4\pi)$, where g_s is the strong coupling associated with the SU(3) gauge symmetry of the strong force.

Quarks and gluons cannot be observed as individual particles. As they are pulled apart, the energy of the strong field becomes big enough to force a quark-antiquark pair production. As a result, a quark or gluon produced in a particle collision undergoes what is called fragmentation. The result of the fragmentation is a stream of collinear particles referred to as a jet.

1.2 The Top Quark

The discovery of the bottom quark in 1977 [15] indicated the existence of a third generation of quarks. Searches for its electroweak isospin partner, the top quark, immediately started and were conducted at electron-positron and proton-antiproton colliders during the 1980s and early 1990s. The top quark was finally discovered in 1995 at the Fermilab Tevatron proton-antiproton collider by the CDF and DØ Collaborations [3, 4].

The top quark is the heaviest elementary particle known to date, with a mass more than 35 times larger than that of the bottom quark. The most recent value of the top quark mass is 171.4 GeV/c^2 with an uncertainty of 1.2% [39].

1.2.1 Top Quark Pair Production

In the $p\bar{p}$ collisions at the Tevatron, top quarks are primarily produced in pairs via the strong interaction. In the parton model, the protons and antiprotons are regarded as a composition of quasi-free quarks and gluons. In the collisions at the Tevatron, the proton and antiproton both carry the same longitudinal momentum p_z. The parton i has the longitudinal momentum $p_{z,i}$, i.e. it carries the momentum fraction $x_i = p_{z,i}/p_z$. According to the factorization theorem, the $p\bar{p} \to t\bar{t}$ cross section calculation can be separated into a short distance interaction between two partons i and j, and a long distance term representing the probability of finding parton i within the proton and parton j within the antiproton, carrying momentum fractions x_i and x_j respectively. The factorization property of the cross section can be proven to all orders in perturbation theory [40]. The long distance part is obtained from integration over the parton distribution functions (PDFs) f_i and f_j. The short distance part is the hard parton-parton cross section $\hat{\sigma}_{ij}$.

The $p\bar{p} \to t\bar{t}$ cross section can thus be calculated as:

$$\sigma(p\bar{p} \to t\bar{t}) = \sum_{i,j} \int dx_i dx_j f_{i,p}(x_i, \mu^2) f_{j,\bar{p}}(x_j, \mu^2) \cdot \hat{\sigma}_{ij}(ij \to t\bar{t}; \hat{s}, \mu^2) \tag{1.8}$$

The variable $\hat{s}$ in Eq. 1.8 is the square of the center-of-mass energy of the colliding partons $\hat{s} = 4x_i x_j p^2$, where it is assumed that the proton and antiproton carry the same momentum p. The sum in Eq. 1.8 runs over all pairs of light partons (i, j) contributing to the process.

The parton distribution functions depend on the factorization scale μ_F introduced by the factorization ansatz. In addition, $\hat{\sigma}_{ij}$ depends on the renormalization scale μ_R due to the renormalization procedure invoked to regulate divergent terms in the perturbation series when calculating the parton-parton cross section. Since both scales are to some extent arbitrary parameters the practice is to use one scale $\mu = \mu_F = \mu_R$. For calculating heavy quark production the scale is usually set to the order of the heavy quark mass. If the complete perturbation series could be calculated, the resulting cross section would be independent of μ. However, since calculations are performed to finite order in perturbation theory, cross section predictions do in general depend on the choice of μ. The μ-dependence is usually tested by varying the scale between $\mu/2$ and 2μ.

Parton Distribution Functions

The parton distribution functions are extracted from deep-inelastic scattering experiments where either electrons, positrons or neutrinos collide with partons inside the nucleons. Parameterizations of proton PDFs have been extracted from the experimental data by several groups. As an example, a proton PDF derived by the CTEQ Collaboration [41] is shown in Fig. 1.2. Indicated are also the minimum momentum fraction needed to produce a $t\bar{t}$ pair at the LHC and the Tevatron, assuming both incoming partons carry the same momentum. The energy needed to produce a $t\bar{t}$ pair is $\hat{s} = 2m_t \approx 350$ GeV. In this simplified scheme, the momentum fraction needed to create a pair of top quarks is $x_{\text{min}} = \sqrt{m_t^2/4p^2}$. At the Tevatron, where the beam energy is 980 GeV, the momentum fraction needed to produce a $t\bar{t}$ pair is $x_{\text{min}} \approx 0.18$, whereas at the LHC, with a beam energy of 7 TeV, the minimum momentum fraction is $x_{\text{min}} \approx 0.025$. Figure 1.2 shows that a parton with momentum fraction $x = 0.18$ is likely to be a valance quark whereas a parton with momentum fraction $x = 0.025$ most likely is a gluon. As a consequence of this, $t\bar{t}$ production at the Tevatron is dominated by quark-quark annihilation whereas $t\bar{t}$ production at the LHC will be dominated by gluon-gluon fusion.

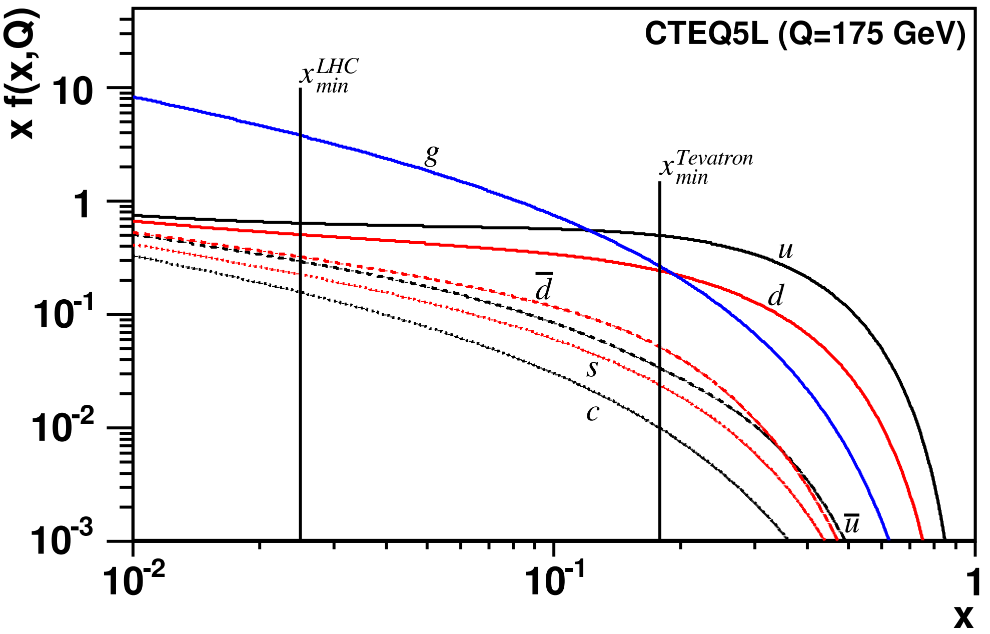

Figure 1.2: Probability to find a certain type of quark or gluon in the proton as a function of the momentum fraction x, given by the CTEQ5L [41] parameterizations. The minimum values of x needed to produce a $t\bar{t}$ pair at the LHC and the Tevatron are indicated by the vertical bands, assuming both incoming partons carry the same momentum fraction.

The Parton Cross Section

The cross section $\hat{\sigma}_{ij}$ of the hard parton-parton process $ij \rightarrow t\bar{t}$ can be calculated in perturbative QCD, i.e. as a perturbation series in the QCD coupling constant α_s. The leading order processes, contributing with α_s^2 to the perturbation series, are quark-antiquark annihilation and gluon-gluon fusion. The Feynman diagrams for these processes are shown in Fig. 1.3.

The differential cross section for quark-antiquark annihilation is given by

$$\frac{d\hat{\sigma}}{d\hat{t}}(q\bar{q} \rightarrow t\bar{t}) = \frac{4\pi\alpha_s^2}{9\hat{s}^4} \cdot \left[(m_t^2 - \hat{t})^2 + (m_t^2 - \hat{u})^2 + 2m_t^2\hat{s}\right] \tag{1.9}$$

where $\hat{s}$, $\hat{t}$ and $\hat{u}$ are the invariant Mandelstam variables of the process. They are defined by $\hat{s} = (p_q + p_{\bar{q}})^2$, $\hat{t} = (p_q - p_t)^2$ and $\hat{u} = (p_q - p_{\bar{t}})^2$ with p_i being the corresponding momentum 4-vector of the quark i. The variable m_t denotes the top quark mass. The differential cross section for the gluon-gluon fusion process is given

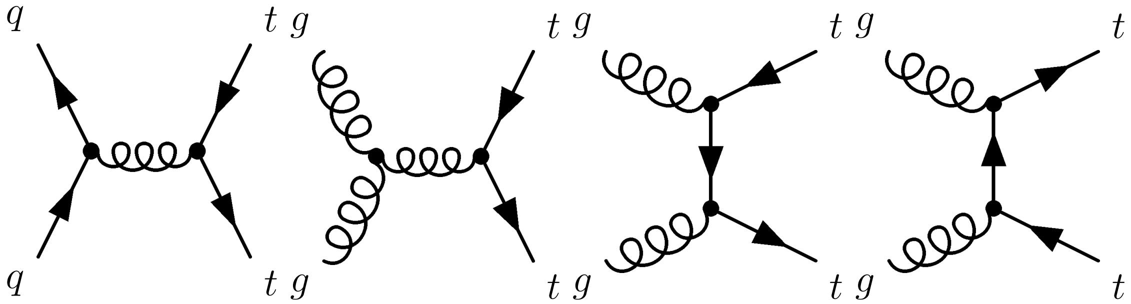

Figure 1.3: Feynman diagrams of the leading order process for $t\bar{t}$ production. The left diagram shows quark-antiquark annihilation, and the three right diagrams show gluon-gluon fusion.

by

$$\begin{aligned}\frac{d\hat{\sigma}}{d\hat{t}}(g_1 g_2 \to t\bar{t}) = & \frac{\pi\alpha_s^2}{8\hat{s}^2} \cdot \left[\frac{6(m_t^2-\hat{t})(m_t^2-\hat{u})}{\hat{s}^2} - \frac{m_t^2(\hat{s}-4m_t^2)}{3(m_t^2-\hat{t})(m_t^2-\hat{u})}\right. \\ & +\frac{4}{3}\cdot\frac{(m_t^2-\hat{t})(m_t^2-\hat{u})-2m_t^2(m_t^2+\hat{t})}{(m_t^2-\hat{t})^2} \\ & +\frac{4}{3}\cdot\frac{(m_t^2-\hat{t})(m_t^2-\hat{u})-2m_t^2(m_t^2+\hat{u})}{(m_t^2-\hat{u})^2} \\ & -3\cdot\frac{(m_t^2-\hat{t})(m_t^2-\hat{u})-m_t^2(\hat{u}-\hat{t})}{\hat{s}(m_t^2-\hat{t})^2} \\ & \left.-3\cdot\frac{(m_t^2-\hat{t})(m_t^2-\hat{u})-m_t^2(\hat{t}-\hat{u})}{\hat{s}(m_t^2-\hat{u})^2}\right]\end{aligned} \tag{1.10}$$

The invariant variables in this case are $\hat{s} = (p_{g_1} + p_{g_2})^2$, $\hat{t} = (p_{g_1} - p_t)^2$, and $\hat{u} = (p_{g_1} - p_{\bar{t}})^2$.

The $t\bar{t}$ production cross section has been calculated at next-to-leading order (NLO) in perturbation theory. The results are $6.70^{+0.71}_{-0.88}$ pb [42] and 6.77 ± 0.42 pb [43]. The first result includes resummation of next-to-leading logarithms (NNL), whereas the latter result includes next-to-next-to-leading order soft gluon corrections as well as some subleading terms including next-to-next-to-next-to-leading logarithms and virtual terms. The production cross section as a function of the top quark mass is shown in Fig. 1.4.

1.2.2 Single Top Quark Production

Top quarks can be produced singly via electroweak interaction involving the Wtb vertex. The three dominant production modes are:

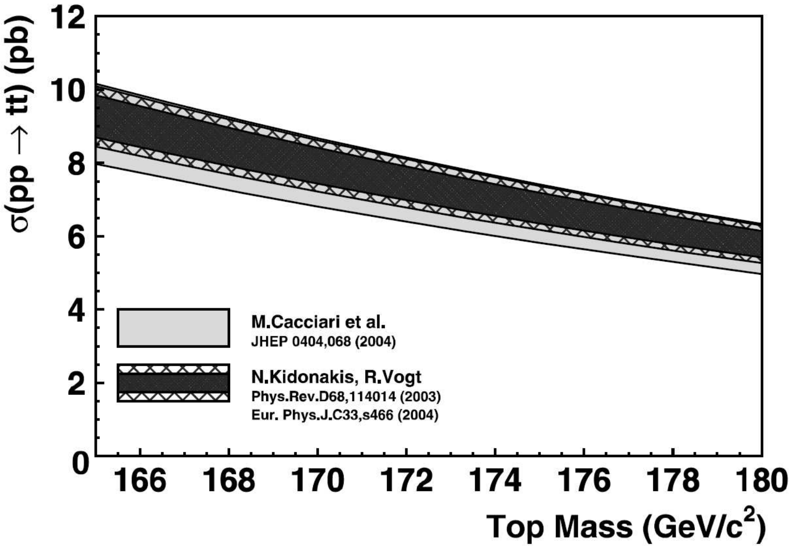

Figure 1.4: The $t\bar{t}$ production cross section in $p\bar{p}$ collisions at $\sqrt{s} = 1.96$ TeV as a function of the top quark mass. The error band for the calculations of Caccari et al. [42] contains scale and PDF uncertainties. The inner error band for the calculation of Kidonakis and Vogt [43, 44] contains kinematics uncertainties while the outer error band also includes PDF uncertainties.

t-channel: A virtual W boson interacts with a b quark from the sea inside the proton, turning the bottom quark into a top quark. This mode is also known as W-gluon fusion, since the b quark originates from a gluon splitting into a $b\bar{b}$ pair. At the Tevatron energies the t-channel process is the dominant production mode, and the cross section at NLO is found to be 1.98 ± 0.21 pb [45]. One LO Feynman diagram for this process is shown in Fig. 1.5(a).

s-channel: A timelike W boson is produced by the fusion of two quarks. This process is very similar to the production of an on-shell W boson. But for the W boson to decay into a top and a bottom quark it has to be off-shell, which greatly reduces the cross section. At NLO the cross section for s-channel production at the Tevatron is 0.88 ± 0.07 pb [45]. One LO Feynman diagram for this process is shown in Fig. 1.5(b).

Associated production: The top quark is produced in association with a real, or close to real, W boson. The initial b quark is a sea quark inside the proton. The cross section of associated production is negligible at the Tevatron, but will become important at the LHC [46]. One LO Feynman diagram for this process is shown in Fig. 1.5(c).

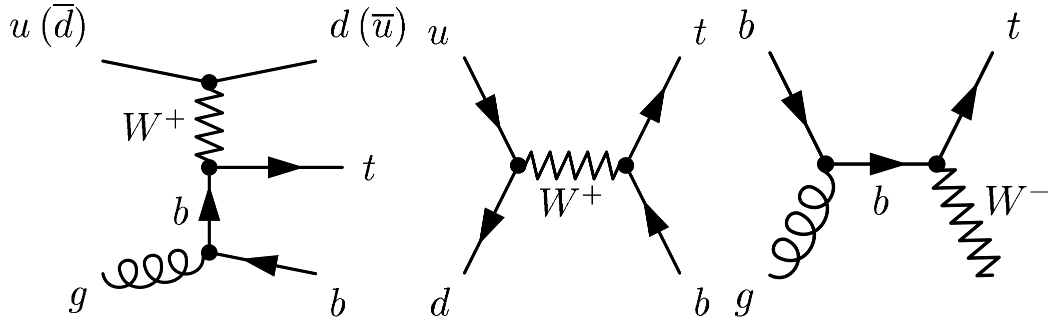

(a) t-channel production (b) s-channel production (c) associated production

Figure 1.5: Examples of leading order Feynman diagrams for single top production.

Even though the single top production is an electroweak process, the total cross section predicted by the standard model is similar to that of top pair production via the strong interaction. One reason is that the single top production is not as kinematically suppressed as the pair production since only one heavy object is produced. The t-channel production mode specifically does not suffer from color suppression.

1.2.3 Top Quark Decay

The top quark decays almost exclusively to a W boson and a b quark via the weak interaction. In the SM, the branching ratio $B(t \to Wb)$ is constrained to be greater than 0.998, due to the large CKM matrix element $|V_{tb}| \simeq 1$ [28]. For the measurements presented in this thesis, the top quark is assumed to decay to a W boson and a bottom quark 100% of the time.

Neglecting the mass of the b quark and higher order terms, the total width of the top quark, Γ_t, is given by [47]

$$\Gamma_t = \frac{G_F m_t^3}{8\pi\sqrt{2}} \left(1 - \frac{m_W^2}{m_t^2}\right)^2 \left(1 + 2\frac{m_W^2}{m_t^2}\right) \left[1 - \frac{2\alpha_s}{3\pi}\left(\frac{2\pi^2}{3} - \frac{5}{2}\right)\right] \tag{1.11}$$

With a top quark mass of 175 GeV/c^2, the width in Eq. 1.11 is approximately 1.5 GeV/c^2. This corresponds to a very short top quark lifetime of approximately $5 \cdot 10^{-25}$ s. The lifetime is about one order of magnitude smaller than the time needed to form hadrons, which means that the top quarks decays essentially as a free quark.

The final state of a $t\bar{t}$ event depends upon the decay of the two W bosons. A W boson can decay to a charged lepton and the corresponding neutrino, or to a $q\bar{q}'$ pair. All three lepton generations (e, μ and τ) are kinematically allowed. The hadronic W decays are kinematically limited to first or second generation quarks (ud

or cs pairs). All three leptonic W decay modes have the same probability if higher order corrections are neglected. A hadronic decay mode is three times as likely to occur as a leptonic one due to the color factor of three. Altogether there are nine potential decay modes, all with the same probability of 1/9 at leading order. Due to higher order corrections this symmetry between the decay modes is slightly broken. A summary of the W boson decay modes is shown in Tab. 1.3.

		$W^+ \rightarrow$			
		$c\bar{s}/u\bar{d}$ 67.60±0.27	$e^+\nu_e$ 10.75±0.13	$\mu^+\nu_\mu$ 10.57±0.15	$\tau^+\nu_\tau$ 11.25±0.20
$W^- \rightarrow$	$\bar{c}s/\bar{u}d$ 67.60±0.27	45.70±0.26	7.27±0.09	7.15±0.11	7.61±0.14
	$e^-\bar{\nu}_e$ 10.75±0.13	7.27±0.09	1.16±0.02	1.14±0.02	1.21±0.03
	$\mu^-\bar{\nu}_\mu$ 10.57±0.15	7.15±0.11	1.14±0.02	1.12±0.02	1.19±0.03
	$\tau^-\bar{\nu}_\tau$ 11.25±0.20	7.61±0.14	1.21±0.03	1.19±0.03	1.27±0.03

Table 1.3: The branching fractions in % for the decay of a real W boson [28]. In the analyses presented in this thesis, an older and lepton-flavor blind value of $(10.68 \pm 0.12)\%$ is used for $W \rightarrow \ell\nu$ (where $\ell = e, \mu, \tau$) [48].

The possible final states of $t\bar{t}$ events are categorized according to the decays of the two W bosons:

Dilepton ($t\bar{t} \rightarrow \ell\ell$): Both W bosons decay leptonically. The final state contains two charged leptons, two neutrinos and two b quarks.

Lepton+jets ($t\bar{t} \rightarrow \ell + \text{jets}$): One W boson decays leptonically and the other one hadronically. The final state contains one charged lepton, one neutrino, a $q\bar{q}'$ pair and two b quarks.

All hadronic ($t\bar{t} \rightarrow \text{jets}$): Both W bosons decay hadronically. The final state contains two $q\bar{q}'$ pairs and two b quarks.

1.2.4 Top Quark Measurements by the Tevatron Experiments

The Run I of the Tevatron produced a large number of results in the top quark sector. Most of these measurements are however limited by statistics, since the Run I data set corresponded to an integrated luminosity of only 125 pb^{-1}. In

Run II the increased collision energy and luminosity allow for the study of the top quark in more detail. This section briefly reviews a selection of top quark related measurements made by the CDF and DØ Collaborations. So far all results are consistent with the SM expectations.

Top Pair Production Cross Section

Precise measurements of the top quark pair production cross section are relevant for many reasons. Since top quark pairs are produced via the strong interaction the measured production cross sections are important tests of perturbative QCD calculations. In addition, any deviations from the theoretically predicted value could be an indication of physics beyond the standard model. The existence of anomalous decay channels such as $t \rightarrow H^+b$ may appear as a total measured cross section lower than expected [49]. An abnormally high cross section may be an indication of additional production mechanisms, introduced for example in the theory of technicolor [50].

Anomalous top quark decay modes or exotic particles decaying to top-like final states can alter the ratio of the cross sections measured in different final states. As an example, the existence of a $t \rightarrow H^+b$ decay mode would change the ratio of the cross sections measured in dilepton and lepton+jets final states. It is therefore important to measure and compare the top quark pair production cross section in several final states.

The top pair production cross section has been measured by the CDF and DØ Collaborations in the dilepton, lepton+jets and all hadronic final states [51–64]. The measurements of the top quark pair production cross section presented by the CDF and DØ Collaborations at the summer and fall conferences in 2006 are summarized in Fig. 1.6 and Fig. 1.7 respectively.

Top-Antitop Resonance Production

Resonance production of $t\bar{t}$ pairs can occur in the standard model if there exists a heavy Higgs boson ($H \rightarrow t\bar{t}$) [65] as well as in various extensions of the SM. An example is the Z' boson predicted by the top-color-assisted technicolor model [66–68]. Searches for $t\bar{t}$ resonances have been performed by the CDF and DØ Collaborations and no significant deviations from standard model $t\bar{t}$ production were observed [69–71].

Single Top Production Cross Section

In addition to $t\bar{t}$ production, top quarks are also expected to be produced singly via the electroweak process. Single top quark events can be used to study the Wtb coupling and to measure the magnitude of the CKM matrix element without assuming only three generations of quarks. Single top quark production can also be used to measure the top quark partial decay width $\Gamma(t \rightarrow Wb)$ and hence the top

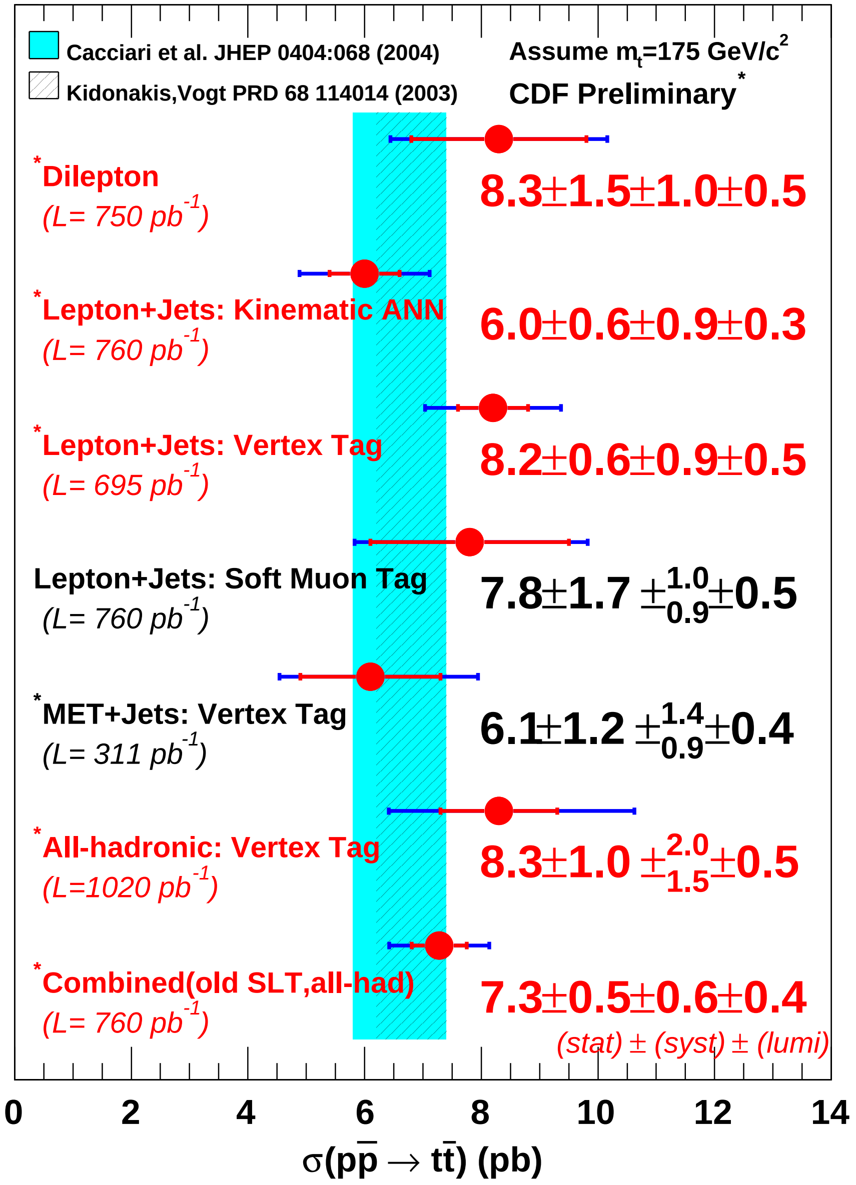

Figure 1.6: The top quark pair production cross section measurements presented by the CDF Collaboration at the summer and fall conferences in 2006, shown together with the theoretical predictions for $m_t = 175$ GeV/c^2.

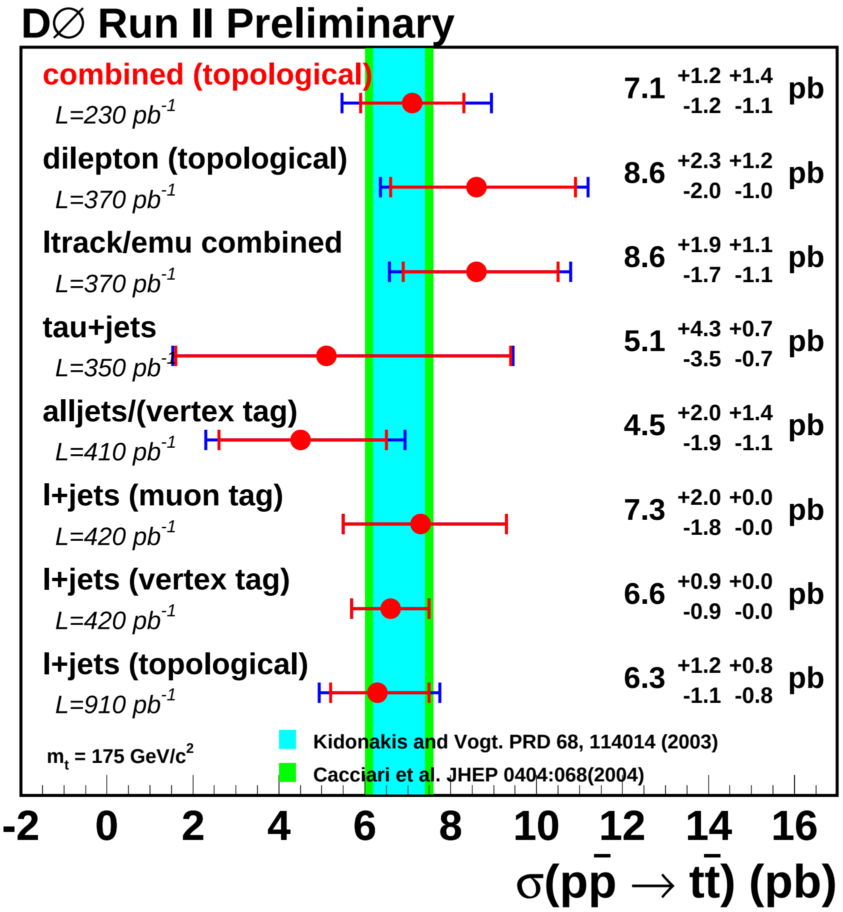

Figure 1.7: The top quark pair production cross section measurements presented by the DØ Collaboration at the summer and fall conferences in 2006, shown together with the theoretical predictions for $m_t = 175$ GeV/c^2. The result labeled “ltrack/emu combined” corresponds to the measurement presented in Paper II. The uncertainties included are ± stat ± syst. The measurements labeled “l+jets (muon tag)” and “l+jets(vetex tag)” estimate a combined statistical and systematic uncertainty. The uncertainty on the luminosity determination is 6.1–6.5% and is not included here.

quark lifetime.

Evidence for single top quark production was recently announced by the DØ Collaboration [72]. The measured cross section for the combined s- and t-channel is $\sigma(p\bar{p} \rightarrow tb + X, tqb + X) = 4.9 \pm 1.4$ pb, which is in good agreement with the predictions from perturbative QCD calculations.

Coupling of the Top Quark to Down-Type Quarks

Within the SM, the ratio $R = B(t \rightarrow Wb)/\sum_{q=d,s,b} B(t \rightarrow Wq)$ can be expressed at LO in terms of CKM matrix elements

$$R = \frac{|V_{tb}|^2}{|V_{tb}|^2 + |V_{ts}|^2 + |V_{td}|^2} = |V_{tb}|^2. \tag{1.12}$$

From the unitarity of the CKM matrix and measurements of other CKM matrix elements, $|V_{tb}|^2$ is constrained to be in the interval 0.9980-0.9984 at 90% C.L. [73]. A fourth quark generation or non-SM processes in the production or decay of the top quark could lead to significant deviations from the SM prediction.

Both the CDF and DØ Collaborations have measured R by comparing the number of events with two identified b-jets to the number of events with one or zero identified b-jet in the final state [73–75]. All measurements are consistent with the SM expectation.

Top Quark Decays to Charged Higgs

The simplest extension of the standard model Higgs sector is made by the introduction of another Higgs doublet, resulting in a two Higgs doublet model (2HDM) [77]. In these models, electroweak symmetry breaking results in five physical bosons, three of which are neutral (h^0, H^0 and A^0) and two of which are charged ($H^{\pm}$). If kinematically allowed, the top quark can decay to H^+b competing with the standard model top decay $t \rightarrow W^+b$.

Searches for charged Higgs bosons in top decays have been carried out by both the CDF and DØ Collaborations [78–83].

Flavor Changing Neutral Current Decays of the Top Quark

Another example where searches in the top sector could reveal new physics is through observations of flavor changing neutral current (FCNC) decays of the top quark. Within the context of the SM these decays are predicted to be extremely rare whereas in many models of physics beyond the SM, such as the 2HDM and the minimal supersymmetric standard model, FCNC can be highly enhanced. Searches for FCNC decays have been performed by the CDF Collaboration [76]. No evidence for FCNC decays are observed and limits are set on the branching fractions $B(t \rightarrow cZ)$, $B(t \rightarrow uZ)$, $B(t \rightarrow c\gamma)$ and $B(t \rightarrow u\gamma)$.

Helicity of the W Boson in Top Quark Decays

In the limit of a massless b quark, the standard $V - A$ coupling at the tWb vertex requires that the b quark in top decays is produced left-handed, restricting the helicity of the W^+ boson to values of 0 and -1. Observations of a significant $+1$ helicity component in W^+ decays (i.e. a $V + A$ coupling in the tWb vertex) would indicate the presence of physics beyond the SM.

In the SM, top quarks decay to longitudinally polarized W bosons (W_0) with the branching ratio

$$B(t \to W_0 b) = \frac{m_t^2}{m_t^2 + 2m_W^2} \approx 0.7, \tag{1.13}$$

and thus the negative helicity component (W_-) is expected to have a branching ratio of 0.3.

The helicity of the W boson in top quark decays can be measured by studying the angle between the b quark and the lepton or by studying the p_T distributions for the leptons in the final state. The results from the CDF and DØ Collaborations are consistent with the SM expectation [84–89].

Top Quark Spin Correlation

According to Eq. 1.13, 70% of the $t\bar{t}$ pairs have opposite helicity, while 30 % have the same helicity. Defining the correlation as:

$$C = \frac{\sigma(t_R\bar{t}_R + t_L\bar{t}_L) - \sigma(t_R\bar{t}_L + t_L\bar{t}_R)}{\sigma(t_R\bar{t}_R + t_L\bar{t}_L) + \sigma(t_R\bar{t}_L + t_L\bar{t}_R)} \tag{1.14}$$

the helicities of the top and anti-top quarks have a correlation of -40% in this basis. For lighter quarks, which hadronizes before they decay, the spin information from their production is lost. Therefore, an observation of spin correlation is experimental evidence for a top quark life time shorter than the hadronization time. Such measurement would also put a lower bound on the top quark width and V_{tb} [90]. The DØ Collaboration has in Run I set a lower limit on the spin correlation [91].

The Top Quark Mass

The top quark mass is a fundamental parameter in the SM. It plays an important role in electroweak radiative corrections and is therefore contributing to the mass of the Higgs bosons as discussed in more detail below. The large value of the top quark mass indicates a strong coupling to the Higgs, and could provide special insights in our understanding of electroweak symmetry breaking [92]. The top quark mass could have a different origin than the masses of the lighter quarks. Thus precise measurements of the top quark mass provide a crucial test of the consistency of the standard model.

The top quark mass has been measured in lepton+jets, dilepton and all hadronic final states by the CDF and DØ Collaborations [52, 93–109]. At present the world average for the top quark mass, obtained from a combination of the measurements from the CDF and DØ Collaborations, is 171.4 ± 2.1 GeV/c^2 [39].

Constraining the Mass of the Higgs Boson

At tree level all electroweak quantities can be determined from the two electroweak gauge couplings g_W and g_Z and the vacuum expectation value of the Higgs field. These three parameters can at tree level be expressed in terms of the fine structure constant α, the mass of the Z boson m_Z, and the Fermi weak interaction coupling constant G_F, all of which are well-measured electroweak quantities. Expressed in terms of these quantities, the mass of the W boson is written [110]

$$m_W^2 = \frac{1}{2}m_Z^2\left(1+\sqrt{1-\frac{4\pi\alpha}{\sqrt{2}G_F m_Z^2}}\right), \tag{1.15}$$

which can be reduced to

$$m_W^2 = \frac{\frac{\pi\alpha}{\sqrt{2}G_F}}{\sin^2\theta_W}. \tag{1.16}$$

by introducing $\sin^2\theta_W$. At one-loop level, Eq. 1.16 is modified to

$$m_W^2 = \frac{\frac{\pi\alpha}{\sqrt{2}G_F}}{\sin^2\theta_W(1-\Delta r)}, \tag{1.17}$$

where Δr contains the one-loop corrections. The top quark mass enters the one-loop corrections to m_W^2 quadratically, as

$$(\Delta r)_{\text{top}} \approx -\frac{3G_F m_t^2}{8\sqrt{2}\pi^2}\frac{1}{\tan^2\theta_W}. \tag{1.18}$$

The one-loop top quark diagram contributing to Δr are shown in Figure 1.8. The

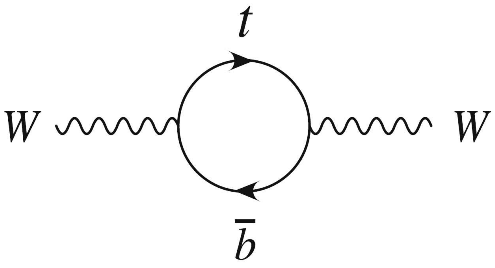

Figure 1.8: Virtual top quark loop contributing to the mass of the W boson.

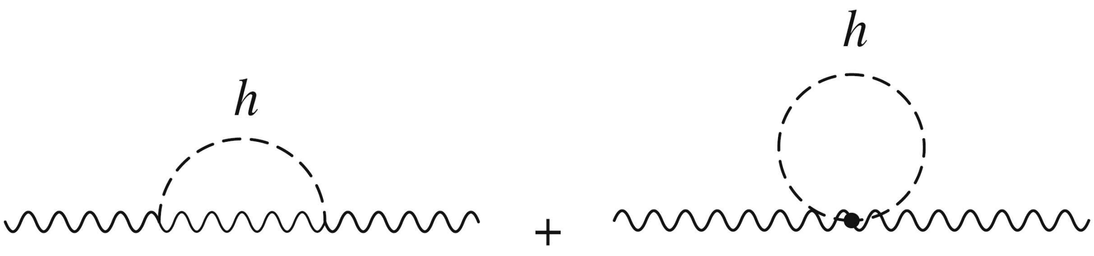

Figure 1.9: Virtual Higgs boson loops contributing to the mass of the W boson.

Higgs boson also contributes to Δr via the one-loop diagrams shown in Figure 1.9. The contribution to Δr from the Higgs mass is

$$(\Delta r)_{\text{Higgs}} \approx \frac{11 G_F m_Z^2 \cos^2\theta_W}{24\sqrt{2}\pi^2} \ln \frac{m_H^2}{m_Z^2}. \tag{1.19}$$

Thus, a precision measurement of the top quark mass will, together with m_W, m_Z, α and G_F, constrain the mass region in which to search for the Higgs boson. The constraint on the mass of the Higgs boson based on the most recent world average [39] is shown in Fig. 1.10 [111].

The Electric Charge of the Top Quark

In the standard model, the top quark has electric charge $+\frac{2}{3}e$, a property that, until recently, had never been directly measured by experiments. The particle found at Fermilab in 1995 was in principle allowed to have an electric charge $-\frac{4}{3}e$ due to the ambiguity when pairing the W bosons to the b quarks in the data events. Interpreting the particle found at Fermilab as an exotic quark with charge $-\frac{4}{3}e$ was consistent with current electroweak precision data [112–114].

A recent measurement done by the DØ Collaboration excludes at 92% C.L. the possibility that the top quark found at Fermilab is an exotic quark with electric charge $-\frac{4}{3}e$ [115].

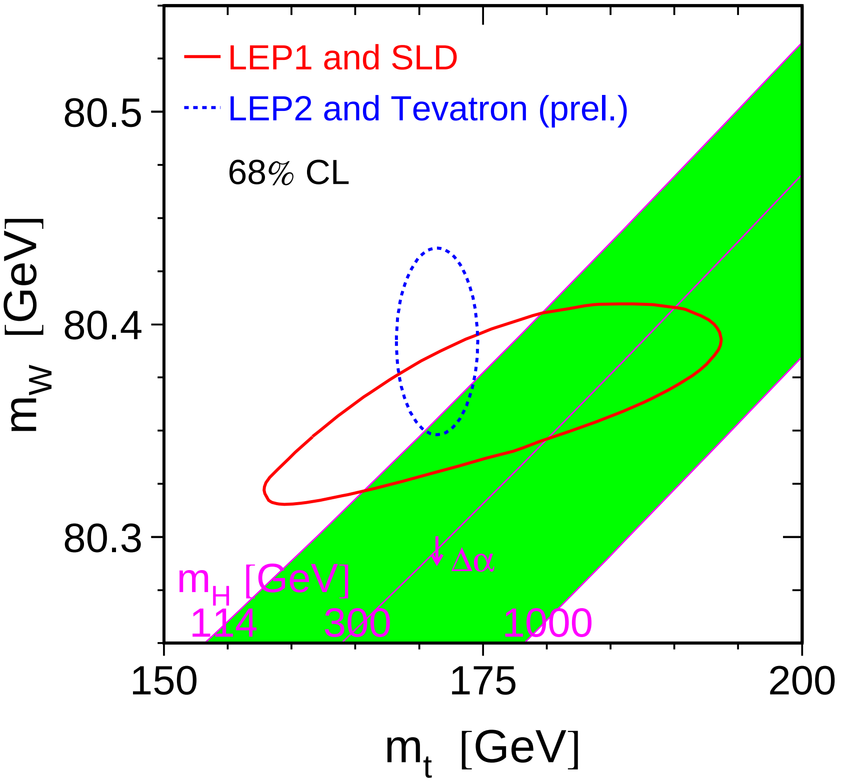

Figure 1.10: Contour curves of 68% confidence level in the (m_t, m_W) plane, both for indirect (LEP1, SLD data) and direct (LEP2, Tevatron data) determination. Also shown is the correlation between m_t and m_W as expected in the SM for different masses of the Higgs boson. The arrow labeled $\Delta\alpha$ shows the variation of this relation if $\alpha(m_Z^2)$ is changed by one standard deviation. The diagram was made by the LEP Electroweak Working Group in the summer of 2006 [111].

2 Experimental Apparatus

2.1 The Fermilab Accelerator Complex

The Tevatron accelerator began to operate in 1992. In the Run I of the Tevatron, which lasted from 1992 to 1996, the CDF and DØ experiments collected a data sample corresponding to an integrated luminosity[1] of 125 pb^{-1} at a center-of-mass energy of 1.8 TeV. Between 1996 and 2001 the Fermilab accelerator complex, as well as the CDF and DØ detectors, underwent major upgrades. The Tevatron Run II started in March 2001, and the Tevatron accelerator is now operating at an increased collision energy of 1.96 TeV. In addition, the bunch spacing has been reduced from 3.5 μs to 396 ns and the number of bunches increased from 6×6 to 36×36. The bunch crossing time of 396 ns results in a collision rate of 2.5 MHz. The transverse size of the Tevatron beam is approximately 30 μm and the length of each bunch approximately 38 cm.

Since the start of Run II, the Tevatron accelerator has delivered an integrated luminosity of 2.3 fb^{-1} to the DØ experiment out of which 2.0 fb^{-1} has been recorded by the experiment. The integrated luminosity as a function of time is shown in Fig. 2.1. The Tevatron is scheduled to run until 2009, and the goal of Run II is to collect between 4 and 8 fb^{-1} of data. The final luminosity will mainly depend on how well the Fermilab accelerator complex can create and store antiprotons.

The Tevatron is the final stage in a chain of seven accelerators [116–118]. A Cockcroft-Walton pre-accelerator, a linear accelerator (the Linac), and a synchrotron (the Booster) provide a source of 8 GeV protons. A nickel target, the Debuncher and the Accumulator make up the Antiproton Source which provides 8 GeV antiprotons. These can be stored either in the Antiproton Source itself or in an additional storage ring called the Recycler. The Main Injector serves as the final boosting stage for both protons and antiprotons before injection into the Tevatron. It also provides the high energy protons needed for the creation of antiprotons in the Antiproton Source. An overview of the Fermilab accelerator complex is shown in Fig. 2.2.

---

[1] The concept of luminosity is described in more detail in Sec. 2.2.5.

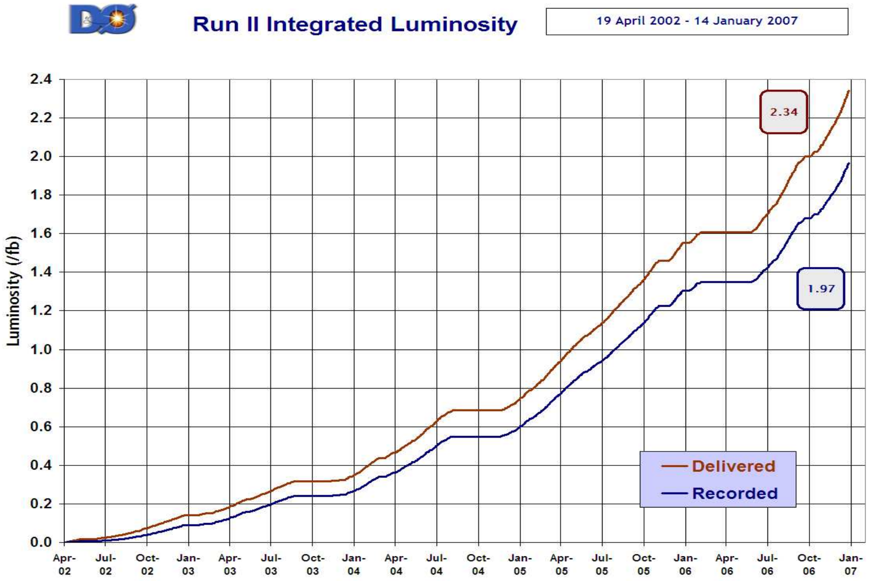

Figure 2.1: The integrated luminosity delivered by the Tevatron accelerator between April 2002 and December 2006. Shown is also the integrated luminosity recorded by the DØ experiment.

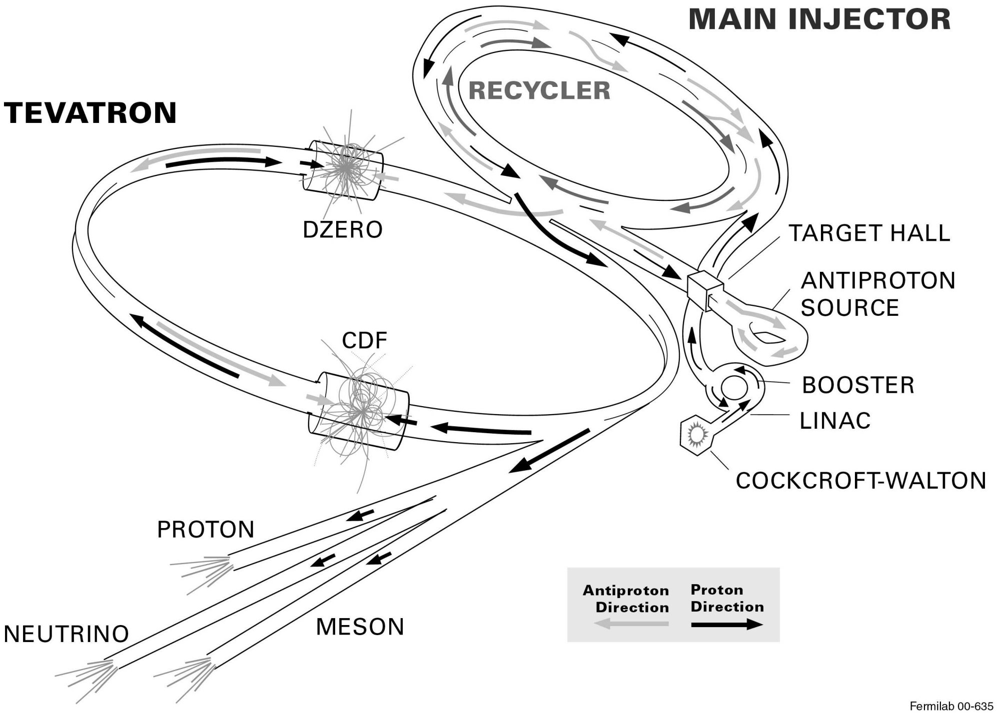

Figure 2.2: A schematic view of the Fermilab accelerator complex.

2.1.1 The Pre-accelerator

In the Pre-accelerator the negatively charged hydrogen ions are created and accelerated to 750 keV before being injected into the Linac.

An 18 keV negative hydrogen ion beam is created by a magnetron surface-plasma source [119]. The ion source is located within a metal enclosure kept at -750 kV by a commercial five stage dual-leg Cockcroft-Walton generator. After being accelerated to 750 keV, the beam travels through a transport line and then enters the Linac.

2.1.2 The Linac

The Linac is the next level of acceleration for the negatively charged hydrogen ions. It takes ions with an energy of 750 keV and accelerates them to an energy of 400 MeV. The Linac consists of two main sections, a low energy Alvarez drift-tube linac, and a high energy side-coupled linac.

The drift-tube linac is 79 m long and makes up the first five RF stations. It accelerates the ions to 116 MeV. The last seven RF stations make up the 67 m long side-coupled linac. These RF stations use Klystron amplifiers instead of the tube technology of the low energy end. The side-coupled cavity linac modules accelerates the beam to the full energy of 400 MeV. After the beam is accelerated in the Linac it is sent through the 400 MeV transfer line which connects the Linac to the Booster.

2.1.3 The Booster

The Booster is the next level of acceleration, and is the first circular accelerator in the chain, with a radius of 75 m. It receives negative hydrogen ions with an energy of 400 MeV. The electrons are stripped off the negative hydrogen ions which results in a proton beam. The protons are then accelerated to 8 GeV by 18 RF cavities.

2.1.4 The Main Injector

The Main Injector is a circular synchrotron with seven times the circumference of the Booster. It has 18 accelerating cavities which can be used to accelerate protons from the Booster as well as antiprotons from the Antiproton Source. As a step in the production of antiprotons, protons coming from the Booster are accelerated to 120 GeV before being sent to the Antiproton Source. Protons from the Booster and antiprotons from the Antiproton Source which are to be injected into the Tevatron are accelerated to 150 GeV.

2.1.5 The Antiproton Source

The Antiproton Source consists of an antiproton target station, the Debuncher and the Accumulator.

In the target, 120 GeV protons from the Main Injector strike a nickel target which creates a spray of secondary particles. Using magnets, 8 GeV antiprotons can be selected from this spray. These antiprotons are directed via a transfer line to the Debuncher.

The Debuncher is a rounded, triangular-shaped synchrotron with a mean radius of 90 m. It is one of the two synchrotrons which make up the Antiproton Source and it accepts 8 GeV antiprotons from the target station. Its primary purpose is to efficiently capture the antiprotons coming off the target and actively decrease their momentum spread (referred to as cooling). The Debuncher does not accelerate the antiprotons but keeps the beam at a constant energy of 8 GeV.

The Accumulator is the second stage synchrotron of the antiproton source. It is also triangular-shaped with a radius of 75 m. It is housed in the same tunnel as the Debuncher and is a storage ring for the antiprotons. They are kept here at 8 GeV and cooled until needed.

2.1.6 The Recycler

The Recycler is a high reliability antiproton storage ring located along the ceiling of the Main Injector tunnel. It receives antiprotons from the Accumulator and stores them until the Tevatron is ready for its next store. It also collects the antiprotons from the Tevatron at the end of a store. These antiprotons can then be used alongside those from the Antiproton Source.

2.1.7 The Tevatron

The Tevatron is the largest of the Fermilab accelerators with a circumference of approximately 6.5 kilometers. It is a circular synchrotron with eight accelerating cavities. The Tevatron can accept both protons and antiprotons from the Main Injector and accelerate them from 150 GeV to 980 GeV. In collider mode the Tevatron can store beam for hours at a time.

The Tevatron is the only cryogenically cooled accelerator at Fermilab. The magnets used in the Tevatron produce a magnetic field of 4.2 T. They are made up of a superconducting niobium/titanium alloy that needs to be kept at $\sim$4 K in order to remain a superconductor.

The Tevatron is not a perfect circle, but is divided into six segments (A0-F0). The CDF detector is located in the B0 sector whereas the DØ detector is located in the D0 sector.

2.2 The DØ Detector

The DØ detector, shown in Fig 2.3, is a multi-purpose detector designed to identify, and precisely measure the four-momenta of the particles created in the proton-antiproton collisions. The detector consists of three major sub-systems, a central tracking system, a calorimeter and a muon system. The DØ detector is described in greater detail in [120, 121].

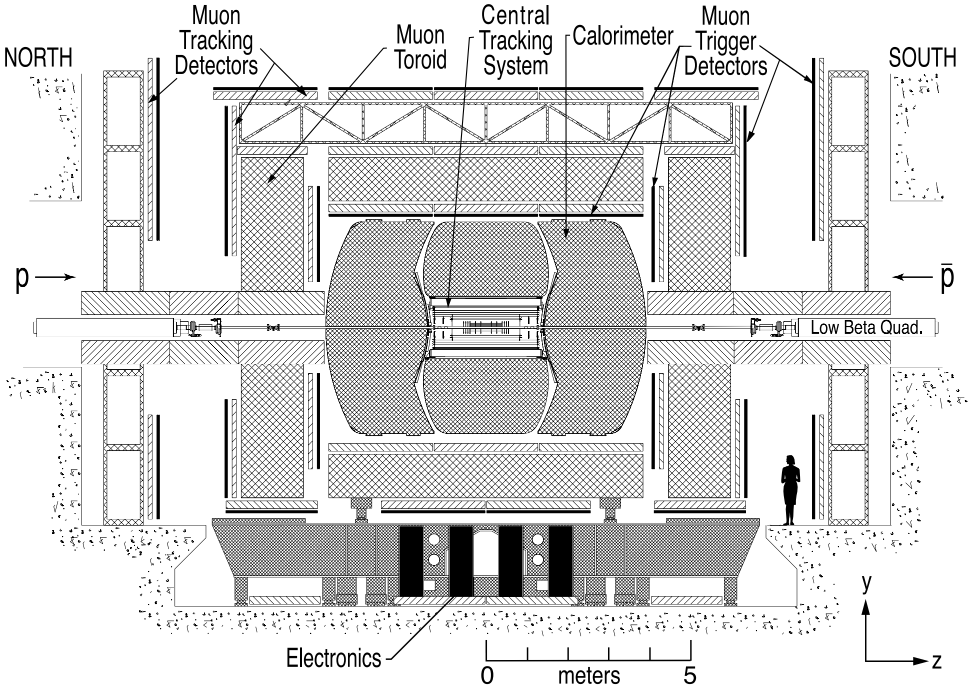

Figure 2.3: Cross section of the DØ detector in the vertical plane. The definition of the DØ coordinate system is shown in the lower right corner.

The DØ coordinate system is shown in Fig. 2.3. It is a right-handed coordinate system with the positive z-axis pointing along the direction of the proton beam, the positive x-axis pointing radially outward from the center of the Tevatron accelerator and the positive y-axis pointing vertically upwards. The x- and y-axes define the transverse plane. The coordinate system is often expressed in terms of the standard polar coordinates

$$\begin{aligned} r &= \sqrt{x^2+y^2} && (2.1)\\ \theta &= \arccos\frac{z}{\sqrt{x^2+y^2+z^2}} && (2.2)\\ \phi &= \arctan\frac{x}{y} && (2.3) \end{aligned}$$

where θ takes values from 0 to π and ϕ from 0 to 2π.

Since the angle θ is not invariant under Lorentz transformations along the z-axis, it is more common to use the rapidity y

$$y = \frac{1}{2}\ln\left(\frac{E + p_z}{E - p_z}\right) \tag{2.4}$$

or the pseudorapidity η

$$\eta = -\ln\left(\tan\frac{\theta}{2}\right). \tag{2.5}$$

The pseudorapidity is equal to the rapidity for massless particles. For highly relativistic particles the pseudorapidity is a good approximation of the rapidity. The separation between two directions, labeled 1 and 2, can be expressed as the Lorentz invariant distance ΔR between them in the (η, ϕ)-plane

$$\Delta R = \sqrt{(\eta_1 - \eta_2)^2 + (\phi_1 - \phi_2)^2}. \tag{2.6}$$

2.2.1 The Central Tracking System

In order to identify charged particles and measure their momenta, the DØ detector is equipped with a set of tracking detectors located inside of a solenoid providing a 2 T magnetic field. To get many measurement points, the tracking system consists both of a silicon microstrip tracker (SMT) and a central fiber tracker (CFT). A schematic view of the tracking system is shown in Fig. 2.4.

The central tracking system is located closest to the interaction point to ensure precise measurements of the primary interaction point and the impact parameter of tracks from charged particles. The magnetic field bends the trajectories of charged particles in the (x, y)-plane as they pass through the tracking detectors. The momentum of a particle is inferred from the radius of its trajectory:

$$p_T[\mathrm{GeV}/c] = 0.3 \cdot r[\mathrm{m}] \cdot \mathrm{B[T]}\ \mathrm{GeV}/c^2 \tag{2.7}$$

where r is the radius and B the magnetic field.

The two tracking detectors locate the primary interaction vertex with a resolution of about 35 μm along the beam direction and about 15 μm in the transverse $(r - \phi)$ plane. A high resolution of the interaction vertex allows for accurate measurements of the transverse momentum of leptons, transverse energy of jets and missing transverse energy. It is also crucial for the identification of jets originating from b quarks (b-tagging).

The Silicon Microstrip Tracker

The SMT is the high resolution part of the tracking system, and is designed to enable tracking for particles at pseudorapidities as high as $|\eta| = 3$. Since the luminous region extends over 60 cm in the z direction, the SMT has to cover a significant region in z. To meet these criteria it is built up of both barrels and disks. The

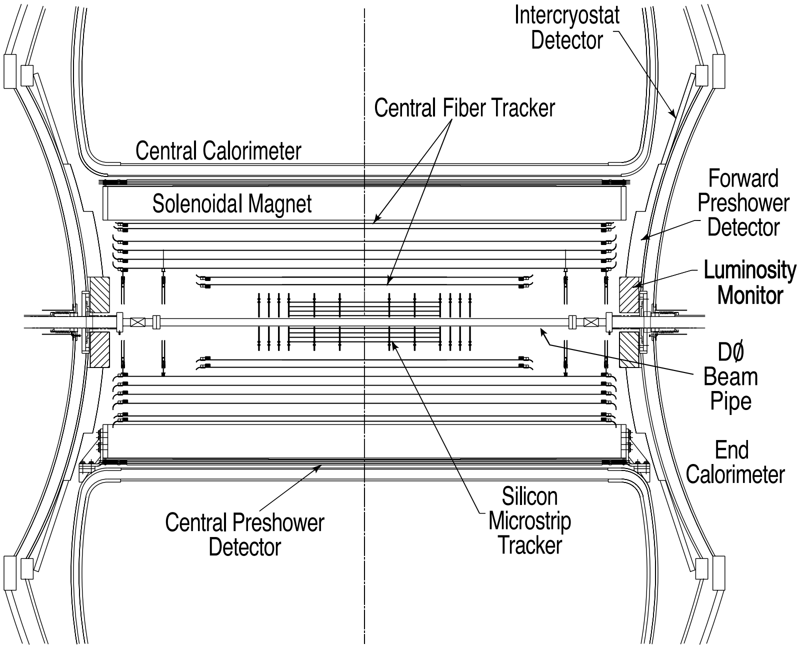

Figure 2.4: The DØ tracking system. Also shown are the locations of the solenoid, the preshower detectors, luminosity monitors and the calorimeters.

design of the SMT is shown in Fig. 2.5. The central part of the SMT extends to $|z| = 40$ cm and consists of six barrels, each capped at high $|z|$ by a disk, referred to as an F-disk. On each side of the central structure there are three additional F-disks and further out, at $|z| = 100$ cm and $|z| = 120$ cm, two larger disks called H-disks. Tracks with low pseudorapidity are measured primarily in the barrels while high pseudorapidity tracks pass mainly through the disks.

The barrels and disks are constructed from silicon microstrip sensors with a hit resolution of approximately 10 μm. The silicon units in the barrels are named ladders whereas those in the disks are called wedges. Each barrel in the SMT consists of eight layers, where two layers are needed to achieve full coverage. The innermost 4 layers are made up of 6 ladders per layer and the outermost 4 layers of 12 ladders per layer. The barrel structure of the SMT is shown in Fig. 2.6(a). Each F-disk contain 12 wedges whereas the H-disks are made up of 24 wedges. An (r,ϕ)-view of an F-disk is shown in Fig. 2.6(b).

The silicon sensors are micro-bonded to SVXIIe readout chips [122, 123]. Each chip is connected to 128 silicon strips with widths varying from 50-150 μm. In total the SMT consists of 793,000 strips. There are five different types of silicon sensors in the SMT, called 3-chip, 6-chip and 9-chip ladders after the number of readout chips, as well as F-wedges and H-wedges. The layout of a 9-chip ladder is shown in Fig. 2.7. The 3-chip ladders are the only single-sided sensors in the barrel region.

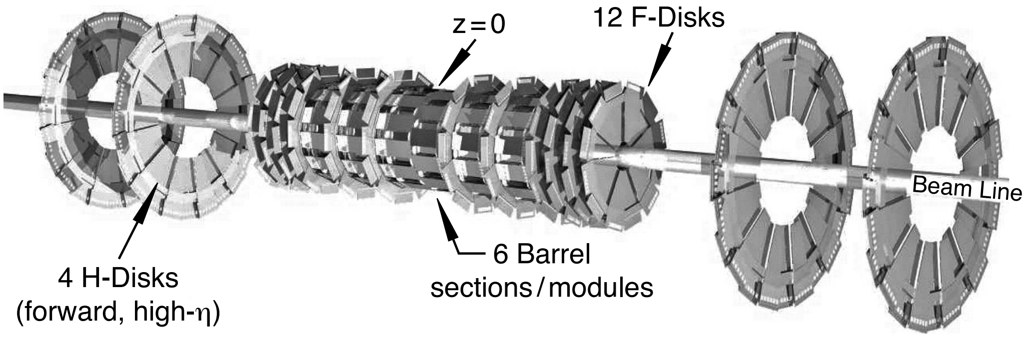

Figure 2.5: The geometry of the DØ Silicon Microstrip Tracker. There are six barrels, 12 smaller F-disks located in between and just outside the barrels and 4 larger H-disks.

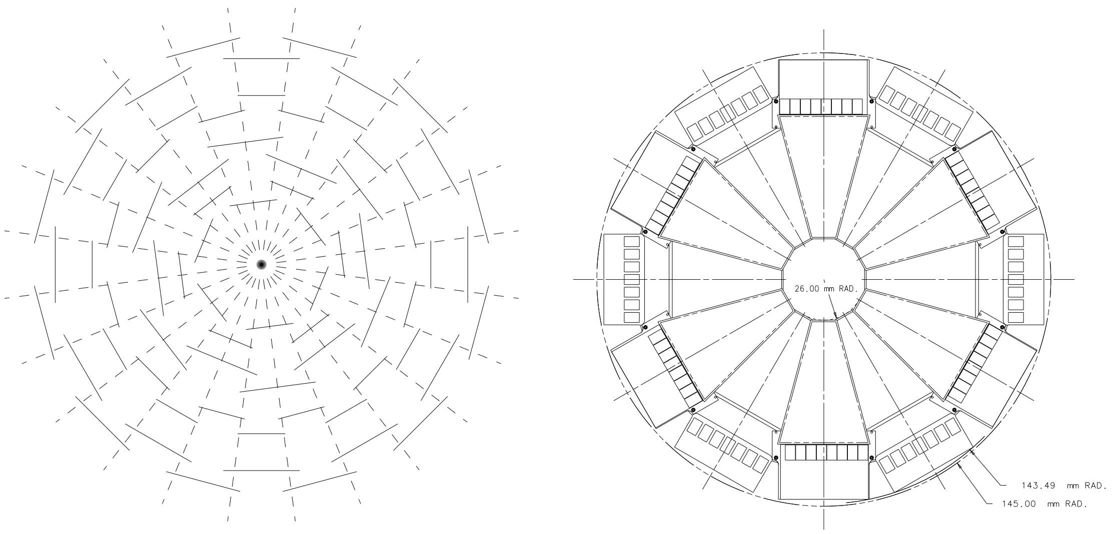

(a) Drawing of the ladder structure in an SMT barrel. A barrel consists of eight layers. Two layers are needed to provide a complete coverage in ϕ.

(b) A drawing of the F-disk layout in the (r,ϕ)-plane.

Figure 2.6: Layouts of the SMT barrels and disks, viewed in the (r,ϕ)-plane.

They populate layers 1 and 3 of the outer barrels. The 6-chip ladders are double-sided, double-metal sensors with a stereo angle of 90° and populate layers 2 and 4 of all barrels. The 9-chip ladders, which populate layers 1 and 3 of the innermost barrels, have a less complicated double-sided design with a stereo angle of 2°. The F-wedges are double-sided with a effective stereo angle of 30°, whereas the H-wedges consist of two single-sided detectors glued together to form a double-sided sensor with an effective stereo angle of 15°.

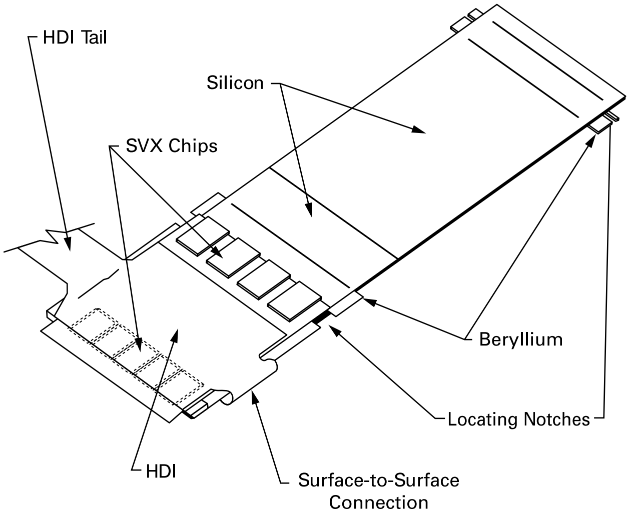

Figure 2.7: Drawing of a silicon ladder showing the sensor, the readout chips and the High Density Interconnect (HDI).

The Central Fiber Tracker

The central fiber tracker consists of 835 μm scintillating fibers mounted on eight concentral support cylinders. The CFT occupies the radial space from 20 to 52 cm from the center of the beampipe. The outer six cylinders are 2.52 m long whereas the inner two cylinders are only 1.66 m long in order to accommodate the SMT H-disks. The CFT covers the rapidity range $|\eta| < 1.7$.

Each CFT cylinder supports one doublet layer of fibers oriented along the beam direction (axial layer) and a second doublet layer of fibers at a stereo angle of alternating $+3°$ and $-3°$ (stereo layers). Within each doublet layer the outer layer is offset by half the fiber spacing with respect to the inner layer in order to improve the coverage. A wedge of the CFT with the eight axial layers showing is depicted in Fig. 2.8. The small fiber diameter gives the CFT an inherent doublet layer resolution of about 100 μm as long as the location of the individual fibers is known to better than 50 μm. The total number of readout channels in the CFT is approximately 77,000.

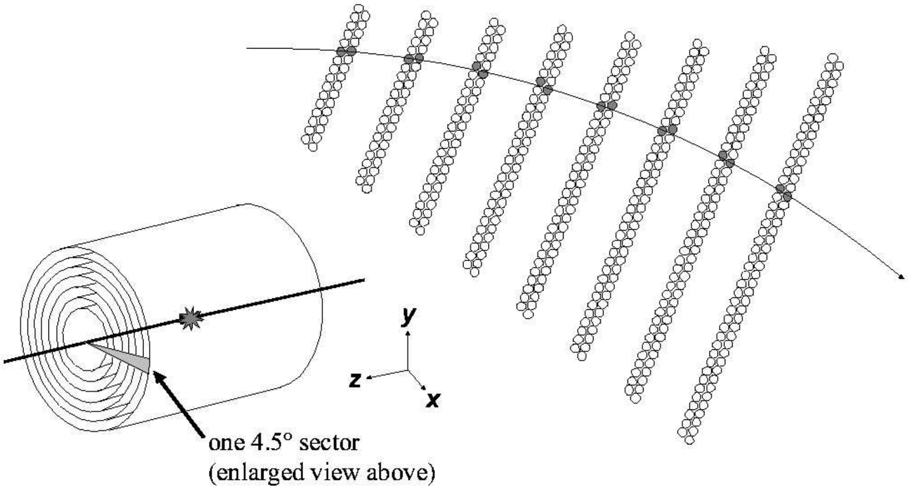

Figure 2.8: A 4.5° wedge of the CFT, showing the eight axial layers. Each axial layer consists of two layers of fibers, one layer offset by half the fiber spacing with respect to its partner. Outside each axial layer there is a stereo layer which is not shown in this picture.

Light from the fibers is observed at only one end of the fiber. The opposite end is covered with an aluminum coating that provides a reflectivity of about 90%. The fibers are coupled to clear fiber waveguides which carry the scintillator light to visible light photon counters (VLPCs) for readout. The VLPCs are impurity-band silicon avalanche photodetectors which are capable of detecting single photons. They convert the light generated by charged particles traversing the CFT fibers to electric signals. The VLPC signals are in turn processed by analog frontend boards (AFE boards). For reasons of simplicity the readout chips on the AFE boards are the same SVXIIe chips used by the SMT. However, because the signals from the CFT are used also in the first level of the trigger (L1) and the SVXIIe digitization speed is too slow to generate a trigger signal, the AFE boards are also equipped with faster chips named SIFT chips.

2.2.2 The Calorimeter System

The calorimeter system is designed to measure the energy of electrons, photons, jets and, indirectly, neutrinos. It consists of preshower detectors which aid in the electron identification as well as of electromagnetic and hadronic calorimeters. Passive layers of dense material, where electrons, photons and hadrons initiate particle showers, are followed by active layers where the shower energy is sampled. In general, muons deposit only a small fraction of their energy in the calorimeter system. Neutrinos deposit no energy in the detectors, but can be reconstructed from the transverse energy imbalance in the event.

Electrons passing through matter lose energy primarily through ionization and bremsstrahlung. Above the critical energy E_c bremsstrahlung is the dominant process. The critical energy can be approximated by [28]:

$$E_c = \frac{800}{Z + 1.2}\ \mathrm{MeV}, \tag{2.8}$$

where Z is the atomic number. The emitted photons produce e^+e^- pairs which in turn radiate photons. The resulting shower of electrons and photons grows until the energy of the electrons falls below the critical energy, where they primarily interact through ionization. The mean distance over which an electron loses all but $1/e$ of its energy is called the radiation length X_0 [28],

$$X_0 = \frac{716.4A}{Z(Z+1)\ln(287/\sqrt{Z})}\ \mathrm{g\,cm^{-2}}, \tag{2.9}$$

where A is the atomic mass of the medium in $\mathrm{g\,mol^{-1}}$.

Photons interacting with matter produce e^+e^- pairs, creating an electromagnetic shower in the calorimeter. Since photons are not electrically charged they do not leave a track in the tracking detectors. This is what mainly distinguishes the photon signature from that of the electron.

Hadronic particles passing through matter interact inelastically with nuclei to primarily produce pions and nucleons. At high energies the produced particles in turn interact with nearby nuclei to produce a shower of hadronic particles. The characteristic length scale is the nuclear interaction length λ_I [28],

$$\lambda_I \approx 35 \cdot A^{1/3}\ \mathrm{g\,cm^{-2}}, \tag{2.10}$$

where A is the atomic mass of the medium in $\mathrm{g\,mol^{-1}}$. A significant fraction of the energy of the initial hadron escapes detection. The main sources of energy loss are through unbinding of nuclei by spallation, non-ionizing collisions and neutrino production.

The Preshower Detectors

The preshower detectors aid in electron identification and background rejection during both triggering and offline reconstruction. They function as calorimeters as well as tracking detectors, enhancing the spatial match between tracks and calorimeter showers.

The preshower detectors are made from triangular strips of scintillating material, as shown in Fig. 2.9. Since the triangles are interleaved there is no dead space, and most particles traverse more than one strip. Embedded at the center of each strip is

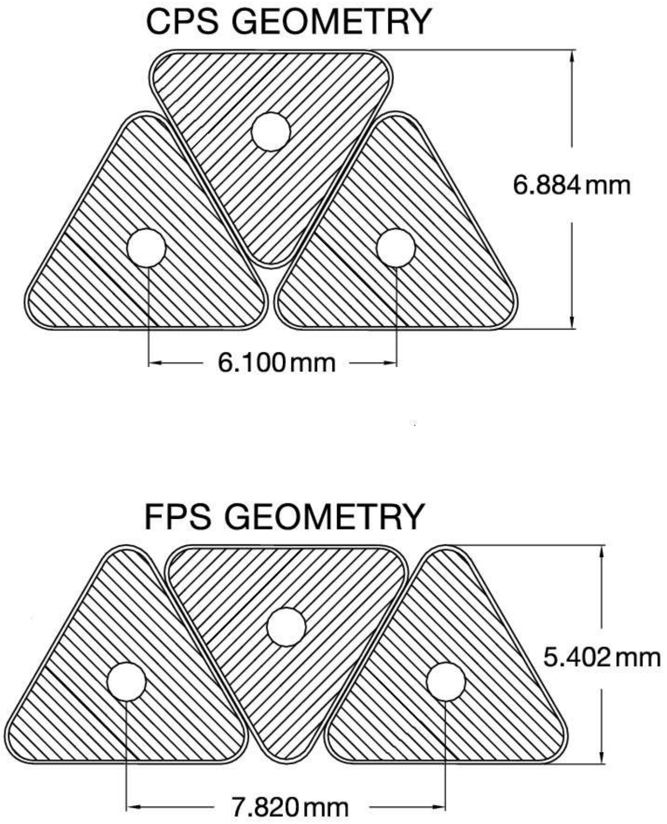

Figure 2.9: Cross section of a layer in the CPS and the FPS. The circles inside the triangular scintillators show the location of the fibers used to read out the light signals.

a wavelength-shifting fiber which collects the light created by the traversing charged particles. The light is transported via clear fibers to VLPCs for readout.

The central preshower detector (CPS) covers the region $|\eta| < 1.3$ and is located in the 5 cm space between the solenoid and the central calorimeter. Between the solenoid and the CPS is a lead radiator which is approximately one radiation length (X_0) thick. The solenoid itself is $0.9X_0$ thick, providing a total of about two radiation lengths of material for particles at $|\eta| \approx 0$, increasing to about four radiation lengths at the largest angles. The CPS is made up of one axial layer and two stereo layers of scintillators with a stereo angle of approximately 24°.

The forward preshower detectors (FPS) are attached to the faces of the end calorimeters. Each detector is made from two layers, where each layer consists of two sublayers of scintillator strips. The two planes have a stereo angle of 22.5° with respect to each other. A $2X_0$-thick lead-stainless-steel absorber separates the two layers. The layer closest to the interaction point are referred to as the minimum ionizing particle (MIP) layer, whereas the layer behind the absorber is called the shower layer. The shower layer covers $1.5 < |\eta| < 2.5$ whereas the MIP layers cover the region $1.65 < |\eta| < 2.5$. A complete ϕ-segment of the FPS is shown in Fig. 2.10.

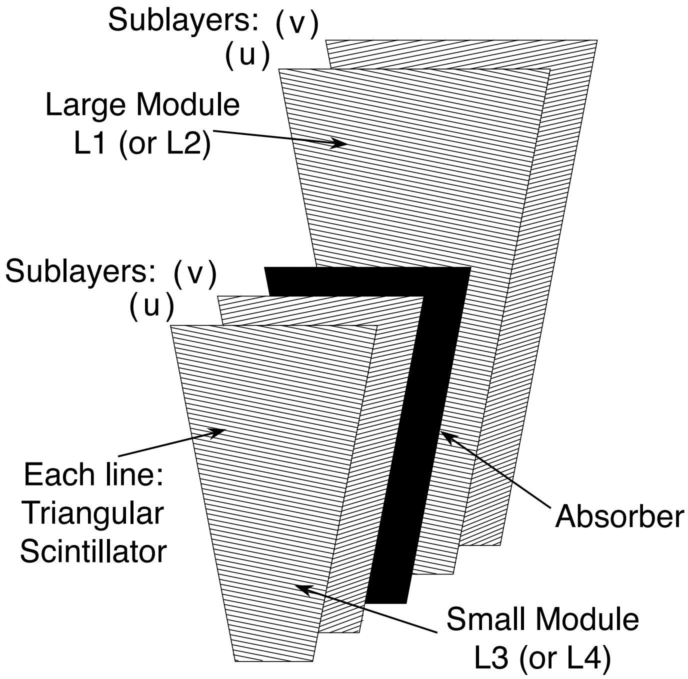

Figure 2.10: Complete ϕ-segment of a FPS module showing the overlapping MIP and shower layers, separated by a lead and stainless steel absorber.

The Calorimeters

In addition to the preshower detectors, the DØ calorimeter system consists of three sampling calorimeters and an intercryostat detector. The calorimeters, which are depicted in Fig. 2.11(a), are unchanged from Run I but have significantly more upstream material in Run II ($2 \leq X_0 \leq 4$ depending on η). Also the front-end electronics has been replaced in order to handle the higher collision rate.

The central calorimeter (CC) covers $|\eta| \leq 1$ and the two end calorimeters (EC) extend the coverage to $|\eta| = 4$. Each calorimeter contains an electromagnetic (EM) section closest to the interaction region followed by fine and course hadronic (H) sections whose size increases with the radial distance from the interaction region.

The active medium for all three calorimeters is liquid argon which is ionized by the charged particles within a shower. Each of the three calorimeters is located in its own cryostat maintaining the detector temperature at approximately 90 K. Different absorber plates are used in different regions. The electromagnetic sections use thin plates (3-4 mm thick) of nearly depleted uranium. The hadronic sections have 6 mm thick uranium-niobium alloy. The coarse hadronic modules contain relatively thick (46.5 mm) plates of copper (CC) or stainless steel (EC).

A typical calorimeter readout cell contains the absorber plates, the liquid argon and a signal board, made from copper pads covered in resistive material, for collecting the signal. The electric field is established by grounding the absorber plates and connecting the resistive surfaces of the signal board to high voltage (typically 2 kV). The electron drift time across the 2.3 mm liquid argon gap is approximately 450 ns.

There are four separate depth layers for the electromagnetic modules in CC an EC. In the CC the layers are approximately 1.4, 2.0, 6.8 and 9.8 X_0 thick. In the EC they are approximately 1.6, 2.6, 7.9 and 9.3 X_0 thick. In the CC the fine hadronic modules have three longitudinal gangings of approximately 1.3, 1.0 and 0.76 λ_I. The nuclear interaction length λ_I is much longer than the radiation length. In uranium

$$1\lambda_I^{Ur} \approx 10.5 \text{ cm} \approx 30X_0^{Ur}. \tag{2.11}$$

The single coarse hadronic module has a thickness of about 3.2 λ_I. The inner and middle EC fine hadronic readout cells are 0.9 to 1.1 λ_I thick whereas the course hadronic ones are 4.1 to 4.4 λ_I thick. The outer hadronic modules of the EC are made from stainless steel plates and have a maximum thickness of 6.0 λ_I.

The transverse sizes of the readout cells are comparable to the transverse sizes of showers (1-2 cm for electromagnetic showers and about 10 cm for hadronic showers). Calorimeter readout cells form pseudo-projective towers as shown in Fig. 2.11(b) with each tower subdivided in depth. The towers in both electromagnetic and hadronic modules are $\Delta\eta = 0.1$ and $\Delta\phi \approx 0.1$. The third layer of electromagnetic modules, located at the electromagnetic shower maximum, is segmented twice as finely in both η and ϕ to allow for a more precise location of the electromagnetic

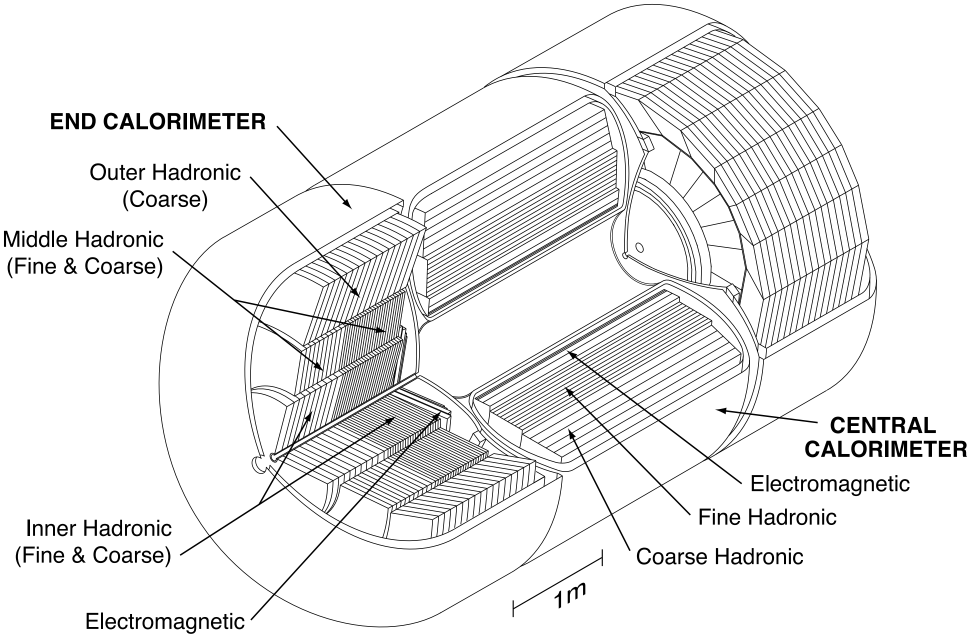

(a) Isometric view of the central calorimeter and the two end calorimeters.

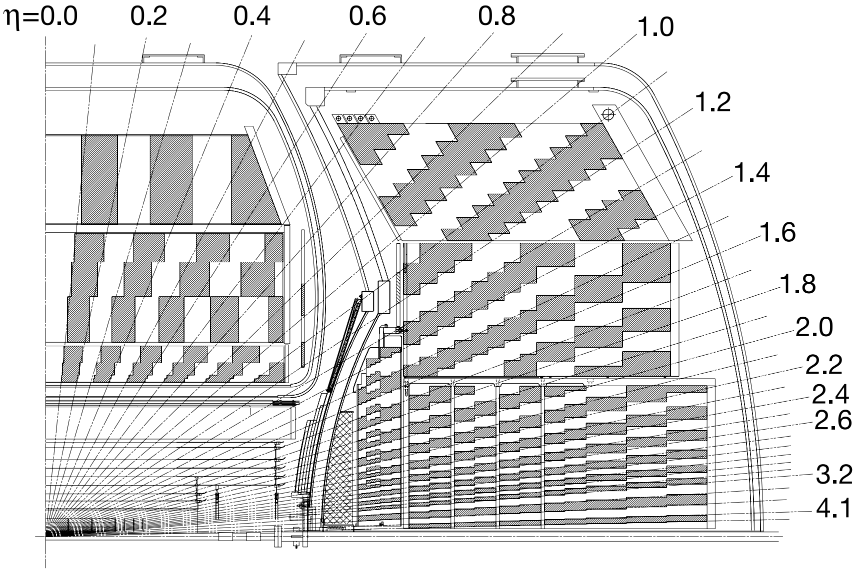

(b) Drawing of one quadrant of the DØ calorimeter. The shading pattern indicates groups of cells ganged together into readout towers. The rays indicate pseudorapidity intervals from the center of the detector.

Figure 2.11: Drawings of the DØ calorimeter.

shower centroids. The cell sizes increases in both η and ϕ at larger η to avoid very small cells.

Given that the calorimeter is housed in three separate cryostats it provides incomplete coverage in the region $0.8 \leq |\eta| \leq 1.4$. Additional layers of sampling detectors in the form of scintillating counters are added between the CC and EC cryostats. These counters are called the intercryostat detector (ICD) and are visible in Fig. 2.4. They have a segmentation of $\Delta\eta \times \Delta\phi = 0.1 \times 0.1$. In addition, separate single-cell scintillator structures called massless gaps are installed in both the CC and EC.

2.2.3 The Muon System

Muons originating from the central collision point traverse the calorimeter without being stopped. The muon system is therefore the outermost part of the DØ detector and serves to detect these muons as well as provide a rough measurement of their momenta and charge.

The muon system is depicted in Fig. 2.12. It consists of scintillator counters used for triggering and wire chambers used for precise coordinate measurements as well as for triggering. To allow for local measurements of muon momenta, the muon system also contains toroidal magnets giving an internal field of 1.8 T. The muon system has three layers of wire chambers called A, B and C. The A layer is the innermost one and is located between the calorimeter and the toroid whereas the B and C layers are located outside the magnet. The region directly below the DØ detector has only partial muon coverage due to the presence of detector support structures and readout electronics.

The central muon system provides coverage to $|\eta| = 1$ and consists of proportional drift tubes (PDTs) and scintillation counters. Each PDT consists of a gas-filled rectangular shaped aluminum enclosure with an anode wire at the center. Two cathode pads, made of thin copper-clad strips, are placed above and below the anode wire to determine the longitudinal position of the muon hits. The gas mixture used in the PDTs consists of 84% argon, 8% methane and 8% CF_4.

Two neighboring wires are connected to decrease the number of electronics channels and each wire pair is read out only at one end. To distinguish which of the two neighboring wires that is hit there is a delay line in the middle.

The PDTs register the electron drift time, the difference ΔT in the arrival time of the signal pulse at the end of the hit cell's wire and the end of its readout partner's wire, and the charge deposition on the cathode pads. The PDTs have a maximum drift time of 500 ns. Both ΔT and the charge deposition are used to determine the hit position along the wire. The coordinate resolution based solely on timing information is 10-50 cm. Using charge division the resolution is about 5 mm. Only the A-layer pads are fully instrumented compared to only 10% of the pads in the B and C layers. For tracks traversing all three layers, pad coordinates in the B- and

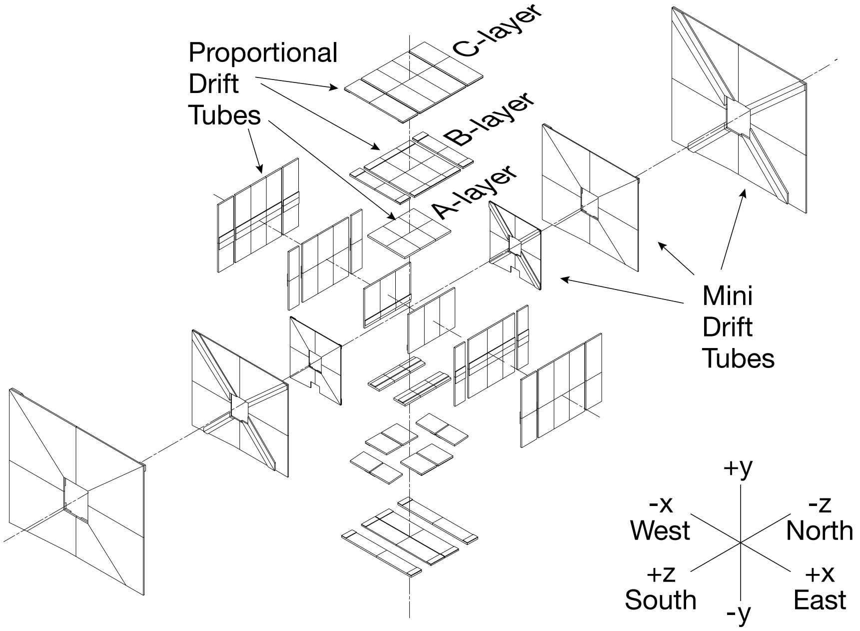

(a) Exploded view of the muon wire chambers.

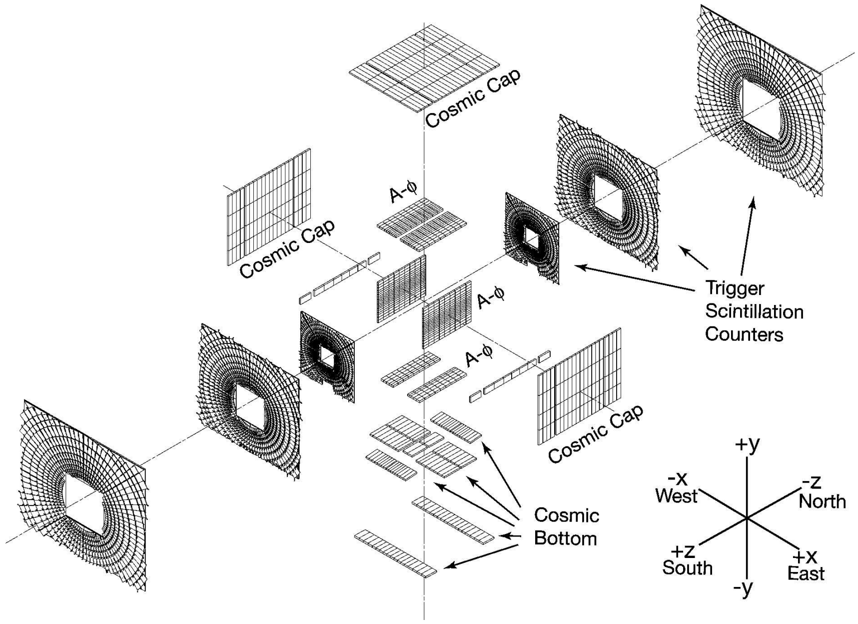

(b) Exploded view of the muon scintillator detectors.

Figure 2.12: The DØ muon system, which consists of wire chambers and scintillator detectors.

C-layers would not improve the pattern recognition or resolution significantly.

The forward muon system extends the coverage to $|\eta| \leq 2$ and consists of mini drift tubes (MDTs) rather than PDTs and also includes scintillating counters. Each MDT consists of eight 1×1 cm^2 cells, each containing a gold-plated tungsten anode wire. The MDTs have a shorter drift time (40-60 ns) and better coordinate resolution (≈ 0.7 mm) compared to the PDTs. The gas mixture used in the MDT system is 90% CF_4 and 10% CH_4.

2.2.4 The Trigger System

Most of the proton-antiproton collisions occurring at DØ result in low energy QCD processes which are of little interest in physics analyses. Collisions which create heavy particles such as W bosons, Z bosons and top quarks are very rare. In order to accumulate a large number of the most interesting events without having to store and reconstruct a staggering number of less interesting ones, the DØ detector is equipped with a trigger that decides whether an event should be recorded or discarded. The DØ trigger has to reduce the input rate of 2.5 MHz (given by the time between bunch crossings) to 50 Hz which is the event rate possible for the reconstruction software to process.

Three distinct levels form the trigger system. Each subsequent level handles a lower event rate and can therefore examine the event in more detail. The first stage, called Level 1 (L1) comprises a collection of hardware trigger elements. In L1 the 2.5 MHz input rate is reduced to approximately 2 kHz which is the input rate for the second level trigger (L2). At L2 hardware engines and embedded microprocessors associated with specific subdetectors provide information to a global processor which constructs a trigger decision based on individual objects as well as object correlations. The L2 trigger system reduces the rate by a factor of two and has an accept rate of approximately 1 kHz. Events which are passed by L1 and L2 are sent to the L3 trigger farm for real time reconstruction. Here sophisticated algorithms reduce the rate to 50 Hz. The events accepted by L3 are stored for offline reconstruction. An overview of the DØ trigger system is shown in Fig. 2.13.

Due to improvements made to the Tevatron accelerator complex, the instantaneous luminosity has been increasing since the start of Run II. In order to keep the L3 accept rate constant, the sets of triggers used to collect the data have to be updated accordingly. A specific set of triggers running online is referred to as a trigger list. The data set used in this thesis is collected with trigger list versions 8–13.

The Level 1 Trigger

The L1 trigger is implemented in specialized hardware and is tightly connected with the subdetectors.

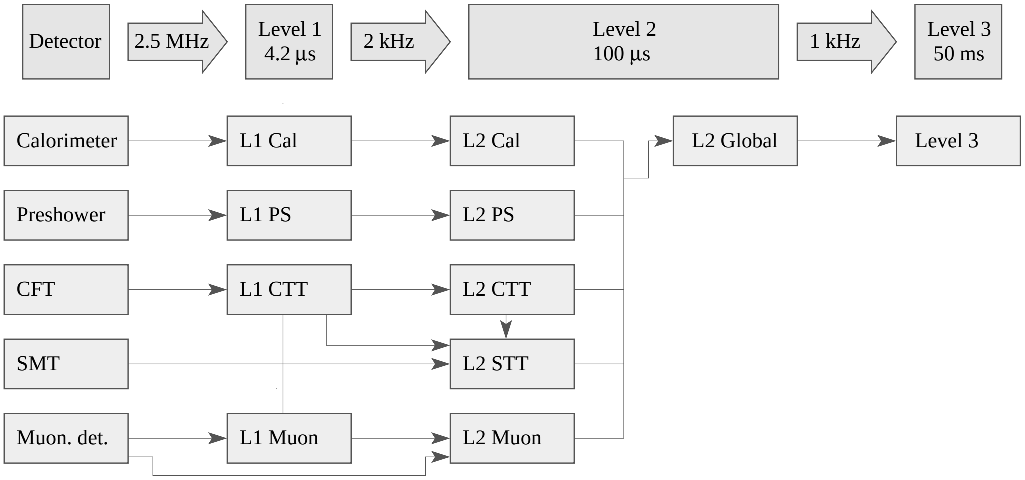

Figure 2.13: A summary of the components of the L1 and L2 trigger and the input rate at each level of the trigger system.

The calorimeter trigger (L1Cal): The calorimeter trigger looks at the energies deposited in towers of size $\Delta\eta \times \Delta\phi = 0.2 \times 0.2$. A L1Cal trigger requires a certain number of trigger towers above an adjustable energy threshold. The trigger inputs consists of electromagnetic and hadronic tower energies made up of fast analog pickoffs from the standard calorimeter readout. The tower energies are converted to E_T, the pedestals are subtracted and the energy scale is adjusted. The variables used in the L1Cal are actually the EM transverse energies and the total (EM+H) transverse energies. The EM towers are used to trigger on electrons and photons whereas the EM+H towers are used to trigger on hadronic jets.

The central track trigger (L1CTT): The central track trigger is designed for the ability to trigger on charged particles with $p_T > 1.5$ GeV/c and to find preshower clusters and match them to tracks. It reconstructs the trajectories of charged particles using fast SIFT chip data provided by the CFT (axial fibers only), the CPS (axial strips only) and the FPS. The CFT fibers are arranged in 4.5° trigger sectors in the transverse plane. The fiber hits from each 4.5° trigger sector are compared with approximately 20,000 predefined analytically generated track equations.

The muon trigger (L1Muon): The muon trigger is divided into three regions: central, north and south. The central region ($|\eta| < 1$) takes input from the central muon system and the north ($-2 < \eta < -1$) and south ($1 < \eta < 2$) regions use data from the forward muon system. Both scintillation counter hits and wire chamber centroids are used. The scintillator confirmation is necessary since the drift time of the PDTs (≈ 500 ns) is larger than the beam crossing time, so that centroids can originate from any of several crossings. L1 muons are classified according to their p_T (above 2, 4, 7 or 11 GeV), their pseudorapidity region and their quality (loose, medium or tight). The quality reflects how many muon detectors or layers are used in forming the candidate muons. Loose L1 muons are constructed from scintillator hits only, while tight L1 muons include hits in the wire chambers. The L1 muon trigger can also operate together with the L1CTT, matching CFT tracks with scintillator hits.

The final L1 trigger decision is taken by combining information from the various L1 systems and comparing it to a set of predefined trigger terms.

The Level 2 Trigger

The L2 trigger consists of two stages, preprocessors which are specific to each subdetector and a global processor which combines information from the different preprocessors to make a trigger decision. The L2 trigger system is the first one in the chain to look at event-wide variables to create objects like muons, electrons or jets.

The calorimeter trigger (L2Cal): The calorimeter preprocessor identifies electrons/photons and jets and calculates the event $\not\!\!E_T$ to be used by the L2 global processor. The jet algorithm operates by clustering $n \times n$ groups of calorimeter trigger towers which are centered on seed towers. The seed towers for jets are required to have $E_T \geq 2$ GeV. The electron/photon algorithm uses seed towers with $E_T \geq 1$ GeV and combines them with the neighboring tower having the largest E_T. The fraction of the tower energy deposited in the EM calorimeter is used to reduce the background from jets. The L2 calorimeter $\not\!\!E_T$ algorithm calculates the vector sum E_T from the E_T of each individual trigger tower.

The central track trigger (L2CTT): The L2 track trigger is composed of three preprocessors: the L2CFT which receives tracks from L1CTT, the L2STT which takes input from the SMT and L1CTT, and the L2PS which formats the L1CTT preshower clusters. Information from all three preprocessors is used in the global L2 trigger decision.

The muon trigger (L2Muon): So called second level input computers take the L1 muon outputs and incorporates calibration information and more precise timing from the scintillators. From this information they form A and B+C layer track segments. These are sent to the muon preprocessor where the track segments in the A and B+C layers are matched to form muon candidate tracks.

The Level 3 Trigger

At the L3 trigger stage the precision readout is available and can be used instead of less detailed information from the trigger system electronics. The data at L3 is handled by the standard data acquisition system (DAQ). The L3 trigger system is a high level, fully programmable software trigger which runs on a Linux farm. Its decisions are based on complete physics objects (e.g. electrons, muons and jets) as well as objects based on relationships between physics objects (such as the ΔR between two physics objects or their invariant mass). The objects are generated by specific software algorithms (filter tools). The tools perform the bulk of the work, such as unpacking raw data, locating hits, forming clusters, applying calibration as well as reconstructing electrons, muons, tau leptons, jets, vertices and $\not\!\!E_T$.

The L3 jet tools: The L3 jet tools reconstruct jets with a simple cone algorithm. The tools rely on the precision calorimeter readout and the primary vertex position available at L3. Noisy calorimeter cells are suppressed which improves the performance compared to earlier levels of the trigger.

The L3 electron tools: The L3 electron tools use a narrow jet cone algorithm. The electron candidates can be selected based on E_T, the fraction of energy deposited in the electromagnetic section of the calorimeter as well as transverse shower shape information. Loose L3 electrons are required to pass electromagnetic fraction and shower shape cuts. Tight L3 electrons must survive more stringent shower shape cuts. An electron candidate can also be required to match a preshower cluster.

The L3 track tool: The L3 tracking uses both CFT and SMT information. It separately reconstructs tracks in the CFT and in the SMT. Then it performs a CFT-SMT match. Since L3 has access to the primary vertex position it is capable of triggering on tracks with high impact parameter.

The L3 muon tool: Both wire and scintillator hits from the muon system are used to reconstruct L3 muon track segments in the A and BC layers. Track-finding algorithms link these segments to identify tracks in three dimensions, taking into account the toroidal magnetic field between the A and B layers. At L3 the calorimeter and the central tracking system can also be used to confirm the muon candidate. L3 improves the ability to separate prompt and out-of-time hits by reconstructing the particle velocity from the scintillator hits available along the track. The availability of primary vertex position and the ability to match muon tracks to tracks in the central tracking system improves the muon momentum resolution compared to earlier trigger levels.

2.2.5 The Luminosity Monitor

In a particle collider the event rate R is proportional to the interaction cross section σ_{int} through the relation

$$R = \mathcal{L} \cdot \sigma_{\text{int}} \tag{2.12}$$

where the factor of proportionality $\mathcal{L}$ is called the instantaneous luminosity, or simply luminosity. The primary purpose of the luminosity monitor (LM) is to determine the instantaneous luminosity at the DØ interaction region. This is accomplished by detecting inelastic $p\bar{p}$ collisions. The LM also serves to measure beam halo rates and to make a fast measurement of the z coordinate of the primary interaction vertex.

The LM detector consists of two arrays of 24 plastic scintillation counters located at $z \pm 140$ cm. The position of the LM is shown together with the layout of an array in Fig. 2.14. The arrays are located in front of the end calorimeters and occupy the radial region between the beampipe and the forward preshower detector, covering the pseudorapidity range $2.7 < |\eta| < 4.4$.

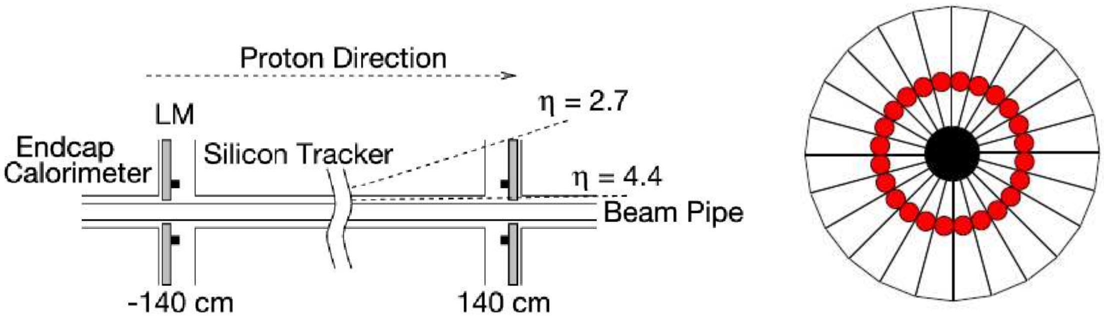

(a) The location of the luminosity detectors.

(b) An (r, ϕ)-view of one array of LM counters.

Figure 2.14: The layout of the luminosity monitor.

The luminosity $\mathcal{L}$ is determined from the average number of inelastic collisions per beam crossing $\bar{N}_{\text{inel}}$ as measured by the LM:

$$\mathcal{L} = \frac{f \bar{N}_{\text{inel}}}{\epsilon A \sigma_{\text{inel}}} \tag{2.13}$$

where f is the beam crossing frequency, σ_{inel} is the inelastic cross section and ϵ and A are the efficiency and acceptance of the LM. The instantaneous luminosity at the DØ experiment for a typical Tevatron store is shown as a function of time in Fig. 2.15. Due to proton-antiproton collisions and beam gas interactions the number of protons and antiprotons, and therefore the instantaneous luminosity, falls during a store. For convenience, the store is therefore broken down into short periods of

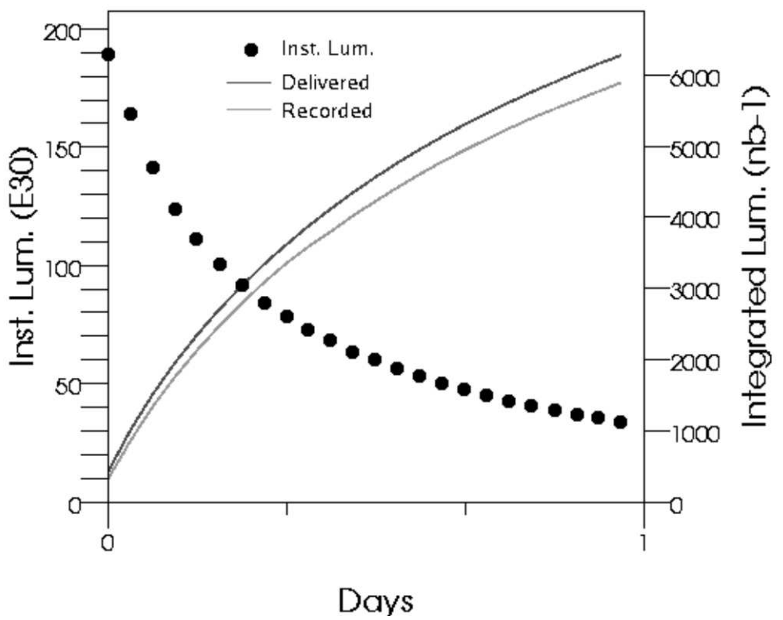

Figure 2.15: The instantaneous luminosity as a function of time during a typical Tevatron store.

time called luminosity blocks, and in each luminosity block $\mathcal{L}$ is assumed to be constant.

Since $\bar{N}_{\text{inel}}$ is typically greater than one, it is important to account for multiple $p\bar{p}$ collisions in a single beam crossing. This is done by counting the fraction of beam crossings with no collisions and using Poisson statistics to determine $\bar{N}_{\text{inel}}$.

To accurately measure the luminosity it is necessary to distinguish between $p\bar{p}$ interactions and the beam halo background. These processes are separated by making precise time-of-flight measurements of particles traveling at small angles with respect to the beams. The z coordinate of the interaction vertex is estimated from the difference in time-of-flight $z_v = \frac{c}{2}(t_- - t_+)$ where t_+ and t_- are the time-of-flights measured for particles hitting the LM detectors at ±140 cm. Beam-beam collisions are selected by requiring $|z_v| < 100$ cm. Beam halo particles traveling in the $\pm\hat{z}$ direction have $z_v \approx \mp 140$ cm, and are eliminated by the $|z_v| < 100$ cm requirement.

Measuring the Inelastic Cross Section

The instantaneous luminosity is determined by measuring the rate of a reference interaction with a known cross section. At the Tevatron the process used is the inelastic $p\bar{p}$ cross section σ_{inel}, which is related to the total and the elastic cross sections as:

$$\sigma_{\mathrm{inel}} = \sigma_{\mathrm{tot}} - \sigma_{\mathrm{el}}. \tag{2.14}$$

The inelastic cross section is measured by independently determining the elastic and total cross sections. The total cross section can be determined from event rates only, without knowing the luminosity, by using the optical theorem.

The optical theorem relates the total cross section σ_{tot} to the imaginary part of the forward elastic scattering amplitude $[F(\Theta)]_{\Theta=0} = F(0)$ by

$$\sigma_{\mathrm{tot}} = \frac{4\pi}{k} \mathfrak{Im}[F(0)] \tag{2.15}$$

where k is the momentum of the incoming hadron. Squaring Eq. 2.15 yields

$$\sigma_{\mathrm{tot}}^2 = \frac{16\pi^2}{k^2} \frac{\mathfrak{Im}[F(0)]^2}{\mathfrak{Im}[F(0)]^2 + \mathfrak{Re}[F(0)]^2} \cdot |F(0)|^2. \tag{2.16}$$

By defining the variable $\rho = \frac{\mathfrak{Re}[F(0)]}{\mathfrak{Im}[F(0)]}$ Eq. 2.16 can be simplified to

$$\sigma_{\mathrm{tot}}^2 = \frac{16\pi^2}{k^2} \frac{1}{1+\rho^2} \cdot |F(0)|^2. \tag{2.17}$$

Since the number of particles is a conserved quantity in elastic collisions, the scattering amplitude $F(\Theta)$ can be expressed in terms of the differential elastic cross section

$$|F(\Theta)|^2 = \frac{1}{2\pi} \frac{\mathrm{d}\sigma_{\mathrm{el}}}{\mathrm{d}\cos\Theta} \tag{2.18}$$

By introducing the Mandelstam variable $t = -2k^2(1 - \cos\Theta)$, and using $\sigma_{\mathrm{el}} = R_{\mathrm{el}}/\mathfrak{L}$, Eq. 2.18 can be written as

$$|F(0)|^2 = \left[\frac{1}{2\pi} \frac{\mathrm{d}\sigma_{\mathrm{el}}}{\mathrm{d}\cos\Theta}\right]_{\Theta=0} = \frac{1}{\mathfrak{L}} \frac{2k^2}{2\pi} \left[\frac{\mathrm{d}R_{\mathrm{el}}}{\mathrm{d}t}\right]_{t=0}. \tag{2.19}$$

If inserting Eq. 2.19 into Eq. 2.17 one obtains

$$\sigma_{\mathrm{tot}}^2 = \frac{16\pi}{1+\rho^2} \cdot \frac{1}{\mathfrak{L}} \left[\frac{\mathrm{d}R_{\mathrm{el}}}{\mathrm{d}t}\right]_{t=0}. \tag{2.20}$$

The total cross section can also be expressed as

$$\sigma_{\mathrm{tot}} = \frac{1}{\mathfrak{L}}(R_{\mathrm{el}} + R_{\mathrm{inel}}). \tag{2.21}$$

where R_{el} and R_{inel} are the elastic and inelastic event rates. By dividing Eq. 2.20 with Eq. 2.21 the total cross section can be expressed as function of measurable quantities:

$$\sigma_{\mathrm{tot}} = \frac{16\pi}{1+\rho^2} \frac{\left[\frac{\mathrm{d}R_{\mathrm{el}}}{\mathrm{d}t}\right]_{t=0}}{R_{\mathrm{el}} + R_{\mathrm{inel}}}. \tag{2.22}$$

Using Eq. 2.14 and Eq. 2.22 the inelastic cross section can be measured from the elastic and inelastic events rates without knowing the instantaneous luminosity. Measurements of ρ for different center-of-mass energies can be found in [28]. The inelastic cross section has been measured at $\sqrt{s} = 1.8$ TeV by the E710, E811 and CDF collaborations [124–126]. The average of the three measurements is scaled up to $\sqrt{s} = 1.96$ TeV and is found to be [127]

$$\sigma_{\text{inel}} = 60.7 \pm 2.4 \text{ mb}. \tag{2.23}$$

Knowing the inelastic cross section, the luminosity can be calculated according to Eq. 2.13.

Part II

Radiation Damage in the Silicon Microstrip Tracker

3 Introduction to Silicon Detectors

In this chapter some basic features of silicon detectors are introduced. A silicon detector with high position resolution situated close to the interaction point greatly improves the impact parameter resolution and helps in the identification of jets originating from b quarks. The closer the first layer of silicon is to the beampipe, the better the resolution. This proximity to the beam however means that the silicon sensors operate in a very harsh radiation environment. The effects of radiation damage are discussed in Chapter 4. In Chapter 5, a measurement of the radiation damage in the DØ silicon tracker is described.

3.1 p- and n-doped Silicon

In order to make silicon p-doped, boron atoms are in most cases placed in the silicon lattice. Since boron only has three valence electrons whereas silicon has four, boron has to borrow an electron from the lattice to be able to complete its valence bonds. Left in the lattice is a lack of negative charge called a hole. Because of its capacity to accept an electron from the lattice the boron atom is classified as an acceptor.

To make silicon n-doped on the other hand, phosphorus atoms are normally added to the silicon lattice. Phosphorous has five valence electrons and will, after it has completed its valence bonds, have an excess electron which is loosely bound. This electron can migrate through the lattice. The phosphorous atom is therefore classified as a donor.

3.2 The pn Junction

A pn junction is created by bringing one part of p-doped and one part of n-doped silicon in contact with each other. Free holes from the p-side and free electrons from the n-side then start to wander across the junction due to thermal diffusion. Both the p- and n-side are electrically neutral to start with, and the diffusion of positively charged holes and negatively charged electrons over the junction results in an excess of negative charge on the p-side and positive charge on the n-side. This creates two space charge regions, one on each side of the junction. An electric potential builds up as the space charge increases, creating a potential barrier Φ_{bi} which finally exceeds the energy available for electrons and holes to cross the junction by thermal diffusion. At that point the flow of charge stops. The region around the junction containing the positive and negative space charge is called the depletion region. This region is depleted of all mobile charge carriers, and the voltage corresponding to the potential difference Φ_{bi} inside this region is called the built-in voltage V_{bi}. An illustration of a pn-junction is shown in Fig. 3.1.

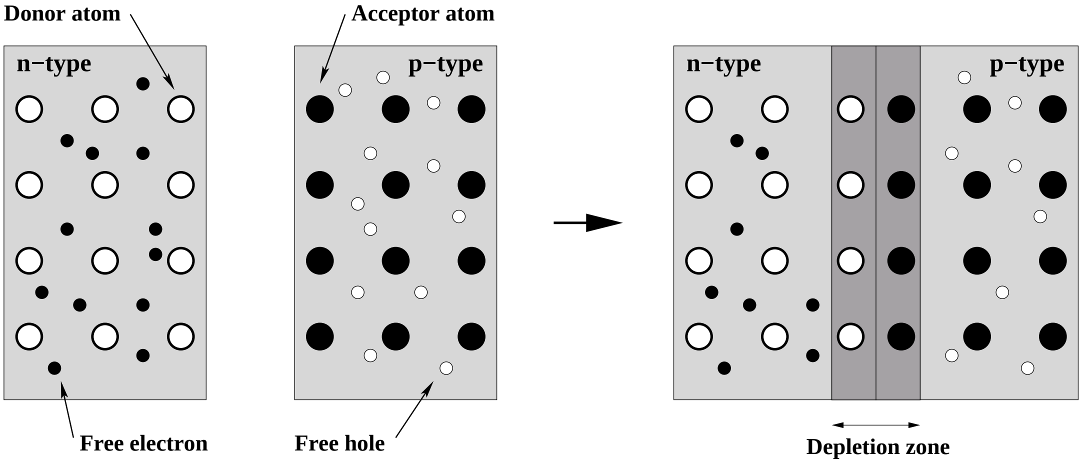

Figure 3.1: An illustration of the pn junction.

An external voltage applied to a pn junction is referred to as applying a bias voltage. The pn junction is asymmetric with respect to the charge flow. A pn junction can therefore be biased in two different ways, namely forward bias with positive supply on the p-side and negative supply on the n-side and reverse bias with positive supply on the n-side and negative supply on the p-side. Forward bias yields a large charge flow whereas reverse bias gives only a very small charge flow, referred to as the leakage current.

3.3 The Depletion Voltage

The p- and n-sides of the junction in a silicon sensor are normally not equally doped, so that the depletion region extends much further into the less doped side. The depletion region, with a width W, is in the following discussion approximated to extend only into the least doped side of the junction. The features of an abrupt pn-junction between a thin layer of heavily p-doped silicon and a slightly n-doped silicon bulk are depicted in Fig. 3.2.

An expression for the field strength and the potential in the depletion zone can be found by solving Poisson's equation

$$-\frac{d^2\Phi(x)}{dx^2} = \frac{\rho_{\text{el}}}{\epsilon\epsilon_0} = \frac{q_0 N_{\text{eff}}}{\epsilon\epsilon_0}, \tag{3.1}$$

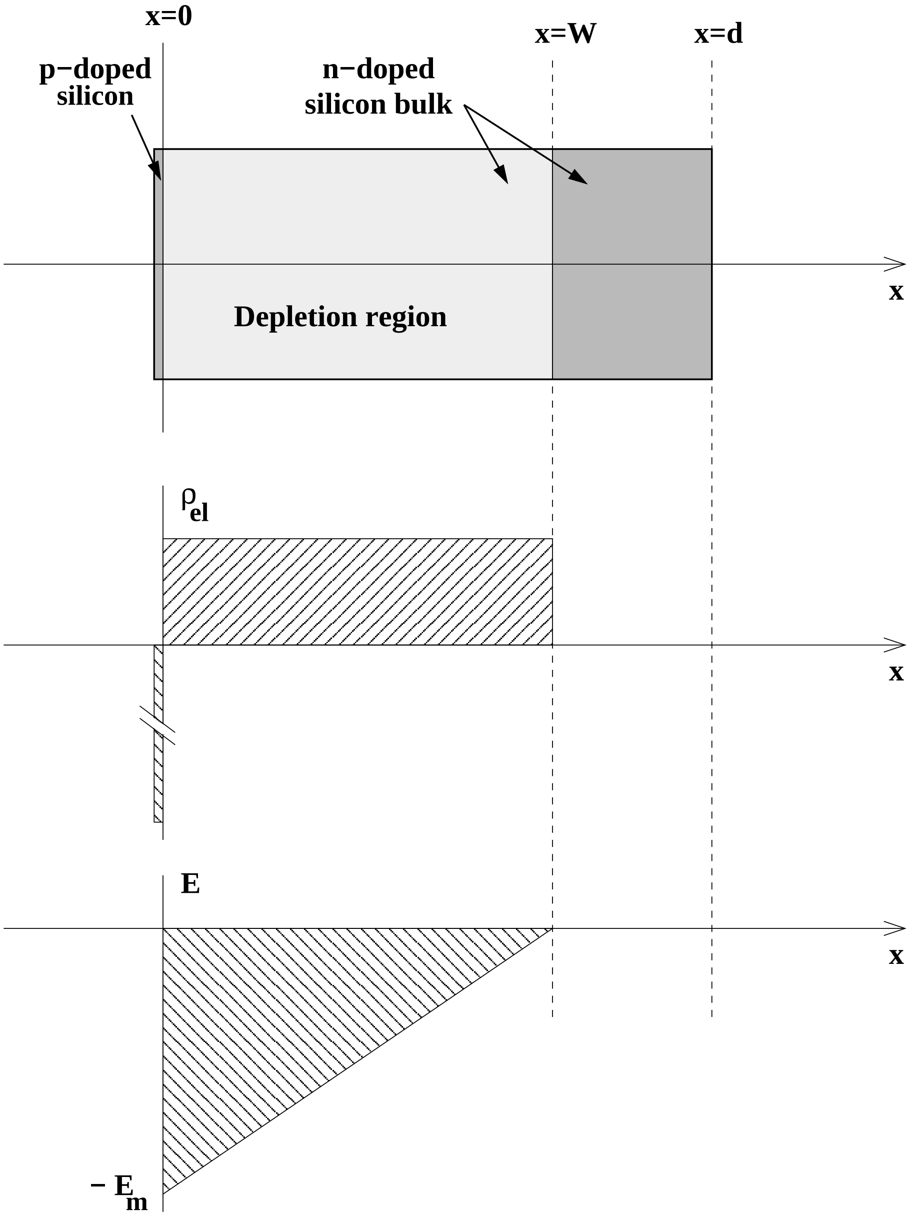

Figure 3.2: Schematic figure of the features of an abrupt pn junction. The top plot shows the pn junction with heavily p-doped silicon to the left and a slightly n-doped silicon bulk to the right of the junction. The middle plot shows the electric charge density and the bottom plot shows the electric field strength.

where x is defined in Fig. 3.2, ρ_{el} is the electric charge density, q_0 is the electron charge, ϵ_0 is the permittivity of free space, ϵ is the relative permittivity of silicon, Φ is the electric potential and N_{eff} the effective doping concentration defined as the difference between the concentration of ionized donors and acceptors in the space charge region. The first integration of Eq. (3.1) gives

$$-\frac{d\Phi(x)}{dx} = \frac{q_0 N_{\text{eff}}}{\epsilon\epsilon_0} \cdot x + C_1. \tag{3.2}$$

The constant C_1 is determined from the boundary condition $E(W) = 0$ and from the definition of the electric field $E(x) = -\nabla\Phi$, giving:

$$\frac{d\Phi(x)}{dx} = \frac{q_0 N_{\text{eff}}}{\epsilon\epsilon_0} \cdot (W - x) \qquad \text{for } W \leq d, \tag{3.3}$$

Here d is the maximum width of the depletion zone, normally the width of the silicon. The electric field strength is found to reach its maximum value E_m at $x = 0$:

$$E_m = -\frac{q_0 N_{\text{eff}}}{\epsilon\epsilon_0} \cdot W. \tag{3.4}$$

By integrating a second time and implying the boundary condition $\Phi(W) = 0$, the potential is found to be

$$\Phi(x) = -\frac{1}{2}\frac{q_0 N_{\text{eff}}}{\epsilon\epsilon_0}(x - W)^2 \qquad \text{for } 0 \leq x \leq W \text{ and } W \leq d. \tag{3.5}$$

With the constraint $\Phi(0) = -V_{\text{bi}} - V$, where V is the bias voltage, the expression for the depletion width becomes

$$W(V) = \sqrt{\frac{2\epsilon\epsilon_0}{q_0|N_{\text{eff}}|}(V + V_{\text{bi}})} \qquad \text{for } W \leq d. \tag{3.6}$$

According to this expression the depletion region expands with increasing reverse bias until the edge of n-doped bulk is reached, that is when $W = d$. When this condition is met the silicon is said to be fully depleted, and the voltage needed to obtain full depletion is called the depletion voltage V_{depl}. If the condition $W = d$ is put into Eq. (3.6) the depletion voltage is found to be

$$V_{\text{depl}} + V_{\text{bi}} = \frac{q_0}{2\epsilon\epsilon_0}|N_{\text{eff}}|d^2. \tag{3.7}$$

In the case of silicon sensors the built-in voltage V_{bi} is normally much smaller than the depletion voltage V_{depl}, and can therefore be neglected, giving

$$V_{\text{depl}} = \frac{q_0}{2\epsilon\epsilon_0}|N_{\text{eff}}|d^2. \tag{3.8}$$

3.4 Silicon Strip Sensors

The most commonly used silicon sensors in particle physics experiments are so called strip sensors. They are made from a slightly n-doped silicon bulk (n-material) with a conducting surface on one side and etched strips of heavily p-doped material (p^+-material) on the other. A schematic view of a silicon strip sensor is shown in Fig. 3.3. Upon application of a reverse bias voltage, the sensor volume becomes depleted of free charges, as was discussed in Sec. 3.3. A charged particle passing through the silicon volume creates electron-hole pairs. Due to the electric field (see Fig. 3.2), the electrons and holes drift in opposite directions resulting in an electric signal. Each silicon strip constitutes a detector element. To read out the signal, each strip is in most cases covered by a metal layer which is capacitively coupled to the strip.

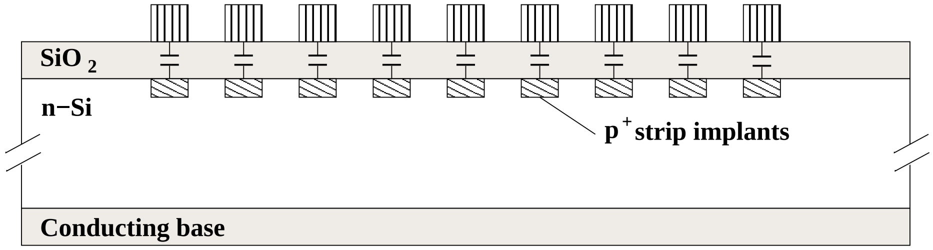

Figure 3.3: A schematic view of a single-sided silicon sensor.

The basic type of silicon sensor described above is called a single-sided sensor and it only gives one-dimensional hit information. A way to obtain two-dimensional hit information is to make the sensors double sided with a stereo angle between the strips on the two sides of the sensor. A double-sided silicon sensor has p^+-strips on one side of the sensor, referred to as the p-side, and and strips made from heavily n-doped silicon (n^+-material) on the so called n-side. For double-sided sensors with n-doped bulk, the depletion region starts extending from the p-side, and reaches the n-side only when the sensor is fully depleted. This is illustrated in Fig. 3.4. The n-side strips will thus be operational only if the sensor is fully depleted. If the sensor is only partially depleted, the signals from the n-side strips will contain a lot of noise.

The DØ silicon tracker consists of both single- and double-sided sensors. There are two types of double-sided sensors in the barrel region: 9-chip sensors which have a stereo angle of 2° (2-degree sensors) and 6-chip sensors which have a stereo angle of 90° (90-degree sensors). The large stereo angle of the 90-degree sensors introduces some additional design complications. The readout chips are placed on the short end of the sensor and the strips on the n-side run parallel to the short end. The standard procedure of micro-bonding the the readout chips and the strips can therefore not be applied. The solution chosen was to add an extra metal layer on top of the first one which leads the signals from the strips to the chips for readout.

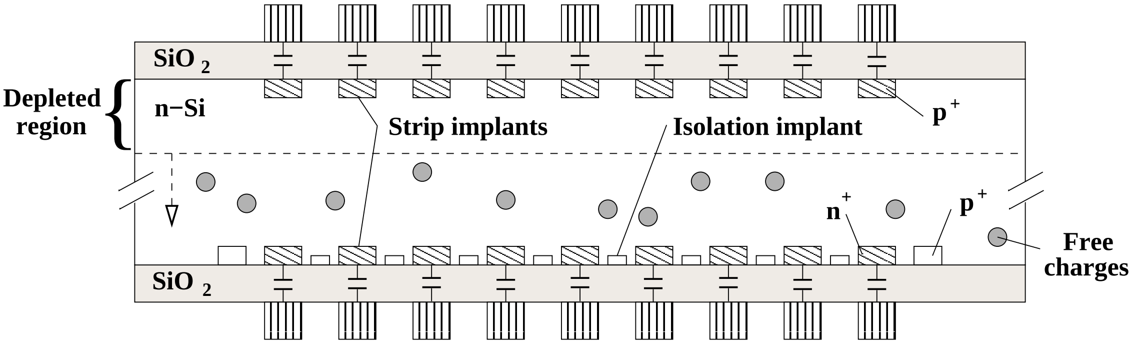

Figure 3.4: A schematic view of a double-sided silicon sensor with a small stereo angle. For a double-sided sensor with n-doped bulk, the depletion region starts to extend from the p-side, and reaches the n-side only when the sensor is fully depleted.

It is necessary to insulate the first metal layer from the second. This is done by placing an additional layer of SiO_2 between the two metal layers, using a PECVD (plasma enhanced chemical vapor deposition) technique.

4 Radiation Damage in Silicon

Radiation damage can be divided into bulk and surface damage. While the former depends on a few properties of the silicon bulk, the latter is very sensitive to the specific silicon sensor design. The main effects of bulk damage are an increase of the leakage current, a decrease of the charge collection efficiency and a change in the effective impurity concentration. The latter effect is expected to limit the lifetime of the DØ silicon tracker.

Radiation damage in silicon is a very complex field and this chapter only describes the most important effects. An detailed review of radiation damage in silicon is given in [130].

4.1 Silicon Bulk Radiation Damage

When particles penetrate the silicon they can give rise to bulk damage caused by the displacement of silicon atoms in the lattice. The bulk damage produced by hadrons and leptons with high energy is initiated by the displacement of an atom (called a primary knock on atom or PKA) out of its lattice site. The PKA moves through the lattice and loses energy in two processes, namely ionization and further displacements of silicon atoms. The PKAs and other recoiling atoms create point defects along their paths. If the recoil energy is high enough, a recoiling atom will not only give rise to point defects, but will also form, at the end of its path, a dense agglomeration of defects called a cluster. Both point defects and clusters contribute to the bulk damage. Ionization on the other hand is a fully reversible process and does not lead to permanent bulk damage [130].

The defects formed can be classified as acceptors, donors or amphoteric defects (a defect with both acceptor and donor levels). Acceptors are defects that are negatively charged when occupied with an electron, whereas donors are neutral when occupied with an electron.

The bulk damage gives rise mainly to three effects in the silicon sensors:

- Increase of the leakage current
- Loss in the charge collection efficiency
- Change in the effective impurity concentration

The increase in leakage current leads to larger noise and higher power consumption, but can be strongly suppressed by decreasing the temperature at which the silicon sensors are operated.

A loss in the charge collection efficiency means that only a fraction of the signal created by the charged particle passing through the silicon sensor is collected at the strips. The smaller signal size leads to a worse signal to noise ratio. This effect is however small, showed by measurements of the charge collection efficiency for minimum ionizing particles [131, 132]. The loss in charge collection efficiency is therefore not the most critical problem for the use of silicon detectors in high energy physics experiments.

The change in effective impurity concentration eventually results in a situation where it takes a very high voltage to deplete the sensors. At some point the increased depletion voltage causes a thermal run-away of the leakage current (referred to as the breakdown voltage) [133]. But normally the sensors become inoperable already at depletion voltages lower than the breakdown voltage due to noise from micro-discharges along the strip edges [134–136]. If a sensor cannot be fully depleted, parts of the silicon volume is insensitive to traversing particles. The change in effective impurity concentration is therefore considered the most limiting parameter of the silicon detector lifetime.

The radiation-induced bulk damage depends on the radiation dose. In addition, the changes to the silicon bulk evolve as a function of time after irradiation, a phenomenon referred to as annealing.

4.1.1 The NIEL Scaling Hypothesis

When trying to describe the radiation effects in silicon one assumes that the displacement damage caused by penetrating particles is linearly dependent on the energy transfered in the displacing collisions (NIEL, Non-Ionizing Energy Loss). This is called the NIEL scaling hypothesis, and it makes it possible to compare the radiation damage caused by different types of particles at different energies. According to this hypothesis, any particle fluence can be scaled to an equivalent 1 MeV neutron fluence Φ_{eq} producing the same bulk damage in a specific semiconductor. Given any particle fluence Φ, the equivalent 1 MeV neutron fluence is

$$\Phi_{\mathrm{eq}} = \kappa\Phi, \tag{4.1}$$

where κ is called the hardness parameter and depends on the particle type and energy [128–130].

4.1.2 Leakage Current

The current through a reverse biased diode is called the leakage current. A very important characteristic of the leakage current is its strong temperature dependence, which can be parameterized as [138]:

$$\frac{I_2(T_2)}{I_1(T_1)} = \left(\frac{T_2}{T_1}\right)^2 \exp\left(-\frac{E_g}{2k_B}\frac{(T_1 - T_2)}{T_1 \cdot T_2}\right). \tag{4.2}$$

The parameterization in Eq. 4.2 relates the leakage current I_2 at temperature T_2 with the leakage current I_1 at temperature T_1. The energy bandgap E_g is 1.1 eV in silicon and k_B is the Boltzmann constant. To suppress the leakage current, silicon detectors are normally operated cooled. The DØ silicon tracker is operated at 5 °C which, according to Eq. 4.2, reduces the leakage current by almost a factor of four compared to room temperature (20 °C).

Experimentally the increase in leakage current induced by radiation is found to be proportional to the particle fluence, and to a damage coefficient α [130]:

$$I = I_0 + \alpha \cdot \Phi_{\mathrm{eq}} \cdot V, \tag{4.3}$$

where V is the sensor volume and I_0 is the leakage current before irradiation. The value of α is found not to depend on silicon sensor properties or differences in the silicon material [137]. The increase in leakage current normalized to volume ($\Delta I/V$) is shown in Fig. 4.1.

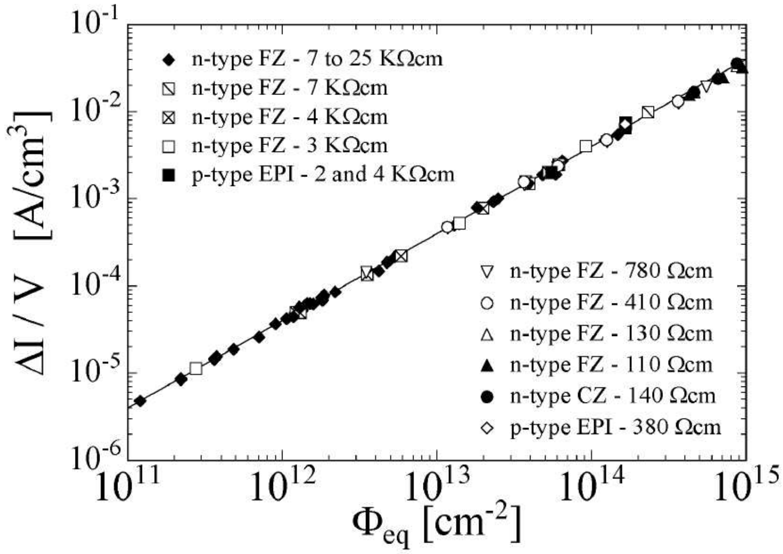

Figure 4.1: Fluence dependence of the leakage current for silicon sensors produced by various process technologies (denoted FZ, CZ and EPI) from different silicon materials [130].

The value of α, and hence the leakage current itself, decreases as a function of the time after irradiation which is referred to as annealing. The annealing behavior of α is usually described with the following functional form [137, 148]:

$$\alpha(t) = \alpha_0 \sum_i a_i \exp(-t/\tau_i), \quad \sum_i a_i = 1 \tag{4.4}$$

where t is the time after irradiation, α_0 is the value of α at $t = 0$ and τ_i are the time constants for the various annealing processes taking place. The time constants τ_i in Eq. 4.4 are also functions of the annealing temperature such that a higher temperature leads to faster annealing.

4.1.3 Charge Collection Efficiency

The charge collection efficiency depends on the bias voltage applied to the sensors. The minimum voltage needed to collect the signal from the entire sensor volume is the depletion voltage. A slight overbias, i.e. the application of a bias voltage larger than the depletion voltage, ensures that the electric field does not drop to zero at the end of the depletion region.

The charge collection efficiency decreases for irradiated silicon sensors due to radiation induced defects acting as traps for electrons and holes. The trapping leads to a reduced number of carriers $N_{e,h}$ collected after a time t, due to the exponential decrease of the number of initially created electron-hole pairs according to [139]:

$$N_{e,h}(t) = N_{e,h,0} \cdot \exp\left(-\frac{t}{\tau_{\text{eff}}}\right), \tag{4.5}$$

where $N_{e,h,0}$ is the initial number of charge carriers and τ_{eff} the effective trapping time. The time t available to collect the signal is typically the integration time of the frontend electronics. Measurements of the inverse effective trapping time as a function of fluence for neutron irradiated silicon is shown in Fig. 4.2. The charge collection efficiency for an overbiased diode is reduced by only 10% after a fluence of 10^{14} cm^{-2} [131, 132].

4.1.4 Effective Impurity Concentration

The effective impurity concentration N_{eff} is defined as the difference between the concentration of donors N_D and acceptors N_A:

$$N_{\text{eff}} = N_D - N_A. \tag{4.6}$$

As discussed in Sec. 3.3, the depletion voltage scales linearly with the absolute value of the effective impurity concentration.

In particle physics experiments the bulk material in silicon detectors is in most cases slightly n-doped. Under the influence of radiation however donor states are removed and acceptor states created leading to a decrease in the effective impurity

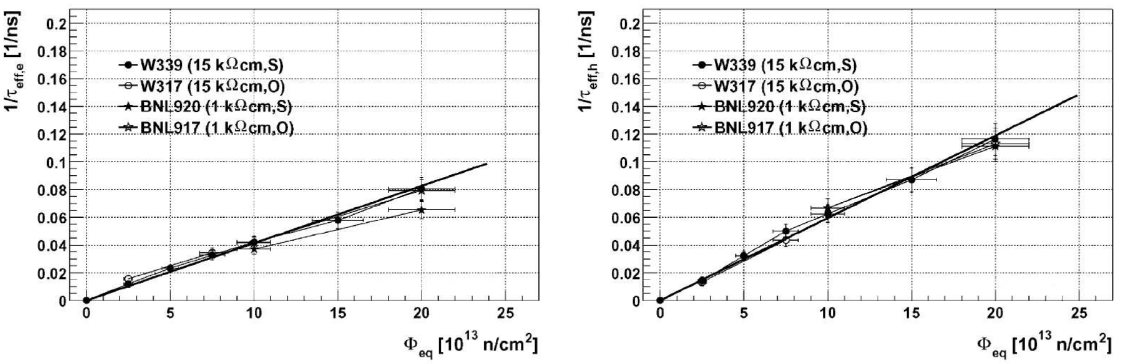

Figure 4.2: Fluence dependence of the inverse effective trapping time for electrons (left) and holes (right) in neutron-irradiated silicon [140].

concentration. At some point the number of donors equals the number of acceptors, making the material intrinsic. If the irradiation continues the absolute value of the effective impurity concentration starts to increase again, but the bulk material is now p-doped. This phenomena is referred to as type inversion and is confirmed by many experiments. One example is presented in Fig. 4.3.

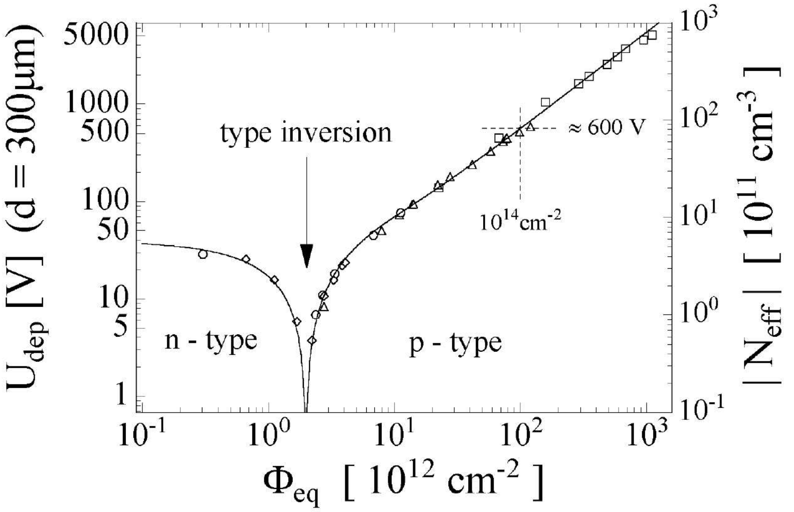

Figure 4.3: The depletion voltage and effective impurity concentration for standard silicon a function of the particle fluence [130, 142].

The change in effective impurity concentration can be divided into three different parts, namely N_c which only depends on the particle fluence, and two annealing parts

N_a and N_y depending on both the fluence and the time after irradiation:

$$N_{\text{eff}}(\Phi, t) = N_{\text{eff},0} - N_c(\Phi) - N_a(\Phi, t) - N_y(\Phi, t), \tag{4.7}$$

where $N_{\text{eff},0}$ is the initial effective impurity concentration and t is the time after irradiation.

Since N_c only depends on the particle fluence it is often called the stable damage part and can be parameterized as

$$N_c(\Phi) = N_{c0}(1 - \exp(-c \cdot \Phi)) + g_c \cdot \Phi, \tag{4.8}$$

where N_{c0}, c and g_c are experimentally determined constants. The first term in this equation corresponds to an incomplete donor removal that depends exponentially on the fluence and has the final value N_{c0}. The second term indicates that the acceptor states increases linearly with fluence.

The term N_a describes the so called short term annealing with a time constant $\tau_a \sim 50$ h at room temperature. It causes the effective impurity concentration to increase by the annealing of acceptor states. Since the short term annealing somewhat mitigates the effect of the radiation damage it is also called beneficial annealing. N_a is actually built up by a sum of exponentials, but since most of the time constants are very small only the longest one gives an observable contribution, and N_a reduces to

$$N_a = g_a \cdot \exp\left(-\frac{t}{\tau_a}\right) \cdot \Phi \tag{4.9}$$

where g_a is an experimentally determined constant.

The second part of the annealing process, N_y, has a much larger time constant $\tau_y \sim 500$ days at room temperature. In contrast to the short term annealing, N_y increases the effective impurity concentration and is therefore called reverse annealing. It can be parameterized as

$$N_y = g_y \left(1 - \frac{1}{1 + \frac{t}{\tau_y}} \cdot \Phi\right) \tag{4.10}$$

where g_y is an experimentally determined constant.

Figure 4.4 illustrates a simulation of the three different terms participating in the time dependence of the effective impurity concentration ΔN_{eff}. The simulation is carried out with $g_c = 1.9 \cdot 10^{-2}$ cm^{-1}, $g_a = 1.8 \cdot 10^{-2}$ cm^{-1}, $g_y = 6.6 \cdot 10^{-2}$ cm^{-1}, $\tau_a = 28$ days and $\tau_y = 27$ years, parameter values from Ref. [130]. The fluence is set to $\Phi = 4 \cdot 10^{13}$ cm^{-2} of 1 MeV neutrons and the temperature to $T = 5$ °C.

4.2 Surface Radiation Damage

Contrary to the bulk damage, the effects of surface damage strongly depend on the sensor design and are difficult to parameterize. Surface damage is therefore only briefly discussed here.

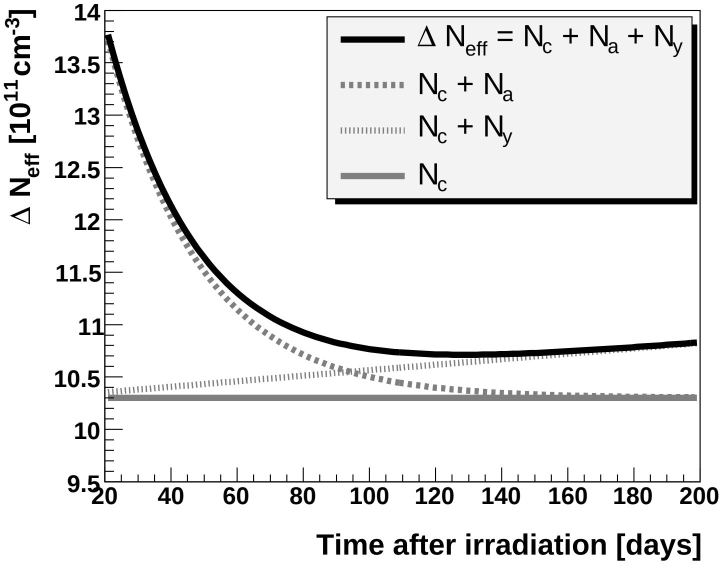

Figure 4.4: A simulation of the annealing behavior, i.e. the change in effective impurity concentration as a function of the time after irradiation. The simulation is based on Eqs. (4.8), (4.9) and (4.10).

Typically, surface damage leads to the creation of trapped charge in the oxide layers of the sensor. Ionizing particles traversing the surface layer of a sensor create electron-hole pairs which either recombine or separate in the electric field. The electrons move towards the interface between the oxide layer and the silicon bulk and get injected into the silicon bulk. The holes drift towards the metallic surface of the sensor and get trapped. This leads to a charge build-up in the oxide layers. The positive charges trapped in the oxide layer attract free electron carriers underneath, which alters the electric properties of the sensor.

5 Estimate of the Silicon Detector Lifetime

As discussed in Sec. 3.3, silicon sensors require sufficient bias voltage to be fully operational. Radiation damage changes the effective impurity concentration and hence the depletion voltage. After type inversion, the depletion voltage increases linearly with fluence and will at some point reach the system limit. The DØ silicon tracker is designed to be operational to bias voltages of 150 V, when the noise from micro-discharges becomes unacceptable [149, 150].

To ensure that the silicon sensors can be depleted at all times it is necessary to study the change in depletion voltage. This chapter describes a method to extract the depletion voltage of double-sided silicon sensors from the noise recorded at the n-side strips. From these results, extrapolations are made to estimate the lifetime of the DØ silicon tracker.

5.1 Background

In preparation for Run II of the Tevatron, all types of sensors installed in the DØ silicon tracker were tested for radiation hardness [150]. The tests were performed in the radiation damage facility (RDF) located at the Fermilab Booster, which provides an 8 GeV proton beam.

Out of the tested sensors, the 90-degree sensor reacted differently to radiation then the other types of sensors. This was especially clear when studying the depletion voltage as a function of the accumulated radiation dose, shown in Fig. 5.1. The fact that the 90-degree sensors seem less radiation hard is especially troublesome as they occupy the innermost layers of the DØ silicon tracker. With this in mind, efforts have been made to monitor the radiation hardness of the 90-degree sensors more closely.

5.2 Extracting the Depletion Voltage from the n-side Noise

In Secs. 3.3 and 3.4 it was shown that the depletion region reaches the strips on the n-side of a double-sided sensor only when the sensor is fully depleted. For bias voltages below the depletion voltage the bulk region close to the n-side strips

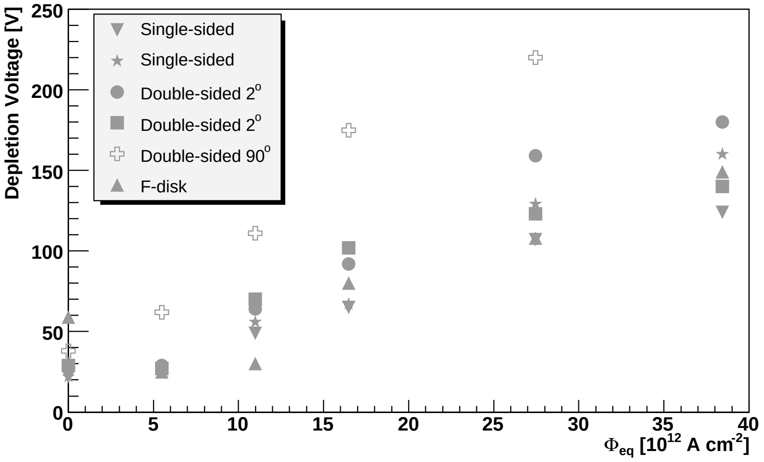

Figure 5.1: The depletion voltage as a function of the normalized 1 MeV neutron fluence for the six sensors irradiation in the Fermilab RDF facility [150]. The double-sided 90° sensors clearly shows an abnormal behavior.

contains free charges, which leads to a large noise. When the depletion is reached, the entire silicon bulk is depleted of free charge carriers and the noise in the n-side strips drops. Studying the n-side noise as a function of the bias voltage can therefore be used to determine the depletion voltage of a sensor.

Single-sided sensors only have strips on the p-side. Since the depletion region starts extending from the p-side, the bulk near the p-side strips is depleted of free charges even at very low bias voltages. The n-side noise method can therefore only be applied to double-sided sensors. The study presented in this chapter is limited to sensors in the barrel region where there are two types of double-sided sensors: 2- and 90-degree sensors. These two sensor types show very different noise behavior as a function of the bias voltage. Different procedures of extracting the depletion voltage are therefore developed for the two sensor types.

5.2.1 Differential Noise Determination

The detector elements in the SMT suffer from coherent noise, where the signal in a large fraction of the readout channels fluctuate in a correlated fashion. This noise component is caused by the readout electronics and is not related to the bias voltage. In order to look at the incoherent part of the noise, unfolding the effect of coherent noise, the differential noise is used in the depletion voltage studies. The differential noise is defined using the difference between the signal in one strip and its neighbor, $\Delta p_i = p_i - p_{i+1}$, where the width of the Δp_i distribution is the differential noise for strip i.

Since the depletion voltage is a sensor-wide quantity, the variable of interest is an estimate of the average differential noise for all channels on a sensor, σ^{diff}. Two different methods of extracting σ^{diff} have been developed, one which is only applied to data taken without any beam circulating in the Tevatron, and one which can be applied regardless of whether or not there are collisions taking place. The two methods are:

RMS method: The differential noise for channel i, σ_i^{diff}, is defined as:

$$\sigma_i^{\mathrm{diff}} = \frac{\mathrm{RMS}\,(p_i - p_{i+1})}{\sqrt{2}}, \qquad i = 1 \tag{5.1}$$

$$\sigma_i^{\mathrm{diff}} = \frac{\mathrm{RMS}\,(p_i - p_{i-1})}{\sqrt{2}}, \qquad i > 1 \tag{5.2}$$

where RMS stands for root-mean-square, and p_i is the signal in strip i. The sensor-wide quantity σ^{diff} is obtained by averaging over all the N strips on the sensor:

$$\sigma^{\mathrm{diff}} = \frac{1}{N}\sum_{i=1}^{N}\sigma_i^{\mathrm{diff}}. \tag{5.3}$$

This method has the disadvantage of being sensitive to outliers. If some of the channels included in the determination have occasionally been hit by charged particles, the larger signal in these strips will artificially increase the differential noise. Therefore this method is only used on data where no beam was circulating in the Tevatron.

Fitting method: For each sensor, the difference between the signal in two neighboring strips, $p_i - p_{i+1}$, is put into a histogram. A Gaussian is then fitted to each histogram, and the fitted standard deviation is taken as a measure of the differential noise. An example of such a fit is shown in Fig. 5.2. This method is less sensitive to outliers, and can therefore be used also on data taken with beam.

The "RMS method" is used for the studies of the depletion voltage as a function of the distance from the beampipe (described in Sec. 5.3) , and the "Fitting method" is used for studies of the depletion voltage as a function of fluence (described in Sec. 5.4).

5.2.2 Bias Voltage Scans

In order to determine the depletion voltage, data from so called bias voltage scans is studied. In a bias voltage scan 11 runs are taken, with the bias voltage setting varied in steps of 10%, from 0–100% of the bias voltage used in normal operations. These scans are performed regularly to allow for monitoring of the depletion voltage as a function of time.

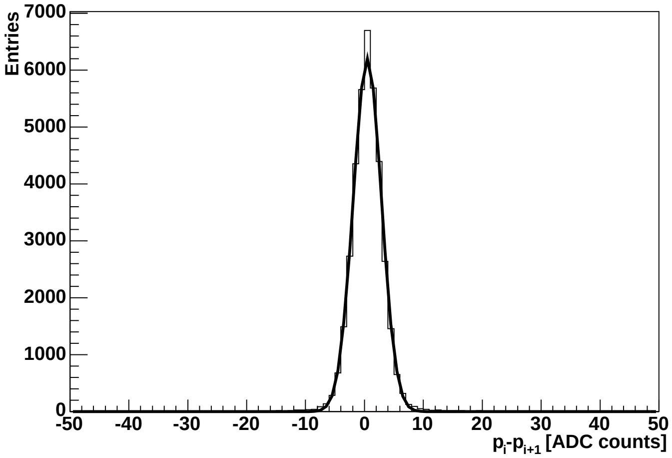

Figure 5.2: The distribution of the difference between the signal in two neighboring channels together with a fitted Gaussian.

5.2.3 The Depletion Voltage for 2-degree Sensors

Most of the 2-degree sensors show an expected noise behavior as a function of bias voltage, as show in Fig. 5.3. At low voltages the noise is large, and rapidly decreases to a stable and lower noise level as soon as the bias voltage reaches the depletion voltage.

The depletion voltage for a 2-degree sensor is found using a two-step approach. First the function $f(x)$ is fitted to the data points:

$$f(x) = (a_1 + b_1 \cdot x) + 0.5 \cdot (a_2 + b_2 \cdot x) \cdot (1 - \mathrm{erf}(g(x))) \tag{5.4}$$

$$g(x) = (x - hp)/(\sqrt{x} \cdot s) \tag{5.5}$$

where the error function $\mathrm{erf}(g(x))$ gives a Gaussian turn-off behavior, centered at the half-point hp with a width determined by s. In this function a_1, b_1, a_2, b_2, hp and s are the fitted parameters. The depletion voltage is then determined by stepping through the fitted function from high to low bias voltages. For each point the second derivative is calculated. The end of the turn-off region is defined as the point where the second derivative is larger than some cutoff value (here 0.005 is used). The depletion voltage is then defined as the voltage for which the noise has increased by 10% of the maximum noise difference (maximum noise - minimum noise) with respect to the noise at the end of the turn-off region. The procedure is illustrated in Fig. 5.4.

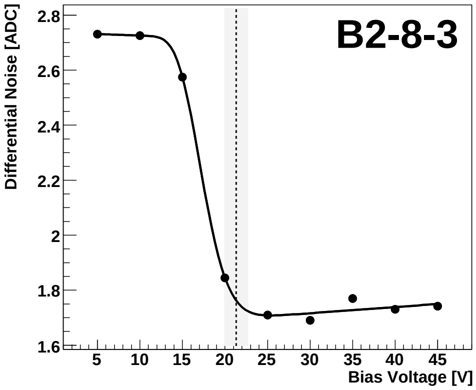

Figure 5.3: An example of the differential noise as a function of the bias voltage for a 2-degree sensor named B2-8-3.

5.2.4 The Depletion Voltage for 90-degree Sensors

The 90-degree sensors show a rather unexpected noise behavior as a function of the bias voltage. There is no abrupt decrease in the noise at the n-side when the depletion voltage is reached. Instead, the noise is decreasing rather monotonically with increasing bias voltage. For some 90-degree sensors a small kink in the noise can be seen at a certain bias voltage. An example of a sensor with a differential noise behavior showing such a kink is shown in Fig. 5.5(a). The position of the kink is changing as a function of the radiation dose and is therefore interpreted as indicating the depletion voltage. Only about 50% of the 90-degree sensors show a distinct kink. An example of a sensor for which it is impossible to determine the depletion voltage using the n-side noise method is shown in Fig. 5.5(b).

For the sensors showing a pronounced kink, an algorithm has been developed to locate the kink position, defined as the bias voltage point with the largest derivative change. The derivative change Δ_i for point i is defined as:

$$\begin{aligned}\Delta_i^- &= (\sigma_i^{\text{diff}} - \sigma_{i-1}^{\text{diff}})/(V_i^{\text{bias}} - V_{i-1}^{\text{bias}}) && (5.6)\\ \Delta_i^+ &= (\sigma_{i+1}^{\text{diff}} - \sigma_i^{\text{diff}})/(V_{i+1}^{\text{bias}} - V_i^{\text{bias}}) && (5.7)\\ \Delta_i &= \Delta_i^- - \Delta_i^+ && (5.8)\end{aligned}$$

where σ_i^{diff} and V_i^{bias} are the differential noise and bias voltage for point i. The depletion voltage is defined as the V_i^{bias} for the point with the largest Δ_i. In addition it is required that $|\Delta_i^-| > |\Delta_i^+|$, and $\Delta_i^- < 0$. The uncertainty on the depletion voltage is set to $(V_{i+1}^{\text{bias}} - V_i^{\text{bias}})/2$.

The unexpected noise behavior observed for the 90-degree sensors could be related to their more complicated design. As discussed in Sec. 3.4, the 90-degree sensors have an additional metal layer, insulated from the first with a thin layer of

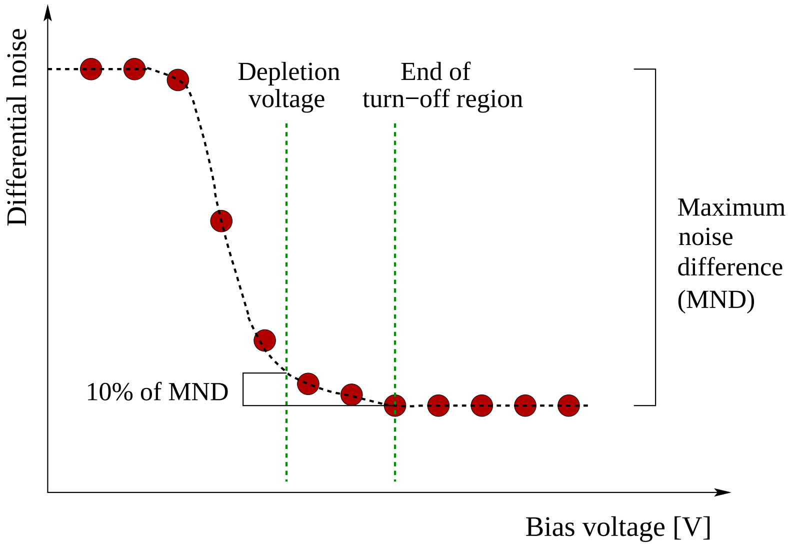

Figure 5.4: Illustration of the procedure to determine the depletion voltage for 2-degree sensors.

SiO_2. Charge build-up in this insulation layer, caused by radiation, could change the behavior of the noise as a function of the bias voltage. Before the start of Run II, the n-side noise was measured for a non-irradiated 90-degree test sensor. The result is shown in Fig. 5.6, and here the abnormal behavior is not present. This indicates that the change in noise behavior is due to radiation damage.

5.3 Depletion Voltage as a Function of Radius

The silicon sensors in the innermost layer suffer more radiation damage than those in the outermost layer. Exactly how the dose decreases with the distance from the beam depends on the beam environment as well as the magnetic field. Figure 5.7 shows the difference between the depletion voltage observed after an integrated luminosity of 1 fb^{-1} and that extracted before the sensors were installed in the DØ silicon tracker as a function of the radius. Each point represents the average depletion voltage change of the double-sided sensors in this layer. The “RMS method” is used to obtain the differential noise and the procedures described in Secs. 5.2.3 and 5.2.4 are used to obtain depletion voltage estimates. Only sensors that showed reasonable noise behavior (approximately 80% of the 2-degree sensors and 50% of the 90-degree sensors) are included in this plot. As expected, the absolute value of the depletion voltage change decreases with radius since the integrated dose is smaller at larger radii.

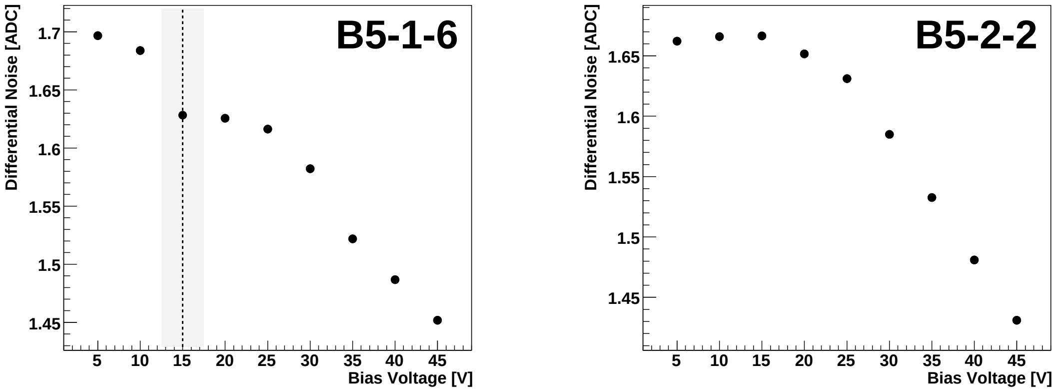

(a) The sensor B5-1-6 shows a depletion voltage kink.

(b) The sensor B5-2-2 does not show a depletion voltage kink.

Figure 5.5: The left plot shows an example of a 90-degree sensor for which the depletion voltage could be determined. The 90-degree sensor in the right plot does not show any kink, making it impossible to use the n-side noise method to determine the depletion voltage.

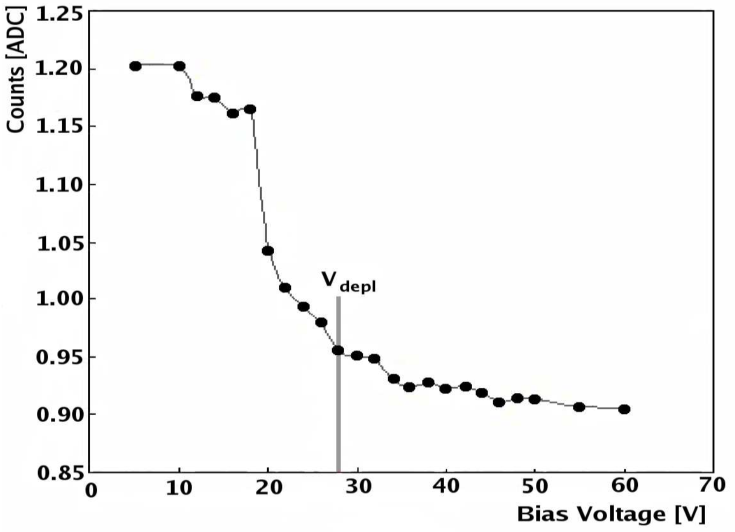

Figure 5.6: The differential noise as a function of the bias voltage for a non-irradiated 90-degree test sensor, measured before the start of Tevatron Run II. The noise is extracted with a procedure similar to the “Fitting method”.

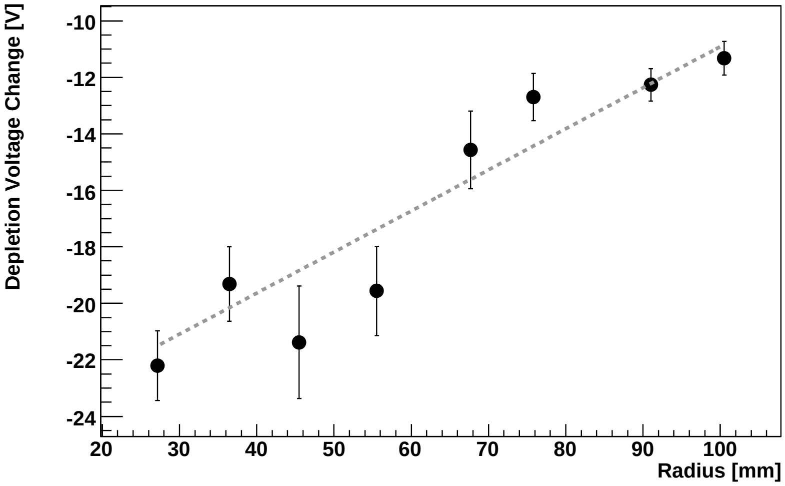

Figure 5.7: The depletion voltage change as a function of the radius. The depletion voltage change is defined as the difference between the depletion voltage observed after an integrated luminosity of 1 fb^{-1} and that extracted before the sensors were installed in the DØ silicon tracker. A first degree polynomial is fitted to the data for illustrative purposes. The "RMS method" is used in the extraction of the depletion voltage at 1 fb^{-1}.

5.4 Depletion Voltage as a Function of Integrated Luminosity

Figure 5.8 shows the depletion voltage measured with the n-side noise method as a function of integrated luminosity for four 90-degree sensors in the innermost layer. For the four sensors shown in Fig. 5.8, the depletion voltage is decreasing with integrated luminosity, suggesting that they have not yet undergone type inversion.

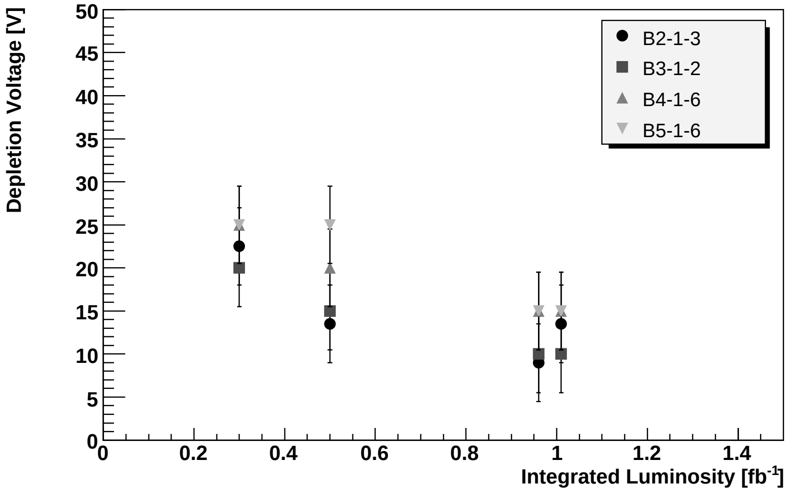

Figure 5.8: The depletion voltage as a function of integrated luminosity for sensors in the innermost layer.

5.5 Cross-Check Using the Charge Collection Efficiency

A second method for extracting the depletion voltage has been developed and used as an independent cross-check of the n-side noise method. It is based on the dependence of the charge collection efficiency on the bias voltage and is presented in some detail in Paper III. The depletion voltages extracted with the charge collection efficiency method are in agreement with those obtained with the n-side noise method. The comparison for a 90-degree sensor in the innermost layer is shown in Fig. 5.9.

5.6 Fluence Determination

As discussed in Sec. 4.1.2 the leakage current of a silicon sensor depends linearly on the fluence. The fluence is in turn proportional to the integrated luminosity delivered by the Tevatron accelerator. Therefore the leakage current is also expected to show a linear behavior as a function of the integrated luminosity, which is shown

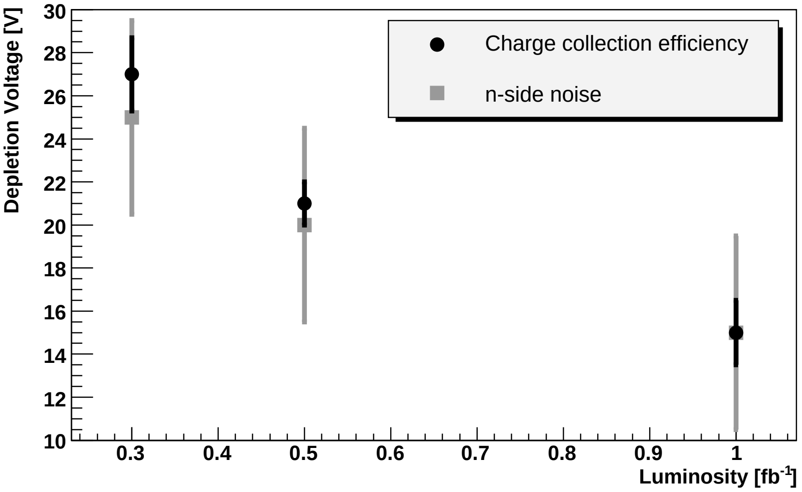

Figure 5.9: Comparison of the depletion voltage as a function of the integrated luminosity obtained with the n-side noise and the charge collection efficiency methods for a 90-degree sensor in the innermost layer.

in Fig. 5.10 for a set of sensors from the DØ silicon tracker. The drop in leakage current at an integrated luminosity of 0.6 fb^{-1} corresponds to the shutdown in the fall of 2004, when the silicon tracker was warmed up to 15 °C for one month. The higher temperature accelerated the annealing process, making the leakage current decrease.

Using Eqs. 4.3 and 4.4, taking $\alpha = 3 \cdot 10^{-17}$ A $\cdot$ cm^{-1} as well as annealing time constants τ_i and amplitudes a_i from Ref. [148], measurements of the leakage current can be translated into measurements of the normalized 1 MeV neutron fluence. From leakage current measurements the relation between the luminosity and the normalized 1 MeV neutron fluence is found to range between $4.0 \cdot 10^{12}$ and $5.3 \cdot 10^{12}$ particles/cm^{2}fb^{-1}. The spread can be due to uncertainties in the parameterizations used to define the relation between the leakage current and the normalized 1 MeV neutron fluence, as well as non-uniform radiation doses.

5.7 Comparison with Previous Studies

As shown in Fig. 5.1, it was predicted from the irradiation studies made in the RDF before the start of Tevatron Run II that type inversion for the DØ silicon bulk material would take place for a normalized particle fluence of approximately $5 \cdot 10^{12}$ particles/cm^2 [151]. The measurements of the depletion voltage and the fluence presented in this chapter allows to compare the behavior of the silicon sensors installed in the DØ detector with those irradiated in the RDF.

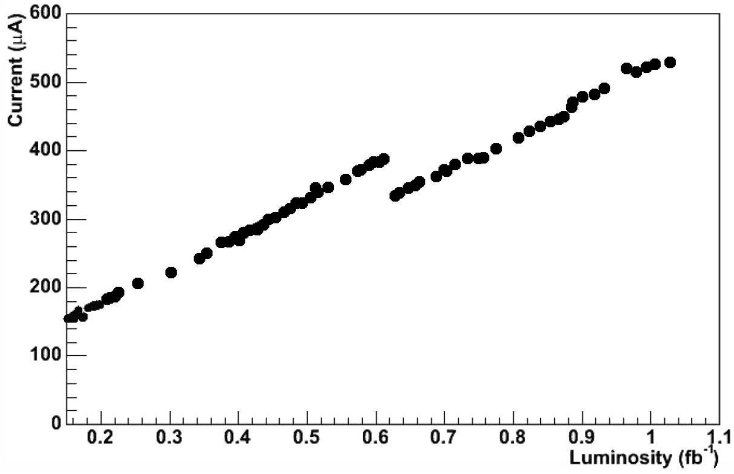

Figure 5.10: The leakage current, normalized to 20 °C, as a function of the integrated luminosity.

Figure 5.11 shows the comparison between the depletion voltage of the 90-degree sensors in the n-side noise study and all sensors irradiated in the RDF. For the sensors irradiated in the RDF, the conversion from radiation dose to 1 MeV neutron equivalent fluence $\kappa = 0.52$ [152] and 1 MRad = $3.52 \cdot 10^{13}$ (8 GeV protons)/cm^2 [153] are used. For the sensors in the DØ detector the conversion from integrated luminosity to fluence from Sec. 5.6 is used.

The comparison clearly shows that the 90-degree sensors installed in the DØ detector are much less affected by the radiation than the 90-degree sensor irradiated in the RDF. The discrepancy most likely has to do with slow annealing of the charge trapped in the insulation layer between the two metal layers. In the studies performed in the RDF, the sensors were irradiated at a much higher rate than what is typical during normal running of the Tevatron accelerator, and annealing did not take place to the same extent.

As discussed in the introduction to this chapter, the sensors in the silicon detector are expected to function up to depletion voltages of approximately 150 V [149, 150]. Based on the results from the RDF study, the 90-degree sensors in the innermost layer were expected to reach a depletion voltage of 150 V after an integrated luminosity of 3.5 to 6 fb^{-1} [121]. The new data from the n-side noise study shows that the silicon sensors will survive larger radiation doses than what was earlier believed to be the case. The amount of depletion voltage data collected at this point is however not enough to make sophisticated fits to the depletion voltage as a function of the fluence. In order to make a projection it is instead assumed that the 90-degree sensors in the DØ tracker will follow the radiation hardness behavior observed for the single-sided, 2-degree double-sided and F-disk sensors in the RDF study. In that

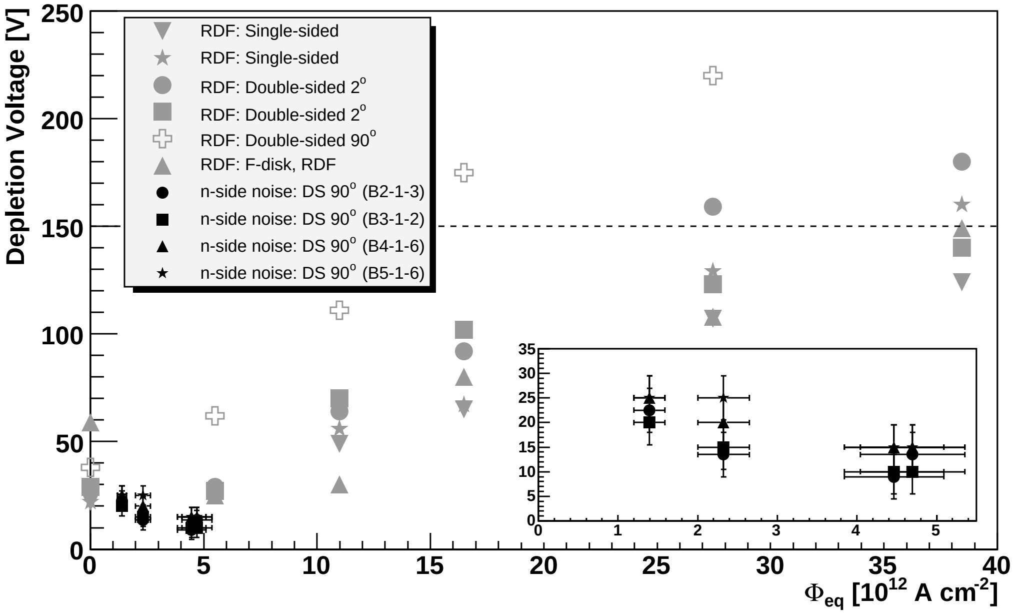

Figure 5.11: Depletion voltage for the silicon modules installed in the innermost layer of the DØ detector and those irradiated at the Radiation Damage Facility for different radiation doses. The inset shows a blow-up with the 90-degree sensors in the n-side study.

scenario, the innermost layer of the DØ silicon tracker is expected to be operational up to fluences of approximately $3 \cdot 10^{13}$ cm^{-2} to $4 \cdot 10^{13}$ cm^{-2}, corresponding to a delivered luminosity between 6 and 8 fb^{-1}. These extrapolations are however associated with large uncertainties, and it is important to keep monitoring the depletion voltages of the sensors in the innermost layer.

Part III

Top Quark Pair Production Cross Section Measurements

6 Cross Section Analysis Overview

This part of the thesis concerns two measurement of the top quark pair production cross section using events with two leptons in the final state. The first measurement is based on a data set corresponding to an integrated luminosity of 158 $\text{pb}^{-1}$and uses events with one fully identified muon and one fully identified electron. This analysis is referred to as the $e\mu$ analysis. The second measurement is based on a data set corresponding to an integrated luminosity of 425 pb^{-1}. In this analysis, referred to as the $\ell +$ track analysis, one of the two leptons in the event is identified by an isolated track, without requiring any confirmation from the calorimeter or muon system. In both measurements b-tagging is used to reject background events. The two cross section analyses are presented in more detail in Chapters 10 and 11.

This chapter gives on overview of the cross section analyses. The signature of $t\bar{t} \to \ell\ell$ events is described as well as the major backgrounds which mimic the $t\bar{t}$ signal. The last part of this chapter introduces the techniques used to estimate the signal efficiency and the number of background events. The method used to extract the top pair production cross section is also presented.

The signal selection is based on objects such as electrons, muons, tracks, jets and missing transverse energy. These are defined in detail in Chapter 7. An important part of a cross section analysis is knowing the efficiency for the signal and background events to pass the selection criteria. The estimates of object efficiencies are presented in Chapter 8. A detailed description of the samples used in the analyses, including the signal samples, is given in Chapter 9.

6.1 The $t\bar{t} \to \ell\ell$ Signature and its Backgrounds

The experimental signature of a $t\bar{t}$ event decaying into a dilepton final state consists of two high p_T charged leptons, two high p_T jets from the hadronization of b quarks and substantial $\not\!\!E_T$ from two undetected neutrinos. Additional jets are often produced from initial and final state radiation.

Several other processes mimic the $t\bar{t} \to \ell\ell$ signature and are referred to as background processes. They are divided into two categories: irreducible backgrounds and instrumental backgrounds. Common to all background processes is the fact that the jets mostly originate from light quarks or gluons. Requiring at least one jet to be tagged as originating from a b quark (referred to as a b-tagged jet) is therefore the single most effective cut to reduce the backgrounds.

6.1.1 Irreducible Backgrounds

The irreducible backgrounds are processes in which the two charged leptons arise from electroweak boson decays and the $\not\!\!E_T$ originates from high p_T neutrinos. The irreducible backgrounds to the $t\bar{t} \to \ell\ell$ signature are:

$Z/\gamma^*(\to \tau\tau \to \ell\ell\nu\nu\nu\nu) + \text{jets}$: The production of two charged tau leptons via a Z boson or a virtual photon, where each tau lepton in turn decays into a lighter charged lepton and two neutrinos, resembles the $t\bar{t}$ events. Although the inclusive Z boson production cross section is large, the branching fraction for $Z \to \tau\tau \to \ell\ell\nu\nu\nu\nu$ is only 0.4%. Requiring jets in the final state also reduces this background. In addition, the lepton p_T spectrum is softer than in $t\bar{t}$ events and the $\not\!\!E_T$ is usually smaller.

$WW(\to \ell\ell\nu\nu) + \text{jets}$: The WW production cross section is small, but the event characteristics are close to those of $t\bar{t}$ events. The requirement of jets in the final state reduces the size of this background.

6.1.2 Instrumental Backgrounds

There are several backgrounds which arise from instrumental effects such as mismeasured $\not\!\!E_T$ and misidentification of isolated electrons, muons and tracks.

$Z/\gamma^*(\to \ell\ell)$+jets: This is the largest source of background in the ℓ + track analysis. These events have all the characteristics of $t\bar{t}$ events except real $\not\!\!E_T$ from high p_T neutrinos. The events passing the analyses selection criteria have apparent $\not\!\!E_T$ coming from finite lepton and jet p_T resolutions and from noise in the calorimeter.

$W(\to \ell\nu) + \text{jets}$: This process has a large production cross section and significant $\not\!\!E_T$, but only one high p_T isolated lepton. The second isolated lepton in the event must come from misidentification. The most likely source of fake isolated leptons is either a jet with high electromagnetic content being identified as an electron, a muon from a heavy flavor decay inside of a jet to appear isolated or, in the ℓ + track analysis, a track originating from a jet being isolated from other tracks.

Multijet: This process has by far the largest production cross section of all backgrounds. The contribution from this background is however greatly reduced by the requirement of two isolated leptons and substantial $\not\!\!E_T$, since all of these objects have to originate from misidentification.

6.2 Estimating Signal and Background Contributions

The cross section analyses presented in this thesis are carried out in two subsequent steps. In the first part of the analyses, the so called preselection, the events are required to have two isolated high p_T leptons (identified as electrons, muons or isolated tracks) and substantial $\not\!\!E_T$. Applying these selection criteria greatly reduces the contribution from instrumental backgrounds. The preselected sample in the $e\mu$ analysis contains approximately equal amounts of $t\bar{t}$ and background events. In the $\ell+$track analysis the preselected samples are greatly dominated by Z/γ^* background events. A good agreement at this stage between the observed and predicted number of events and between predicted and observed distributions of kinematic variables gives confidence that the background processes are well modeled.

The last analysis step is to require at least one jet to be b-tagged. This greatly reduces the number of background events while keeping approximately 50% of the signal events and results in samples expected to be dominated by $t\bar{t}$ events.

6.2.1 The Expected Number of Preselected Events

The expected number of events in the preselected sample is obtained differently depending on the physics process. Some processes are estimated primarily from simulation, whereas others are estimated partly or fully from data events with little or no input from the simulation.

The expected number $t\bar{t}$ and WW events in the preselected sample are obtained from an estimated efficiency to pass the preselection criteria ϵ^{presel}, a production cross section σ, and the integrated luminosity L:

$$N^{\text{presel}} = \sigma \cdot L \cdot \epsilon^{\text{presel}} \tag{6.1}$$

The cross section for WW production comes from NLO perturbative QCD calculations [171]. The $t\bar{t}$ cross section is fixed to 7 pb for comparisons between observation and prediction, but is fitted to the data in the final extraction of the top pair production cross section.

The number of Z/γ^* background events in the preselected sample is estimated from a combination of data and simulation. Simulated Z/γ^* events are used to provide the kinematics of the events, but the overall normalization of this background comes from Z/γ^* events in data, as discussed in Secs. 10.1.1 and 11.1.1.

Multijet and W events only contribute to the preselected sample if they contain misidentified leptons. Since the probability for such misidentification to take place is not well modeled in the simulation, the number of multijet and W events in the preselected sample are estimated with very little input from simulated events as discussed in Secs. 10.1.3 and 11.1.4.

6.2.2 Event Tagging Probability

An event containing at least one b-tagged jet is referred to as a b-tagged event. The expected number of b-tagged events in a certain jet multiplicity bin i, N_i^{tag}, is obtained by multiplying the expected number of preselected events N_i^{presel} with an event tagging probability $\epsilon_i^{\mathrm{evttag}}$:

$$N_i^{\mathrm{tag}} = \epsilon_i^{\mathrm{evttag}} \cdot N_i^{\mathrm{presel}}. \tag{6.2}$$

The event tagging probability depends on the number of jets in the event as well as the tagging probability for each jet. The tagging probability for each jet in turn depends on the jet flavor (b, c or light), the jet p_T and the jet η.

Two alternative ways of obtaining the event tagging probability are used in this thesis:

Data method For most background processes, the event tagging probability is obtained from independent data samples by applying the tagging algorithm to the events and counting how many of the selected events have at least one b-tagged jet. The event tagging probability is thus obtained as:

$$\epsilon^{\mathrm{evttag}} = \frac{N^{\mathrm{tagged}}}{N^{\mathrm{all}}}. \tag{6.3}$$

This method is used to obtain event tagging probabilities for Z/γ^*, W and multijet events.

Data and simulation method For the $t\bar{t}$ signal and the WW background[1], the probability for an event to have at least one b-tagged jet is determined by

$$\epsilon^{\mathrm{evttag}} = 1 - \prod_{i=1}^{N_{\mathrm{jets}}} (1 - \epsilon_i^{\mathrm{jet}(\alpha)}(p_T, \eta)) \tag{6.4}$$

where N_{jets} is the number of jets with $p_T > 15$ GeV/c and $|\eta| < 2.5$ and $\epsilon_i^{jet(\alpha)}(p_T, \eta)$ is the probability for a jet of flavor α with a given p_T and η to be both taggable and b-tagged. The per-jet tagging efficiencies $\epsilon_i^{jet(\alpha)}(p_T, \eta)$ are obtained using a combination of data and simulation as described in Chapter 8. The average event tagging probability is obtained by averaging over all simulated events passing the preselection criteria.

---

[1] The event tagging probability for WW events in the $\ell +$ track analysis is taken to be the same as that of W events, and is obtained using the "Data method".

6.3 Extracting the Top Pair Production Cross Section

The excess of b-tagged events over the predicted number of background events is interpreted as coming from $t\bar{t}$ production. The production cross section $\sigma_{t\bar{t}}$ is related to the number of observed $t\bar{t}$ events $N_{t\bar{t}}$ through:

$$N_{t\bar{t}} = L \cdot \sigma_{t\bar{t}} \cdot B(t\bar{t} \rightarrow \ell\ell) \cdot \epsilon_{t\bar{t}}^{\text{presel}} \cdot \epsilon_{t\bar{t}}^{\text{evttag}} \tag{6.5}$$

where L is the integrated luminosity, $B(t\bar{t} \rightarrow \ell\ell)$ is the branching fraction for a pair of top quarks to decay into a dilepton final state, $\epsilon_{t\bar{t}}^{\text{presel}}$ is the preselection efficiency with respect to all $t\bar{t} \rightarrow \ell\ell$ events and $\epsilon_{t\bar{t}}^{\text{evttag}}$ is the event tagging probability[2].

The signal to background ratio in events with exactly one jet is lower than that in events with two or more jets. To gain sensitivity, each jet multiplicity bin is therefore regarded as a separate channel in the extraction of the cross section. The $\ell +$ track analysis is in addition performed separately for $e +$ track and $\mu +$ track events. This results in two independent channels to combine in the $e\mu$ analysis and four independent channels to combine in the $\ell +$ track analysis. For each independent channel i, the expected number of events $\tilde{N}_i$ is:

$$\tilde{N}_i = N_i^{t\bar{t}} + N_i^{\text{bkg}} \tag{6.6}$$

where $N_i^{t\bar{t}}$ is the number of $t\bar{t}$ events defined in Eq. 6.5 and N_i^{bkg} is the expected number of background events. A likelihood function for each independent channel i is defined as the Poisson probability of observing N_i^{obs} events given an expectation of $\tilde{N}_i$ events:

$$\mathscr{L}_i = \frac{\tilde{N}_i^{N_i^{\text{obs}}}}{N_i^{\text{obs}}!} e^{-\tilde{N}_i} \tag{6.7}$$

When combining several independent channels, a combined likelihood function $\mathscr{L}$ is constructed from the product of the individual likelihood functions:

$$\mathscr{L} = \prod_{i=1}^{N} \mathscr{L}_i \tag{6.8}$$

The most likely cross section is that for which the combined likelihood function reaches its maximum value.

---

[2] In the $e\mu$ analysis, the preselection efficiency is derived with respect to all $t\bar{t} \rightarrow e\mu$ events and the branching fraction used is $B(t\bar{t} \rightarrow e\mu)$.

7 Object Identification

Many of the particles searched for and studied in particle physics experiments decay rapidly into lighter particles. As the decay products traverse the detector, each type of particle leaves a characteristic trace which can be used to identify it. The signatures of different particles going through the DØ detector are illustrated in Fig. 7.1. The process of going from the raw data read out from the detector to identified particles, or collections of particles, is called object reconstruction and identification. This chapter provides an overview of the reconstruction and identification of objects important to the cross section measurements presented in this thesis.

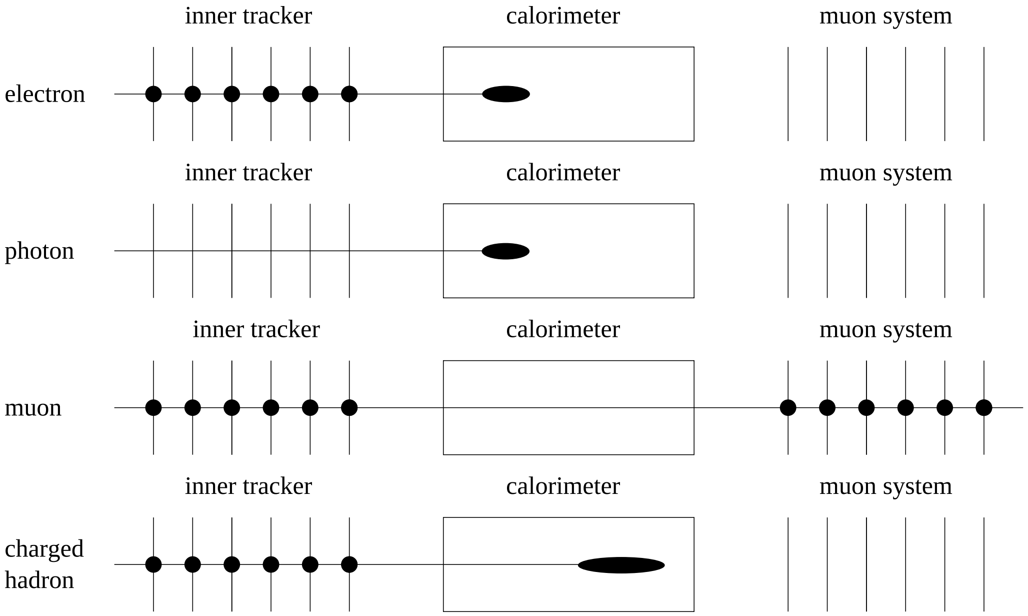

Figure 7.1: Signatures of particles going through the DØ detector. The charged particles leave hits in the tracking detectors. All SM particles except muons and neutrinos produce showers in the calorimeter and are stopped there. Muons produce hits in the muon detectors outside the calorimeter.

7.1 Primary Interaction Point

7.1.1 Primary Vertex Finding Algorithm

The luminous region in DØ spans of the order of a meter in the z direction. Therefore the primary interaction point (or primary vertex, PV) has to be reconstructed on an event by event basis. A precise determination of the PV position is important when reconstructing the direction of physics objects such as electrons, muons and jets. A precise reconstruction of the primary vertex position in the (x, y)-plane is crucial for the identification of secondary decay vertices coming from long-lived particles. The primary vertex resolution derived in $t\bar{t}$ events generated with ALPGEN [162–164] and passed through a simulation of the DØ detector response is shown in Fig. 7.2.

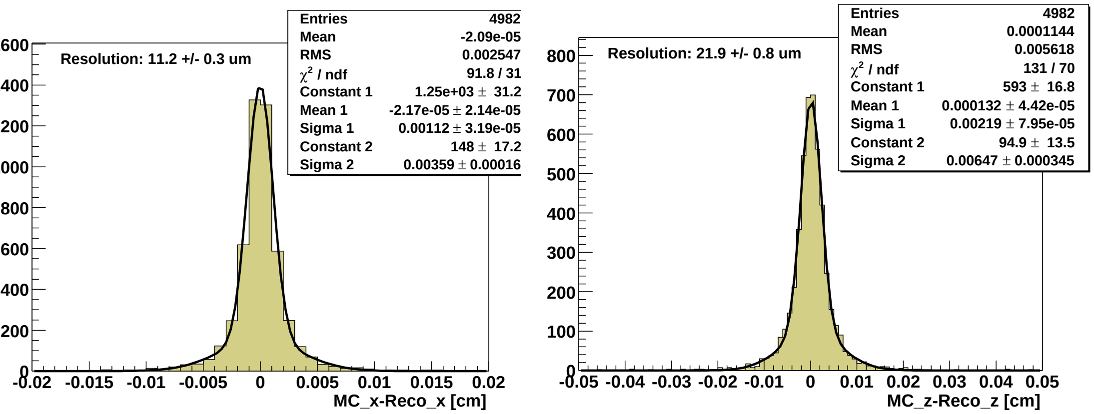

Figure 7.2: The resolution of the primary vertex algorithm in the x and z directions, derived in $t\bar{t}$ events generated with ALPGEN and passed through a simulation of the DØ detector response. The resolution in the y direction is equal within uncertainties to that in the x direction. The resolutions are derived from the difference between the true vertex position obtained from the generator information (MC) and the measured primary vertex position (Reco).

The reconstruction of the primary vertex consists of three main steps,: locating the beam spot, vertex fitting and vertex selection. Tracks originating from the primary interaction point are expected to have a small impact parameter in the (x, y)-plane, also referred to as distance of closest approach or d_{ca}. The impact parameter with respect to the origin and to a reconstructed primary vertex is defined in Fig. 7.3. The algorithm starts by locating the position of the beam spot center. In this step, all tracks with an impact parameter significance $(d_{ca}/\sigma_{d_{ca}}) < 100$, calculated with respect to $(x, y) = (0, 0)$, are fitted to a common PV. Before the final vertex fitting begins the d_{ca} of each track is recalculated using this new beam spot position. The tracks which participate in the final track fitting procedure must have $p_T > 0.5$ GeV/c, at least two hits in the silicon detector and $d_{ca}/\sigma_{d_{ca}} \leq 3.0$. The

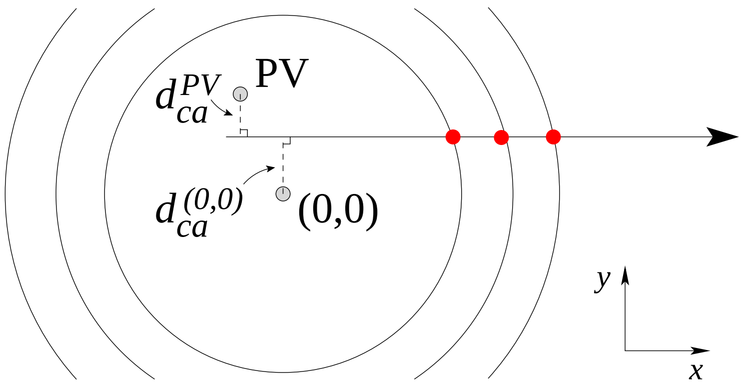

Figure 7.3: Definition of the track impact parameter in the (x, y)-plane of a track with respect to the origin, $d_{ca}^{(0,0)}$, and to the reconstructed primary vertex, d_{ca}^{PV}.

tracks are grouped in 2 cm wide clusters in the z-direction. The tracks in each cluster are then fitted to a common vertex using the Kalman filter technique [154,155]. After the initial vertex fitting, the track with the largest contribution $\Delta\chi^2$ to the vertex χ^2 is removed if $\Delta\chi^2 > 10$, and the vertex is refitted. This process is repeated until the χ^2 of the fitted vertex is < 10. When a vertex is found the fitter repeats the procedure with all tracks excluded from the previously found vertex.

The fitting process can find more than one vertex in each event. Most vertices normally come from minimum bias interactions which contain few high p_T tracks. The last step of the primary vertex reconstruction is therefore to select, among all vertices in the event, the one which is the most likely hard scatter vertex. The selection is based on the p_T of the tracks attached to the vertex. Each track in the vertex is assigned a probability based on the expected track p_T distribution for minimum bias tracks. The vertex with the lowest probability of being a minimum bias vertex is selected as the hard scatter vertex. The expected p_T distribution of tracks in minimum bias events is simulated with PYTHIA. The p_T distribution of tracks from minimum bias interactions in both data and simulation is shown in Fig. 7.4. The data distribution is obtained on $Z/\gamma^* \rightarrow \mu\mu$ events where the hard scatter vertex is assumed to be the one containing two reconstructed muons of opposite charge. Any other vertex found in the event more than 10 cm away in z from the dimuon vertex is considered to be a minimum bias interaction.

7.1.2 Primary Vertex Identification

To ensure a good quality of the primary vertex, it is required to be reconstructed within the fiducial region of the silicon detector ($|z_{\text{PV}}| < 60$ cm), and to have at least three associated tracks. These selections are referred to as the primary vertex quality criteria.

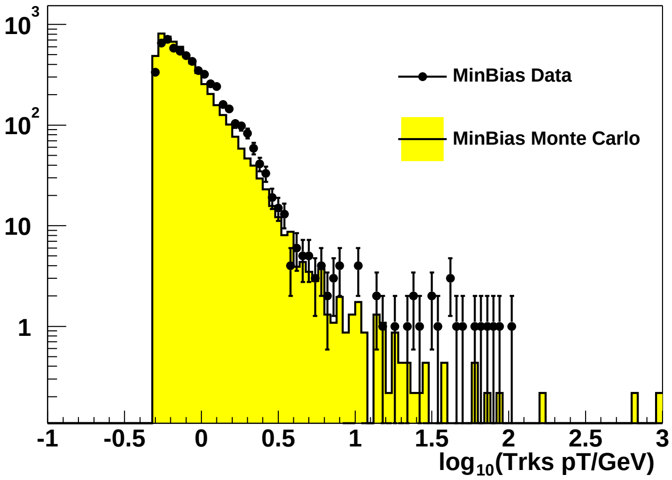

Figure 7.4: The p_T distribution of minimum bias tracks in data and simulated events. The data distribution is obtained from minimum bias vertices in $Z/\gamma^* \to \mu\mu$ events.

The reconstruction algorithms of many objects use a primary vertex obtained with a slightly different primary vertex algorithm, referred to as $\mathrm{PV}_{\mathrm{reco}}$. The $\mathrm{PV}_{\mathrm{reco}}$ algorithm imposes less stringent track selections ($d_{ca}/\sigma_{d_{ca}} < 5.0$ and no requirement on SMT hits for simulated tracks). and it does not use z-clustering. The vertex fitting is performed by minimizing the impact parameter of the tracks with respect to a common vertex position. In the $\ell +$ track analysis, the z positions of the two primary vertices found by the two different algorithms are not allowed to differ by more than 5 cm ($\Delta z(\mathrm{PV}, \mathrm{PV}_{\mathrm{reco}}) < 5$ cm).

7.2 Tracks from Charged Particles

7.2.1 Tracking Algorithms

The trajectories of charged particles traversing the central tracking detectors are curved due to the presence of the solenoidal magnetic field. The particles leave hits in the tracking detectors from which tracks can be reconstructed. Due to the large number of readout channels, the track reconstruction is one of the most CPU-intensive tasks in the reconstruction chain. Figure 7.5 shows an event display with hits and reconstructed tracks in the DØ tracking detectors.

The track reconstruction is divided into three parts called hit clustering, pattern recognition and track fitting. A charged particle passing through the SMT or CFT often deposits charge in several adjacent strips or wires. At the hit clustering stage, hits which are likely to originate from the same charged particle are grouped together.

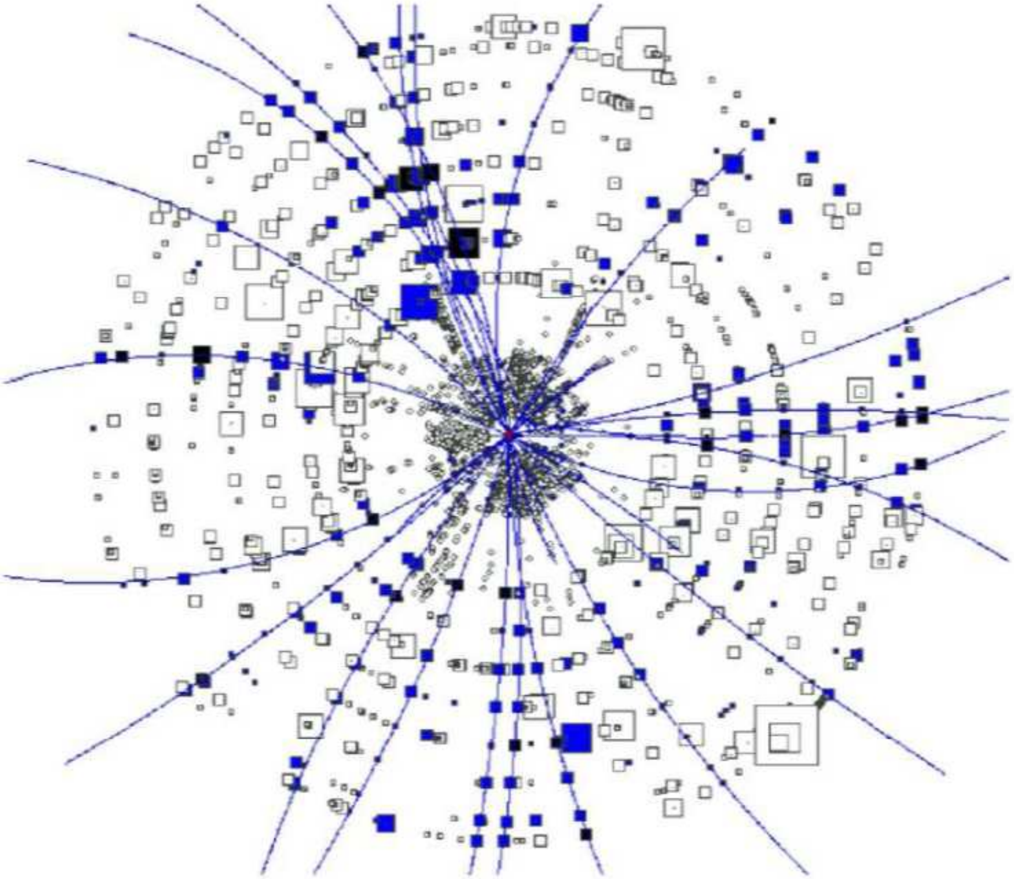

Figure 7.5: View in the (x, y)-plane of a data event showing hits in both the SMT (circles) and the CFT (squares) as well as reconstructed tracks (solid lines). Hits associated with a track are indicated by filled markers. The curvature of the tracks is due to the solenoidal magnetic field which is pointing outwards from the page.

Pattern recognition algorithms group together clusters which are located along a physical path. Two complementary pattern recognition algorithms are used. The first is the histogramming method, based upon the Hough Transform – a method originally developed to find tracks in bubble chambers [156]. The technique involves mapping the spatial coordinates of hits into a binned track parameter space. If one considers tracks originating from the center of the detector, then a hit position in the (x, y)-plane (with some uncertainty) corresponds to a band in (ρ, ϕ)-space, where $\rho = qB/p_T$ is the curvature of the track, q is the charge of the particle, B is the magnetic field and ϕ is the direction of the track at the point of closest approach to the origin. The set of bands corresponding to hits deposited by a single track intersect in the region surrounding the track's true parameters. The track finding algorithm thus proceeds by histogramming the bands corresponding to all hits in a detector region and considering local maxima in the parameter space as defining track candidates. Overall the histogramming method is robust against noise and has a high efficiency for high p_T tracks originating near the primary vertex.

An alternative track-finding approach, referred to as the road method, begins with groups of three (x, y)-hits in the SMT barrels. These are fitted to a track hypothesis and the result is used to form a road in which to search for hits in additional detector layers. Any hits found are added to the track unless they significantly degrade the quality of the fit or result in unreasonable tracks, for example by having very large impact parameters or very small curvatures. Track candidates in three dimensions are formed using sets of stereo hits corresponding to the (x, y)-hits associated with the track. Once a preliminary set of tracks is found, they are used to calculate a preliminary primary vertex position which is used to define roads for starting new searches in the CFT. Any resulting tracks are projected back into the SMT and duplicates are discarded. Compared to the histogramming method, the road method has a better efficiency for low p_T tracks and tracks with high impact parameter. It is also less susceptible to fakes.

The lists of candidate tracks resulting from the two approaches described above are combined and, after removal of duplicates, passed on to the Kalman track fitter [154,155,157–159]. This makes use of an interacting propagator which propagates tracks through the DØ tracking detectors while taking into account the curvature in the magnetic field and interactions with detector material. The fitter incrementally adds hits to tracks using the input candidates to define roads. The Kalman fitter technique provides the optimal track parameters with their associated errors.

7.2.2 Isolated Track Identification

In the $\ell +$ track analysis isolated high p_T tracks are used to identify leptons from W boson decays. In order for a track to be a good isolated lepton candidate it has to fulfill certain quality and isolation criteria:

- To reject tracks originating from minimum bias interactions and heavy flavor decays, the track has to originate from the primary interaction point. This is ensured by requiring that the distance in z between the track and the primary vertex, $\Delta z(\mathrm{track}, \mathrm{PV})$, is less than 1 cm. Also the d_{ca} significance of the track has to be less than 5.

- To remove poorly reconstructed tracks and reject fake tracks, the χ^2 per degree of freedom of the track fit has to be less than 4.
- To remove tracks originating from cosmic muons, the track is not allowed to be matched to an out-of-time muon.
- To reduce the background from tracks originating from quark or gluon fragmentation, the track has to be isolated from surrounding activity in the tracking detectors. The transverse momenta of all tracks, p_T^{track}, in a cone with radius $\Delta R = 0.5$ around the track (not including the track itself) should be small compared to the transverse momentum of the track itself, p_T^{isotrack}:

  $$\sum_{\Delta R<0.5} \frac{p_T^{\mathrm{track}}}{p_T^{\mathrm{isotrack}}} < 0.5. \tag{7.1}$$

  In addition, the track is not considered if found within the cone of a reconstructed jet (i.e. requiring $\Delta R(\mathrm{track}, \mathrm{jet}) > 0.5$).

The set of selection criteria described above define the *loose* isolated tracks. *Tight* isolated tracks are loose tracks with a tighter track isolation:

$$\sum_{\Delta R<0.5} \frac{p_T^{\mathrm{track}}}{p_T^{\mathrm{isotrack}}} < 0.12. \tag{7.2}$$

Defining two sets of selection criteria, loose and tight, allows for a determination of the instrumental backgrounds in the $\ell+\mathrm{track}$ analysis, as explained in Sec. 11.1.4.

All isolated tracks used in this thesis are required to have $p_T > 15$ GeV/c and $|\eta| < 2.0$.

7.2.3 Momentum Correction in Lepton+Track Events

Electrons moving through the tracking detectors lose energy due to Bremsstrahlung. This energy loss depends on the amount of material that the electron traverses. Since the description of the material in the detector simulation is not accurate enough, the energy loss for electron tracks is different in data and simulation. To bring the electron track p_T distribution in better agreement with that in data a correction is applied to the p_T of simulated electron tracks. The correction is derived on $Z/\gamma^* \to ee$ events in five regions of track η. For each η region the following relations are defined:

$$p_T^{\text{track,data}} = \alpha \cdot p_T^{e,\text{data}} \tag{7.3}$$

$$p_T^{e,\text{sim}} = \beta \cdot p_T^{\text{track,sim}} \tag{7.4}$$

where Eq. 7.3 gives the relation in data events between the p_T of the central track and the p_T of the electron measured in the calorimeter. Equation 7.4 translates the track p_T in simulated events into the p_T of the electron. Since the electron p_T is well described in simulation, it is assumed that $p_T^{e,\text{sim}} = p_T^{e,\text{data}}$, i.e. that the left-hand side of Eq. 7.4 can be used as the argument in Eq. 7.3. The corrected electron track momentum, p'_T is then obtained from:

$$p'_T = \alpha \cdot \beta \cdot p_T, \tag{7.5}$$

where p_T is the transverse momentum of the central track in the simulation. The parameters α and β are extracted from Z/γ^* events in data and simulation respectively.

7.3 Muons

7.3.1 Muon Tracks

Muons are identified from tracks in the muon system (so called local muons), and matched to tracks in the central tracking system. The central track match greatly improves the p_T resolution. A local muon is required to have at least two wire hits and at least one scintillator hit in the A layer as well as at least two wire hits and at least one scintillator hit in the BC layers. In addition, loose timing cuts based on A and BC layer scintillator hits are applied in order to reject cosmic muons.

The matching to a central track is done by extrapolating the local muon track to the point of closest approach (p_{ca}) to the z-axis and compare the track parameters to those of tracks in the central tracking system. A global fit is performed with each central track within one radian in azimuthal and polar angle from the extrapolated local muon track. The central track with the highest χ^2 probability is considered matched to the muon candidate. The measurement of the muon track parameters are taken from the matched central track.

7.3.2 Isolated Muon Identification

To remove poorly reconstructed muons, and to ensure that the muon originates from the primary interaction point, additional criteria are applied to the central track matched to the local muon:

- The χ^2 per degree of freedom of the muon track has to be less than 4 to reject poorly measured tracks.

- The distance between the muon and the primary vertex along the z direction, $\Delta z(\mu, \mathrm{PV})$ is required to be less than 1 cm. This is to further reject cosmic muons, poorly reconstructed tracks and muons originating from minimum bias interactions.

- The d_{ca} significance should be less than 3, to reject muons from semileptonic heavy flavor decays. This is also a powerful way to reject cosmic muons.

- In the $\ell +$ track analysis, the muon is not considered if found within the cone of a reconstructed jet (i.e. requiring $\Delta R(\mu, \mathrm{jet}) > 0.5$).

The set of selection criteria listed above define *loose* muons.

A muon from the decay of a W boson in a top quark event is expected to be isolated from surrounding activity in both the tracking detectors and the calorimeter. For *tight* muons, additional isolation criteria are therefore required:

- The transverse momentum of all tracks, p_T^{track}, in a cone of radius $\Delta R = 0.5$ around the muon (excluding the muon itself) should be small relative to the transverse momentum of the muon, p_T^{μ}:

$$\sum_{\Delta R<0.5} \frac{p_T^{\mathrm{track}}}{p_T^{\mu}} < 0.12. \tag{7.6}$$

- The energy of all cells, E_{cell}, in a hollow cone around the muon in the calorimeter should be small compared to the transverse momentum of the muon:

$$\sum_{\Delta R<0.4} \frac{E_{\mathrm{cell}}}{p_T^{\mu}} - \sum_{\Delta R<0.1} \frac{E_{\mathrm{cell}}}{p_T^{\mu}} < 0.12. \tag{7.7}$$

Defining two sets of selection criteria, loose and tight, allows for a determination of the instrumental backgrounds in the $\ell +$ track analysis, as explained in Sec. 11.1.4.

All muons used in this thesis are required to have $p_T > 15$ GeV/c and $|\eta| < 2.0$.

7.3.3 Muon Momentum Scale and Resolution

Studies of the dimuon invariant mass distribution show that the muon momentum scale and resolution in the simulation differs from that observed in data. Therefore, additional corrections are applied to simulated muons. The corrected muon momentum p_T' is defined by:

$$\frac{1}{p_T'} = \frac{1}{\alpha p_T} + \mathrm{Gaus}(\mu = 0, \sigma) \tag{7.8}$$

where α is a correction factor which accounts for the overall energy scale and $\mathrm{Gaus}(\mu = 0, \sigma)$ is a Gaussian smearing term. An additional correction is applied to muons matched to central tracks with no hits in the SMT. The central tracks matched to these muons are refitted such that their d_{ca} calculated with respect to the primary vertex is zero. The agreement between data and simulation after corrections is shown in Fig. 7.6.

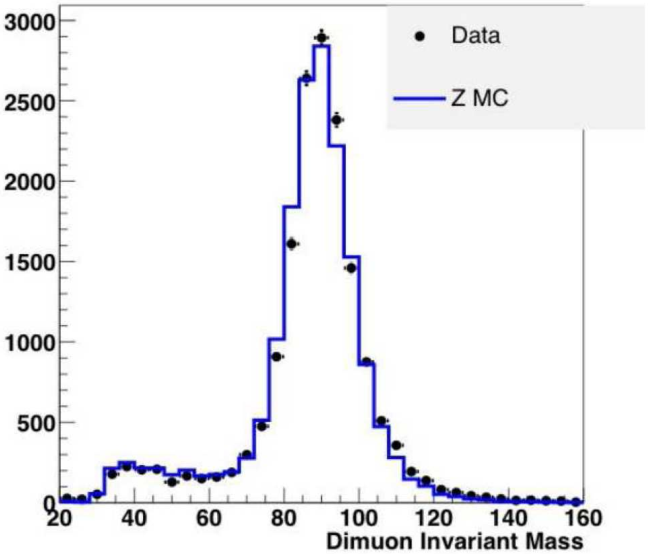

Figure 7.6: The dimuon invariant mass peak in $Z/\gamma^* \rightarrow \mu\mu$ events in data and simulation after momentum scale and resolution corrections are applied to the simulated muons.

The muon momentum measurement is based solely on information from the central tracking system. The above corrections are therefore also applied to candidate tracks in $\ell +$ track events.

7.4 Electrons

7.4.1 Electron Algorithm

Electrons are reconstructed from information in both the calorimeter and the central tracker. The characteristic signature of an electron is a narrow shower in the EM calorimeter section, a shower in the preshower detectors and a matching track in the central tracker.

The EM clusters in the calorimeter are reconstructed using a simple cone algorithm. The algorithm clusters calorimeter cells around seeds with $E_T > 1.5$ GeV in a cone of radius $\Delta R = \sqrt{\Delta\eta^2 + \Delta\phi^2} = 0.4$.

Since photons are particles with no charge they do not leave signals in the tracking system. An EM calorimeter cluster without a track match is therefore classified as a photon.

7.4.2 Electron Identification

Additional variables are used to aid in the electron identification process. Electrons generally deposit most of their energy in the EM part of the calorimeter. The ratio of the clusters electromagnetic to total energy in the calorimeter, called the EM fraction,

$$f_{\mathrm{EM}} = \frac{E_{\mathrm{EM}}(\Delta R < 0.2)}{E_{\mathrm{tot}}(\Delta R < 0.2)} \tag{7.9}$$

is therefore required to be large. To further reduce the rate at which jets are misidentified as electrons, electron candidates should be isolated, requiring the f_{iso} variable:

$$f_{\mathrm{iso}} = \frac{E_{\mathrm{tot}}(\Delta R < 0.4) - E_{\mathrm{EM}}(\Delta R < 0.2)}{E_{\mathrm{EM}}(\Delta R < 0.2)} \tag{7.10}$$

to be small. Here $E_{\mathrm{tot}}(\Delta R < 0.4)$ is the total cluster energy in a cone of radius $\Delta R = 0.4$ and $E_{\mathrm{EM}}(\Delta R < 0.2)$ is the clusters electromagnetic energy in a cone of radius $\Delta R = 0.2$.

Isolated calorimeter clusters ($f_{\mathrm{iso}} < 0.2$) with a large electromagnetic fraction ($f_{\mathrm{EM}} > 0.90$) are referred to as *extra-loose* electrons. A large fraction of the extra-loose electrons are jets which have been misidentified as electrons. The extra-loose electrons are therefore used to estimate instrumental backgrounds in the $e\mu$ analysis, as discussed in Sec. 10.1.3.

Electron clusters should also have an electron-like longitudinal and transverse shower shape profile. A variable called χ^2_{cal} is constructed from variables which describe the shower shape. In the $e\mu$ analysis the χ^2_{cal} is constructed from eight variables whereas the χ^2_{cal} used in the $\ell +$ track analysis is based on seven variables. In common to both χ^2_{cal} definitions are the following six variables:

- The fractional energies in the first, second, third and fourth layers of the EM calorimeter section
- The total shower energy
- The z position of the primary vertex

The $e\mu$ analysis in addition uses the following two variables:

- The transverse shower width in ϕ and z

The $\ell +$ track analysis instead uses:

- The $r - \phi$ cluster size in the third layer of the calorimeter, where electrons generally reach their shower maximum

A *loose* electron is defined as an extra-loose electron with these additional criteria:

- $f_{\text{EM}} > 0.9$
- $f_{\text{iso}} < 0.15$
- $\chi^2_{\text{cal}} < 75$ in the $e\mu$ analysis and $\chi^2_{\text{cal}} < 50$ in the $\ell +$ track analysis
- Central track match within $\Delta\phi < 0.05$ and $\Delta\eta < 0.05$
- The distance between the electron and the primary vertex along the z direction, $\Delta z(e, \text{PV})$ is required to be less than 1 cm
- In the $\ell +$ track analysis, the electron is not considered if found within the cone of a reconstructed jet (i.e. requiring $\Delta R(e, \text{jet}) > 0.5$).

Loose electrons are used when estimating instrumental backgrounds in the $\ell +$ track analysis.

The definition of *tight* electrons include, in addition to the loose electron criteria, a cut on an electron likelihood variable, e_{lhood}, The electron likelihood is built from eight input variables, measured in both the calorimeter and the central tracking system:

- The χ^2 probability of the spatial match between the EM cluster and the central track
- The E_T of the cluster divided by the p_T of the central track
- The χ^2_{cal} shower shape variable
- The EM fraction f_{EM}
- The distance of closest approach to the primary vertex
- The number of tracks in a narrow cone of radius $\Delta R = 0.05$ around the matched track
- The scalar sum of the p_T of all tracks in a cone of radius $\Delta R = 0.4$ around the matched track

The likelihood cuts used to select tight electrons are $e_{\text{lhood}} > 0.75$ (CC electrons), $e_{\text{lhood}} > 0.80$ (EC electrons) in the $e\mu$ analysis and $e_{\text{lhood}} > 0.85$ (all electrons) in the $\ell +$ track analysis.

All electrons used in this thesis are required to have $p_T > 15$ GeV/c and $|\eta| < 1.1$ or $1.5 < |\eta| < 2.5$.

7.4.3 Electron Energy Scale and Resolution

The electron energy scale is obtained by requiring that the reconstructed $Z/\gamma^* \rightarrow ee$ mass peak matches the world average Z boson mass computed by the Particle Data Group [28]. The energy scale factors are derived separately for electrons reconstructed in the central and in the endcap calorimeters. Samples of $J/\psi \rightarrow e^+e^-$ events are used to check the calibration at lower energies.

The energy as well as the resolution of simulated electrons is corrected using parameters tuned by comparing the position and width of the $Z/\gamma^* \rightarrow ee$ invariant mass peak in data and simulation. The energy resolution of electrons can be parameterized as:

$$\frac{\sigma_E}{E} = C \oplus \frac{S}{\sqrt{E}} \oplus \frac{N}{E}, \tag{7.11}$$

where C, S and N represent the constant, sampling and noise terms respectively. The following formula can therefore be used to adjust the scale and width of simulated electrons:

$$E' = E \times (\alpha + \xi_1 + \xi_2 + \xi_3)\,, \tag{7.12}$$

where E is the uncorrected electron energy, E' is the corrected electron energy, α is the scale factor and

$$\begin{aligned} \xi_1 &= \text{Gaus}(\mu = 0, \sigma = \alpha c) \\ \xi_2 &= \text{Gaus}(\mu = 0, \sigma = s\sqrt{\alpha/E}) \\ \xi_3 &= \text{Gaus}(\mu = 0, \sigma = n/E) \end{aligned} \tag{7.13}$$

The variables c, s and n are the smearing coefficients in the constant, sampling and noise terms. Studies show that the parameterization:

$$E' = E \times (\alpha + \xi_1)\,, \tag{7.14}$$

is sufficient to bring the electron energy scale and resolution in data and simulation in agreement. Figure 7.7 shows the agreement between data and simulation after the correction described Eq. 7.14 is applied.

7.5 Jets

7.5.1 Jet Algorithm

The fragmentation of quarks and gluons typically results in cone-shaped jets of particles. The idea behind a jet algorithm is to find the energy of the initial parton by grouping together items in cones of fixed radius having their origin at the interaction point. A good jet algorithm should fulfill a number of basic requirements. Since QCD has poles for the emission of low energy partons at any angle and for the collinear emission of partons, the ideal jet algorithm should be infrared and

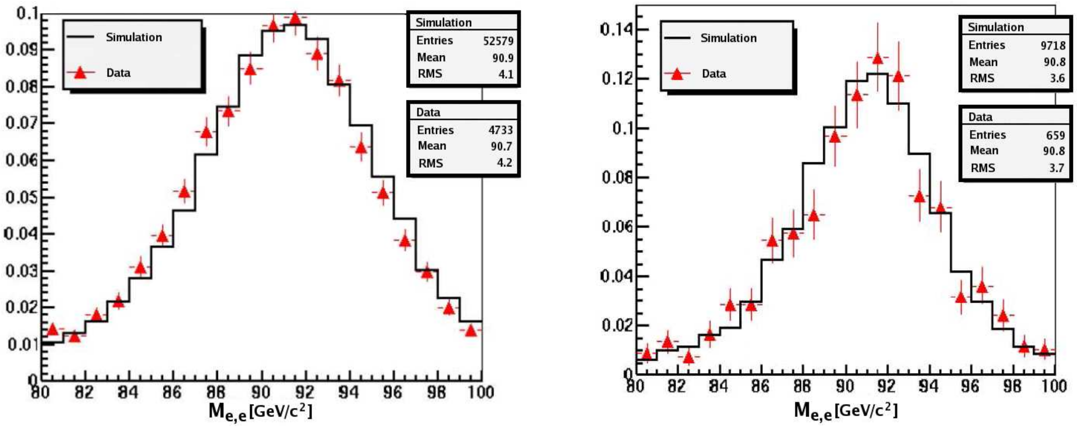

Figure 7.7: The invariant mass peak of $Z/\gamma^* \to ee$ events in data and simulation after electron energy scale and resolution corrections are applied to the simulated electrons. The left plot shows electrons reconstructed in the central calorimeter whereas the right plot shows electrons reconstructed in the endcap calorimeters.

collinear safe in order to give meaningful theoretical predictions. The algorithm should therefore be insensitive to the emission of soft partons (infrared safety) as well as to replacing two close partons with one parton carrying the same energy as the two original partons (collinear safety). An ideal algorithm should also be as independent as possible of detector characteristics such as geometry and granularity and it should be invariant under longitudinal boosts along the beam axis. In DØ the reconstruction of jets is done using the seed-based improved legacy cone algorithm [160].

The first step of the algorithm is to form preclusters using a simple cone algorithm. Starting from a list of E_T-ordered calorimeter towers, preclusters are formed around seed towers with $E_T > 500$ MeV by grouping all towers containing at least 1 MeV of transverse energy within a cone of $\Delta R < 0.3$. The preclusters are not allowed to contain only one tower and the total transverse energy of the precluster has to be at least 1 GeV.

In the next step, the preclusters are used as seeds when forming so called proto-jets. All towers within a cone of radius $\Delta R_y = 0.5$[1] having positive energy are included in the proto-jet. The proto-jet is then in turn used as a seed for the next iteration of proto-jet formation. The iterative process is repeated until a stable cone is obtained.

Using a seed-based algorithm gives rise to infrared and collinear instabilities. To address this problem, the algorithm also has to use as starting points for proto-jets so called “midpoints”, which are defined as the E_T-weighted sum of two proto-jets.

---

[1] $\Delta R_y = \sqrt{\Delta y^2 + \Delta\phi^2}$ is defined using the true rapidity y instead of pseudorapidity η.

The last step of the jet algorithm is to merge or split proto-jets which share energy. Any two proto-jets are merged into one jet if the shared E_T is more than 50% of the E_T of the lower energy jet. Otherwise the two proto-jets are split so that energy is no longer shared. Only jets which have $p_T > 8$ GeV/c are considered.

7.5.2 Jet Identification

Additional quality criteria are applied to jets in order to suppress backgrounds originating from noise. The coarse hadronic fraction (f_{CH}), which is the fraction of the total jet energy contained in the coarse hadronic section of the calorimeter, is required to be less than 0.4. The hot fraction (f_{hot}), which is the ratio of the energy of the most energetic cell in a jet to that of its next-to-highest energy cell, is required to be less than 10. The number of cells containing 90% of the total jet energy (N_{90}) is required to be greater than 1. Since noise generally does not appear simultaneously in the precision readout chain and the separate Level 1 calorimeter trigger readout, the ratio of the L1 energy to the precision readout energy in a jet (f_{L1}) is another powerful discriminant against noise, and is required to be greater than 0.4 for central jets and greater than 0.2 for forward jets. To remove isolated electromagnetic particles, the electromagnetic fraction of the energy in the jet (f_{EM}) is required to be less than 0.95. To suppress noise jets, the electromagnetic fractions is in addition not allowed to be less than 0.05. The jets are also required to be within $|\eta| < 2.5$ and to have $p_T > 20$ GeV/c (after jet energy scale corrections). The jet identification requirements are summarized in Table 7.1.

Cut	Target
$0.05 < f_{\text{EM}} < 0.95$	Electromagnetic particles and noise.
$f_{\text{CH}} < 0.4$	Noise in coarse hadronic layers.
$f_{\text{hot}} < 10$	Jets clustered around a single cell.
$N_{90} > 1$	Jets clustered around a single cell.
$f_{\text{L1}} > 0.4$ ($|\eta| < 0.7$)	Noise in readout electronics.
$f_{\text{L1}} > 0.2$ ($0.7 < |\eta| < 1.6$)	Noise in readout electronics.

Table 7.1: The identification criteria applied to jet candidates. The variable definitions are provided in the text.

Electrons and photons with transverse momentum greater than 8 GeV/c are also often identified as jets. In order to avoid double counting, jets which are also identified as electrons or photons are not considered to be jets.

7.5.3 Jet Energy Scale Corrections

The calorimeter is very effective at absorbing the hadronic energy of the jet. However there are a number of mechanisms which cause the energy of the reconstructed jet to differ from that of the original parton. The most important effects are:

Calorimeter response (R) A significant fraction of the parton energy is invisible to the calorimeter. The main sources of invisible energy are unbinding of nuclei by spallation, non-ionizing collisions and neutrino production. Furthermore the measured jet energy can be distorted due to different response of the calorimeter to different particles, a non-linear response of the calorimeter to particle energy, un-instrumented regions and dead material.

Energy offset (O) Energy in the clustered cells which is due to the underlying event, multiple interactions, energy pile-up from previous bunch-crossings, electronics noise and noise from the uranium absorber can provide an offset to the energy of the jet.

Showering correction (S) Particles associated with the hadron shower can deposit their energy outside the jet cone.

Jet energy scale (JES) corrections are applied to adjust jet energies back to the particle level using the following relation:

$$E_{\text{jet}}^{\text{particle}} = \frac{E_{\text{jet}}^{\text{meas}} - O}{R \times S}, \tag{7.15}$$

where $E_{\text{jet}}^{\text{meas}}$ is the measured energy of the jet and $E_{\text{jet}}^{\text{particle}}$ is the particle-level energy. The calorimeter response R is determined from events containing a jet and a photon in a back-to-back configuration. The energy of the photon is purely electromagnetic and its electromagnetic energy scale can be calibrated independently using $Z/\gamma^* \to ee$ events. The transverse energy of the jet should balance the transverse energy of the photon. The energy offset O is determined from energy densities in events which have been triggered by activity in the luminosity monitors (so called minimum bias triggers). The shower correction S is determined from studying measured profiles of the jet energy. Since the processes described above are not perfectly modeled in the simulation, JES corrections are derived separately for events in data and simulation.

7.5.4 Jet Energy Resolution

The jet energy resolution is measured using events containing two jets in a back-to-back configuration. The sample is split in several bins of p_T and for each bin the asymmetry variable:

$$A_{\text{jet1,jet2}} = \frac{|p_T^{\text{jet1}} - p_T^{\text{jet2}}|}{p_T^{\text{jet1}} + p_T^{\text{jet2}}} \tag{7.16}$$

is studied. The width of the A distribution, $\sigma_{A_{\mathrm{jet1,jet2}}}$, is obtained from a fit to a Gaussian function with a mean value of zero. The jet energy resolution is then given by

$$\frac{\sigma_{p_T^{\mathrm{jet}}}}{p_T^{\mathrm{jet}}} = \sqrt{2}\sigma_{A_{\mathrm{jet1,jet2}}}. \tag{7.17}$$

The single jet trigger used to obtain the data sample is only fully efficient for jet with $p_T > 40$ GeV/c. To parameterize the jet energy resolution for jets with lower transverse momentum, events containing a jet and a photon in a back-to-back configuration are used. These events are collected with a single EM trigger. In the photon+jet events the asymmetry variable is defined as

$$A_{\gamma,\mathrm{jet}} = \frac{|p_T^{\mathrm{jet}} - p_T^{\gamma}|}{p_T^{\gamma}}. \tag{7.18}$$

Given that the energy resolution of the photon is much better than that of the hadronic jet, ($\sigma_{p_T}^{\gamma}$ is negligible compared to $\sigma_{p_T}^{\mathrm{jet}}$), and the jet energy resolution can be expressed as:

$$\frac{\sigma_{p_T^{\mathrm{jet}}}}{p_T^{\mathrm{jet}}} = \sigma_{A_{\gamma,\mathrm{jet}}} \times R_{\gamma,\mathrm{jet}}, \tag{7.19}$$

where $R_{\gamma,\mathrm{jet}} = \frac{p_T^{\gamma}}{p_T^{\mathrm{jet}}}$ quantifies the energy imbalance between the photon and the jet. Within the uncertainty of the JES, $R_{\gamma,\mathrm{jet}}$ is consistent with unity.

The jet resolutions as a function of the jet p_T, derived from dijet and photon+jet events are fitted together using

$$\frac{\sigma_{p_T}}{p_T} = C \oplus \frac{S}{\sqrt{p_T}} \oplus \frac{N}{p_T}, \tag{7.20}$$

where C, S and N are defined in Sec. 7.4.3. To bring the resolution in the simulation to agree with that observed in data, jet energies in the simulation are smeared according to a Gaussian distribution with the width

$$\sigma_{p_T} = \sqrt{(\sigma_{p_T}^{\mathrm{data}})^2 - (\sigma_{p_T}^{\mathrm{sim}})^2}. \tag{7.21}$$

7.6 Missing Transverse Energy

The presence of a neutrino in an event is deduced from the imbalance of the visible energy in the transverse plane (referred to as the $\not\!\!E_T$). Calculations of this quantity begin with the vector sum of the transverse energies of all calorimeter cells containing at least a minimal amount of energy. Cells in the coarse hadronic layers are included in the $\not\!\!E_T$ calculation only if they belong to an identified jet. The opposite of the resulting vector is called the raw missing transverse energy ($\not\!\!E_T^{\mathrm{raw}}$).

The energy of calorimeter cells which are part of a reconstructed jet, electron or photon are subtracted from the $\not\!\!E_T^{\text{raw}}$ and replaced by the energies of the particles obtained after jet energy and electron energy scale corrections. The resulting quantity is called the calorimeter missing transverse energy ($\not\!\!E_T^{\text{cal}}$).

To obtain a better estimate of the true energy imbalance in the event the muons are also taken into account in the $\not\!\!E_T$ calculation. Since muons are minimum ionizing particles which deposit only a small fraction of their energy in the calorimeter, $\not\!\!E_T^{\text{cal}}$ does not account for the full muon momentum. Therefore, the momenta of all identified muons in an event are vectorially subtracted from $\not\!\!E_T^{\text{cal}}$ after first deducting the expected energy depositions of the muons in the calorimeter. The resulting vector, simply called the missing transverse energy ($\not\!\!E_T$), is used in the $e\mu$ analysis presented in this thesis.

In the $\ell +$ track selection, one of the two leptons in the event is reconstructed as an isolated track, without requiring any confirmation from the calorimeter or muon system. This type of event selection introduces the need of two additional $\not\!\!E_T$ corrections, one which is applied to both the $e +$ track and $\mu +$ track channels but is most important in the $\mu +$ track channel and one which is targeted only at the $e +$ track channel.

Muon-track correction Due to inefficiencies in the muon identification criteria, as well as the reduced muon system coverage in parts of the detector, it is not uncommon that the selected isolated track in the $\ell +$ track analysis comes from a muon which is not reconstructed in the muon system. Additional $\not\!\!E_T$ corrections taking into account these muons are therefore needed. In the $\ell +$ track analysis, the p_T of the selected isolated track is vectorially subtracted from the $\not\!\!E_T$ if:

- the isolated track does not point to ($\Delta R > 0.5$) a reconstructed muon, electron or jet.
- the $\not\!\!E_T$ is aligned with the isolated track, $\Delta\phi(\text{track}, \not\!\!E_T) < 0.5$.

Electron-track correction Electrons cannot be identified in the ICD region of the calorimeter. In the $\ell +$ track analysis however, the selected isolated track is allowed to point to the ICD region. To improve the $\not\!\!E_T$ resolution for these events, the p_T of the isolated track is used instead of the energy deposited in the calorimeter. The energy in the calorimeter in a cone of radius $\Delta R = 0.4$ around the isolated track is vectorially added to the $\not\!\!E_T$, and the p_T of the track is then vectorially subtracted. The correction is only applied to electron+track events where the invariant mass of the electron and the track is consistent with the mass of the Z boson ($75 < M_{e,\text{track}} < 105$ GeV/c^2) and where the track does not point to any track-matched local muon.

The $\not\!\!E_T$ obtained after the above corrections is used throughout the $\ell +$ track analysis. Figure 7.8 shows the $\Delta\phi$ between the selected isolated track and the $\not\!\!E_T$

in simulated $Z/\gamma^* \to \ell\ell$ events. In the $\mu +$ track channel the effect of the additional corrections is substantial, whereas the corrections make very little difference in the $e +$ track channel.

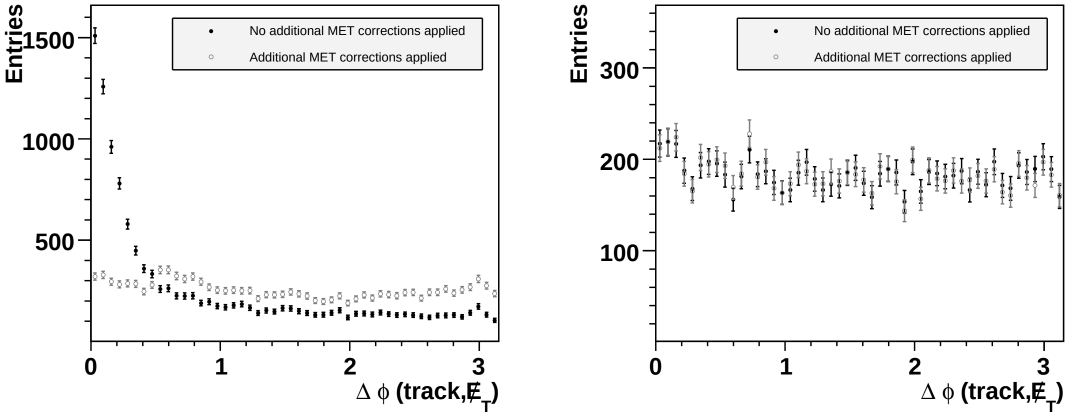

(a) The $\mu +$ track channel. (b) The $e +$ track channel.

Figure 7.8: The $\Delta\phi$ between the lepton and the $\not\!\!E_T$ before and after the additional $\not\!\!E_T$ corrections are applied.

The $\not\!\!E_T^Z$ variable

Although the isolated track candidates in the $\ell +$ track analysis are required to be of good quality, some poorly measured tracks still remain in the sample. Since the p_T of the isolated track is often used in the calculation of the $\not\!\!E_T$, a poorly measured track p_T translates into a poorly measured $\not\!\!E_T$. This could cause processes without neutrinos in the final state, for example $Z/\gamma^* \to \ell\ell$, to have large apparent $\not\!\!E_T$ and mimic the top quark signature.

To reduce the amount of misreconstructed Z/γ^* events in the $\ell +$ track sample, a $\not\!\!E_T^Z$ variable is used. The variable is constructed under the assumption that the selected lepton and isolated track originate from a Z boson decay. The invariant mass of the lepton-track pair is assumed to be that of the Z boson, and the p_T of the isolated track is recalculated. The recalculated track p_T then replaces the standard p_T in the calculation of $\not\!\!E_T^Z$. Events which have a large $\not\!\!E_T$ but a small $\not\!\!E_T^Z$ are likely to be misreconstructed Z boson events.

7.7 Jets from b Quarks

According to the standard model, top quarks decay almost exclusively into a W boson and a b quark. The b quarks hadronize and form B mesons which typically travel a few millimeters in the detector before decaying. The presence of such a secondary decay vertex, displaced from the PV, inside the jet cone indicates that the jet originated from a b quark. The process of identifying jets originating from b quarks is called b-tagging and is a very powerful discriminant against background processes which predominantly contain jets from light quarks or gluons.

7.7.1 The Secondary Vertex Tagging Algorithm

The b-tagging algorithm used throughout this thesis is the secondary vertex tagging (SVT) algorithm which explicitly reconstructs secondary vertices inside of jets. It consists of three main steps: the the primary vertex finding, the reconstruction of track-based jets (track jets) and secondary vertex finding within track jets.

Track jets are reconstructed using a $\Delta R = 0.5$ cone algorithm. A track with $p_T > 1$ GeV/c is used as the seed. Only tracks with $p_T > 0.5$ GeV/c, at least two hits in the SMT, $d_{ca} < 0.2$ cm and $\Delta z(\text{track}, \text{PV}) < 0.4$ cm are used in the track jet formation.

Only tracks of good quality are allowed to form secondary vertices. In addition to the selections applied in the track jet formation, the tracks must have $\chi^2/N_{\text{dof}} < 3$ to ensure a good impact parameter resolution. The tracks are also required to have $p_T > 1$ GeV/c, $d_{ca} < 0.15$ cm and an impact parameter significance $d_{ca}/\sigma(d_{ca}) > 3.5$. Pairs of tracks with an invariant mass consistent with coming from γ conversions or the decays of K^0_S and Λ particles are not considered.

The secondary vertex finding uses as so called build-up algorithm. It starts by forming seed vertices from pairs of tracks within a track jet. Additional tracks are added to a given vertex if the contribution to the vertex χ^2 from the additional track is less than 15. From the resulting list of vertices, those which fulfill the following criteria are selected:

- The decay length L_{xy}, defined as $L_{xy} = \vec{r}_{\text{SV}} - \vec{r}_{\text{PV}}$, fulfills $L_{xy} < 2.6$ cm
- The unsigned decay length significance fulfills $|L_{xy}|/\sigma_{L_{xy}} > 7.0$
- The collinearity C, defined as $\hat{L}_{xy} \cdot \hat{p}_{\text{SV}}$, fulfills $C > 0.9$. The quantity $\hat{p}_{\text{SV}}$ is the normalized secondary vertex momentum vector computed from the vector sum of the momenta of all tracks attached to the secondary vertex.
- The vertex $\chi^2/N_{\text{dof}} < 10$

A jet is said to be b-tagged if a secondary vertex is found within the $\Delta R = 0.5$ jet cone. A secondary vertex originating from the decay of a heavy quark is expected to have a positive decay length. A negative decay length is assigned to a secondary vertex when the tracks meet at a point behind the primary vertex with respect to the jet axis. If the signed decay length significance of the secondary vertex is less than -7.0, the jet is called negatively tagged, and if it is greater than 7.0 the jet is called positively tagged or simply tagged. The difference between a positive and negative tag is illustrated in Fig. 7.9.

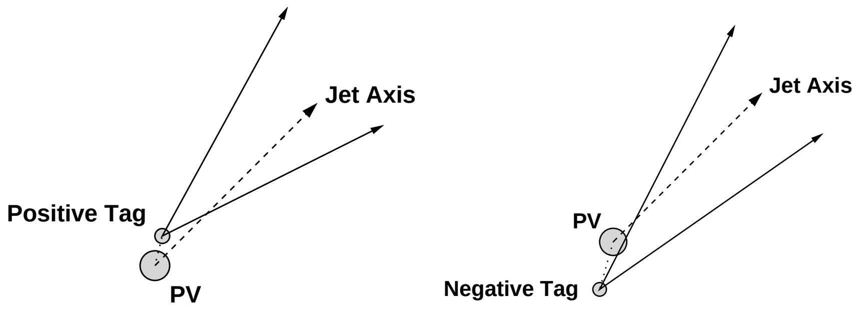

(a) Positive tag. (b) Negative tag.

Figure 7.9: In negative tags the tracks meet behind the primary vertex (PV), as opposed to positive tags where they meet in front of the PV.

7.7.2 Taggability

In order to decouple the efficiency of the b-tagging algorithm from inefficiencies in the tracking or jet algorithms, jets are considered for b-tagging only if the jet cone contains enough high quality tracks. Such a jet is referred to as a taggable jet, and the probability for a jet to be taggable is called taggability. The probability $\epsilon^{\text{tag}}(\alpha)$ for a given jet flavor α (b, c or light) to be b-tagged is the product of the taggability $\epsilon^{\text{taggability}}(\alpha)$ and the tagging efficiency $\epsilon^{\text{SVT}}(\alpha)$:

$$\epsilon^{\text{tag}}(\alpha) = \epsilon^{\text{taggability}}(\alpha) \cdot \epsilon^{\text{SVT}}(\alpha). \tag{7.22}$$

where the b-tagging efficiency $\epsilon^{\text{SVT}}(\alpha)$ is derived with respect to taggable jets only. For a jet to be taggable, it must be matched to within $\Delta R < 0.5$ of a track jet. Only calorimeter jets with $p_T > 15$ GeV/c and $|\eta| < 2.5$ are considered in the definition of taggability.

8 Object Identification Efficiencies

A important piece of a cross section analysis is knowing the efficiency for signal and background events to pass the selection criteria applied to the data events. For background events, the efficiency to pass a certain selection criterion is determined in data if a suitable independent sample can be selected. If such as sample cannot be found, which is necessarily true for the $t\bar{t}$ signal, the efficiency is obtained from simulated events. If needed, the efficiency obtained in simulated events is corrected by applying a correction factor. The data-to-simulation correction factor for a certain cut, denoted κ_{cut}, is the ratio of the efficiency observed in data to that observed in simulation:

$$\kappa_{\text{cut}} = \frac{\epsilon_{\text{cut}}^{\text{data}}}{\epsilon_{\text{cut}}^{\text{simulation}}}. \tag{8.1}$$

The correction factors κ_{cut} associated with lepton selections are generally derived on $Z/\gamma^* \to \ell\ell$ events since they provide a clean sample of isolated leptons in data. The dependence of the correction factors on kinematic properties of the events have been studied. When appropriate, the correction factors are parameterized as functions of p_T and η to account for such a dependence. The largest difference between the efficiency in data and simulation is observed for track-related variables due to the unrealistic performance of the tracking detectors in the detector simulation.

This chapter describes efficiency parameterizations and correction factors used in the $e\mu$ and $\ell+$ track cross section analyses. Since the $\ell+$ track analysis is performed on a data sample with more than twice the integrated luminosity of that used in the $e\mu$ analysis, and with a refined version of the reconstruction software, the correction factors are estimated separately in the two data sets. Unless explicitly stated, the efficiency parameterizations and correction factors presented are not found to depend on the number of jets in the event.

8.1 Primary Interaction Point

The selection criteria applied to the primary vertex are summarized in Sec. 7.1. Primary vertex cut efficiencies are determined in simulated events and are scaled with correction factors derived in $Z/\gamma^* \to ee$ and $Z/\gamma^* \to \mu\mu$ events. The correction factors are given in Tab. 8.1. Generally, no significant differences are observed between the correction factors obtained in $Z/\gamma^* \to ee$ and $Z/\gamma^* \to \mu\mu$ events, and the average of the two correction factors is used. In cases where the correction factors derived on $Z/\gamma^* \to ee$ and $Z/\gamma^* \to \mu\mu$ are significantly different, the difference is taken as a systematic uncertainty.

In the $e\mu$ analysis, the correction factor for the primary vertex quality cuts is derived separately for events with exactly one and at least two jets. In the $\ell + \text{track}$ analysis, the correction factors are found not to depend on the number of jets in the event.

Cut	κ_{cut}
$e\mu$	
PV quality ($\text{N}_{\text{jets}} = 1$)	0.978 ± 0.004
PV quality ($\text{N}_{\text{jets}} \geq 2$)	1.004 ± 0.005
$\ell + \text{track}$	
PV quality	0.993 ± 0.004
$\Delta z(\text{PV}, \text{PV}_{\text{reco}}) < 5$ cm	0.998 ± 0.002
$\Delta z(\text{PV}, \ell) < 1$ cm	0.987 ± 0.001

Table 8.1: Data-to-simulation correction factors for the primary vertex cut efficiencies applied in the $e\mu$ and $\ell + \text{track}$ analyses.

8.2 Tracks

The $\ell + \text{track}$ analysis select events with isolated tracks which are defined in Sec. 7.2. The efficiencies described in this section are only used in the $\ell + \text{track}$ analysis.

Tracks are reconstructed from hits in the central tracking system as described in Sec. 7.2.1. The efficiency to reconstruct the track from a charged lepton is different in data and simulation, due to an unrealistic description of dead detector elements and noise. A correction factor, derived on $Z/\gamma^* \to \mu\mu$ events, is found to be:

$$\kappa_{\text{tracking eff}} = 0.982 \pm 0.025 \tag{8.2}$$

Additional correction factors are derived to account for differences in the efficiency for a track to pass the isolated track identification criteria defined in Sec. 7.2.2. They are derived from $Z/\gamma^* \to ee$ and $Z/\gamma^* \to \mu\mu$ events as functions of track p_T and η. A first correction factor is derived for the efficiency of a track originating from a weak boson decay to pass all the loose isolated track identification criteria. A second correction factor is derived for the efficiency of a loose isolated track to pass the tight identification cut. The correction factors are derived separately for tracks originating from electrons and muons, due to their different dE/dx. A second degree polynomial is used to describe the shape of the correction factor as a function of the track p_T whereas a fourth degree polynomial is used for the shape as a function of the track η. The two-dimensional parameterizations as a function of track p_T and η, shown in Fig. 8.1, are obtained by taking the product of the two one-dimensional parameterizations. This assumes that the p_T and η dependencies are uncorrelated. The factorizability of the two-dimensional parameterization is validated by applying the two-dimensional efficiency parameterizations back onto the sample from which they are derived and ensure they reproduce the observed efficiencies. This procedure is used to validate a number of other parameterizations, and the method will be referred to as a closure test.

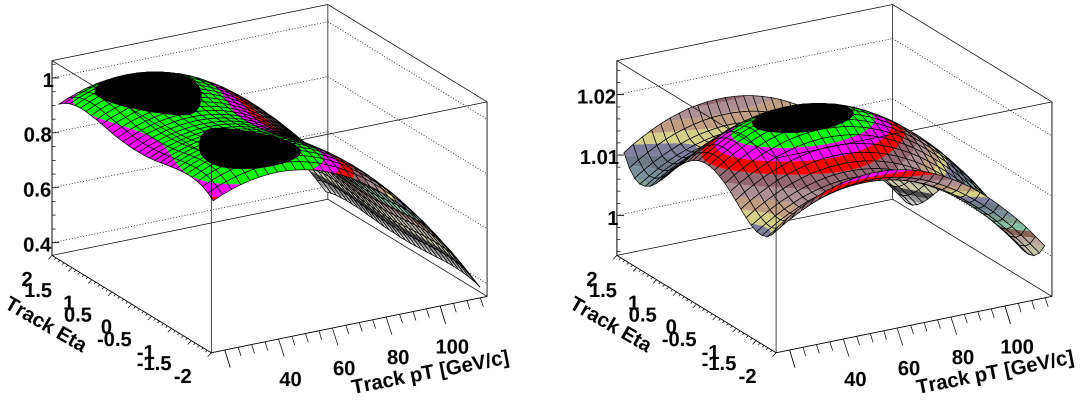

(a) Correction factor for the loose track selection applied in the e+track channel.

(b) Correction factor for the loose track selection applied in the μ+track channel.

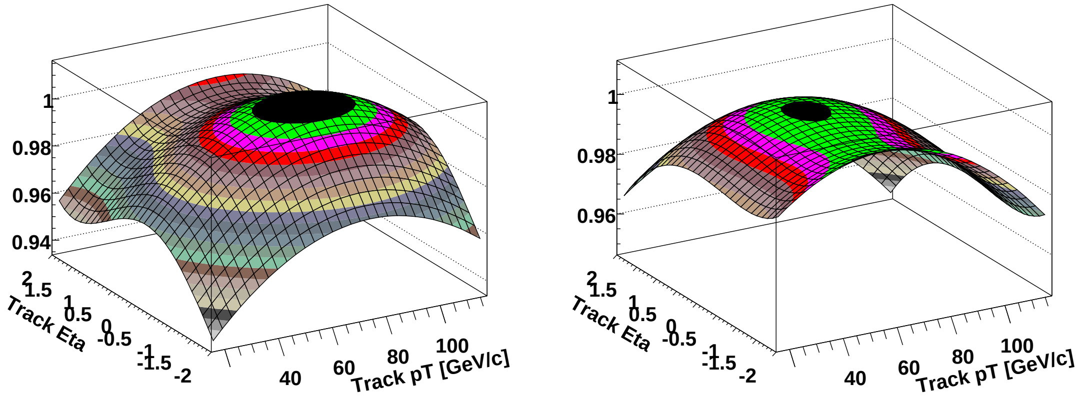

(c) Correction factor for the tight track selection, with respect to loose isolated tracks, applied in the e+track channel.

(d) Correction factor for the tight track selection, with respect to loose isolated tracks, applied in the μ+track channel.

Figure 8.1: Two dimensional correction factors for the loose and tight track selections as a function of track p_T and η.

8.3 Muons

The muon selection criteria are summarized in Sec. 7.3. The correction factors applied to the muon cut efficiencies are derived on $Z/\gamma^* \to \mu\mu$ events and are summarized in Tab. 8.2.

Cut	κ_{cut}
$e\mu$	
Local muon	η-dependent parameterization
Central track match	0.99 ± 0.01
Loose muon	0.99 ± 0.02
Tight muon	0.93 ± 0.03
$\ell + \text{track}$	
Local muon	1.00 ± 0.04
Central track match	0.99 ± 0.03
Loose muon	0.980 ± 0.003
Tight muon	1.001 ± 0.004

Table 8.2: Data-to-simulation correction factors for the muon cut efficiencies applied in the $e\mu$ and $\ell + \text{track}$ analyses. The muon selection criteria are defined in Sec. 7.3.

8.4 Electrons

The electron selection criteria are listed in Sec. 7.4, and the correction factors applied to the electron cut efficiencies are summarized in Tab. 8.3. They are derived on $Z/\gamma^* \to ee$ events and are estimated separately for electrons in the central (CC) and in the endcap (EC) calorimeters.

8.5 Taggability

As discussed in Sec. 7.7.2, the b-tagging algorithm is only applied to taggable jets. The probability for a jet to be taggable is called the taggability. It is measured in data events and applied to simulated events. The taggability strongly depends on the number of tracks within the jet cone. This variable is however not well described by the simulation and therefore cannot be used to parameterize the taggability. Instead the jet p_T, which is correlated with the number of tracks, is used. The tracking efficiency, as well as the quality of tracks, depends on the rapidity. Therefore, the taggability must also be parameterized as a function of the jet η. In each (p_T, η)-region the taggability is defined as the ratio of the number of taggable jets to the

Cut	κ_{cut} (CC)	(EC)
$e\mu$		
Loose electron	0.942 ± 0.006	0.76 ± 0.02
Tight electron	0.931 ± 0.004	0.920 ± 0.008
$\ell + \mathrm{track}$		
Loose electron	0.98 ± 0.03	0.69 ± 0.09
Tight electron	0.91 ± 0.02	0.96 ± 0.03

Table 8.3: Data-to-simulation correction factors for the loose and tight electron cut efficiencies in the $e\mu$ and $\ell + \mathrm{track}$ analyses. The electron selection criteria are defined in Sec. 7.4.

total number of jets:

$$\epsilon^{\mathrm{taggability}}(p_T, \eta) = \frac{N^{\mathrm{taggable}}(p_T, \eta)}{N^{\mathrm{all}}(p_T, \eta)}. \tag{8.3}$$

If a jet contains a muon within its cone, the muon p_T is subtracted from the jet p_T.

8.5.1 Taggability in the Electron-Muon Analysis

The shape of the taggability as a function of jet p_T and η is parameterized on data events which have passed the $e\mu$ signal trigger, defined in Sec 9.1.1, and the primary vertex quality criteria. The events are required to have one local muon and one extra-loose electron, as defined in Secs. 7.3 and 7.4. This sample is referred to as the extra-loose taggability sample. A two-dimensional taggability parameterization is built by combining the one-dimensional p_T and η dependent parameterizations. The factorizability of the parameterization is confirmed with a closure test.

The inclusive taggability (integrated over p_T and η) defined as

$$\epsilon^{\mathrm{taggability}} = \frac{N^{\mathrm{taggable}}}{N^{\mathrm{all}}} \tag{8.4}$$

in the extra-loose taggability sample is lower than the inclusive taggability observed in a data sample with one loose muon and one loose electron. The latter sample is referred to as the loose taggability sample. The taggability parameterization derived in the extra-loose taggability sample is therefore scaled with a correction factor $\kappa^{\mathrm{taggability}}$:

$$\kappa^{\mathrm{taggability}} = \frac{\epsilon^{\mathrm{taggability}}_{\mathrm{loose}}}{\epsilon^{\mathrm{taggability}}_{\mathrm{extra-loose}}}. \tag{8.5}$$

where $\epsilon_{\rm loose}^{\rm taggability}$ is the inclusive taggability observed in the loose taggability sample and $\epsilon_{\rm extra-loose}^{\rm taggability}$ is the taggability observed in the extra-loose taggability sample.

The final two-dimensional parameterization, corrected for differences between the extra-loose and loose taggability samples, is shown in Fig. 8.2.

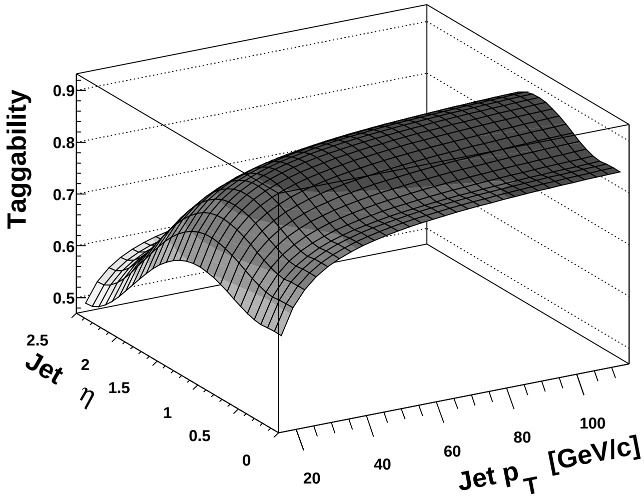

Figure 8.2: The final two-dimensional taggability parameterization as a function of jet p_T and $|\eta|$, derived on $e\mu$ data events.

8.5.2 Taggability in the Lepton+Track Analysis

The taggability is measured in a sample of data events containing one isolated electron or muon and large $\not\!\!E_T$. The two-dimensional taggability parameterizations are derived from one-dimensional p_T- and η-dependent parameterizations. The factorizability of the parameterization is confirmed with a closure test. The taggability also depends on the z position of the primary vertex (PV$_z$) and whether the jet is pointing towards (PV$_z \cdot \eta_{\rm jet} < 0$) or away from (PV$_z \cdot \eta_{\rm jet} > 0$) the center of the detector. This geometric dependence is illustrated in Fig. 8.3. The taggability parameterization defined in Eq. 8.3 is therefore derived in six different regions of (PV$_z$, PV$_z \cdot \eta_{\rm jet}$). The parameterizations are shown in Fig. 8.4.

8.5.3 Flavor Dependence of the Taggability

The taggability measured in data represents an average over all jet flavors. The data sample is dominated by light-flavor jets. The taggability is expected to be higher for b-jets and c-jets than for light-flavor jets due to the difference in fragmentation giving higher track multiplicities and tracks with higher transverse momentum. This

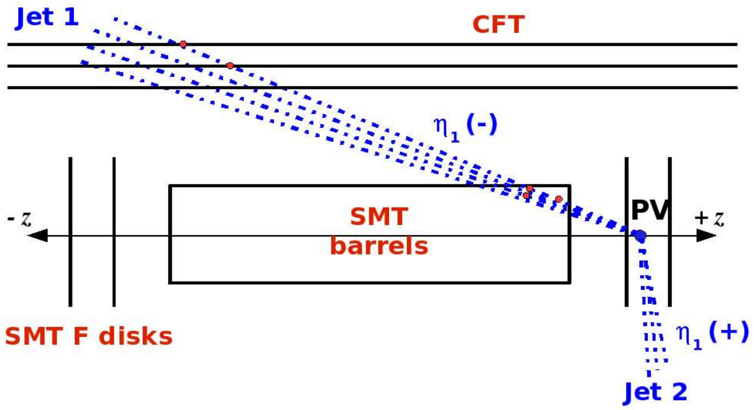

Figure 8.3: Schematic drawing showing the geometric dependence of the taggability. Shown in the picture is an event with two jets where the primary vertex is located outside the SMT barrel region. For jet 1, the product of the primary vertex position along the z-axis and the jet pseudorapidity, $\mathrm{PV}_z \times \eta_1$, is negative. This means that the tracks in the jet have a high probability of having hits in the SMT. That is not the case for jet 2 since PV_z and η_2 have the same sign.

is confirmed by simulated heavy-flavor and light-flavor jets. The ratios of b-jet to light-flavor jet and c-jet to light-flavor jet taggabilities are shown in Fig. 8.5. The parameterized ratios are used as flavor dependent correction factors to the taggability.

8.6 Efficiency for Heavy Flavor Jets

Measuring the b-tagging efficiency in data is complicated since the flavor composition of the data sample is not known a priori. Information about the flavor content can be obtained for jets containing muons within their jet cone. The data sample used to derive the b-tagging efficiency is required to have two taggable jets with $p_T > 15$ GeV/c and $|\eta| < 2.5$. One of these two jets is required to contain a muon with $p_T > 8$ GeV/c (by requiring $\Delta R(\mu, \mathrm{jet}) < 0.5$). This sample is called the muon-in-jet sample and is enriched in b-jets where the b quark has decayed semileptonically, i.e. $b \rightarrow \mu + X$. The jet containing the muon is referred to as the probe jet and the other jet is called the tag jet.

The b-tagging efficiency is derived with a method [161] based on a system of eight equations. The method considers two samples with different fractions of b-jets, called the n and p samples. The n sample is the sample with the smaller fraction of b-jets and the p sample, having a larger b-jet fraction, is a subsample of the n sample. To these two samples, two different and uncorrelated tagging algorithms are applied to

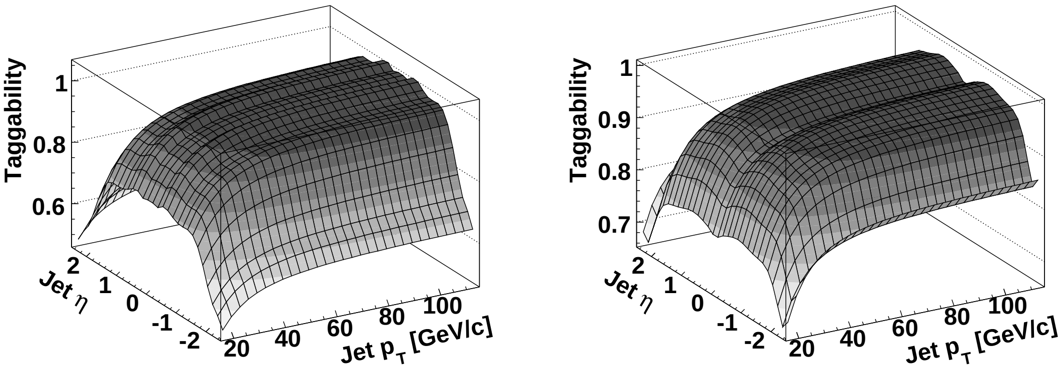

(a) $|\mathrm{PV}_z| < 20$ cm and $\mathrm{PV}_z \cdot \eta_{\mathrm{jet}} > 0$. (b) $|\mathrm{PV}_z| < 38$ cm and $\mathrm{PV}_z \cdot \eta_{\mathrm{jet}} < 0$.

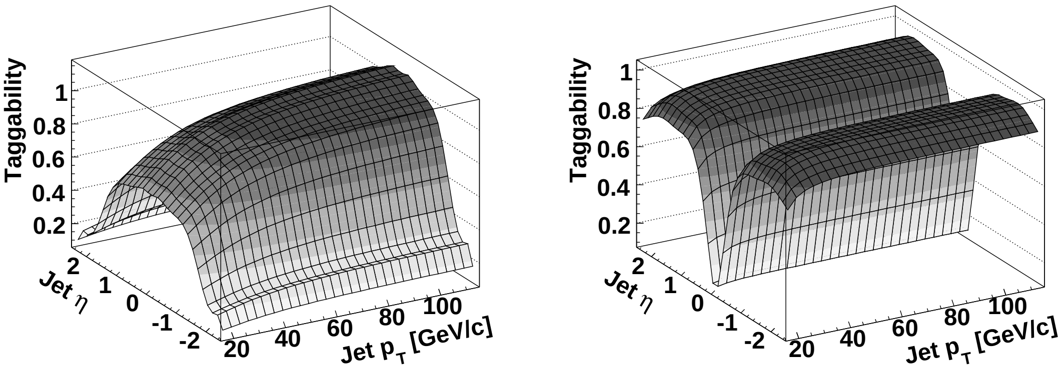

(c) 20 cm $< |\mathrm{PV}_z| < 36$ cm and $PV_z \cdot \eta_{\mathrm{jet}} > 0$. (d) 38 cm $< |\mathrm{PV}_z| < 46$ cm and $PV_z \cdot \eta_{\mathrm{jet}} < 0$.

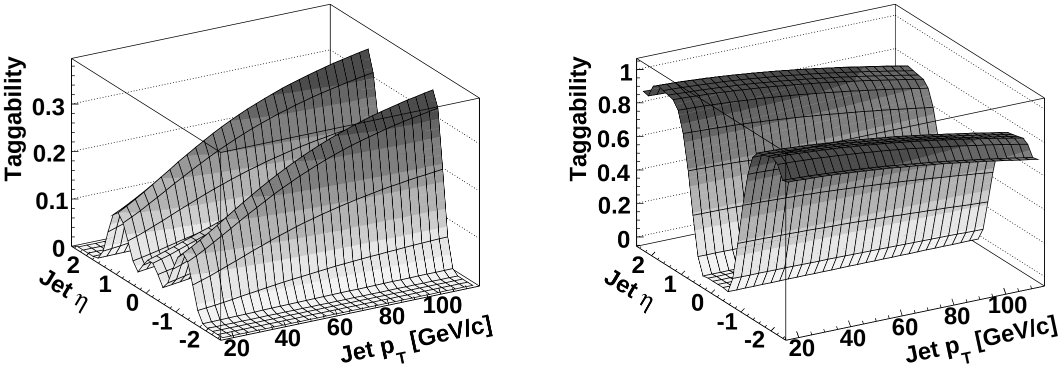

(e) 36 cm $< |\mathrm{PV}_z| < 60$ cm and $PV_z \cdot \eta_{\mathrm{jet}} > 0$. (f) 46 cm $< |\mathrm{PV}_z| < 60$ cm and $\mathrm{PV}_z \cdot \eta_{\mathrm{jet}} < 0$.

Figure 8.4: The taggability parameterizations as a function of jet p_T and η in six $(\mathrm{PV}_z, \mathrm{PV}_z \cdot \eta_{jet})$ bins.

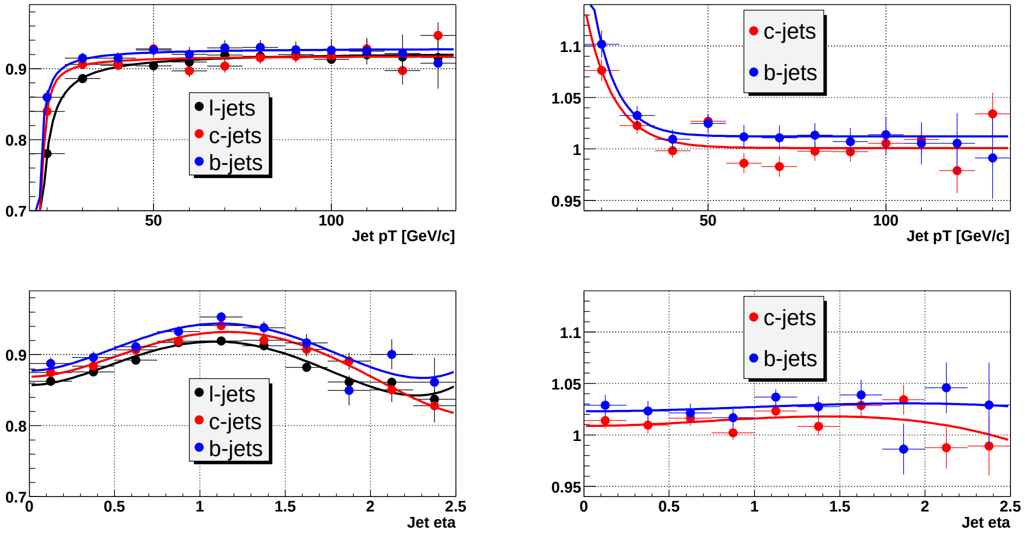

Figure 8.5: The left plots show the taggability as a function of the jet p_T and η for b-jets, c-jets and light-quark jets in simulated multijet events. The right plots show the ratios of b-jet to light-quark jet and c-jet to light quark jet taggabilities.

the probe jet. The total number of events in the n and p samples, together with the number of events tagged by the two algorithms is used to construct a system of eight equations which can be solved for the b-tagging efficiency.

The events in the muon-in-jet sample define the n sample. The p sample is obtained by requiring that the tag jet (the jet not containing the muon) is b-tagged by the SVT algorithm. The two tagging algorithms applied to the probe jet are the SVT algorithm and the muon tagger. The probe jet is considered muon-tagged if the muon has $p_{Trel} > 1$ GeV/c, where p_{Trel} is defined as the transverse momentum of the muon relative to the combined muon plus jet axis.

Denoting events tagged by the SVT and the muon tagger with superscript SVT and μ respectively, the system of eight equations can be written as:

$$\begin{aligned}
n &= n_b + n_{\text{non}-b} \\
n^{\mu} &= \epsilon_b^{\mu} n_b + \epsilon_{\text{non}-b}^{\mu} n_{\text{non}-b} \\
n^{\text{SVT}} &= \epsilon_b^{\text{SVT}} n_b + \epsilon_{\text{non}-b}^{\text{SVT}} n_{\text{non}-b} \\
n^{\mu,\text{SVT}} &= \epsilon_b^{\mu}\epsilon_b^{\text{SVT}} n_b + \epsilon_{\text{non}-b}^{\mu}\epsilon_{\text{non}-b}^{\text{SVT}} n_{\text{non}-b} \\
p &= p_b + p_{\text{non}-b} \\
p^{\mu} &= \epsilon_b^{\mu} p_b + \epsilon_{\text{non}-b}^{\mu} p_{\text{non}-b} \\
p^{\text{SVT}} &= \epsilon_b^{\text{SVT}} p_b + \epsilon_{\text{non}-b}^{\text{SVT}} p_{\text{non}-b} \\
p^{\mu,\text{SVT}} &= \epsilon_b^{\mu}\epsilon_b^{\text{SVT}} p_b + \epsilon_{\text{non}-b}^{\mu}\epsilon_{\text{non}-b}^{\text{SVT}} p_{\text{non}-b}
\end{aligned} \tag{8.6}$$

The quantities on the left hand side of the equations are the observed number of events in the untagged samples (n and p) as well as the number of events in the two samples tagged by the SVT tagger (n^{SVT} and p^{SVT}), the muon tagger (n^{μ} and p^{μ}) or both of them ($n^{\mu,\mathrm{SVT}}$ and $p^{\mu,\mathrm{SVT}}$). The right hand side consists of eight unknown quantities, namely the number of b-jets and non-b-jets in the samples (n_b, $n_{\mathrm{non}-b}$, p_b and $p_{\mathrm{non}-b}$) and the tagging efficiencies for b-jets and non-b-jets for the two tagging algorithms ($\epsilon_b^{\mathrm{SVT}}$,$\epsilon_{\mathrm{non}-b}^{\mathrm{SVT}}$,$\epsilon_b^{\mu}$ and $\epsilon_{\mathrm{non}-b}^{\mu}$). The quantity of interest is the efficiency for the SVT algorithm to tag a b-jet, $\epsilon_b^{\mathrm{SVT}}$.

Similarly to the taggability, the b-tagging efficiency depends on the p_T and η of the jet. The n and p samples are therefore divided into bins of either jet p_T or jet η. The system of equations is solved for each subsample to obtain the one-dimensional b-tagging efficiency parameterization as a function of either the jet p_T or the jet η. A combined two-dimensional parameterization is derived assuming that the p_T and η dependencies are uncorrelated and can be factorized. The resulting two-dimensional efficiency parameterization is shown in Fig. 8.6.

The method described above allows to derive the b-tagging efficiency for b-jets containing a muon, $\epsilon_{b\to\mu X}^{\mathrm{data}}(p_T,\eta)$, referred to as the semileptonic b-tagging efficiency. The b-tagging efficiency for all types of b-jets, called the inclusive b-tagging efficiency and denoted $\epsilon_b^{\mathrm{data}}(p_T,\eta)$, can be derived from the semileptonic b-tagging efficiency and ratios of efficiencies obtained on simulated events:

$$\begin{aligned}
\epsilon_b^{\mathrm{data}}(p_T,\eta) &= \epsilon_{b\to\mu X}^{\mathrm{data}}(p_T,\eta)\cdot\frac{\epsilon_b^{\mathrm{sim}}(p_T,\eta)}{\epsilon_{b\to\mu X}^{\mathrm{sim}}(p_T,\eta)} \\
&= \epsilon_b^{\mathrm{sim}}(p_T,\eta)\cdot\frac{\epsilon_{b\to\mu X}^{\mathrm{data}}(p_T,\eta)}{\epsilon_{b\to\mu X}^{\mathrm{sim}}(p_T,\eta)} \\
&= \epsilon_b^{\mathrm{sim}}(p_T,\eta)\cdot\kappa_b(p_T,\eta).
\end{aligned} \tag{8.7}$$

The inclusive and semileptonic b-tagging efficiencies are derived in the simulated $t\bar{t}$ sample. The parameterizations are shown in Fig. 8.7. The inclusive and semileptonic efficiencies are found to be very similar, except in the low p_T region where the presence of the muon track increases the tagging efficiency for semileptonic decays. At higher values of jet p_T, this effect is less important due to the higher track multiplicity.

It is not straightforward to measure the c-tagging efficiency in data, or the corresponding c-tagging correction factor κ_c. The correction factor is assumed to be equal to the b-tagging correction factor,

$$\kappa_c(p_T,\eta) = \kappa_b(p_T,\eta), \tag{8.8}$$

and the c-tagging efficiency can then be defined in analogue with the b-tagging efficiency,

$$\epsilon_c(p_T,\eta) = \epsilon_c^{\mathrm{sim}}(p_T,\eta)\cdot\kappa_c(p_T,\eta). \tag{8.9}$$

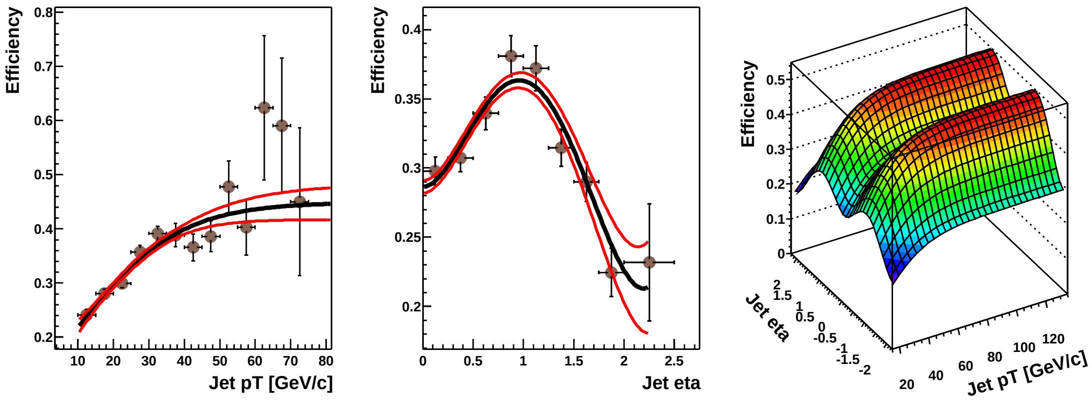

(a) Efficiency used in the $e\mu$ analysis.

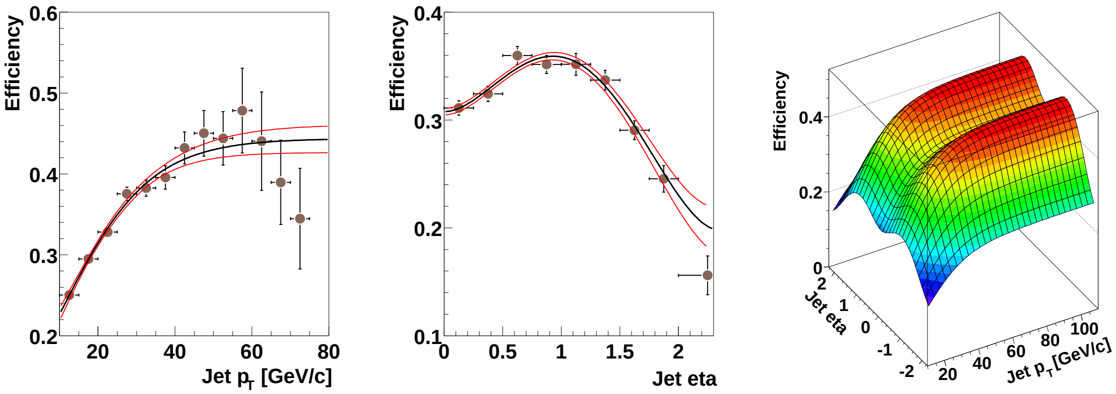

(b) Efficiency used in the $\ell +$ track analysis.

Figure 8.6: Semileptonic b-tagging efficiency in data $\epsilon^{\text{data}}_{b\rightarrow\mu X}$, as a function of jet p_T and η.

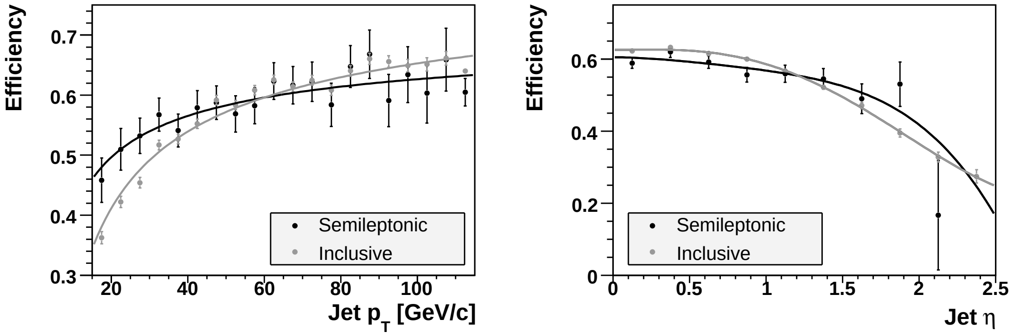

(a) Efficiencies used in the $e\mu$ analysis.

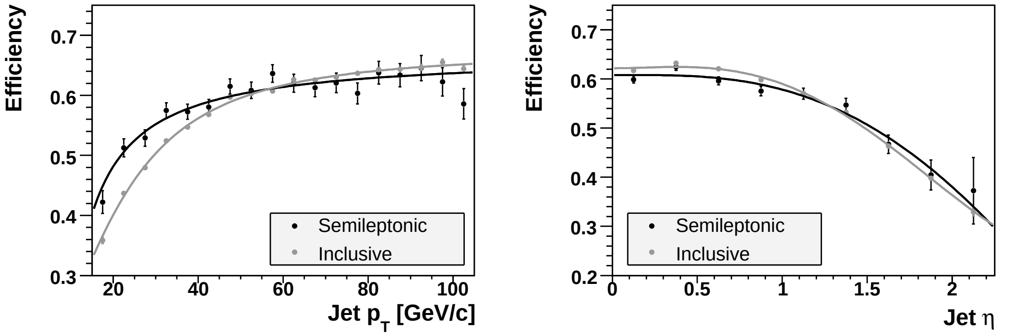

(b) Efficiencies used in the $\ell +$ track analysis.

Figure 8.7: The inclusive and semileptonic b-tagging efficiencies, ϵ_b^{sim} and $\epsilon_{b\to\mu X}^{\text{sim}}$, evaluated in simulated $t\bar{t}$ events as a function of jet p_T (left) and jet η (right).

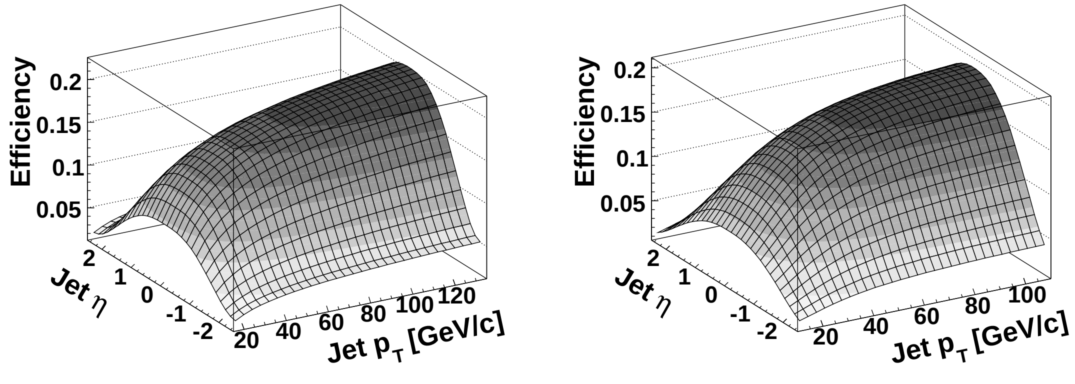

(a) Efficiency used in the $e\mu$ analysis.

(b) Efficiency used in the $\ell +$ track analysis.

Figure 8.8: The inclusive c-tagging efficiency ϵ_c^{sim}, evaluated in simulated $t\bar{t}$ events.

The parameterization of the inclusive c-tagging efficiency is shown in Fig. 8.8.

Evaluating the tagging efficiencies for b- and c-jets in simulation is straightforward since the jet flavor is known. The efficiency is defined as the ratio of the number of tagged jets to the total number of taggable jets of a particular flavor:

$$\epsilon_{b,c}^{\mathrm{sim}}(p_T, \eta) = \frac{N_{b,c}^{\mathrm{tagged}}(p_T, \eta)}{N_{b,c}^{\mathrm{taggable}}(p_T, \eta)}. \tag{8.10}$$

The b- and c-tagging efficiencies are obtained as functions of the jet p_T and η and combined into two-dimensional parameterizations assuming that the p_T and η dependencies are not correlated and can be factorized.

8.7 Mistag Rate

A b-tagged light-flavor jet (a jet from a u, d or s quark or a gluon) is called a mistagged jet (or simply mistag). Tracks originating from the primary vertex can appear displaced due to resolution effects in the tracker or due to misreconstruction, the former being the dominant source. The mistag rate due to resolution effects can be evaluated using the negative tags defined in Sec. 7.7.1.

Resolution effects are expected to contribute equally to both the positive and negative tag rate. Therefore the negative tag rate in data is a good first order estimate of the rate at which light-flavor jets are mistagged. The negative tag rate measured in data, $\epsilon_{\mathrm{neg}}^{\mathrm{data}}(p_T, \eta)$, for taggable jets is defined as:

$$\epsilon_{\mathrm{neg}}^{\mathrm{data}}(p_T, \eta) = \frac{N^{\mathrm{neg\ tagged}}(p_T, \eta)}{N^{\mathrm{taggable}}(p_T, \eta)} \tag{8.11}$$

and is evaluated in a multijet data sample. The sample is selected by requiring at least one extra-loose electron, at least one jet and $\not\!\!E_T < 10$ GeV and is referred to as the mistag sample. The measured negative tag rate is parameterized as a function of jet p_T and η. A two-dimensional parameterization, shown in Fig. 8.9, is obtained from the p_T and η parameterizations assuming they are factorizable.

There are two major effects which need to be taken into account in order to translate negative tag rate into the mistag rate:

Heavy-flavor contamination The jets in the mistag sample are not all light-flavor jets. Jets from heavy-flavor quarks have a higher negative tag rate than light flavor jets. The displaced tracks from the decay of a B- or D-hadron increase the probability to form a negative tag. The negative tag rate measured in the multijet sample is an overestimate of the magnitude of resolution effects due to the contamination from heavy-flavor jets. To compensate for the heavy-flavor contamination, a correction factor κ_{hf} is introduced.

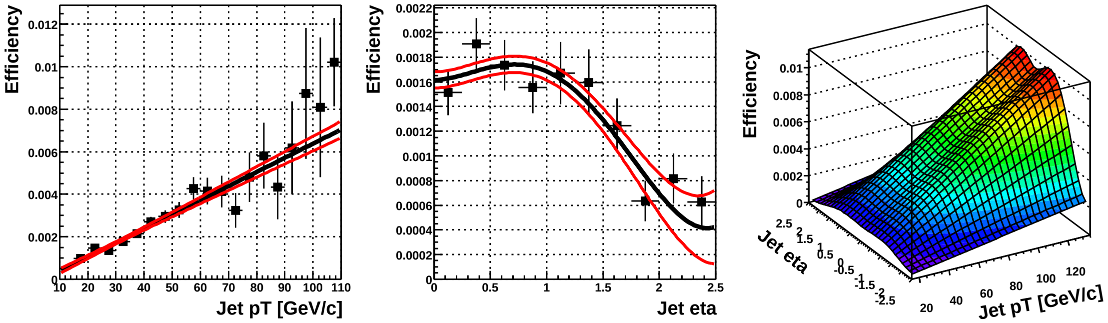

(a) The negative tag rate used in the $e\mu$ analysis.

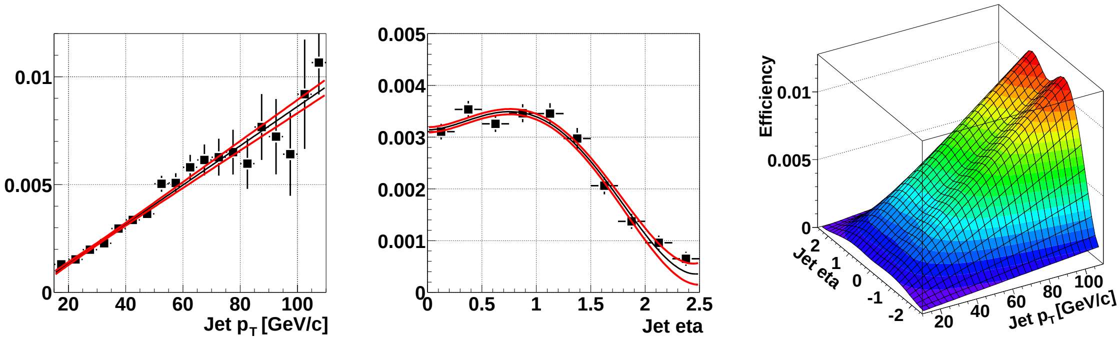

(b) The negative tag rate used in the $\ell +$ track analysis.

Figure 8.9: The negative tag rate $\epsilon_{\text{neg}}^{\text{data}}$, as a function of the jet p_T and η together with the two-dimensional parameterization.

Additional mistag rate from long-lived particles Light-flavor jets can be mistagged due to the presence of tracks from K^0_S or Λ^0 decays and γ-conversions which are not removed in the track selection stage of the SVT algorithm. The mistag rate of light-flavor jets is therefore underestimated if only resolution effects are considered. To take into account the additional mistag rate due to long-lived particles, a correction factor $\kappa_{\rm ll}$ is introduced.

The two correction factors $\kappa_{\rm hf}$ and $\kappa_{\rm ll}$ are obtained from simulated multijet events. The correction factor $\kappa_{\rm hf}$ is defined as the ratio of the negative tag rate for light-flavor jets to the negative tag rate for inclusive jet flavors:

$$\kappa_{\rm hf} = \frac{\epsilon_{\rm neg}^{\rm light}}{\epsilon_{\rm neg}}. \tag{8.12}$$

The correction factor $\kappa_{\rm ll}$ is defined as the ratio of positive to negative tag rate for light-flavor jets:

$$\kappa_{\rm ll} = \frac{\epsilon_{\rm pos}^{\rm light}}{\epsilon_{\rm neg}^{\rm light}}. \tag{8.13}$$

In the $e\mu$ analysis, the two correction functions are parameterized as a function of jet p_T as shown in Fig. 8.10. In the $\ell+$track analysis, $\kappa_{\rm hf}$ is parameterized as a function of both jet p_T and η as shown in Fig. 8.11. A constant correction factor is used to account for long-lived particles:

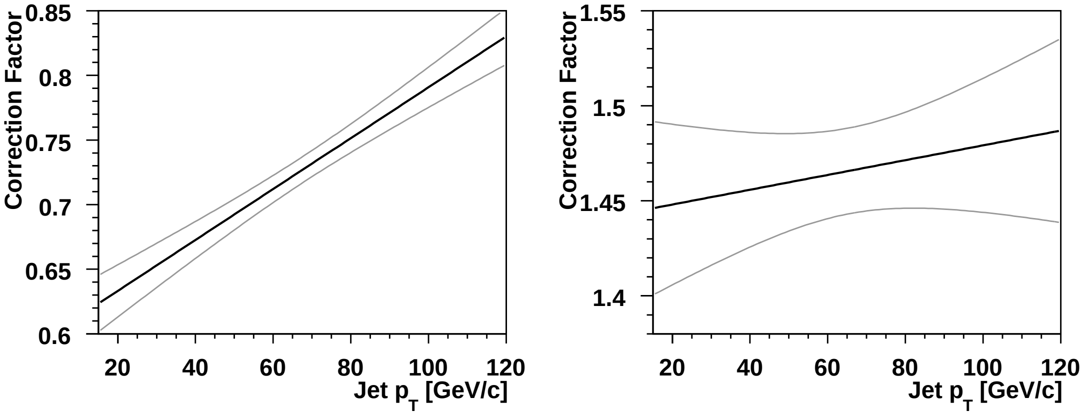

Figure 8.10: Correction factors, with uncertainty bands, applied to the negative tag rate in the $e\mu$ analysis. The left plot shows $\kappa_{\rm hf}$ which corrects for the contribution of heavy-flavor jets to the measured negative tag rate, and the right plot shows the contribution to the mistag rate from long-lived particles, $\kappa_{\rm ll}$.

$$\kappa_{\rm ll}^{\ell+{\rm track}} = 1.50 \pm 0.04 \tag{8.14}$$

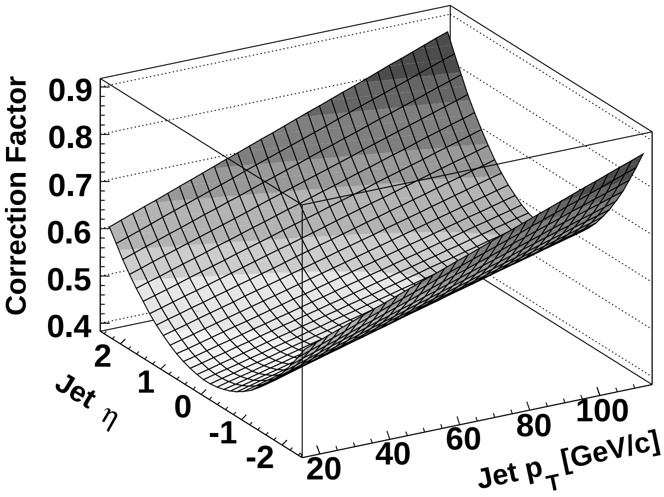

Figure 8.11: Correction factor $\kappa_{\rm hf}$ used in the $\ell +$ track analysis for the contribution of heavy-flavor jets to the measured negative tag rate.

The product of the negative tag rate measured in the mistag sample and the two correction factors is used to estimate the mistag rate for light-flavor jets $\epsilon_l(p_T, \eta)$:

$$\epsilon_l(p_T, \eta) = \epsilon_{\rm neg}^{\rm data}(p_T, \eta) \cdot \kappa_{\rm hf}(p_T, \eta) \cdot \kappa_{\rm ll}(p_T, \eta). \tag{8.15}$$

9 Sample Definitions

This chapter defines the preselected and b-tagged signal samples used in the $e\mu$ and $\ell +$ track analyses. The triggers used to collect the data are presented as well as the selection criteria applied in each analysis. At the end of the chapter the simulated samples and the auxiliary data samples used to estimate the composition of the signal samples are defined.

9.1 The Electron-Muon Signal Samples

9.1.1 The Triggered Dataset

The $e\mu$ cross section analysis uses data recorded between June 2002 and September 2003, corresponding to an integrated luminosity of 158 pb^{-1}. The triggers used to collect the data requires one electron and one muon, and are summarized in Tab. 9.1.

Level 1 Conditions	Level 2 Conditions	Level 3 Conditions	$\int \mathcal{L}dt$ (pb^{-1})
1 e, E_T >5 GeV AND 1 loose μ	none	1 loose e, E_T >10 GeV	119
1 e, E_T >6 GeV AND 1 loose μ	none	1 loose e, E_T >12 GeV	39

Table 9.1: Trigger requirements used to collect data for the $e\mu$ analysis. The integrated luminosity to which each trigger set is exposed is given in the last column. Here the terms loose muon and loose electron refer to the loose L1 muons and loose L3 electrons defined in Sec. 2.2.4.

9.1.2 The Preselected Signal Sample

The $e\mu$ preselection is based on the requirement of a tight electron, a tight muon and large $\not\!\!E_T$. These selection criteria greatly reduce the multijet background, leaving a sample dominated by the $t\bar{t}$ signal and the irreducible backgrounds. The $e\mu$ preselected signal sample is obtained by requiring the events to have:

- passed the triggers listed in Tab. 9.1.
- a primary vertex passing the quality criteria.
- at least one tight electron.
- at least one tight muon.
- $\Delta R(e, \mu) > 0.25$.
- $\not\!\!E_T > 25$ GeV.
- at least one jet.

The $\Delta R(e, \mu) > 0.25$ requirement is designed to remove $Z/\gamma^* \rightarrow \mu\mu$ events where one of the muons radiates a photon which is matched to the muon track and hence misidentified as an electron.

9.1.3 The b-tagged Signal Sample

The signal sample from which the cross section is extracted is obtained from the preselected $e\mu$ sample by requiring at least one jet in the event to be tagged by the SVT algorithm.

9.2 The Lepton+Track Signal Samples

9.2.1 The Triggered Datasets

The $\ell +$ track cross section analysis uses data recorded between June 2002 and August 2004, corresponding to an integrated luminosity of approximately 425 pb^{-1}. The triggers used to collect the data for the $\ell +$ track analysis makes selections based on electrons, muons, tracks and jets. In the early data, corresponding to trigger versions 8–11, a lepton+jets trigger is used. The later data, corresponding to trigger versions 12 and 13, is collected using a logical OR of lepton+jets and single lepton triggers. The triggers used in the $e +$ track channel are summarized in Tab. 9.2 and the corresponding summary for the $\mu +$ track channel is shown in Tab. 9.3.

9.2.2 The Preselected Signal Samples

The $\ell +$ track preselection is based on the requirement of a tight isolated track, a tight electron or muon and large $\not\!\!E_T$. These selection criteria greatly reduce the multijet background, leaving a sample dominated by Z/γ^* events.

Level 1 Conditions	Level 2 Conditions	Level 3 Conditions	$\int \mathcal{L} dt$ [pb^{-1}]
1 e, $E_T > 10$ GeV AND 2 jets, $E_T > 5$ GeV	1 e, $E_T > 10$ GeV AND 2 jets, $E_T > 10$ GeV	1 tight e, $E_T > 15$ GeV AND 2 jets, $E_T > 15$ GeV	(8-11) 128
1 e, $E_T > 11$ GeV	none	1 tight e, $E_T > 15$ GeV AND 2 jets, $E_T > 20$ GeV	(12) 244
1 e, $E_T > 11$ GeV OR 2 e, $E_T > 6$ GeV OR 2 e, $E_T > 3$ GeV, 1 e, $E_T > 9$ GeV	none	1 tight e, $E_T > 20$ GeV	
1 e, $E_T > 11$ GeV OR 2 e, $E_T > 6$ GeV OR 2 e, $E_T > 3$ GeV, 1 e, $E_T > 9$ GeV	none	1 loose e, $E_T > 50$ GeV	
1 e, $E_T > 11$ GeV	1 e, $E_T > 15$ GeV	1 tight e, $E_T > 15$ GeV AND 2 jets, $E_T > 20$ GeV AND 1 jet, $E_T > 25$ GeV	(13) 54
1 e, $E_T > 11$ GeV OR 2 e, $E_T > 6$ GeV OR 2 e, $E_T > 3$ GeV, 1 e, $E_T > 9$ GeV	1 e, $E_T > 15$ GeV	1 tight e, $E_T > 20$ GeV	
1 e, $E_T > 11$ GeV OR 2 e, $E_T > 6$ GeV OR 2 e, $E_T > 3$ GeV, 1 e, $E_T > 9$ GeV	1 e, $E_T > 15$ GeV	1 loose e, $E_T > 50$ GeV	

Table 9.2: Trigger requirements used to collect data for the e+track analysis. The integrated luminosity to which each trigger set is exposed is given in the last column, where the trigger version used to collect this part of the data is given in parenthesis. Here the term loose electron refers to the loose L3 electrons defined in Sec. 2.2.4.

Level 1 Conditions	Level 2 Conditions	Level 3 Conditions	$\int \mathcal{L}dt$ [pb^{-1}]
1 loose μ AND 1 jet $E_T > 5$ GeV	1 μ	1 jet, $E_T > 20$ GeV	(8-11) 132
1 loose μ AND 1 jet, $E_T > 3$ GeV	1 μ AND 1 jet, $E_T > 10$ GeV	1 jet, $E_T > 25$ GeV	(12) 244
1 tight μ	1 μ, $p_T > 3$ GeV/c	1 track, $p_T > 10$ GeV/c	
1 tight μ AND 1 jet, $E_T > 5$ GeV	1 μ AND 1 jet, $E_T > 8$ GeV	1 jet, $E_T > 25$ GeV	(13a) 30
1 loose μ w. trackmatch AND 1 track, $p_T > 10$ GeV/c	none	1 track, $p_T > 10$ GeV/c OR 1 μ, $p_T > 15$ GeV/c	
1 tight μ AND 1 track, $p_T > 10$ GeV/c	1 μ, $p_T > 3$ GeV/c	1 μ, $p_T > 15$ GeV/c	
1 loose μ AND 1 track, $p_T > 10$ GeV/c	1 μ	1 μ, $p_T > 15$ GeV/c	
1 tight μ AND 1 jet, $E_T > 5$ GeV	1 μ AND 1 jet, $E_T > 8$ GeV	1 μ, $p_T > 3$ GeV/c AND 1 jet, $E_T > 25$ GeV	(13b) 16
1 loose μ w. trackmatch AND 1 track, $p_T > 10$ GeV/c	none	1 track, $p_T > 10$ GeV/c OR 1 μ, $p_T > 15$ GeV/c	
1 tight μ AND 1 track, $p_T > 10$ GeV/c	1 μ, $p_T > 3$ GeV/c	1 μ, $p_T > 15$ GeV/c	
1 loose μ AND 1 track, $p_T > 10$ GeV/c	1 μ	1 μ, $p_T > 15$ GeV/c	

Table 9.3: Trigger requirements used to collect data for the μ+track analysis. The integrated luminosity to which each trigger set is exposed is given in the last column, where the trigger version used to collect this part of the data is given in parenthesis. The term loose muon refers to the loose L1 muons defined in Sec. 2.2.4.

Preselection Criteria Common to Electron+Track and Muon+Track

Some preselection criteria are common to both the $e+$ track and $\mu+$ track channels. These are aimed at ensuring a good event quality by requiring low calorimeter noise and a well reconstructed primary vertex. The events are required to have:

- low calorimeter noise.
- a primary vertex passing the quality criteria.
- a small distance in the z direction between the standard primary vertex (PV) and the low-level reconstruction PV ($\mathrm{PV_{reco}}$): $\Delta z(\mathrm{PV}, \mathrm{PV_{reco}}) < 5$ cm.
- at least one jet.

The Muon+Track Preselection Criteria

In addition to the common selection criteria, the $\mu+$ track preselected sample is obtained by requiring one tight muon, one tight isolated track and large $\not\!\!E_T$. Furthermore the events are not allowed to contain any loose electrons in order to make the selection orthogonal to both the $e+$ track and any $e\mu$ analyses. Orthogonal samples makes it straightforward to combine the measurements in the $e+$ track and $\mu+$ track channels with each other and also with measurements in the $e\mu$ channel. The $\mu+$ track preselected signal sample is obtained by requiring the events to have:

- passed the common preselection criteria defined above.
- passed the triggers defined in Tab. 9.3.
- at least one tight muon.
- at least one tight isolated track.
- opposite electric charge of the muon and the track candidates.
- $\Delta R(\mu, \mathrm{track}) > 0.5$.
- $\not\!\!E_T$ and $\not\!\!E_T^Z > 25$ GeV.
- $\not\!\!E_T$ and $\not\!\!E_T^Z > 35$ GeV if the invariant mass of the muon and the track $M_{\mu,\mathrm{track}}$, falls in the Z mass window ($70 < M_{\mu,\mathrm{track}} < 110$ GeV/c^2).
- passed the electron veto. Events are vetoed if they contain a loose electron[1].

---

[1] For the veto, the $\Delta R(e, \mathrm{jet}) > 0.5$ cut is not included in the loose electron definition.

The Electron+Track Preselection Criteria

In addition to the common selection criteria, the $e+\text{track}$ preselected sample is obtained by requiring one tight electron, one tight isolated track and large $\not\!\!E_T$. Furthermore the events are not allowed to contain any tight muons in order to make the selection orthogonal to both the $\mu+\text{track}$ and any $e\mu$ analyses. The $e+\text{track}$ preselected signal sample is obtained by requiring the events to have:

- passed the common preselection criteria defined above.
- passed the triggers defined in Tab. 9.2.
- at least one tight electron.
- at least one tight isolated track.
- opposite electric charge of the electron and the track candidates.
- $\Delta R(e, \text{track}) > 0.5$.
- $\not\!\!E_T$ and $\not\!\!E_T^Z > 15$ GeV.
- $\not\!\!E_T$ and $\not\!\!E_T^Z > 20$ GeV if the invariant mass of the electron and the track $M_{e,\text{track}}$), falls in the Z mass window ($70 < M(e, \text{track}) < 100$ GeV/c^2).
- passed the muon veto. Events are vetoed if they contain a tight muon[2].

9.2.3 The b-tagged Signal Samples

The b-tagged signal samples are defined from the preselected $e+\text{track}$ and $\mu+\text{track}$ signal samples by requiring that at least one jet is b-tagged by the SVT algorithm.

9.3 Simulated Samples

Simulated samples of $t\bar{t}$ events and various background processes are necessary to estimate the efficiency of the event selection. The samples are obtained from event generators which use Monte Carlo techniques [28] to perform the integration of the cross section. This is referred to as a Monte Carlo simulation.

Events are generated with either ALPGEN [162–164] or PYTHIA [165]. The samples generated with ALPGEN are interfaced to PYTHIA for parton showering. To simulate the detector response, the generated events are processed through a GEANT [166] simulation of the DØ detector. The events are then reconstructed using the same software as for data events. The simulated samples used in the $e\mu$ analysis are listed in Tab. 9.4 and the samples used in the $\ell+\text{track}$ analysis are listed in Tab. 9.5.

---

[2] For the veto, the $\Delta R(\mu, \text{jet}) > 0.5$ cut is not included in the tight muon definition.

Process	Generator	PDF	N_{evts}	σ(pb)
$t\bar{t} \rightarrow \ell\ell\nu\nu bb$	ALPGEN 1.2	CTEQ6.1M	47,000	-
$Z/\gamma^* \rightarrow \tau\tau$	PYTHIA 6.2	CTEQ5L	150,729	333.1 ± 14.1
$Z/\gamma^* \rightarrow \mu\mu$	PYTHIA 6.2	CTEQ5L	261,500	266.5 ± 11.8
$Z/\gamma^*(\rightarrow \ell\ell)jj$ (15< $M_{\ell,\ell}$ <60 GeV/c^2)	ALPGEN 1.2	CTEQ6.1M	150,650	6.27
$Z/\gamma^*(\rightarrow \ell\ell)jj$ (60< $M_{\ell,\ell}$ <130 GeV/c^2)	ALPGEN 1.2	CTEQ6.1M	144,600	26.74
$Z/\gamma^*(\rightarrow \ell\ell)jj$ ($M_{\ell,\ell}$ >130 GeV/c^2)	ALPGEN 1.2	CTEQ6.1M	95,900	0.29
$WW \rightarrow \ell\ell$	ALPGEN 1.2	CTEQ6.1M	170,350	1.38 ± 0.03
$WW(\rightarrow \ell\ell)jj$	ALPGEN 1.2	CTEQ6.1M	19,500	0.29 ± 0.10

Table 9.4: Simulated samples used in the $e\mu$ analysis, together with generators and cross section for the various processes. All decay modes of tau leptons are included.

Process	Generator	PDF	N_{evts}	σ(pb)
$t\bar{t} \rightarrow \ell\ell\nu\nu bb$	ALPGEN 1.3	CTEQ5L	110,000	-
$Z/\gamma^* \rightarrow ee$ (60< $M_{e,e}$ <130 GeV/c^2)	PYTHIA 6.2	CTEQ5L	294,500	-
$Z/\gamma^* \rightarrow \mu\mu$ (60< $M_{\mu,\mu}$ <130 GeV/c^2)	PYTHIA 6.2	CTEQ5L	162,000	-
$Z/\gamma^*(\rightarrow \tau\tau)j$ (15< $M_{\tau,\tau}$ <60 GeV/c^2)	ALPGEN 1.3	CTEQ5L	48,250	61.5
$Z/\gamma^*(\rightarrow \tau\tau)j$ (60< $M_{\tau,\tau}$ <130 GeV/c^2)	ALPGEN 1.3	CTEQ5L	48,500	69.8
$Z/\gamma^*(\rightarrow ee)j$ (15< $M_{e,e}$ <60 GeV/c^2)	ALPGEN 1.3	CTEQ5L	171,000	61.5
$Z/\gamma^*(\rightarrow ee)j$ (60< $M_{e,e}$ <130 GeV/c^2)	ALPGEN 1.3	CTEQ5L	177,000	69.8
$Z/\gamma^*(\rightarrow ee)j$ (130< $M_{e,e}$ <250 GeV/c^2)	ALPGEN 1.3	CTEQ5L	39,000	0.627
$Z/\gamma^*(\rightarrow \mu\mu)j$ (15< $M_{\mu,\mu}$ <60 GeV/c^2)	ALPGEN 1.3	CTEQ5L	206,750	61.5
$Z/\gamma^*(\rightarrow \mu\mu)j$ (60< $M_{\mu,\mu}$ <130 GeV/c^2)	ALPGEN 1.3	CTEQ5L	231,495	69.8
$Z/\gamma^*(\rightarrow \mu\mu)j$ (130< $M_{\mu,\mu}$ <250 GeV/c^2)	ALPGEN 1.3	CTEQ5L	192,500	0.627
$Z/\gamma^*(\rightarrow \tau\tau)jj$ (15< $M_{\tau,\tau}$ <60 GeV/c^2)	ALPGEN 1.3	CTEQ5L	17,500	23.01
$Z/\gamma^*(\rightarrow \tau\tau)jj$ (60< $M_{\tau,\tau}$ <130 GeV/c^2)	ALPGEN 1.3	CTEQ5L	102,000	22.845
$Z/\gamma^*(\rightarrow \tau\tau)jj$ (130< $M_{\tau,\tau}$ <250 GeV/c^2)	ALPGEN 1.3	CTEQ5L	16,500	0.2123
$Z/\gamma^*(\rightarrow ee)jj$ (15< $M_{e,e}$ <60 GeV/c^2)	ALPGEN 1.3	CTEQ5L	86,250	23.01
$Z/\gamma^*(\rightarrow ee)jj$ (60< $M_{e,e}$ <130 GeV/c^2)	ALPGEN 1.3	CTEQ5L	215,450	22.845
$Z/\gamma^*(\rightarrow ee)jj$ (130< $M_{e,e}$ <250 GeV/c^2)	ALPGEN 1.3	CTEQ5L	71,750	0.2123
$Z/\gamma^*(\rightarrow \mu\mu)jj$ (15< $M_{\mu,\mu}$ <60 GeV/c^2)	ALPGEN 1.3	CTEQ5L	31,500	23.01
$Z/\gamma^*(\rightarrow \mu\mu)jj$ (60< $M_{\mu,\mu}$ <130 GeV/c^2)	ALPGEN 1.3	CTEQ5L	206,500	22.845
$Z/\gamma^*(\rightarrow \mu\mu)jj$ (130< $M_{\mu,\mu}$ <250 GeV/c^2)	ALPGEN 1.3	CTEQ5L	52,500	0.2123
$WW \rightarrow \ell\ell$	PYTHIA 6.2	CTEQ5L	30,316	13.5

Table 9.5: Simulated samples used in the ℓ + track analysis, together with generators, number of events and cross section for the various processes. All tau lepton decay modes are included and the underlying event model used in all samples is PYTHIA tuneA [167, 168].

9.3.1 $t\bar{t}$ Samples

The number of preselected and b-tagged signal events is estimated with a sample of simulated $t\bar{t} \rightarrow \ell\ell\nu\nu bb$ events, where $\ell = e, \mu$ and τ. This sample is produced using the ALPGEN [162–164] generator, which contains the leading order matrix element for $t\bar{t}$ production. The set of parton distribution functions used is taken from the CTEQ Collaboration [41]. Parton showering is carried out with PYTHIA [165]. Decays of B-mesons are simulated with EVTGEN [169] and tau-lepton decays are simulated with TAUOLA [170]. Several samples are generated for different values of the top quark mass, and these are used to parameterize the dependence of the signal efficiency on the top quark mass. The central value of the cross section is computed for a top quark mass of 175 GeV/c^2.

9.3.2 Z/γ^* Samples

In both the $e\mu$ and the $\ell +$ track analyses, the Z/γ^* backgrounds are normalized using the number of events observed in control samples selected by altering or inverting some of the selection criteria, such as the $\not\!\!E_T$. The event kinematics and efficiencies for selections applied at later stages of the analyses are obtained from simulated Z/γ^* events.

In the $e\mu$ analysis, $Z/\gamma^* \rightarrow \tau\tau$ and $Z/\gamma^* \rightarrow \mu\mu$ samples generated with PYTHIA [165] are used to extract efficiencies for Z/γ^* events with at most one jet. The set of parton distribution functions used is taken from the CTEQ Collaboration [41]. For events with two or more jets, $Z/\gamma^*(\rightarrow \ell\ell)jj$ samples (where $\ell = e,\ \mu$ and τ) are generated with ALPGEN [162–164] using the the leading-order matrix element for Z/γ^* plus two partons (q or g). The samples are generated in three $M_{\ell,\ell}$ regions: 15-60 GeV/c^2, 60-130 GeV/c^2 and $>$ 130 GeV/c^2. The relative weight of each sample is determined from ratios of their LO cross sections. The $\ell +$ track analysis makes use of $Z/\gamma^*(\rightarrow \ell\ell)j$ and $Z/\gamma^*(\rightarrow \ell\ell)jj$ samples (where $\ell = e,\ \mu$ or τ) generated with ALPGEN [162–164] to extract efficiencies for events with one and at least two jets respectively. The samples are generated in three $M_{\ell,\ell}$ regions: 15-60 GeV/c^2, 60-130 GeV/c^2 and 130-250 GeV/c^2, and again the relative weights are derived from ratios of LO cross sections. In addition, Z/γ^* samples generated with PYTHIA [165] are used to estimate systematic uncertainties on the b-tagging efficiency for Z/γ^* events. In all samples, parton showering, B-meson and tau-lepton decays are simulated in accordance with the prescription described in Sec. 9.3.1.

9.3.3 WW Samples

The $e\mu$ analysis uses $WW(\rightarrow \ell\ell)$ and $WW(\rightarrow \ell\ell)jj$ samples (where $\ell = e$ or μ) generated with ALPGEN. The former (latter) sample is used to extract efficiencies for events with at most one jet (at least two jets). The $\ell +$ track analysis uses a

$WW \rightarrow \ell\ell$ sample (where $\ell = e,\ \mu$ and τ) generated with PYTHIA to estimate efficiencies for all events regardless of their number of jets. In all samples, parton showering, B-meson and tau-lepton decays are simulated in accordance with the prescription described in Sec. 9.3.1.

9.4 Electron-Muon Background Samples from Data

9.4.1 Z/γ^* Samples

Data samples of $Z/\gamma^* \rightarrow ee$ and $Z/\gamma^* \rightarrow \mu\mu$ events are used to normalize the Z/γ^* backgrounds before b-tagging and to estimate the probability of a Z/γ^* event to be b-tagged. The events in the $Z/\gamma^* \rightarrow ee$ and $Z/\gamma^* \rightarrow \mu\mu$ samples are required to have:

- passed dielectron or dimuon triggers.
- a primary vertex.
- at least two tight electrons or at least two tight muons. The two leptons must have opposite charge.
- an invariant mass of the two leptons which is consistent with the mass of the Z boson. The mass windows used are $75 < M_{e,e} < 105$ GeV/c^2 and $70 < M_{\mu,\mu} < 110$ GeV/c^2.

9.4.2 Multijet Sample

A data sample of multijet events is used to estimate the probability for a multijet or W event to be b-tagged. The events in this sample are required to have:

- at least one tight muon.
- $\not\!\!E_T < 10$ GeV.
- at least one jet.

As multijet events do not contain high p_T neutrinos, the requirement of low $\not\!\!E_T$ ensures the data sample to be dominated by multijet events.

9.5 Lepton+Track Background Samples from Data

9.5.1 Z/γ^* Samples

Data samples of Z/γ^* events are used to normalize the Z/γ^* backgrounds, as well as to obtain event tagging probabilities for Z/γ^* events. The data samples of $Z/\gamma^* \rightarrow ee$ and $Z/\gamma^* \rightarrow \mu\mu$ events used are identical to the preselected $e+$track and $\mu +$ track samples with the exception that both the $\not\!\!E_T$ and $\not\!\!E_T^Z$ cuts are inverted. The requirement of low $\not\!\!E_T$ makes these $Z/\gamma^* \to \ell\ell$ samples orthogonal to the preselected signal samples.

9.5.2 Multijet Samples

Data samples of multijet events are used to estimate the probability for a loose isolated electron, muon or track not originating from a W or Z boson decay to pass the corresponding tight selection criteria. These probabilities, referred to as $\epsilon^{\mu}_{\rm bkg}$, $\epsilon^{e}_{\rm bkg}$ and $\epsilon^{\rm track}_{\rm bkg}$, are needed as input to the matrix method which estimates the number of multijet and W events in the preselected sample. The matrix method is described in Sec. 11.1.4. The multijet data samples are also used to compute event tagging probabilities for the multijet background events.

The loose electron (loose muon) multijet sample, from which $\epsilon^{e}_{\rm bkg}$ ($\epsilon^{\mu}_{\rm bkg}$) is determined, is selected by requiring the events to have:

- passed the preselection criteria common to $e +$ track and $\mu +$ track, listed in Sec. 9.2.2.
- passed the triggers listed in Tab. 9.2 (Tab. 9.3).
- at least one loose electron (loose muon).
- $\not\!\!E_T < 10$ GeV.

Events consistent with coming from a Z boson decay are rejected from the sample if the invariant mass of the selected electron (muon) and any other electron (muon) or isolated track in the event is between 75 and 105 GeV/c^2 (70 and 110 GeV/c^2). Events are also rejected if they contain any muon (electron).

The tight electron (tight muon) multijet samples, from which $\epsilon^{\rm evttag}_{\rm multijet}$ is estimated, are obtained by requiring the loose electron (loose muon) to pass the tight electron (tight muon) criteria.

The electron track (muon track) multijet sample, from which $\epsilon^{\rm track}_{\rm bkg}$ is determined, is selected by requiring the events to have:

- passed the preselection criteria common to $e +$ track and $\mu +$ track, listed in Sec. 9.2.2.
- passed the triggers listed in Tab. 9.2 (Tab. 9.3).
- at least one loose isolated track.
- $\not\!\!E_T < 10$ GeV.

In order to suppress contamination from $Z/\gamma^* \rightarrow \ell\ell$, events are rejected from the sample if the invariant mass of the selected track and any other isolated track is between 75 and 105 GeV/c^2, or if the invariant mass of the selected track and any electron or muon is between 75 and 105 GeV/c^2 or 70 and 110 GeV/c^2 respectively. Events are also rejected if they contain any muon (electron).

9.5.3 W Samples

Data samples of W events are used to determine the event tagging probabilities for the W background. These samples are obtained in the same way as the tight electron and tight muon multijet samples defined in Sec. 9.5.2, but with the $\not\!\!E_T < 10$ GeV cut substituted with the standard $\not\!\!E_T$ and $\not\!\!E_T^Z$ cuts defined in Sec. 9.2.2. Selecting high $\not\!\!E_T$ events with one tight lepton results in a sample dominated by W events.

10 The Electron-Muon Analysis

The $e\mu$ final state has the advantage of avoiding the direct contribution from Z/γ^* backgrounds which dominate the ee and $\mu\mu$ final states. There are also two possible permutations when two W bosons decay into an electron and a muon, which gives a factor of two larger branching fraction for the $e\mu$ final state compared to the ee or $\mu\mu$ final states. This chapter is devoted to a more detailed description of the $e\mu$ analysis. The estimates for the expected number of signal and background events are presented as well as the sources of systematic uncertainty. The last section of the chapter gives the measured top pair production cross section.

10.1 Background Estimates

10.1.1 The $Z/\gamma^*(\rightarrow \tau\tau)$+jets Background

The number of preselected $Z/\gamma^* \rightarrow \tau\tau$ events with zero or one jet is estimated using the sample of simulated $Z/\gamma^* \rightarrow \tau\tau$ events in Tab 9.4. The background is normalized to the $Z/\gamma^* \rightarrow \mu\mu$ cross section measured by DØ [172]:

$$\sigma(Z/\gamma^* \rightarrow \ell\ell \ (M_{\ell,\ell} > 30 \text{ GeV}/c^2)) = 333.1 \pm 14.1 \text{ pb}. \tag{10.1}$$

The number of $Z/\gamma^* \rightarrow \tau\tau$ events with two or more jets is estimated from the samples of simulated $Z/\gamma^*(\rightarrow \ell\ell)jj$ events in Tab. 9.4. The LO cross section provided by ALPGEN is multiplied by the ratio of observed to predicted number of $Z/\gamma^* \rightarrow \mu\mu$ events in the mass window from 70 to 110 GeV/c^2:

$$\kappa_Z = \frac{N^{\text{obs}}_{Z/\gamma^*\rightarrow\mu\mu}}{N^{\text{pred}}_{Z/\gamma^*\rightarrow\mu\mu}} = 0.91 \pm 0.10 \tag{10.2}$$

where the uncertainty is statistical only.

The event tagging probability for $Z/\gamma^* \rightarrow \tau\tau$ events is calculated with the "Data method" described in Sec. 6.2.2. It is obtained from averaging the event tagging probability measured in $Z/\gamma^* \rightarrow ee$ and $Z/\gamma^* \rightarrow \mu\mu$ data samples defined in Sec. 9.4.1. As shown in Tab. 10.1, the event tagging probabilities derived from $Z/\gamma^* \rightarrow ee$ and $Z/\gamma^* \rightarrow \mu\mu$ events are consistent within errors, and to reduce the statistical uncertainty the weighted averages are used.

	$N_{\text{jets}} = 1$	$N_{\text{jets}} \geq 2$
$Z/\gamma^* \to ee$		
N_{presel}	1027	156
N_{tagged}	12	4
ϵ^{evttag}	1.2 ± 0.3	2.6 ± 1.3
$Z/\gamma^* \to \mu\mu$		
N_{presel}	765	114
N_{tagged}	4	4
ϵ^{evttag}	0.5 ± 0.3	3.5 ± 1.7
Weighted average		
ϵ^{evttag}	0.8 ± 0.2	2.9 ± 1.0

Table 10.1: The event tagging probabilities in % obtained from $Z/\gamma^* \to ee$ and $Z/\gamma^* \to \mu\mu$ data events as well as their weighted averages. Uncertainties are statistical only.

10.1.2 The WW+jets Background

The number of preselected WW events with zero or one jet is estimated from the simulated WW sample in Tab. 9.4, and normalized using the NLO/LO K-factor derived for the WW process [171]. The number of events with two or more jets is estimated from the simulated sample of $WWjj$ events in Tab. 9.4. Since no NLO $WWjj$ cross section is available, this contribution is normalized by applying the same K-factor used for WW events.

The event tagging probabilities for WW events are obtained from the simulated WW and $WWjj$ samples by applying the "Data and simulation method" described in Sec. 6.2.2.

10.1.3 The Multijet and W+jets Backgrounds

The number of preselected multijet and W events is obtained from data. Let N_{multijet}, $N_{W(\to\mu\nu)+\text{jets}}$ and $N_{W(\to e\nu)+\text{jets}}$ denote the the number of multijet events, $W(\to \mu\nu)+$ jets and $W(\to e\nu)+$ jets events in the extra-loose preselected sample, i.e. before loose and tight electron and muon criteria have been applied. Furthermore, define f_μ to be the probability for a muon in a multijet or in a $W(\to e\nu)+$ jets event to pass the loose and tight isolated muon criteria, and f_e to be the the probability for a jet in a multijet or a $W(\to \mu\nu)+$ jets event to pass the loose and tight isolated electron criteria. The number of multijet and W events in the preselected sample can then be written as:

$$N^{\text{presel}}_{\text{multijet}+W} = N_{\text{multijet}} \cdot f_\mu \cdot f_e + N_{W(\to\mu\nu)+\text{jets}} \cdot f_e + N_{W(\to e\nu)+\text{jets}} \cdot f_\mu. \tag{10.3}$$

The first term $N_{\text{multijet}} \cdot f_\mu \cdot f_e$ is the contribution from multijet events with a fake isolated electron and a fake isolated muon, and the last two terms are the contributions from W events with a fake isolated electron or a fake isolated muon. Muons in multijet and $W(\rightarrow e\nu) + \text{jets}$ events come mainly from heavy flavor jets, which are rare. In addition, the probability for such a muon to be isolated is small. Therefore, the contribution from $N_{W(\rightarrow e\nu)+jets} \cdot f_\mu$ is expected to be negligible. Equation 10.3 then reduces to:

$$N^{\text{presel}}_{\text{multijet}+W} = \left(N_{\text{multijet}} \cdot f_\mu + N_{W(\rightarrow \mu\nu)+\text{jets}}\right) \cdot f_e \tag{10.4}$$

where $N_{\text{multijet}} \cdot f_\mu + N_{W(\rightarrow \mu\nu)+\text{jets}}$ can be identified as the number of data events with an extra-loose electron and a tight muon. The probability for a jet to be misidentified as an isolated electron, f_e, is estimated from a data sample dominated by fake electrons, which is selected by requiring an extra-loose electron and a non-isolated muon. The fake rate is defined by the number of events in which the extra-loose electron pass the loose and tight electron criteria:

$$f_e = \frac{N_e^{\text{tight}}}{N_e^{\text{extra-loose}}}. \tag{10.5}$$

The estimate is done separately for fake electrons reconstructed in the central and endcap calorimeters. The distribution of the events as a function of the muon isolation variables in the extra-loose and tight samples in both the central and endcap calorimeter are shown in Fig. 10.1 and the measured fake probabilities are listed in Tab. 10.2.

	$N_e^{\text{extra-loose}}$	N_e^{tight}	f_e
CC	12401	40	0.32 ± 0.05
EC	4838	36	0.7 ± 0.1

Table 10.2: Estimated electron fake probabilities in % for electrons reconstructed in the central (CC) and endcap (EC) calorimeters. Shown are also the number of events with an extra-loose and tight electron respectively. Uncertainties are statistical only.

The event tagging probabilities for multijet and W events are taken to be the same, and are estimated by applying the "Data method" described in Sec. 6.2.2 to events with a tight muon and low $\not\!\!E_T$ as defined in Sec. 9.4.2.

One concern is that the reversed $\not\!\!E_T$ cut removes events with heavy flavor jets, since semileptonic decays of heavy quarks contain neutrinos. To study this, the event tagging probability is derived as a function of the inverted $\not\!\!E_T$ cut, and the result is shown in Fig. 10.2. The event tagging probability is found to be very stable as a function of the inverted $\not\!\!E_T$ cut.

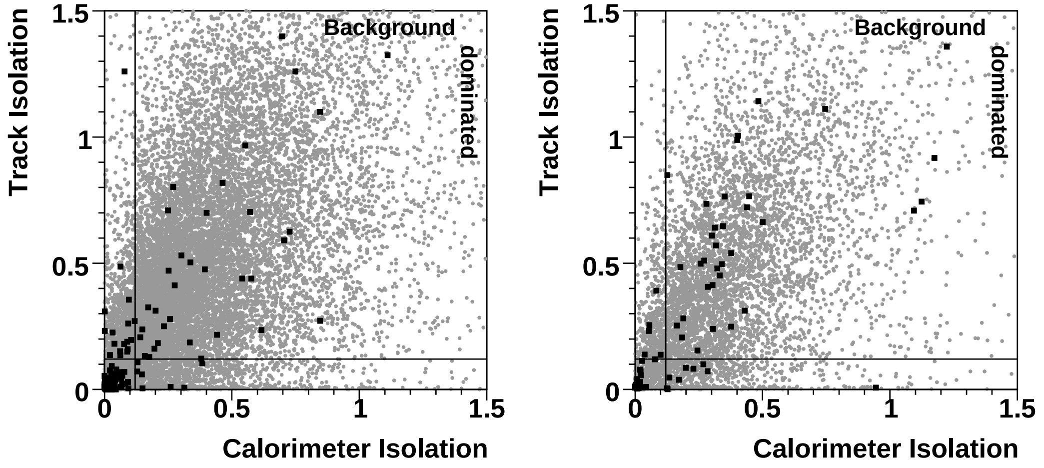

(a) Electron fake rate estimation in CC. (b) Electron fake rate estimation in EC.

Figure 10.1: The number of events passing extra-loose (gray circles) and tight (black squares) electron criteria as a function of the track and calorimeter muon isolation variables defined in Sec. 7.3. Isolated muons from weak boson decays have small values of both the track and calorimeter isolation, and thus the upper right corner in both pictures is the background dominated region. Only events with both track and calorimeter isolation greater than 0.12 are used in the fake rate estimation.

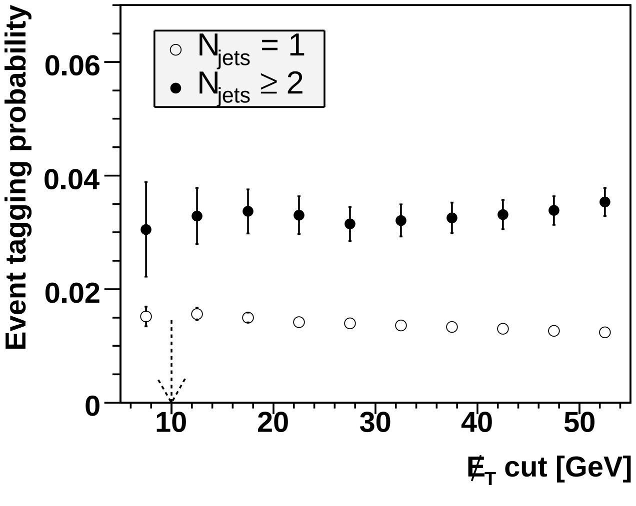

Figure 10.2: The event tagging probabilities for multijet events as a function of the inverted $\not\!\!E_T$ cut. The event tagging probabilities used in the $e\mu$ analysis are obtained for events with $\not\!\!E_T < 10$ GeV.

10.1.4 The $Z/\gamma^*(\rightarrow \mu\mu)$+jets Background

A muon in a $Z/\gamma^* \rightarrow \mu\mu$ event can emit a Bremsstrahlung photon, which is associated to the muon track, and thus misidentified as an electron. The $\Delta R(e,\mu)$ cut is designed to remove this background, but fails to do so in the cases where the muon is not reconstructed.

The number of preselected $Z/\gamma^* \rightarrow \mu\mu$ events with zero or one jet is estimated using the simulated sample of of $Z/\gamma^* \rightarrow \mu\mu$ events in Tab. 9.4. In analogue with the $Z/\gamma^* \rightarrow \tau\tau$ contribution, this background is normalized to the $Z/\gamma^* \rightarrow \mu\mu$ cross section measured by the DØ Collaboration [172]:

$$\sigma(Z/\gamma^* \rightarrow \ell\ell\ (60 < M_{\ell,\ell} < 130\ \mathrm{GeV/c^2})) = 266.5 \pm 11.8\ \mathrm{pb}. \tag{10.6}$$

The number of $Z/\gamma^* \rightarrow \mu\mu$ events with two or more jets is estimated from the simulated samples of $Z/\gamma^*(\rightarrow \ell\ell)jj$ events in Tab. 9.4. The LO cross section provided by ALPGEN is scaled by the same κ_Z factor used for the $Z/\gamma^* \rightarrow \tau\tau$ background.

The event tagging probability for $Z/\gamma^* \rightarrow \mu\mu$ events is taken to be the same as for $Z/\gamma^* \rightarrow \tau\tau$ events.

10.2 The $t\bar{t}$ Signal Efficiency

The preselection efficiencies for $t\bar{t}$ events are determined in the sample of simulated $t\bar{t} \rightarrow \ell\ell$ events in Tab. 9.4. The events are generated with a top quark mass of 175 GeV/c^2. The event tagging probabilities are calculated from the same simulated sample, by applying the “Data and simulation method” described in Sec. 6.2.2.

The efficiency for the $t\bar{t}$ events at various stages of the event selection is shown in Tab. 10.3. The table lists both the marginal and the cumulative efficiencies. Most selection criteria applied have an efficiency above 90%. The most inefficient selection criteria for the $t\bar{t}$ signal are the requirements of an electron and a muon with $p_T > 15$ GeV/c as well the requirement of at least one b-tagged jet. The overall signal efficiency is 1.24% for events with exactly one jet and 7.7% for events with at least two jets. The cumulative efficiencies are derived with respect to all $t\bar{t} \rightarrow e\mu$ events, including electrons and muons from tau-lepton decays.

10.3 Composition of the Preselected and b-tagged Samples

The observed and predicted number of signal and background events in the preselected and b-tagged signal samples are shown in Tab. 10.4 and Tab. 10.5 respectively. For illustration, a $t\bar{t}$ prediction is obtained by assuming a pair production cross section of 7 pb. In the extraction of the cross section the $t\bar{t}$ contribution is instead fitted to the data. The number of observed and predicted events in the b-tagged sample is also shown in Fig. 10.3, where the left plot shows both the signal and background

	$N_{\text{jets}} = 1$		$N_{\text{jets}} \geq 2$	
Cut	Marginal	Cumulative	Marginal	Cumulative
PV quality	97.57 ± 0.30	17.51 ± 0.35	97.90 ± 0.13	79.44 ± 0.74
Electron & muon ID + $p_T > 15$ GeV/c	50.93 ± 0.99	8.92 ± 0.25	42.87 ± 0.46	34.06 ± 0.49
$\Delta R(e, \mu) > 0.25$	99.69 ± 0.15	8.89 ± 0.25	99.74 ± 0.07	33.97 ± 0.48
Muon system hit req. + track match	87.87 ± 0.91	7.81 ± 0.23	88.12 ± 0.46	29.93 ± 0.45
Muon track $\chi^2 < 4$	100.00 ± 0.00	7.81 ± 0.23	99.88 ± 0.05	29.90 ± 0.45
$\Delta z(\text{PV}, \mu) < 1$ cm	99.29 ± 0.25	7.76 ± 0.23	99.35 ± 0.12	29.70 ± 0.45
Muon track and calo isolation	87.25 ± 1.00	6.77 ± 0.22	81.64 ± 0.59	24.25 ± 0.41
Muon $d_{ca}/\sigma(d_{ca}) < 3$	94.89 ± 0.70	6.42 ± 0.21	93.76 ± 0.41	22.74 ± 0.40
Electron track match	87.84 ± 1.07	5.64 ± 0.20	92.89 ± 0.45	21.12 ± 0.38
$\Delta z(\text{PV}, \text{e}) < 1$ cm	100.00 ± 0.00	5.64 ± 0.20	99.97 ± 0.03	21.11 ± 0.38
Electron likelihood	92.28 ± 0.93	5.21 ± 0.19	94.56 ± 0.41	19.96 ± 0.37
$\not\!\!E_T > 25$ GeV	89.24 ± 1.13	4.65 ± 0.18	89.79 ± 0.56	17.92 ± 0.35
Trigger and correction factors	69.98 ± 1.77	3.25 ± 0.13	73.23 ± 0.87	13.13 ± 0.26
b-tagging	38.04 ± 2.10	1.24 ± 0.08	58.85 ± 1.63	7.73 ± 0.26

Table 10.3: The marginal and cumulative efficiencies in % for $t\bar{t}$ events with exactly one and at least two jets. Uncertainties are statistical only.

predictions together with the observation. The right plot shows the details of the background composition. Plots with the observed and predicted number of events in the b-tagged signal sample as a function of various kinematic variables are shown in Appendix A.

	$N_{\text{jets}} = 0$	$N_{\text{jets}} = 1$	$N_{\text{jets}} \geq 2$
$t\bar{t}$	0.052 ± 0.009	1.14 ± 0.04	4.58 ± 0.09
WW	7.40 ± 0.08	0.84 ± 0.03	0.46 ± 0.03
$Z/\gamma^* \to \tau\tau$	1.6 ± 0.1	2.7 ± 0.2	0.6 ± 0.1
$Z/\gamma^* \to \mu\mu$	1.2 ± 0.4	0.6 ± 0.3	0.10 ± 0.04
Multijet/W	2.9 ± 0.1	1.05 ± 0.07	0.33 ± 0.04
Total pred.	13.2 ± 0.4	6.3 ± 0.3	6.1 ± 0.2
Observed	13	7	8

Table 10.4: Observed and predicted number of events in the preselected signal sample. Uncertainties are statistical only.

	$N_{\text{jets}} = 1$	$N_{\text{jets}} \geq 2$
$t\bar{t}$	0.43 ± 0.03	2.70 ± 0.09
WW	< 0.005	0.008 ± 0.002
$Z/\gamma^* \to \tau\tau$	0.021 ± 0.006	0.017 ± 0.007
$Z/\gamma^* \to \mu\mu$	< 0.005	< 0.005
Multijet/W	0.016 ± 0.002	0.011 ± 0.002
Total pred.	0.48 ± 0.03	2.74 ± 0.09
Observed	0	5

Table 10.5: Observed and predicted number of events in the b-tagged signal sample. Uncertainties are statistical only.

10.4 Systematic Uncertainties

The systematic uncertainties on the signal efficiency and the number of b-tagged background events are shown in Tab. 10.6 and Tab. 10.7 respectively. Since the total background is very small, the dominant systematic error on the final result comes from uncertainties on the signal efficiency.

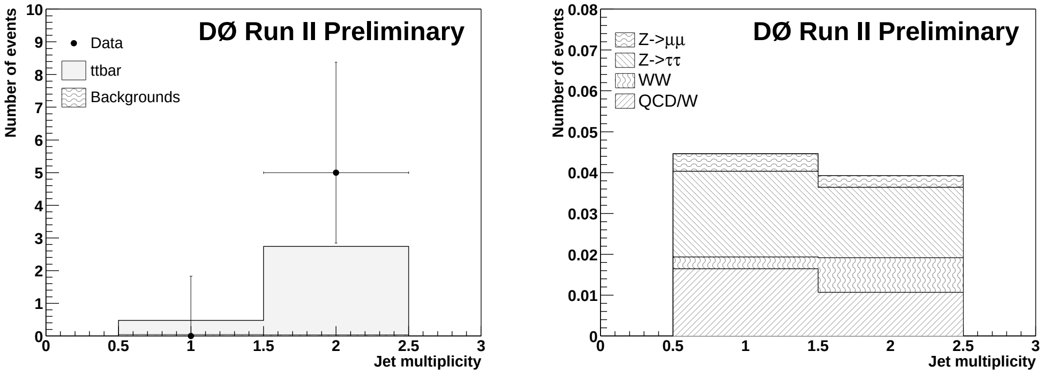

Figure 10.3: Observed and predicted number of tagged events (left) and the background prediction only (right) as a function of the jet multiplicity.

Source	$N_{\text{jets}} = 1$	$N_{\text{jets}} \geq 2$
Primary vertex	± 0.39	± 0.48
Electron trigger	± 0.13	± 1.16
Electron identification	± 0.69	± 0.69
Muon trigger	$+2.27 - 2.87$	$+2.13 - 2.72$
Muon identification	± 4.05	± 4.04
Jet energy scale	$-9.48 + 9.45$	$+5.45 - 6.46$
Jet energy resolution	$+0.85$	$+0.19$
Jet identification	$+19.60$	-5.86
Taggability	$+9.80 - 4.10$	$+7.46 - 3.24$
$\epsilon_{b\to\mu X}^{data}$	± 7.98	$+5.85 - 6.11$
$\epsilon_{b\to\mu X}^{sim}$	$-4.73 + 5.43$	$-3.75 + 4.30$
ϵ_{b}^{sim}	± 1.13	± 0.89
ϵ_{c}^{sim}	< 0.01	± 0.01
κ_c and κ_b	∓ 0.01	-0.025
Decay model dependence	$+2.58$	$+3.04$
Mistag rate	< 0.01	< 0.01
Top quark mass	$-2.91 + 2.98$	$+4.48 - 4.79$
Finite statistics in simulation	± 6.76	± 3.40

Table 10.6: Relative systematic uncertainties (%) on the signal efficiency.

Source	$N_{\text{jets}} = 1$	$N_{\text{jets}} \geq 2$
Primary vertex	± 0.25	± 0.35
Electron trigger	$+1.36 - 1.46$	± 0.69
Electron identification & ID	± 0.43	± 0.50
Muon trigger	$+1.71 - 2.16$	$+2.10 - 2.65$
Muon identification	± 2.58	± 2.98
Jet energy scale	$+17.72 - 13.22$	$+14.33 - 16.73$
Jet energy resolution	< 0.01	-1.27
Jet identification	< 0.01	-1.72
Z/γ^* normalization	± 17.15	± 5.79
WW normalization	± 2.24	± 7.55
Taggability	$+0.63 - 0.26$	$+2.08 - 0.87$
$\epsilon^{\text{data}}_{b \to \mu X}$	± 0.31	± 1.00
$\epsilon^{\text{sim}}_{b \to \mu X}$	$-0.31 + 0.40$	$-0.64 + 0.70$
$\epsilon^{\text{sim}}_{b}$	± 0.04	± 0.03
$\epsilon^{\text{sim}}_{c}$	± 0.19	± 0.72
κ_c and κ_b	-0.31	-1.74
Decay model dependence	$+1.05$	$+3.03$
Mistag rate	± 0.30	± 0.80
ϵ^{evttag}, Z/γ^*	$+29.78 - 18.01$	$+10.85 - 5.85$
ϵ^{evttag}, WW	$+4.55$	$+8.63$
ϵ^{evttag}, Multijet/W	-0.27	$+4.70$
Finite statistics in simulation	± 14.38	± 18.87

Table 10.7: Relative systematic uncertainties (%) on the total background prediction.

Primary Vertex

The data-to-simulation correction factors for the primary vertex cut efficiencies, described in Sec. 8.1, are varied by their uncertainties. The uncertainties always include a statistical component. If applicable and additional component, originating from differences observed between $Z/\gamma^* \rightarrow ee$ and $Z/\gamma^* \rightarrow \mu\mu$ events, is included.

Electron Trigger

The parameterizations of the electron trigger efficiencies are varied by their uncertainties. These uncertainties originate from limited statistics in the data samples used to extract the trigger efficiency parameterizations.

Electron Identification

The data-to-simulation correction factors for the electron identification cut efficiencies, described in Sec. 8.4, are varied by their uncertainties. The dominant source of uncertainty originates from the difference in the electron identification efficiencies observed in various regions of the calorimeter.

Muon Trigger

The parameterization of the muon trigger efficiency is varied by its uncertainty. These uncertainties originate from limited statistics in the data samples used to extract the trigger efficiency parameterizations.

Muon Identification

The data-to-simulation correction factors for the muon cut efficiencies, described in Sec. 8.3, are varied by their uncertainties. The dominant source of uncertainty originates from the difference in the muon identification efficiencies observed in various regions of the detector.

Jet Energy Scale

The effect of the jet energy scale uncertainty is obtained by varying the JES by $\pm 1\sigma$, where

$$\sigma = \sqrt{\sigma^2_{\text{stat,data}} + \sigma^2_{\text{syst,data}} + \sigma^2_{\text{stat,sim}} + \sigma^2_{\text{syst,sim}}}. \tag{10.7}$$

Adding the statistical and systematic uncertainties on the jet energy scale in data and simulation in quadrature is a conservative approach where the two scales are treated as completely uncorrelated.

Jet Energy Resolution

The jet energy resolution in the simulation is smeared to reproduce that measured in dijet and photon+jets data. The systematic uncertainty from the jet energy resolution is evaluated by changing the smearing parameterization by $\pm 1\sigma$.

Jet Identification

A correction factor, derived as the ratio between the jet identification efficiency measured in data and in the simulation is applied to the simulated events in order to bring the jet identification efficiency in simulation in agreement with that measured in data. The correction factor is a function of jet p_T and η and is measured in single photon events. As a systematic uncertainty, the parameterization is varied by its statistical uncertainty.

Z/γ^* Background Normalization

The Z/γ^* backgrounds are normalized to the cross section measured by DØ, and the systematic uncertainty on this background is estimated by varying the cross section by its total uncertainty.

In addition, the predicted number of $Z/\gamma^* \rightarrow \mu\mu$ events with exactly one jet is found to differ by 30% from that observed in data. Therefore, as a systematic uncertainty, the preselection efficiencies for Z/γ^* events in the 1-jet bin are varied by ± 30%.

WW Background Normalization

The WW background is normalized using the NLO/LO K-factor from Ref. [171]. The K-factor quoted in this paper is 1.35. Therefore, as a conservative estimate of the uncertainty, an error of 35% on the cross section is assumed, and propagated to the prediction of this background.

Taggability

The shape of the taggability as a function of jet p_T and η is derived in the extra-loose taggability sample, defined in Sec. 8.5.1. The parametrization is then scaled to reproduce the inclusive taggability in the loose taggability sample. The systematic uncertainty assigned to the taggability parameterization is determined from the variation of the inclusive taggability observed when requiring, in addition to the loose taggability sample selections, either a tight electron or a tight muon. The inclusive taggabilities are shown in Tab. 10.8. Based on these numbers, the relative systematic uncertainty assigned to the taggability is $+4 - 10\%$.

Selection	Inclusive taggability
Loose electron + loose muon	79 ± 1
Loose electron + tight muon	71 ± 4
Tight electron + loose muon	82 ± 3

Table 10.8: The inclusive taggability in % in the loose taggability sample as well as two subsamples, where either a tight electron or tight muon is required.

Semileptonic b-tagging Efficiency in Data

The systematic uncertainty from the b-tagging efficiency in data is obtained by varying the parameterization by:

$$\sigma = \sqrt{\sigma_{\text{stat}}^2 + \sigma_{\text{syst}}^2} \tag{10.8}$$

where σ_{stat} is the statistical error on the parameterization, and σ_{syst} is the systematic uncertainty resulting from the assumptions made when constructing Eqs. 8.6.

Semileptonic b-tagging Efficiency in the Simulation

The tagging efficiency in simulated events with b-jets containing muons is parameterized as a function of jet p_T and η. The limited available statistics leads to a statistical uncertainty on the parameterization. The effect is propagated to the final result by varying the parameterization by $\pm 1\sigma$ and computing the resulting change on the event tagging probabilities.

Inclusive b-tagging Efficiency in the Simulation

The tagging efficiency in simulated events with inclusive b-jets is parameterized as a function of jet p_T and η. The limited available statistics leads to a statistical uncertainty on the parameterization. The effect is propagated to the final result by varying the parameterization by $\pm 1\sigma$ and computing the resulting change on the event tagging probabilities.

Inclusive c-tagging Efficiency in the Simulation

The tagging efficiency in simulated events with inclusive c-jets is parameterized as a function of jet p_T and η. The limited available statistics leads to a statistical uncertainty on the parameterization. The effect is propagated to the final result by varying the parameterization by $\pm 1\sigma$ and computing the resulting change on the event tagging probabilities.

κ_c and κ_b

The ratios κ_c and κ_b are assumed to be the same. By studying the effect that a possible difference in fragmentation between b- and c-jets may have on this ratio, the systematic uncertainty is estimated to be 16%. This estimated error is translated into a systematic uncertainty on the c-tagging efficiency.

Decay Model Dependence of Tagging Efficiency Parameterizations

The inclusive and semileptonic b-tagging efficiencies as well as the inclusive c-tagging efficiency are parameterized on simulated $t\bar{t}$ events. To estimate the impact of a decay-model dependence, the parameterizations are also derived on simulated $Z \rightarrow b\bar{b}$ and $Z \rightarrow c\bar{c}$ events which have a different color flow. The observed change in the event tagging probability is taken as a systematic uncertainty.

Mistag Rate

The negative tag rate is parameterized as a function of jet p_T and η in the mistag sample defined in Sec. 8.7. The uncertainty on the negative tag rate parameterization originates from the finite statistics in this sample. The systematic uncertainty from the negative tag rate is obtained by varying the parameterization by its statistical uncertainty.

The systematic uncertainties from $\kappa_{\rm ll}$ and $\kappa_{\rm hf}$ are obtained by varying the parameterizations by their statistical uncertainties.

Event Tagging Probability in Z/γ^* Events

The event tagging probability for Z/γ^* events is obtained from a combination of $Z/\gamma^* \rightarrow ee$ and $Z/\gamma^* \rightarrow \mu\mu$ data. The systematic uncertainty on the predicted number of b-tagged Z/γ^* events is obtained by replacing the default event tagging probability with those obtained on either $Z/\gamma^* \rightarrow ee$ or $Z/\gamma^* \rightarrow \mu\mu$.

Event Tagging Probability in WW Events

The event tagging probability for WW events with one jet (at least two jets) is obtained from the $WW \rightarrow \ell\ell$ ($WW(\rightarrow \ell\ell)jj$) sample in Tab. 9.4. None of these two samples are generated with a proper heavy flavor content. The $WWjj$ sample contains light and c-jet production (both single c and $c\bar{c}$), whereas the WW sample only includes light-jet production. The direct $b\bar{b}$ production is missing from both samples. These issues have to lead to a large systematic uncertainty on the tagging efficiency for the WW background. The effect of a large systematic uncertainty on the event tagging probability for WW events is modest since it is a small background.

By using the topology from the simulated WW and $WWjj$ samples, and assigning “false” flavors to jets, the event tagging probabilities can be estimated for different event flavor configurations. This is done by assuming the flavor content as in from W events, and the results are shown in Tab. 10.9. A description of how the W flavor fractions are obtained can be found in Ref. [173]. The systematic uncertainty on the predicted number of b-tagged WW events is obtained by replacing the default event tagging probability with these alternative efficiencies.

Flavor	ϵ^{evttag}	Fraction
$N_{\text{jets}} = 1$		
WWj	0.12	93.6
WWc	5.2	5.7
WWb	24.4	0.7
Average $\epsilon^{\text{evttag}} = 0.6$		
$N_{\text{jets}} \geq 2$		
$WWjj$	0.65	87.8
$WWcj$	9.5	9.0
$WWbj$	37.7	1.2
$WWcc$	15.8	1.1
$WWbb$	56.5	0.9
Average $\epsilon^{\text{evttag}} = 2.6$		

Table 10.9: Event tagging probabilities for WW events obtained with the flavor fractions from W. All numbers are presented in %.

Event Tagging Probability in Multijet and W Events

The systematic uncertainty on the event tagging probabilities for multijet and W events is obtained by deriving the tagging probabilities from two alternative data samples. The systematic uncertainty on the predicted number of b-tagged multijet and W events is obtained by replacing the default event tagging probability with those obtained in these alternative samples.

The first sample, referred to as the non-isolated muon sample, contains events with large $\not\!\!E_T$ and a non-isolated muon. This sample allows to study the event tagging probability for multijet events with large $\not\!\!E_T$. The second sample, referred to as the photon sample, contains events with an electron without a matched central track. This sample allows to study the event tagging probability in events containing photons as opposed to muons. The event tagging probabilities derived on these alternative samples are listed in Tab. 10.10.

N_{jets}	ϵ^{evttag}
Non-isolated muon sample	
$= 1$	1.6 ± 0.4
≥ 2	3.9 ± 0.5
Photon sample	
$= 1$	1.1 ± 0.6
≥ 2	3.4 ± 2.4

Table 10.10: The tagging probability in % for multijet events, using the presence of a non-isolated muon or a photon to select multijet events.

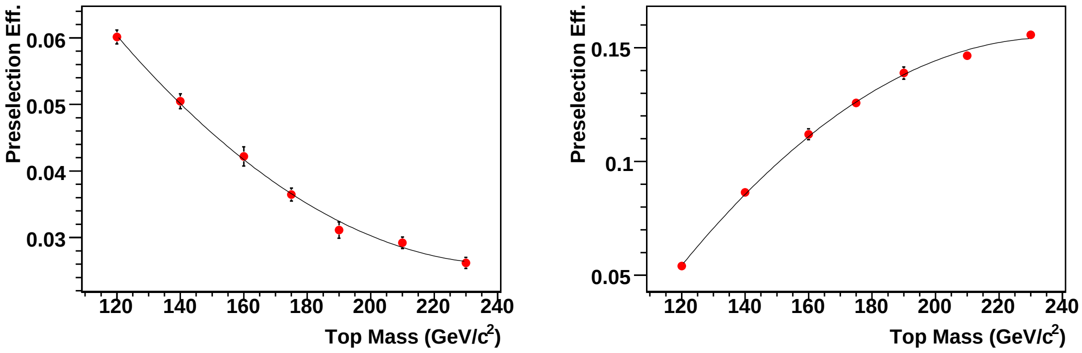

(a) $N_{\text{jets}} = 1$.

(b) $N_{\text{jets}} \geq 2$.

Figure 10.4: Parameterizations of the $t\bar{t}$ preselection efficiency as a function of the top quark mass.

Top Quark Mass

A heavier top quark decays into a more energetic final state than a lighter top quark. This is turn affects both the preselection efficiency and event tagging probability of $t\bar{t}$ events. The error on the top quark mass must therefore be propagated to the $t\bar{t}$ preselection efficiency and the event tagging probability. Figures 10.4 and 10.5 show the preselection efficiency and event tagging probability parameterized as a function of the top quark mass. The systematic uncertainties on the preselection efficiency and event tagging probability are obtained from these parameterizations for a variation of 5 GeV/c^2 from the central value of 175 GeV/c^2.

Finite Statistics in the Simulated Samples

Statistical uncertainties on the background predictions and the signal efficiency arise from the finite statistics of the simulated samples.

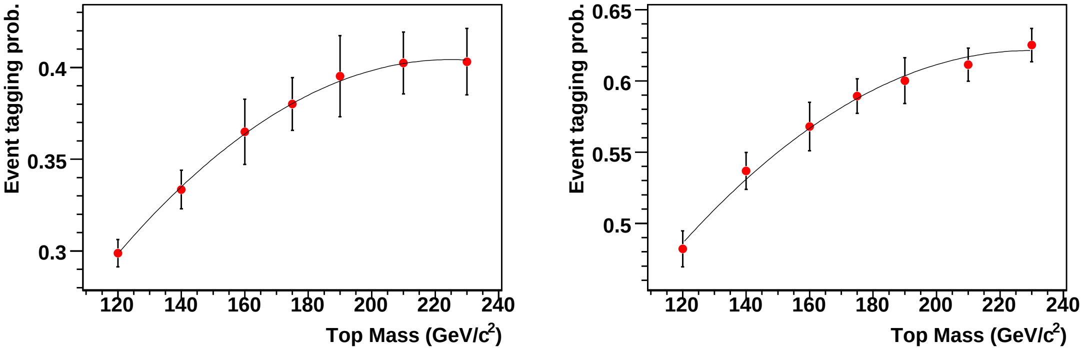

(a) $N_{\text{jets}} = 1$. (b) $N_{\text{jets}} \geq 2$.

Figure 10.5: Parameterizations of the $t\bar{t}$ event tagging probability as a function of the top quark mass.

10.5 Result

The cross section in the $e\mu$ analysis is extracted from two independent channels: events with exactly one jet and events with two or more jets. Table 10.11 summarizes the inputs to the likelihood function. The combined likelihood function for the two channels is shown in Fig. 10.6. The measured cross section in the combined $e\mu$ channel is:

	$N_{\text{jets}} = 1$	$N_{\text{jets}} \geq 2$
Luminosity	158 ± 10	158 ± 10
Branching fraction [%]	3.15 ± 0.07	3.15 ± 0.07
Signal efficiency [%]	1.24 ± 0.08	7.7 ± 0.3
N_{bkg}	0.045 ± 0.006	0.039 ± 0.007

Table 10.11: The inputs to the cross section calculation for the two independent channels. The errors on the signal efficiency and N_{bkg} are statistical only.

$$\sigma_{t\bar{t}} \quad = \quad 11.1\ ^{+5.8}_{-4.3}\ (\text{stat})\ \pm 1.4\ (\text{syst})\ \pm 0.7\ (\text{lumi})\ \text{pb}.$$

The total systematic uncertainty on the cross section is obtained by varying the inputs to the likelihood function. Each source of systematic uncertainty is assumed to be correlated between jet multiplicity bins and between the expected number of signal and background events. All sources of systematic uncertainty

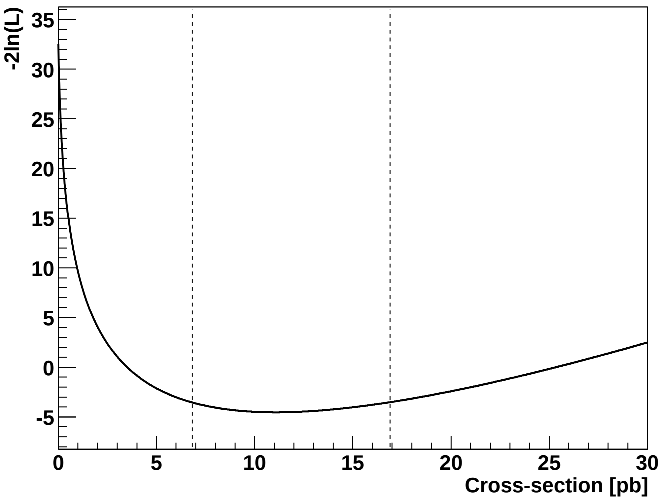

Figure 10.6: The combined likelihood function for the $e\mu$ channel. The vertical lines indicate the $\pm 1\sigma$ points.

are assumed to be fully uncorrelated with each other. Table 10.12 summarizes the various contributions to the systematic uncertainty on the measured cross section. The largest sources of systematic uncertainty are those related to the event tagging probability for $t\bar{t}$ events, such as the semileptonic b-tagging efficiency in data, $\epsilon^{\rm data}_{b\rightarrow\mu X}$ and the taggability. The systematic uncertainty from the luminosity calculation, not included in the table, is 6.5%.

Source	σ^+ [pb]	σ^- [pb]
Primary vertex	0.05	0.05
Electron trigger	0.13	0.13
Electron identification	0.07	0.07
Muon trigger	0.32	0.24
Muon identification	0.45	0.45
Jet energy scale	0.51	0.38
Jet energy resolution	0.02	< 0.01
Jet identification	0.26	< 0.01
Z/γ^* normalization	< 0.01	< 0.01
WW normalization	< 0.01	< 0.01
Taggability	0.39	0.80
$\epsilon_{b\to\mu X}^{\mathrm{data}}$	0.75	0.64
$\epsilon_{b\to\mu X}^{\mathrm{sim}}$	0.45	0.47
$\epsilon_{b}^{\mathrm{sim}}$	0.10	0.10
$\epsilon_{c}^{\mathrm{sim}}$	< 0.01	< 0.01
κ_c and κ_b	< 0.01	< 0.01
Decay model dependence	< 0.01	0.32
Mistag rate	< 0.01	< 0.01
$\epsilon^{\mathrm{evttag}}$, Z/γ^*	0.01	0.01
$\epsilon^{\mathrm{evttag}}$, WW	< 0.01	< 0.01
$\epsilon^{\mathrm{evttag}}$, Multijet/$W$	< 0.01	< 0.01
Top quark mass	0.43	0.37
Finite statistics in simulation	0.34	0.34
Total	1.38	1.44

Table 10.12: Summary of systematic uncertainties in pb on the top pair production cross section measured in the $e\mu$ channel.

11 The Lepton+Track Analysis

The measurements of the top quark pair production cross section in dilepton final states are statistics limited. Loosening kinematic selections is one way of increasing the signal acceptance. In a $\ell +$ track selection, one of the two leptons from the $t\bar{t}$ decay is allowed to be identified solely by an isolated track without confirmation from the calorimeter or muon system. The $\ell +$ track selection is sensitive to all dilepton final states, even single prong hadronic decays of tau leptons. The signal samples are however dominated by ee, $\mu\mu$ and $e\mu$ events. This chapter is devoted to a more detailed description of the $\ell +$ track analysis. The estimates for the expected number of signal and background events are presented as well as the sources of systematic uncertainty. The last section of the chapter gives the measured top pair production cross section.

11.1 Background Estimates

11.1.1 The $Z/\gamma^*(\rightarrow ee)$+jets and $Z/\gamma^*(\rightarrow \mu\mu)$+jets Backgrounds

The number of preselected $Z/\gamma^* \rightarrow \mu\mu$ and $Z/\gamma^* \rightarrow ee$ events with one jet (at least two jets) are estimated using the simulated samples of $Z/\gamma^*(\rightarrow \ell\ell)j$ ($Z/\gamma^*(\rightarrow \ell\ell)jj$) events in Tab. 9.5. The estimate is normalized with a correction factor κ_z such that the observed and predicted $Z/\gamma^* \rightarrow \ell\ell$ yields are in agreement in region not used in the final cross section extraction. The samples used to normalize the Z/γ^* backgrounds are defined in Sec. 9.5.1 and contain events with low $\not{E}_T$. The κ_Z factors applied are shown in Tab. 11.1. The number of observed events have been corrected for other physics processes which contaminate the sample, and are therefore not integers. The κ_Z factors derived without this correction differ very little from the corrected ones.

The event tagging probabilities for Z/γ^* events are obtained by applying the "Data method" described in Sec. 6.2.2 to the same low $\not{E}_T$ samples which are used to derive the κ_Z factors. The number of preselected and tagged events in these samples as well as the event tagging probabilities are listed in Tab. 11.2. Since the efficiencies obtained in the $e +$ track and $\mu +$ track samples are consistent within uncertainties, an average of these event tagging probabilities is used in both channels.

N_{jets}	Observed	Predicted	κ_Z
		$e+$track	
$=1$	2397.7 ± 50.6	1851.5 ± 17.7	1.30 ± 0.03
≥ 2	325.6 ± 19.1	304.5 ± 3.2	1.07 ± 0.06
		$\mu+$track	
$=1$	2578.5 ± 51.7	1796.1 ± 15.8	1.44 ± 0.03
≥ 2	400.9 ± 20.7	397.0 ± 4.1	1.01 ± 0.05

Table 11.1: The κ_Z factors used in the normalization of the Z/γ^* backgrounds. Shown are also the observed and predicted yields from which the κ_Z factors are derived. Uncertainties are statistical only.

N_{jets}	Untagged	Tagged	ϵ^{evttag}
		$e+$track	
$=1$	2437	29	1.2 ± 0.2
≥ 2	344	12	3.5 ± 1.0
		$\mu+$track	
$=1$	2619	23	0.9 ± 0.2
≥ 2	416	17	4.1 ± 1.0
		combined	
$=1$	5056	52	1.0 ± 0.1
≥ 2	760	29	3.8 ± 0.7

Table 11.2: The number of Z/γ^* events before and after b-tagging as well as the event tagging probabilities in % in the $e+$track, $\mu+$track and combined samples. Uncertainties are statistical only.

11.1.2 The $Z/\gamma^*(\rightarrow \tau\tau)$+jets Background

The expected number of preselected $Z/\gamma^* \rightarrow \tau\tau$ events is obtained in the same way as the expected number of preselected $Z/\gamma^* \rightarrow ee$ and $Z/\gamma^* \rightarrow \mu\mu$ events. The yields predicted from the simulated $Z/\gamma^*(\rightarrow \ell\ell)j$ and $Z/\gamma^*(\rightarrow \ell\ell)jj$ events in Tab. 9.5 are corrected by applying the κ_Z correction factors defined in Tab. 11.1.

The event tagging probabilities applied to $Z/\gamma^* \rightarrow \tau\tau$ events are combined ones used for both $Z/\gamma^* \rightarrow ee$ and $Z/\gamma^* \rightarrow \mu\mu$ events.

11.1.3 The WW+jets Background

The expected number of preselected WW events is estimated from the simulated sample of WW events in Tab. 9.5 and normalized using the NLO cross section from [171].

The event tagging probability for WW events is taken to be the same as for W events.

11.1.4 The Multijet and W+jets Backgrounds

The expected number of preselected multijet and W events are estimated with little input from simulated events, using a matrix method, described later in this section.

The event tagging probabilities for multijet events are listed in Tab. 11.3. They are obtained by applying the "Data method" described in Sec. 6.2.2 to the multijet data samples defined in Sec. 9.5.2. The event tagging probabilities for W events are also obtained with the "Data method", from the W data samples defined in Sec. 9.5.3. Events in these samples having less than three jets are almost exclusively W events. For events with three or more jets there is a non-negligible contamination from $t\bar{t}$ events decaying to lepton+jets final states. To subtract the effect of this $t\bar{t}$ contamination, a simulated sample of $t\bar{t} \rightarrow \ell + \text{jets}$ events is used. The $t\bar{t}$ contamination to the $W+\geq 3$ jets samples is evaluated by assuming a $t\bar{t}$ cross section of 7 pb and applying the "Data and simulation method" described in 6.2.2. The number of preselected and tagged data events before and after the subtraction of the expected number of $t\bar{t}$ events, as well as the resulting W tagging efficiencies are listed in Tab.11.4.

N_{jets}	Untagged	Tagged	ϵ^{evttag}
	$e + \text{track}$		
$= 1$	77987	791	1.01 ± 0.04
≥ 2	8016	208	2.6 ± 0.2
	$\mu + \text{track}$		
$= 1$	14890	243	1.6 ± 0.1
≥ 2	1438	47	3.3 ± 0.5

Table 11.3: The number of multijet events before and after b-tagging as well as the resulting event tagging probabilities in %. Uncertainties are statistical only.

The Matrix Method

The matrix method builds on the fact that leptons and tracks originating from decays of W or Z bosons (referred to as real isolated leptons and tracks) have a different probability of passing the tight lepton and track selection criteria than misidentified leptons and tracks in W and multijet events (referred to as fake isolated leptons and tracks). Using four different $\ell +$ track selections allows to select four different data

N_{jets}	Untagged	Untagged ($t\bar{t}$ subtr.)	Tagged	Tagged ($t\bar{t}$ subtr.)	ϵ^{evttag} [%]
	$e+$ track				
$=1$	44605	44599.4	482	480.6	1.08 ± 0.05
≥ 2	10220	10038.3	415	316.3	3.2 ± 0.2
	$\mu+$ track				
$=1$	23933	23929.9	228	227.2	0.95 ± 0.06
≥ 2	5167	5016.2	244	162.5	3.2 ± 0.3

Table 11.4: The number of W events in data before and after b-tagging with and without $t\bar{t}$ subtraction, as well as the event tagging probabilities in %. Uncertainties are statistical only.

samples per channel:

$$\begin{aligned}
\text{LL, LT} &= \text{one loose lepton} + \text{one loose track} \\
\text{TL, LT} &= \text{one tight lepton} + \text{one loose track} \\
\text{LL, TT} &= \text{one loose lepton} + \text{one tight track} \\
\text{TL, TT} &= \text{one tight lepton} + \text{one tight track}
\end{aligned}$$

all with a different fraction of real and fake isolated leptons and tracks. Here loose and tight refers to the loose and tight lepton and track selections defined in Secs. 7.2, 7.3 and 7.4. The tight lepton, tight track (TL, TT) sample is equal to the preselected sample.

The efficiencies for real isolated leptons and real isolated tracks to pass the tight cut are referred to as $\epsilon_{\text{sig}}^{\text{lept}}$ and $\epsilon_{\text{sig}}^{\text{trk}}$ respectively. The corresponding efficiencies for fake isolated leptons and fake isolated tracks to pass the tight cut are called $\epsilon_{\text{bkg}}^{\text{lept}}$ and $\epsilon_{\text{bkg}}^{\text{track}}$. Assuming these efficiencies are known, the following four quantities can be calculated:

$$N_{\text{FL,FT}} = \frac{\epsilon_{\text{sig}}^{\text{lept}}\epsilon_{\text{sig}}^{\text{trk}}N_{\text{LL,LT}} - \epsilon_{\text{sig}}^{\text{lept}}N_{\text{LL,TT}} - \epsilon_{\text{sig}}^{\text{trk}}N_{\text{TL,LT}} + N_{\text{TL,TT}}}{(\epsilon_{\text{bkg}}^{\text{lept}} - \epsilon_{\text{sig}}^{\text{lept}})(\epsilon_{\text{bkg}}^{\text{trk}} - \epsilon_{\text{sig}}^{\text{trk}})} \tag{11.1}$$

$$N_{\text{RL,FT}} = \frac{-\epsilon_{\text{bkg}}^{\text{lept}}\epsilon_{\text{sig}}^{\text{trk}}N_{\text{LL,LT}} + \epsilon_{\text{bkg}}^{\text{lept}}N_{\text{LL,TT}} + \epsilon_{\text{sig}}^{\text{trk}}N_{\text{TL,LT}} - N_{\text{TL,TT}}}{(\epsilon_{\text{bkg}}^{\text{lept}} - \epsilon_{\text{sig}}^{\text{lept}})(\epsilon_{\text{bkg}}^{\text{trk}} - \epsilon_{\text{sig}}^{\text{trk}})} \tag{11.2}$$

$$N_{\text{FL,RT}} = \frac{-\epsilon_{\text{sig}}^{\text{lept}}\epsilon_{\text{bkg}}^{\text{trk}}N_{\text{LL,LT}} + \epsilon_{\text{sig}}^{\text{lept}}N_{\text{LL,TT}} + \epsilon_{\text{bkg}}^{\text{trk}}N_{\text{TL,LT}} - N_{\text{TL,TT}}}{(\epsilon_{\text{bkg}}^{\text{lept}} - \epsilon_{\text{sig}}^{\text{lept}})(\epsilon_{\text{bkg}}^{\text{trk}} - \epsilon_{\text{sig}}^{\text{trk}})} \tag{11.3}$$

$$N_{\text{RL,RT}} = \frac{\epsilon_{\text{bkg}}^{\text{lept}}\epsilon_{\text{bkg}}^{\text{trk}}N_{\text{LL,LT}} - \epsilon_{\text{bkg}}^{\text{lept}}N_{\text{LL,TT}} - \epsilon_{\text{bkg}}^{\text{trk}}N_{\text{TL,LT}} + N_{\text{TL,TT}}}{(\epsilon_{\text{bkg}}^{\text{lept}} - \epsilon_{\text{sig}}^{\text{lept}})(\epsilon_{\text{bkg}}^{\text{trk}} - \epsilon_{\text{sig}}^{\text{trk}})} \tag{11.4}$$

which are defined as:

$N_{\mathrm{FL,FT}}$ = Number of events with a fake isolated lepton and a fake isolated track
$N_{\mathrm{RL,FT}}$ = Number of events with a real isolated lepton and a fake isolated track
$N_{\mathrm{FL,RT}}$ = Number of events with a fake isolated lepton and a real isolated track
$N_{\mathrm{RL,RT}}$ = Number of events with a real isolated lepton and a real isolated track

The matrix method is performed separately for events with exactly one and more than two jets as well as for $e+$ track and $\mu+$ track events. In the $e+$ track channel, $\epsilon_{\mathrm{sig}}^{\mathrm{lept}}$ and $\epsilon_{\mathrm{bkg}}^{\mathrm{lept}}$ are found to be different for electrons reconstructed in the central and endcap calorimeters. Since tighter shower shape requirements are made in later electron trigger versions, $\epsilon_{\mathrm{bkg}}^{\mathrm{lept}}$ has to be derived separately for trigger versions 8-11, 12 and 13. The matrix method in the $e+$ track channel is therefore derived in six different subsamples.

Efficiencies for Real Isolated Leptons and Tracks

The efficiency for a real isolated electron, a real isolated muon or a real isolated track to pass the tight cut, is determined using simulated $Z/\gamma^* \to ee$ and $Z/\gamma^* \to \mu\mu$ events. The efficiency is defined as the ratio of the number of events passing the tight selection criteria to those passing the loose selection criteria. The efficiency is then multiplied by the data-to-simulation correction factor for the tight cut. The corrected efficiencies are listed in Tab. 11.5.

	ϵ_{sig}	
	$N_{\mathrm{jets}} = 1$	$N_{\mathrm{jets}} \geq 2$
Electron CC	0.810 ± 0.008	0.81 ± 0.01
Electron EC	0.86 ± 0.02	0.92 ± 0.02
Muon	0.980 ± 0.003	0.976 ± 0.005
Track, $e+$ track channel	0.936 ± 0.003	0.937 ± 0.004
Track, $\mu+$ track channel	0.965 ± 0.002	0.963 ± 0.003

Table 11.5: The efficiency for a real isolated electron, isolated muon or isolated track to pass the tight cut. The efficiency is derived separately for events with one and two or more jets. Uncertainties are statistical only.

Efficiencies for Fake Isolated Leptons and Tracks

The efficiency for a fake isolated electron to pass the tight cut is obtained in the electron multijet sample defined in Sec. 9.5.2. In the same way the efficiencies for fake isolated muons or fake isolated tracks to pass the tight isolation cut are determined in the corresponding multijet samples. The value of ϵ_{bkg} is defined as ratio of the number of events in the tight and loose samples. The estimated efficiencies are listed in Tab. 11.6. Systematic uncertainties are derived from the shape of the efficiency at low values of $\not\!\!E_T$, as well as from kinematic dependences. The systematic uncertainties are described in more detail in Sec. 11.4.

	ϵ_{bkg}	
	$N_{\text{jets}} = 1$	$N_{\text{jets}} \geq 2$
Electron CC v8-11	0.076 ± 0.001 ± 0.010	0.084 ± 0.002 ± 0.009
Electron CC v12	0.113 ± 0.001 ± 0.008	0.114 ± 0.002 ± 0.014
Electron CC v13	0.107 ± 0.001 ± 0.003	0.100 ± 0.019 ± 0.000
Electron EC v8-11	0.103 ± 0.001 ± 0.006	0.109 ± 0.004 ± 0.010
Electron EC v12	0.140 ± 0.001 ± 0.010	0.121 ± 0.002 ± 0.013
Electron EC v13	0.121 ± 0.002 ± 0.013	0.106 ± 0.005 ± 0.028
Muon	0.185 ± 0.001 ± 0.012	0.181 ± 0.004 ± 0.015
Track, $e +$ track channel	0.378 ± 0.001 ± 0.029	0.362 ± 0.002 ± 0.022
Track, $\mu +$ track channel	0.345 ± 0.001 ± 0.014	0.350 ± 0.008 ± 0.009

Table 11.6: The efficiency for a fake isolated electron, fake isolated muon or fake isolated track to pass the tight cut. The efficiency is derived separately for events with one and two or more jets. The uncertainties shown are ± stat ± syst.

As explained in Sec. 9.5.2, only events having $\not\!\!E_T < 10$ GeV are used for the calculation of ϵ_{bkg}. For illustration, the efficiency for fake electrons collected with trigger list version v12 and reconstructed in the central calorimeter is shown in Fig. 11.1 as a function of the $\not\!\!E_T$. The probability for loose electrons to pass the tight cut increases at high $\not\!\!E_T$ where the W contribution to the sample becomes significant.

11.2 The $t\bar{t}$ Signal Efficiency

The preselection efficiencies for $t\bar{t}$ events are determined from the sample of simulated $t\bar{t} \to \ell\ell$ events defined in Sec. 9.3.1. The event tagging probabilities are calculated with the same simulated sample, by applying the "Data and simulation method" described in Sec. 6.2.2.

The efficiency for the $t\bar{t}$ events to pass the various selection criteria is shown in Tab. 11.7 and Tab. 11.8 for the $e +$ track and $\mu +$ track channels respectively. The tables show both the marginal and cumulative efficiencies. Most selection criteria applied are more than 90% efficient. The most inefficient selection criteria for the $t\bar{t}$ signal are the requirements of an electron or muon, as well as the requirement of at

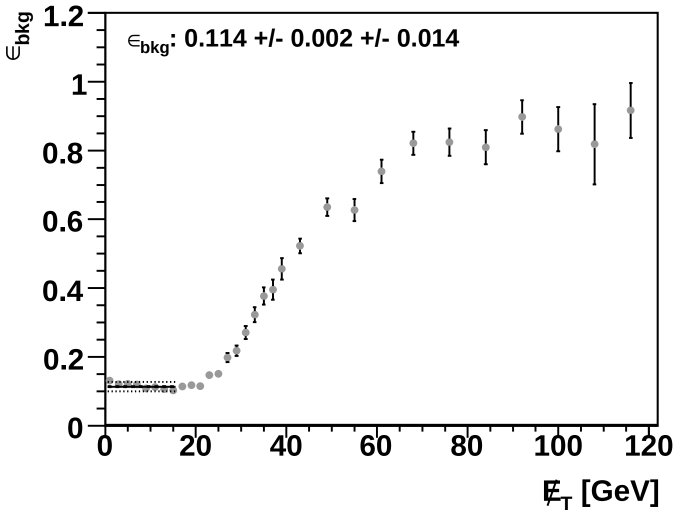

Figure 11.1: Efficiency for a loose electron reconstructed in the central calorimeter to pass the tight cut. The low $\not{E}_T$ region is dominated by processes with fake isolated electrons. The figure shows events with ≥ 2 jets collected with trigger list version 12. The solid line shows the estimated ϵ_{bkg} and the dashed lines indicate the systematic uncertainty assigned to the estimate.

least one b-tagged jet. The muon (electron) veto in the $e+$ track ($\mu+$ track) channel also has a low efficiency since it rejects many of the $e\mu$ events. But as discussed in Sec. 9.2.2, the veto is applied to make the $e+$ track and $\mu+$ track signal samples orthogonal to each other and to analyses using $e\mu$ events. The overall signal efficiency is 0.70% (0.46%) for events with exactly one jet and 2.64% (2.07%) for events with at least two jets in the $e+$ track ($\mu+$ track) channel. The cumulative efficiencies are derived with respect to all $t\bar{t} \rightarrow \ell\ell$ events with $\ell = e,\ \mu,\ \tau$.

11.3 Composition of the Preselected and b-tagged Samples

The number of observed and predicted signal and background events in the preselected and b-tagged signal samples are shown in Tab. 11.9 and Tab. 11.10 respectively. For illustration, a $t\bar{t}$ prediction is obtained by assuming a cross section of 7 pb. In the extraction of the cross section, the $t\bar{t}$ contribution is fitted to the data. The number of observed and predicted events in the preselected and b-tagged signal samples are also shown in Figs. 11.2 and 11.3. Plots with the observed and predicted number of events in the preselected and b-tagged signal samples as a function of various kinematic variables are shown in Appendix B.

	$N_{\text{jets}} = 1$		$N_{\text{jets}} \geq 2$	
Cut	Marginal	Cumulative	Marginal	Cumulative
PV quality cuts	97.04 ± 0.11	19.54 ± 0.12	97.26 ± 0.06	76.12 ± 0.13
Basic electron cuts	62.98 ± 0.33	12.31 ± 0.10	47.99 ± 0.17	36.53 ± 0.15
Electron in CC or EC	96.20 ± 0.16	11.84 ± 0.10	95.46 ± 0.10	34.87 ± 0.14
Electron $p_T > 15$ GeV/c	100.00 ± 0.00	11.84 ± 0.10	100.00 ± 0	34.87 ± 0.14
$\Delta R(e, \text{jet}) > 0.5$	99.96 ± 0.02	11.84 ± 0.10	99.90 ± 0.02	34.83 ± 0.14
Electron track match	86.54 ± 0.30	10.24 ± 0.09	87.81 ± 0.17	30.58 ± 0.14
$\Delta z(e, \text{PV}) < 1$ cm	99.95 ± 0.02	10.24 ± 0.09	99.95 ± 0.01	30.57 ± 0.14
Reconstructed track	100.00 ± 0.00	10.24 ± 0.09	100.00 ± 0.00	30.57 ± 0.14
$\Delta R(e, \text{track}) > 0.5$	100.00 ± 0.00	10.24 ± 0.09	100.00 ± 0.00	30.57 ± 0.14
Track $p_T > 15$ GeV/c	81.91 ± 0.36	8.39 ± 0.08	85.75 ± 0.19	26.21 ± 0.13
Track $\lvert\eta\rvert < 2$	98.11 ± 0.14	8.23 ± 0.08	98.82 ± 0.06	25.90 ± 0.13
$\Delta z(\text{track}, \text{PV}) < 1$ cm	99.41 ± 0.08	8.18 ± 0.08	99.35 ± 0.05	25.74 ± 0.13
Track $\chi^2 < 4$	99.76 ± 0.05	8.16 ± 0.08	99.65 ± 0.03	25.65 ± 0.13
Track $\lvert d_{ca}/\sigma(d_{ca})\rvert < 5$	91.44 ± 0.30	7.46 ± 0.08	88.92 ± 0.19	22.81 ± 0.13
No cosmic muon match	99.35 ± 0.09	7.41 ± 0.08	99.42 ± 0.05	22.67 ± 0.13
Track isolation < 0.5	82.98 ± 0.42	6.15 ± 0.07	76.00 ± 0.27	17.23 ± 0.11
$\Delta R(\text{track}, \text{jet}) > 0.5$	95.79 ± 0.24	5.89 ± 0.07	77.86 ± 0.30	13.42 ± 0.10
Track from top decay (simulation only)	93.64 ± 0.30	5.52 ± 0.07	97.09 ± 0.14	13.03 ± 0.10
Electron likelihood > 0.85	90.54 ± 0.38	5.00 ± 0.07	92.39 ± 0.22	12.03 ± 0.10
Track isolation < 0.12	95.12 ± 0.29	4.75 ± 0.06	96.24 ± 0.17	11.58 ± 0.10
Track and e of opposite charge	99.60 ± 0.09	4.73 ± 0.06	99.58 ± 0.06	11.53 ± 0.10
$\not\!\!E_T$ & $\not\!\!E_T^Z > 15$ GeV	94.10 ± 0.33	4.45 ± 0.06	93.54 ± 0.22	10.79 ± 0.09
$\not\!\!E_T$ & $\not\!\!E_T^Z > 20$ GeV (m_Z window)	99.37 ± 0.11	4.43 ± 0.06	99.36 ± 0.07	10.72 ± 0.09
Vetoes and correction factors	45.59 ± 0.54	2.02 ± 0.04	45.36 ± 0.35	4.86 ± 0.06
Trigger	92.70 ± 1.76	1.87 ± 0.04	93.16 ± 1.14	4.53 ± 0.05
b-tagging	37.30 ± 0.75	0.70 ± 0.01	58.34 ± 0.73	2.64 ± 0.03

Table 11.7: The selection efficiencies in % for $t\bar{t}$ events in the $e +$ track channel. Uncertainties are statistical only.

	$N_{\text{jets}} = 1$		$N_{\text{jets}} \geq 2$	
Cut	Marginal	Cumulative	Marginal	Cumulative
PV quality cuts	97.04 ± 0.11	19.54 ± 0.12	97.26 ± 0.06	76.12 ± 0.13
Local muon	56.54 ± 0.34	11.05 ± 0.09	55.23 ± 0.17	42.04 ± 0.15
Muon track match	100.00 ± 0.00	11.05 ± 0.09	100.00 ± 0.00	42.04 ± 0.15
Muon $p_T > 15$ GeV/c	77.83 ± 0.38	8.60 ± 0.08	76.56 ± 0.20	32.19 ± 0.14
$\Delta z(\mu, \text{PV}) < 1$ cm	99.85 ± 0.04	8.59 ± 0.08	99.87 ± 0.02	32.15 ± 0.14
Muon track $\chi^2 < 4$	99.86 ± 0.04	8.57 ± 0.08	99.90 ± 0.02	32.11 ± 0.14
$\Delta R(\mu, \text{jet}) > 0.5$	94.05 ± 0.24	8.06 ± 0.08	83.19 ± 0.20	26.72 ± 0.13
Muon $\lvert d_{ca}/\sigma(d_{ca})\rvert < 3$	92.86 ± 0.27	7.49 ± 0.08	92.81 ± 0.15	24.80 ± 0.13
Reconstructed track	100.00 ± 0.00	7.49 ± 0.08	100.00 ± 0.00	24.80 ± 0.13
$\Delta R(\mu, \text{track}) > 0.5$	100.00 ± 0.00	7.49 ± 0.08	100.00 ± 0.00	24.80 ± 0.13
Track $p_T > 15$ GeV/c	81.93 ± 0.42	6.14 ± 0.07	86.12 ± 0.21	21.36 ± 0.12
Track $\lvert\eta\rvert < 2$	98.21 ± 0.16	6.03 ± 0.07	98.85 ± 0.07	21.11 ± 0.12
$\Delta z(\text{track}, \text{PV}) < 1$ cm	99.31 ± 0.10	5.98 ± 0.07	99.35 ± 0.05	20.97 ± 0.12
Track $\chi 2 < 4$	99.65 ± 0.07	5.96 ± 0.07	99.60 ± 0.04	20.89 ± 0.12
Track $\lvert d_{ca}/\sigma(d_{ca})\rvert < 5$	91.74 ± 0.34	5.47 ± 0.07	89.66 ± 0.20	18.73 ± 0.12
No cosmic muon match	99.25 ± 0.11	5.43 ± 0.07	99.39 ± 0.05	18.61 ± 0.12
Track isolation < 0.5	85.80 ± 0.45	4.66 ± 0.06	76.61 ± 0.30	14.26 ± 0.11
$\Delta R(\text{track}, \text{jet}) > 0.5$	95.65 ± 0.29	4.46 ± 0.06	78.61 ± 0.33	11.21 ± 0.10
Track from top decay (simulation only)	95.94 ± 0.28	4.27 ± 0.06	99.15 ± 0.08	11.12 ± 0.09
Muon track and calo isolation < 0.12	95.75 ± 0.29	4.09 ± 0.06	95.42 ± 0.19	10.61 ± 0.09
Track isolation < 0.12	94.85 ± 0.33	3.88 ± 0.06	96.49 ± 0.17	10.23 ± 0.09
Track and μ of opposite charge	99.53 ± 0.10	3.86 ± 0.06	99.41 ± 0.07	10.17 ± 0.09
$\not{E}_T$ & $\not{E}_T^Z > 25$ GeV	84.94 ± 0.55	3.28 ± 0.05	85.36 ± 0.33	8.68 ± 0.08
$\not{E}_T$ & $\not{E}_T^Z > 35$ GeV (m_Z window)	97.31 ± 0.27	3.19 ± 0.05	97.27 ± 0.17	8.45 ± 0.08
Vetoes and correction factors	44.25 ± 0.72	1.41 ± 0.03	47.22 ± 0.45	3.99 ± 0.05
Trigger	84.62 ± 2.01	1.20 ± 0.03	89.22 ± 1.25	3.56 ± 0.05
b-tagging	38.11 ± 0.97	0.46 ± 0.01	58.26 ± 0.85	2.07 ± 0.03

Table 11.8: The selection efficiencies in % for $t\bar{t}$ events in the $\mu +$ track channel. Uncertainties are statistical only.

	e + track		μ + track	
	$N_{\text{jets}} = 1$	$N_{\text{jets}} \geq 2$	$N_{\text{jets}} = 1$	$N_{\text{jets}} \geq 2$
WW	3.5 ± 0.2	0.50 ± 0.08	2.0 ± 0.1	0.36 ± 0.07
$Z/\gamma^* \to \tau\tau$	8.6 ± 2.0	3.2 ± 0.4	3.6 ± 1.4	2.2 ± 0.4
$Z/\gamma^* \to ee/\mu\mu$	148.9 ± 4.4	60.0 ± 1.5	144.7 ± 3.9	47.9 ± 1.5
Multijet/W	37.9 ± 6.3	14.6 ± 3.5	9.8 ± 2.8	2.5 ± 1.6
Total bkg	198.9 ± 8.0	78.3 ± 3.8	160.2 ± 5.0	53.0 ± 2.2
$t\bar{t}$	4.92 ± 0.09	11.9 ± 0.1	3.12 ± 0.07	9.3 ± 0.1
Total pred.	203.8 ± 8.0	90.2 ± 3.8	163.3 ± 5.0	62.3 ± 2.2
Observed	250	85	170	56

Table 11.9: Number of observed and predicted events in the preselected samples. Uncertainties are statistical only.

	e + track		μ + track	
	$N_{\text{jets}} = 1$	$N_{\text{jets}} \geq 2$	$N_{\text{jets}} = 1$	$N_{\text{jets}} \geq 2$
WW	0.038 ± 0.002	0.016 ± 0.002	0.019 ± 0.001	0.012 ± 0.002
$Z/\gamma^* \to \tau\tau$	0.09 ± 0.02	0.12 ± 0.02	0.04 ± 0.01	0.08 ± 0.01
$Z/\gamma^* \to ee/\mu\mu$	1.53 ± 0.05	2.29 ± 0.06	1.49 ± 0.04	1.83 ± 0.06
Multijet/W	0.40 ± 0.07	0.4 ± 0.1	0.10 ± 0.03	0.08 ± 0.05
Total bkg	2.06 ± 0.08	2.9 ± 0.1	1.65 ± 0.05	2.01 ± 0.08
$t\bar{t}$	1.84 ± 0.04	6.96 ± 0.09	1.19 ± 0.03	5.41 ± 0.08
Total pred.	3.89 ± 0.09	9.8 ± 0.2	2.83 ± 0.06	7.4 ± 0.1
Observed	7	11	1	6

Table 11.10: Number of observed and predicted events in the b-tagged samples. Uncertainties are statistical only.

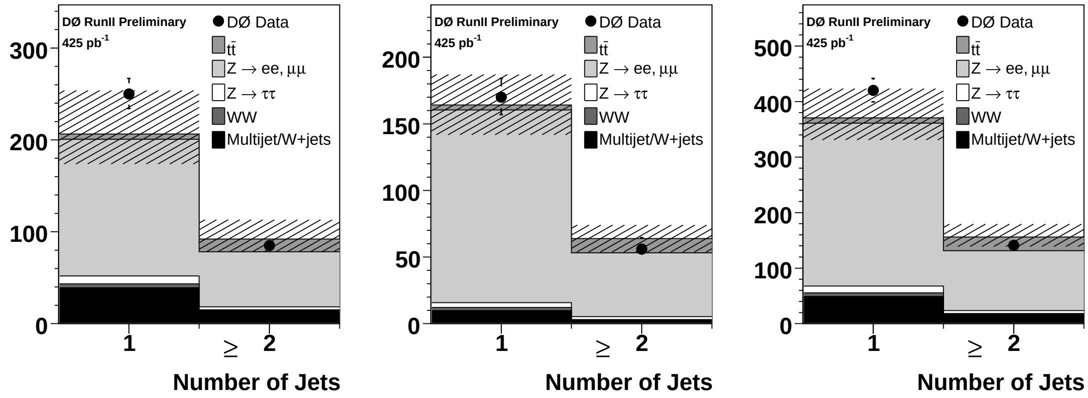

(a) The $e +$ track channel. (b) The $\mu +$ track channel. (c) The $\ell +$ track channel.

Figure 11.2: Observed and predicted event yields in the $e +$ track, $\mu +$ track and $\ell +$ track preselected samples, as a function of the jet multiplicity. The hashed area indicates the total uncertainty on the prediction.

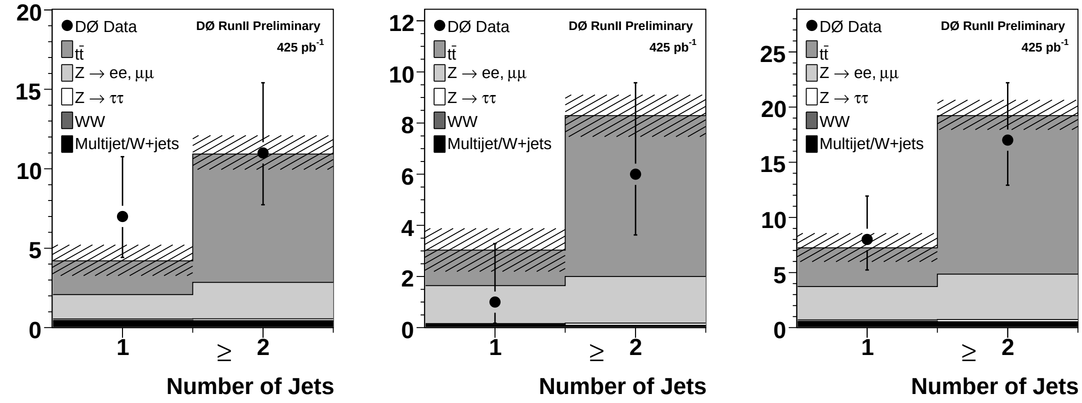

(a) The $e +$ track channel. (b) The $\mu +$ track channel. (c) The $\ell +$ track channel.

Figure 11.3: Observed and predicted event yields in the $e +$ track, $\mu +$ track and $\ell +$ track b-tagged samples, as a function of the jet multiplicity. The hashed area indicates the total uncertainty on the prediction.

11.4 Systematic Uncertainties

The systematic uncertainties on the signal efficiency are shown in Tabs. 11.11 and 11.12 for the $e+$ track and $\mu+$ track channel respectively. The systematic uncertainties on the number of b-tagged background events are shown in Tabs. 11.13 and 11.14. In the description of the sources of systematic uncertainty given below, only those for which the procedure differs from that used in the $e\mu$ analysis are described.

Track Identification

The data-to-simulation correction factors for the track cut efficiencies, described in Sec. 8.2, are varied by their statistical uncertainties.

Track Momentum Smearing

The track p_T smearing applied to tracks and muons in simulated events, as described in Sec. 7.3 is varied by its uncertainty.

Jet Trigger

The parameterizations of the jet trigger efficiencies are varied by their uncertainties. These uncertainties originate from limited statistics in the data samples used to extract the trigger efficiency parameterizations as well as from studies of the trigger efficiency for different jet definitions.

Z/γ^* Background Normalization

The κ_Z factor described in Sec. 11.1.1 is varied by its statistical error as well as by the difference of the κ_Z factors observed in the $e+$ track and $\mu+$ track channels.

Multijet and W Background Normalization

The number of multijet and W events in the preselected sample comes from the matrix method. Systematic uncertainties arise from the uncertainties on $\epsilon_{\text{sig}}^{\text{lept}}$, $\epsilon_{\text{bkg}}^{\text{lept}}$, $\epsilon_{\text{sig}}^{\text{trk}}$ and $\epsilon_{\text{bkg}}^{\text{trk}}$. Due to limited statistics in the four data samples in which the matrix method is performed, there is an additional statistical component to the uncertainty on the number of preselected multijet and W events.

The systematic uncertainties on ϵ_{sig} only originates from the limited statistics of the simulated samples in which they are derived.

To estimate systematic uncertainties on ϵ_{bkg}, the efficiencies are studied as a function of the $\not\!\!E_T$ cut. For some samples there is a clear linear rise of the efficiency as the $\not\!\!E_T$ decreases. Such a rise, however not very pronounced, can be seen in Fig. 11.1. To derive a systematic uncertainty, the the lowest value of the efficiency in the range $0 < \not\!\!E_T < 20$ GeV is identified and the mean of ϵ_{bkg} between this bin

Source	$N_{\text{jets}} = 1$	$N_{\text{jets}} \geq 2$
Primary vertex	± 0.45	± 0.45
Electron trigger	$+0.62 - 1.06$	$+1.95 - 2.36$
Electron identification	± 3.28	± 3.27
Track identification	± 2.65	± 2.62
Track p_T smearing	± 0.28	± 0.14
Jet trigger	± 0.04	± 0.10
Jet energy scale	$-3.09 + 4.02$	$+3.15 - 3.85$
Jet energy resolution	$-3.37 + 0.46$	± 1.40
Jet identification	$-7.80 + 5.64$	$+4.16 - 1.36$
Taggability	± 0.67	± 0.55
$\epsilon^{\text{data}}_{b\to\mu X}$	± 4.00	$+2.99 - 3.06$
$\epsilon^{\text{sim}}_{b\to\mu X}$	$-1.37 + 1.45$	$-1.12 + 1.17$
$\epsilon^{\text{sim}}_{b}$	± 2.70	$+2.04 - 2.07$
$\epsilon^{\text{sim}}_{c}$	< 0.01	< 0.01
Mistag rate	< 0.01	< 0.01
Finite statistics in simulation	± 2.00	± 1.22

Table 11.11: Systematic uncertainties in % on the signal efficiency in the $e+$track channel.

Source	$N_{\text{jets}} = 1$	$N_{\text{jets}} \geq 2$
Primary vertex	± 0.45	± 0.45
Muon trigger	$+2.96 - 3.50$	$+3.00 - 3.57$
Muon identification	± 5.05	± 5.05
Track identification	± 2.68	± 2.67
Track p_T smearing	± 0.64	± 0.54
Jet trigger	$+1.13 - 1.24$	$+0.40 - 0.56$
Jet energy scale	$-2.79 + 2.50$	$+4.23 - 3.36$
Jet energy resolution	± 1.60	$+0.33 - 0.13$
Jet identification	$-5.57 + 12.33$	$+1.16 - 2.86$
Taggability	$+0.68 - 0.70$	± 0.58
$\epsilon_{b\to\mu X}^{\text{data}}$	± 4.09	$+3.00 - 3.07$
$\epsilon_{b\to\mu X}^{\text{sim}}$	$-1.33 + 1.40$	$-1.10 + 1.15$
$\epsilon_{b}^{\text{sim}}$	± 2.53	$+2.02 - 2.05$
$\epsilon_{c}^{\text{sim}}$	< 0.01	< 0.01
Mistag rate	< 0.01	< 0.01
Finite statistics in simulation	± 2.53	± 1.43

Table 11.12: Systematic uncertainties in % on the signal efficiency in the $\mu +$ track channel.

Source	$N_{\text{jets}} = 1$	$N_{\text{jets}} \geq 2$
Primary vertex	± 0.36	± 0.38
Electron trigger	$+0.42 - 0.78$	$+1.24 - 1.44$
Electron identification	± 2.70	± 2.88
Track identification	± 2.13	± 2.24
Track p_T smearing	$+1.38 - 0.019$	$+0.039 - 0.13$
Jet trigger	± 0.10	± 0.11
Jet energy scale	$+18.04 - 7.68$	$+23.41 - 12.46$
Jet energy resolution	$-9.54 + 10.51$	$-6.42 + 3.85$
Jet identification	± 1.04	$+6.98 - 4.05$
Z/γ^* normalization	± 8.62	± 6.95
WW normalization	± 0.75	± 0.21
Multijet/W normalization	$+1.94 - 1.75$	$+1.09 - 1.01$
ϵ^{evttag}, Z/γ^*	± 40.62	± 19.93
ϵ^{evttag}, WW	± 2.15	± 0.61
ϵ^{evttag}, Multijet/W	$+7.72 - 4.84$	± 1.54
Finite statistics in simulation	± 5.23	± 5.52

Table 11.13: Systematic uncertainties in % on the number of background events in the $e+$track channel.

Source	$N_{\text{jets}} = 1$	$N_{\text{jets}} \geq 2$
Primary vertex	± 0.42	± 0.43
Muon trigger	$+2.70 - 3.17$	$+2.72 - 3.28$
Muon identification	± 4.75	± 4.86
Track identification	± 2.52	± 2.60
Track p_T smearing	± 1.02	± 2.18
Jet trigger	$+2.79 - 3.25$	$+1.64 - 2.04$
Jet energy scale	$+7.65 - 2.51$	$+14.92 - 12.20$
Jet energy resolution	± 2.68	$-4.91 + 4.50$
Jet identification	± 2.97	± 3.83
Z/γ^* normalization	± 9.21	± 7.62
WW normalization	± 0.48	± 0.22
Multijet/W normalization	$+0.47 - 0.45$	± 0.35
ϵ^{evttag}, Z/γ^*	± 47.94	± 22.52
ϵ^{evttag}, WW	± 1.36	± 0.62
ϵ^{evttag}, Multijet/W	$+1.63 - 1.28$	± 0.72
Finite statistics in simulation	± 3.52	± 4.40

Table 11.14: Systematic uncertainties in % on the number of background events in the $\mu +$ track channel.

and the neighboring bin is derived. Half the difference between this low estimate and the ϵ_{bkg} obtained on events with $\not{E}_T < 2$ GeV is taken as a systematic uncertainty.

An additional systematic uncertainty is derived from the dependence of ϵ_{bkg} on the electron p_T and the muon and track η. For electrons three different p_T bins are studied ($15 < p_T < 25$ GeV/c, $25 < p_T < 50$ GeV/c and $p_T > 50$ GeV/c), and the systematic uncertainty is taken to be the maximum difference between the inclusive sample and any of these subsamples. The systematic uncertainty on ϵ_{bkg} for muons and track is computed in three η regions ($\eta < -0.5$, $-0.5 < \eta < 0.5$ and $\eta > 0.5$). The systematic uncertainty is again taken as the maximum difference between the inclusive sample and any of the subsamples.

Taggability

Systematic uncertainties on the taggability parameterizations arise from the limited statistics in the samples from which they are derived.

The systematic uncertainty on the flavor dependence of the taggability is obtained by substituting the parameterizations of the flavor dependence derived from simulated multijet events with those obtained on simulated $Wb\bar{b}$ and Wjj samples (for b- and c-jets respectively) and the default simulated multijet sample (for light jets).

Event Tagging Probability for Z/γ^* Events

The total systematic uncertainty on the event tagging probability for Z/γ^* events $\sigma_Z^{\text{tagging}}$, is defined as:

$$\sigma_Z^{\text{tagging}} = \sqrt{(\sigma_Z^{\text{stat}})^2 + \left(\sigma_Z^{\not{E}_T}\right)^2} \tag{11.5}$$

where σ_Z^{stat} is the statistical uncertainty on the event tagging probability coming from the "Data method" and $\sigma_Z^{\not{E}_T}$ accounts for any potential $\not{E}_T$ dependence of the event tagging probability.

The $\not{E}_T$ related uncertainty is determined from the simulated $Z/\gamma^* \rightarrow ee$ and $Z/\gamma^* \rightarrow \mu\mu$ events in Tab. 9.5. The samples are generated with PYTHIA. The event tagging probabilities are obtained separately for events with low and high $\not{E}_T$ using the "Data and simulation method" described in Sec. 6.2.2. The resulting event tagging probabilities are listed in Tab. 11.15. The systematic uncertainty is taken as the difference observed between the tagging probabilities obtained from the low $\not{E}_T$ and high $\not{E}_T$ samples.

Event Tagging Probability for WW Events

The event tagging probability for WW events is assumed to be the same as for W events. The systematic uncertainty on the W tagging efficiency therefore affects also the WW tagging efficiency. Applying the W tagging efficiency also to WW events

	low $\not\!\!E_T$			high $\not\!\!E_T$		
N_{jets}	Untagged	Tagged	ϵ^{evttag} [%]	Untagged	Tagged	ϵ^{evttag} [%]
$= 1$	11295.4	99.4	0.88 ± 0.04	656.4	8.7	1.3 ± 0.2
≥ 2	1125.6	26.5	2.4 ± 0.2	150.3	4.1	2.7 ± 0.6

Table 11.15: The number of preselected and tagged Z/γ^* events as well as the event tagging probabilities obtained in the combined $Z/\gamma^* \rightarrow ee$ and $Z/\gamma^* \rightarrow \mu\mu$ samples for events with low and high $\not\!\!E_T$. The events are simulated with PYTHIA.

is motivated by the similar heavy flavor content in the two processes. However the kinematics of the jets may differ. To take this into account, an additional systematic uncertainty of 100% is applied to the WW event tagging probability. Since the WW background is small, this results in a negligible contribution to the total systematic uncertainty on the measured cross section.

Event Tagging Probability for Multijet and W Events

The event tagging probability for W events is estimated using the W data samples, defined in Sec. 9.5.3. One contribution to the systematic uncertainty arises from limited statistics. A second contribution comes from the $t\bar{t} \rightarrow \ell$+jets contamination to the events with three or more jets. This $t\bar{t}$ contamination is subtracted by making use of a simulated $t\bar{t} \rightarrow \ell$+jets events. The expected number of b-tagged $t\bar{t} \rightarrow \ell$+jets events is estimated assuming a production cross section of 7 pb. This cross section is varied by ±2 pb and the effect is propagated to the W event tagging probability.

The event tagging probability for multijet events is estimated in the multijet data samples defined in Sec. 9.5.2. Systematic uncertainties arise from limited statistics, as well as from the assumption that the tagging probabilities are the same for multijet events with low and high $\not\!\!E_T$. The difference in the event tagging probability between events with high and low $\not\!\!E_T$ is taken to be the same as the variation $\sigma_Z^{\not E_T}$ observed in simulated $Z/\gamma^* \rightarrow ee$ and $Z/\gamma^* \rightarrow \mu\mu$ events.

11.5 Result

The cross section result in the $\ell +$ track analysis is obtained by combining four independent channels: $e +$ track and $\mu +$ track events with exactly one jet and two or more jets. Table 11.16 summarizes the inputs to the likelihood function.

The combined likelihood function from which the cross section is extracted, as well as the four individual likelihood functions, are shown in Fig. 11.4. The cross section measured in the combined $\ell +$ track channel is:

$$\sigma_{t\bar{t}} = 6.3\ ^{+2.1}_{-1.8}\ (\text{stat})\ ^{+1.1}_{-1.1}\ (\text{syst})\ \pm 0.4\ (\text{lumi})\ \text{pb}. \tag{11.6}$$

The cross section is derived as a function of the top quark mass by using param-

	$e + \text{track}$		$\mu + \text{track}$	
	$N_{\text{jets}} = 1$	$N_{\text{jets}} \geq 2$	$N_{\text{jets}} = 1$	$N_{\text{jets}} \geq 2$
Luminosity	426 ± 26	426 ± 26	422 ± 26	422 ± 26
Branching fraction [%]	10.3 ± 0.2	10.3 ± 0.2	10.3 ± 0.2	10.3 ± 0.2
Signal efficiency [%]	0.70 ± 0.01	2.64 ± 0.03	0.46 ± 0.01	2.07 ± 0.03
N_{bkg}	2.06 ± 0.08	2.9 ± 0.1	1.65 ± 0.05	2.01 ± 0.08

Table 11.16: The inputs to the cross section calculation for the four independent channels. The errors on the signal efficiency and N_{bkg} are statistical only.

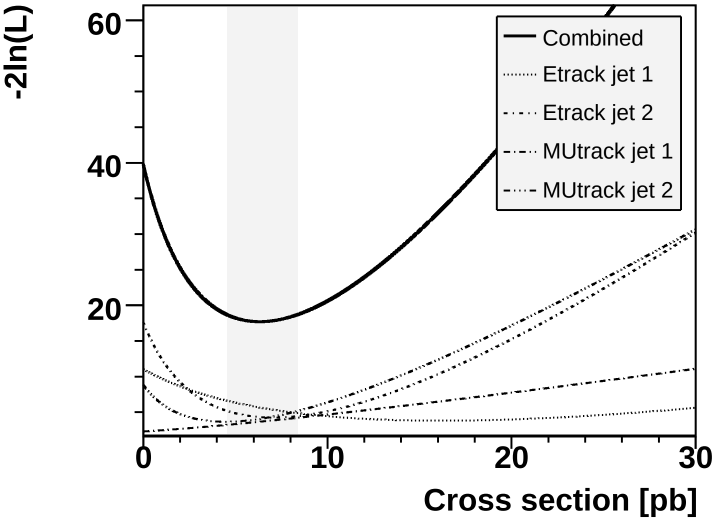

Figure 11.4: The likelihood functions for the $e + \text{track}$, $\mu + \text{track}$ and the combined $\ell + \text{track}$ channels. The highlighted area indicates $\pm 1\sigma$ around the combined cross section.

eterizations of the signal efficiency as a function of the top quark mass. The top mass dependence of the cross section is shown in Fig. 11.5. The cross section quoted above is obtained assuming a top quark mass of 175 GeV/c^2.

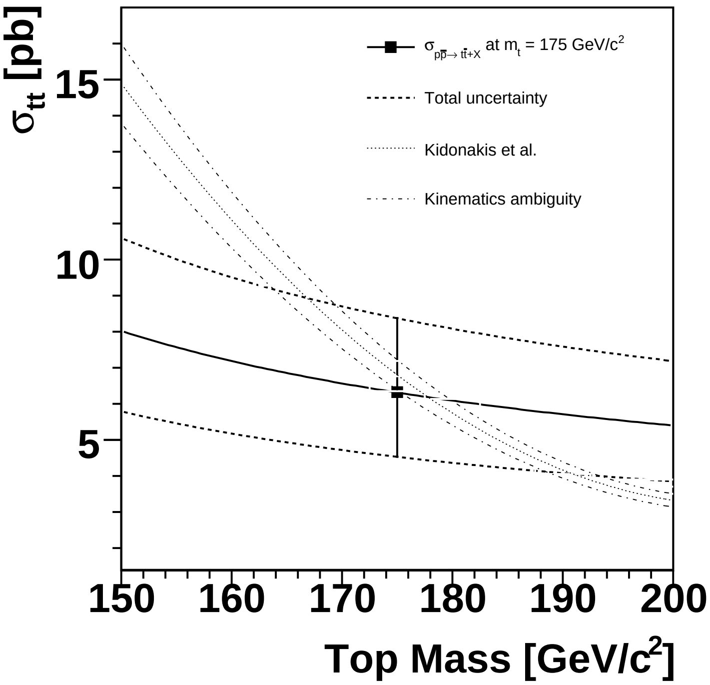

Figure 11.5: The measured top pair production cross section in the ℓ + track analysis as a function of the top quark mass. The overlaid theoretical prediction comes from Kidonakis et al. [43].

The total systematic uncertainty on the cross section is obtained by varying the inputs to the likelihood function. The complete list of systematics, and how the correlations between channels and jet multiplicity bins are treated is shown in Tab. 11.17. Table 11.18 summarizes the various contributions to the systematic uncertainty on the measured cross section. The largest sources of systematic uncertainty are the event tagging probability for Z/γ^* events and the jet energy scale. The systematic uncertainty from the luminosity calculation, which is not included in the table, is 6.1%.

	Correlation between	
Source	channels	jet bins
Primary vertex	×	×
Electron trigger	-	×
Electron identification	-	×
Muon trigger	-	×
Muon identification	-	×
Track identification	×	×
Track p_T smearing	×	×
Jet trigger	×	×
Jet energy scale	×	×
Jet energy resolution	×	×
Jet identification	×	×
Z/γ^* normalization	-	-
WW normalization	×	×
Multijet/W normalization	-	-
Taggability	×	×
$\epsilon_{b\rightarrow\mu X}^{\mathrm{data}}$	×	×
$\epsilon_{b\rightarrow\mu X}^{\mathrm{sim}}$	×	×
$\epsilon_{b}^{\mathrm{sim}}$	×	×
$\epsilon_{c}^{\mathrm{sim}}$	×	×
Mistag rate	×	×
$\epsilon^{\mathrm{evttag}}$, Z/γ^*	×	-
$\epsilon^{\mathrm{evttag}}$, WW	×	×
$\epsilon^{\mathrm{evttag}}$, Multijet/$W$	-	-
Finite statistics in simulation	-	-

Table 11.17: All the systematic uncertainties and how the correlations between channels and jet multiplicity bins are treated. The × means fully correlated, and - means fully uncorrelated.

Source	σ^+ [pb]	σ^- [pb]
Primary vertex	0.04	0.04
Electron Trigger	0.10	0.08
Electron identification	0.17	0.16
Muon Trigger	0.14	0.12
Muon identification	0.21	0.20
Track identification	0.24	0.23
Track p_T smearing	0.03	0.04
Jet trigger	0.05	0.03
Jet energy scale	0.52	0.76
Jet energy resolution	0.13	0.19
Jet identification	0.12	0.19
Z/γ^* normalization	0.14	0.13
WW normalization	0.02	0.01
Multijet/W normalization	0.02	0.02
Taggability	0.04	0.03
$\epsilon^{data}_{b\rightarrow\mu X}$	0.21	0.19
$\epsilon^{sim}_{b\rightarrow\mu X}$	0.07	0.07
ϵ^{sim}_{b}	0.14	0.13
ϵ^{sim}_{c}	< 0.01	< 0.01
Mistag rate	< 0.01	< 0.01
$\epsilon^{\mathrm{evttag}}$, Z/γ^*	0.73	0.57
$\epsilon^{\mathrm{evttag}}$, WW	0.04	0.04
$\epsilon^{\mathrm{evttag}}$, Multijet/$W$	0.06	0.08
Finite statistics in simulation	0.12	0.10
Total	1.05	1.10

Table 11.18: Systematic uncertainties in pb for the $\ell +$ track channel.

Part IV

Conclusions and Outlook

12 Conclusions and Outlook

In preparation for Run II of the Tevatron collider, all sensor types used in the D0 silicon tracker were tested for radiation hardness [151]. In these studies, the double-sided sensor with a double metal layer (90-degree sensors) showed an abnormal behavior, which was very clear when studying the depletion voltage as a function of accumulated radiation dose. The depletion voltage of the 90-degree sensor was consistently higher than those of other sensors types.

Since the 90-degree sensors are located in the innermost layers of the silicon tracker it is important to project their lifetime. This thesis presents a lifetime estimate based on measurements of the depletion voltage for the 90-degree sensors in the innermost layer of the tracker. The 90-degree senors show abnormal noise behavior, but their depletion voltages as a function of the normalized particle fluence are in agreement with standard parameterizations. If the lifetime of the silicon detector turns out to be limited primarily by the increase in depletion voltage, and assuming the 90-degree sensors follow the standard parameterizations, the innermost layer of the D0 silicon tracker will be operational up to delivered luminosities between 6 and 8 fb^{-1}.

This thesis also presents two measurements of the top quark pair production cross section in $p\bar{p}$ collisions at $\sqrt{s} = 1.96$ TeV. The first measurement makes use of 158 pb^{-1} of data in the $e\mu$ final state and measures:

$$\sigma_{t\bar{t}} = 11.1\ ^{+5.8}_{-4.3}\ (\text{stat})\ \pm 1.4\ (\text{syst})\ \pm 0.7\ (\text{lumi})\ \text{pb}. \tag{12.1}$$

The second measurement makes use of 425 pb^{-1} of data in the $\ell +$ track final state and measures:

$$\sigma_{t\bar{t}} = 6.3\ ^{+2.1}_{-1.8}\ (\text{stat})\ ^{+1.1}_{-1.1}\ (\text{syst})\ \pm 0.4\ (\text{lumi})\ \text{pb}. \tag{12.2}$$

The results are derived assuming a top quark mass of 175 GeV/c^2, and are consistent with the theoretical prediction from perturbative QCD calculations [42, 43].

Both analyses require at least one jet in the event to be b-tagged by the secondary vertex algorithm, which is a very powerful way of rejecting backgrounds. The largest backgrounds in the $e\mu$ analysis are $Z/\gamma^* \to \tau\tau$ and WW events, whereas the largest background in the $\ell +$ track analysis are $Z/\gamma^* \to ee$ and $Z/\gamma^* \to \mu\mu$ events with apparent $\not\!\!E_T$ coming from misreconstruction. Both analyses are dominated by the statistical uncertainty. The largest sources of systematic uncertainties in the $e\mu$

analysis are the jet energy scale and the b-tagging efficiency for signal events. In the $\ell +$ track analysis, the dominant systematic uncertainty is the b-tagging efficiency for Z/γ^* events, followed by the jet energy scale.

The most precise measurement of the top quark pair production cross section from the CDF Collaboration is $\sigma_{t\bar{t}} = 7.3\ \pm 0.5$ (stat) ± 0.6 (syst) ± 0.4 (lumi) pb, which is a combination of results obtained in dilepton, lepton+jets and all hadronic final states using 760 pb^{-1} of data [174]. The most precise measurement from the DØ Collaboration is $\sigma_{t\bar{t}} = 6.6\ \pm 0.9$ (stat + syst) ± 0.4 (lumi) pb, which is obtained in the lepton+jets final state with secondary vertex b-tagging using 425 pb^{-1} of data [175].

The Tevatron accelerator is scheduled to run until 2009, with a projected integrated luminosity of 4-8 fb^{-1}. With such a large data sample the Tevatron experiments will be able to significantly reduce the uncertainties in the top pair production cross section measurements. Many of the top quark properties can also be measured with great precision. The world average of top quark mass mass already has an uncertainty of only 2 GeV/c^2, which was the goal of the Tevatron Run II [39]. In order to reduce the uncertainty further, a better understanding of the jet energy scale is needed.

The Large Hadron Collider (LHC) is scheduled for first collisions in 2007. Due to the larger collision energy of 14 TeV, the top pair production cross section will increase to approximately 800 pb. In the initial low luminosity phase of running, the LHC will produce around 8 million $t\bar{t}$ events every year. Uncertainties due to limited statistics will therefore be negligible. Measurements of the top quark pair production cross section are expected to yield uncertainties of 5-10%, limited by the accuracy of the luminosity determination [176]. The achievable resolution on the top quark mass is estimated to approximately 1 GeV/c^2 [177].

13 Summary in Swedish

Elementarpartikelfysiken beskriver materiens allra minsta beståndsdelar och de krafter som verkar mellan dem. De tre krafter som inkluderas i standardmodellen är den elektromagnetiska kraften som binder samman elektronerna med atomkärnan och styr kemiska reaktioner mellan atomer och molekyler, den svaga kraften som är ansvarig bland annat för radioaktivt sönderfall, och den starka kraften som håller ihop protoner och neutroner inuti atomkärnan. Den fjärde kraften vi känner till, den gravitationella kraften, har ännu inte med framgång inkluderats i standardmodellen.

De tolv elementarpartiklar som bygger upp all materia kan delas in i sex kvarkar och sex leptoner, där kvarkarna i sin tur bygger upp tyngre partiklar så som protoner och neutroner. All vanlig materia består av elektroner, protoner och neutroner. Elektronen är en elementarpartikel av typen lepton, medan protoner och neutroner består av upp- och och nerkvarkar. Alla övriga elementarpartiklar är instabila och kan bara existera under väldigt korta tider. De skapades till exempel i det tidiga universum då det var mycket varmt och energirikt. Nuförtiden kan de skapas i partikelkollisioner, men de sönderfaller snabbt till lättare partiklar.

Den tyngsta av alla elementarpartiklar är toppkvarken, med en massa lika stor som en guldatoms. Den upptäcktes 1995 vid Tevatron-acceleratorn utanför Chicago i USA. På grund av sin stora massa är toppkvarken mycket svår att producera, vilket gör den till den minst välkända medlemmen i kvarkfamiljen. Mycket tyder dock på att toppkvarken, just på grund av sin höga massa, kan spela en speciell roll i standardmodellen och lära oss något om teorier bortom standardmodellen. Det är därför viktigt att studera toppkvarkens alla egenskaper i minsta detalj.

Del III i avhandlingen beskriver två mätningar av sannolikheten för att skapa par av toppkvarkar vid Tevatron-acceleratorn. Mätningarna har utförts på data insamlat med DØ-detektorn, en av de två detektorer som byggts för att studera de partiklar som skapas då protoner och antiprotoner kollideras i Tevatron-acceleratorn vid nära nog ljusets hastighet. De erhållna resultaten stämmer väl överens med standardmodellens förutsägelser och tyder således inte på några nya, hittills oupptäckta, fenomen.

För att kunna mäta energin och riktningen på de partiklar som skapas vid partikelkollisionerna i Tevatron-acceleratorn är DØ-detektorn uppbyggd i flera lager. Närmast kollisionspunkten finns spårdetektorer som med hög upplösning mäter de elektriskt laddade partiklarnas bana medan de rör sig genom detektorn. Den innersta spårdetektor är byggd av tunna kiselstrips. Fördelen med kiseldetektorer är att de ger en mycket hög positionsupplösning (ungefär tio mikrometer), medan deras svaghet är att de är känsliga för strålning. Hur länge DØ-detektorn kan samla data av hög kvalitet begränsas därför av livstiden hos kiseldetektorn.

Del II i avhandlingen beskriver en metod för att uppskatta livstiden hos kiseldetektorn. Strålningen som detektorn utsätts för av partiklar från acceleratorn ändrar bland annat brusnivån i detektorerna. Genom att mäta bruset kontinuerligt har vi kunnat utröna att detektorerna reagerar på strålingen helt i enlighet med rådande teorier, och att kiseldetektorn troligen kommer att fungera under återstoden av den planerade datainsamlingen.

A Kinematic Distributions in Electron-Muon Events

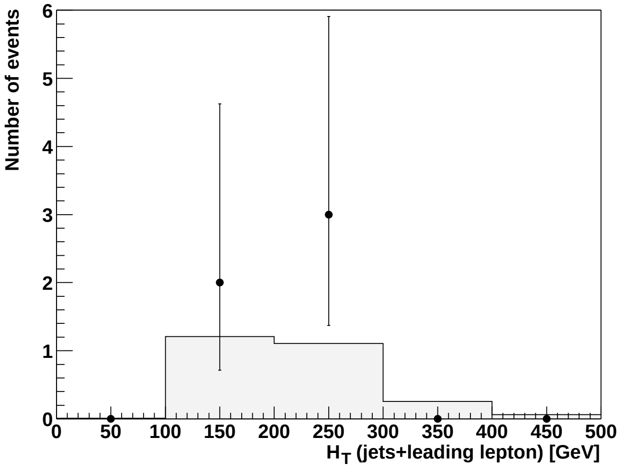

Figure A.1: Observed and predicted H_T for events with two or more jets after b-tagging in the $e\mu$ channel.

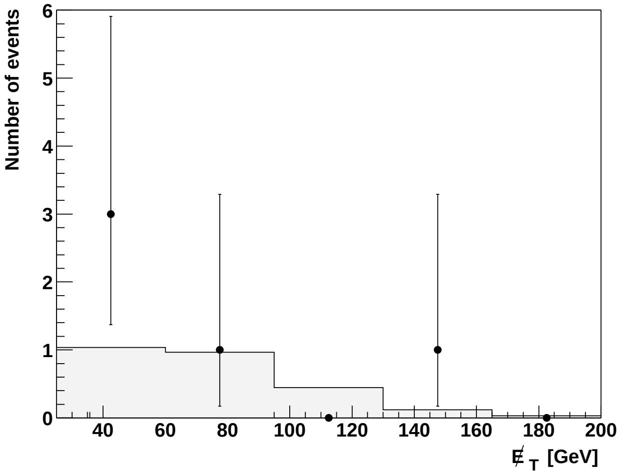

Figure A.2: Observed and predicted $\not{E}_T$ for events with two or more jets after b-tagging in the $e\mu$ channel.

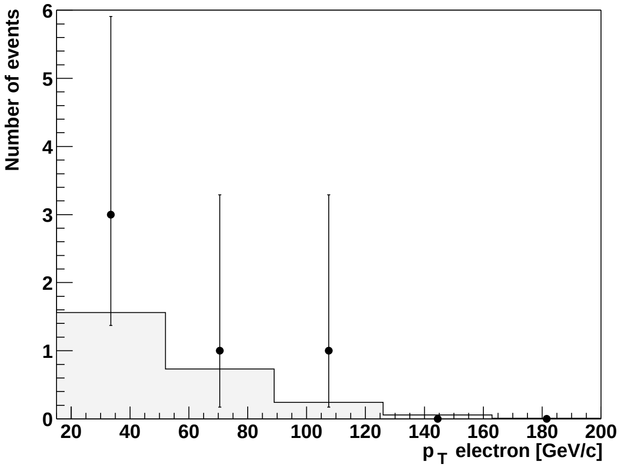

Figure A.3: Observed and predicted electron p_T for events with two or more jets after b-tagging in the $e\mu$ channel.

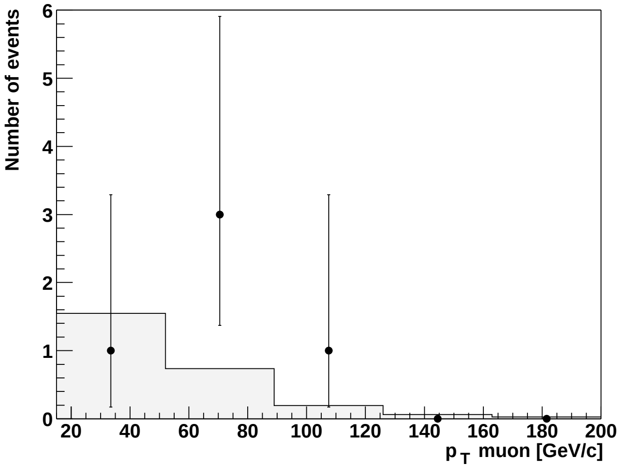

Figure A.4: Observed and predicted muon p_T for events with two or more jets after b-tagging in the $e\mu$ channel.

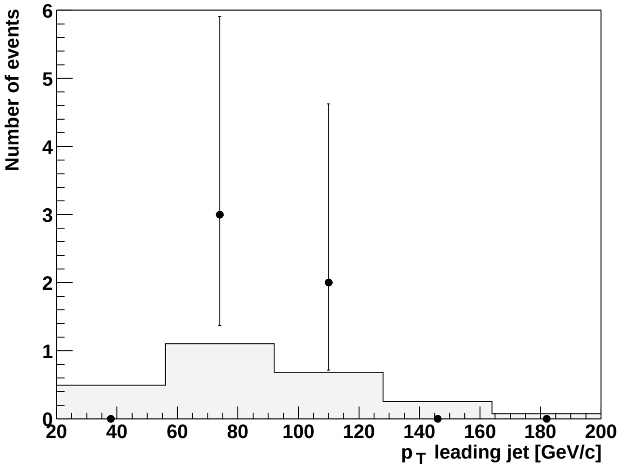

Figure A.5: Observed and predicted leading jet p_T for events with two or more jets after b-tagging in the $e\mu$ channel.

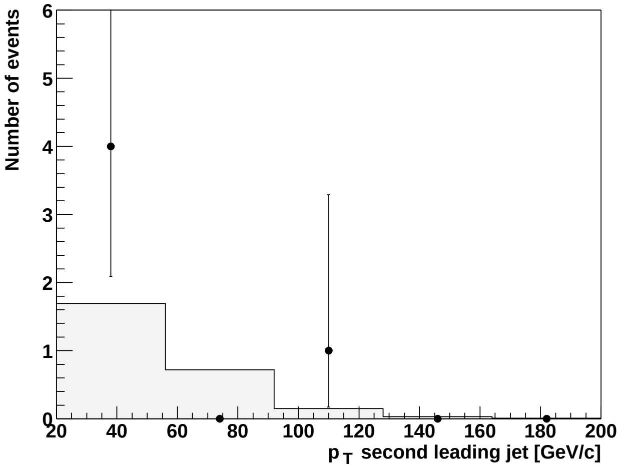

Figure A.6: Observed and predicted second leading jet p_T for events with two or more jets after b-tagging in the $e\mu$ channel.

B Kinematic Distributions in Lepton+Track Events

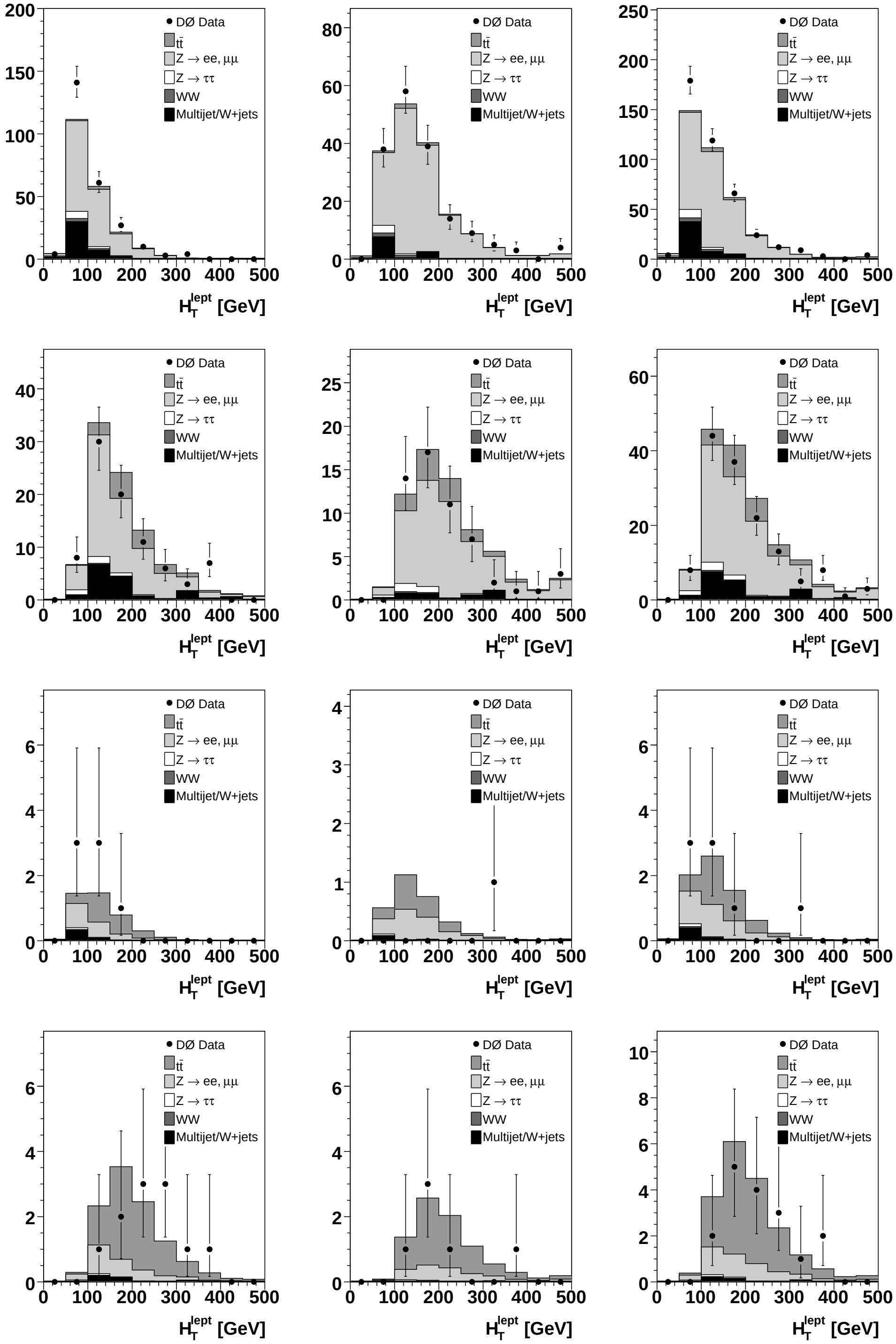

Figure B.1: Observed and predicted H_T^{lept} in the $e +$ track (left), $\mu +$ track (middle), and $\ell +$ track (right) channels. The two top (bottom) rows show the distributions before (after) b-tagging. Rows one and three show events with one jet and rows two and four show events with two or more jets.

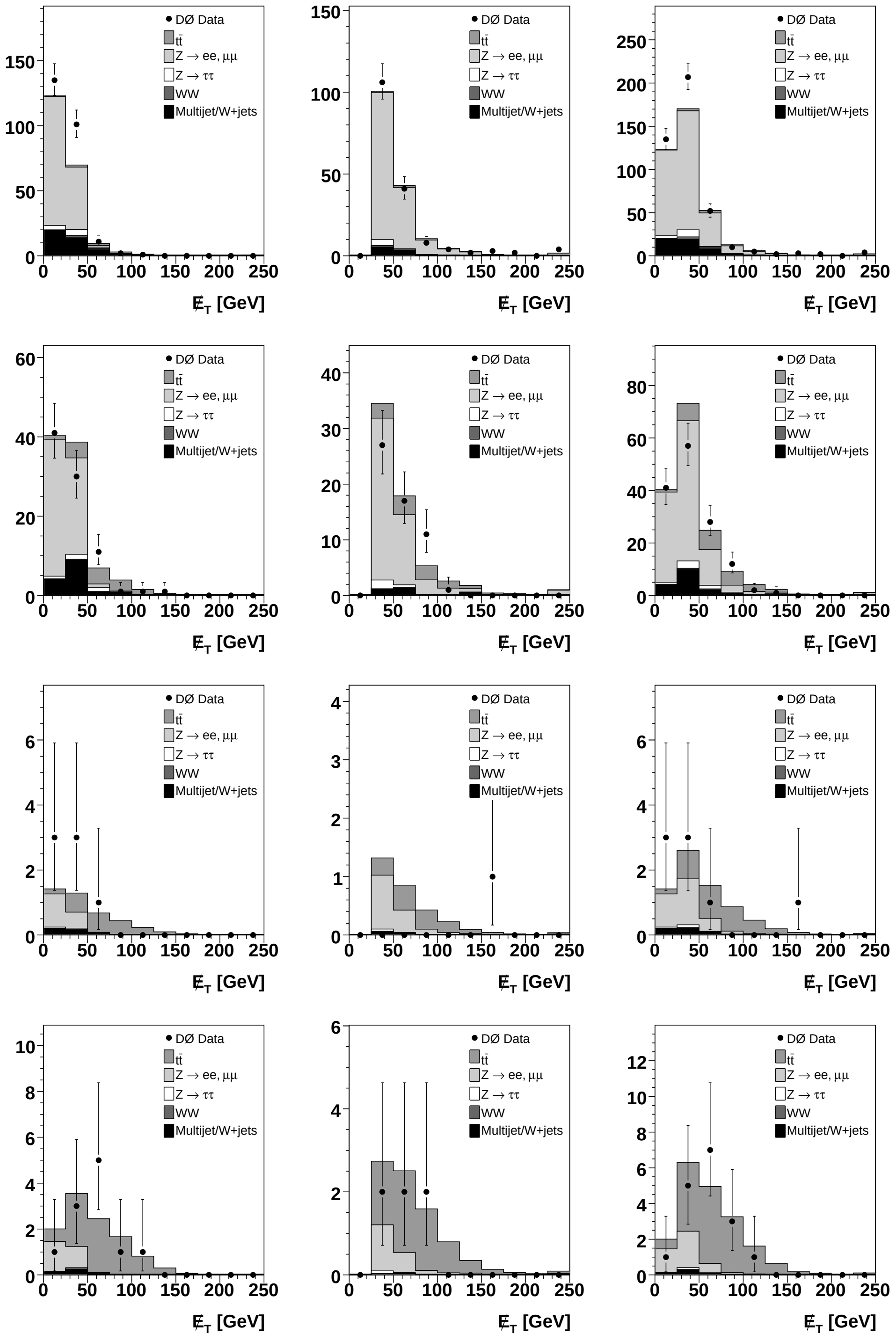

Figure B.2: Observed and predicted $\not\!\!E_T$ in the $e +$ track (left), $\mu +$ track (middle), and $\ell +$ track (right) channels. The two top (bottom) rows show the distributions before (after) b-tagging. Rows one and three show events with one jet and rows two and four show events with two or more jets.

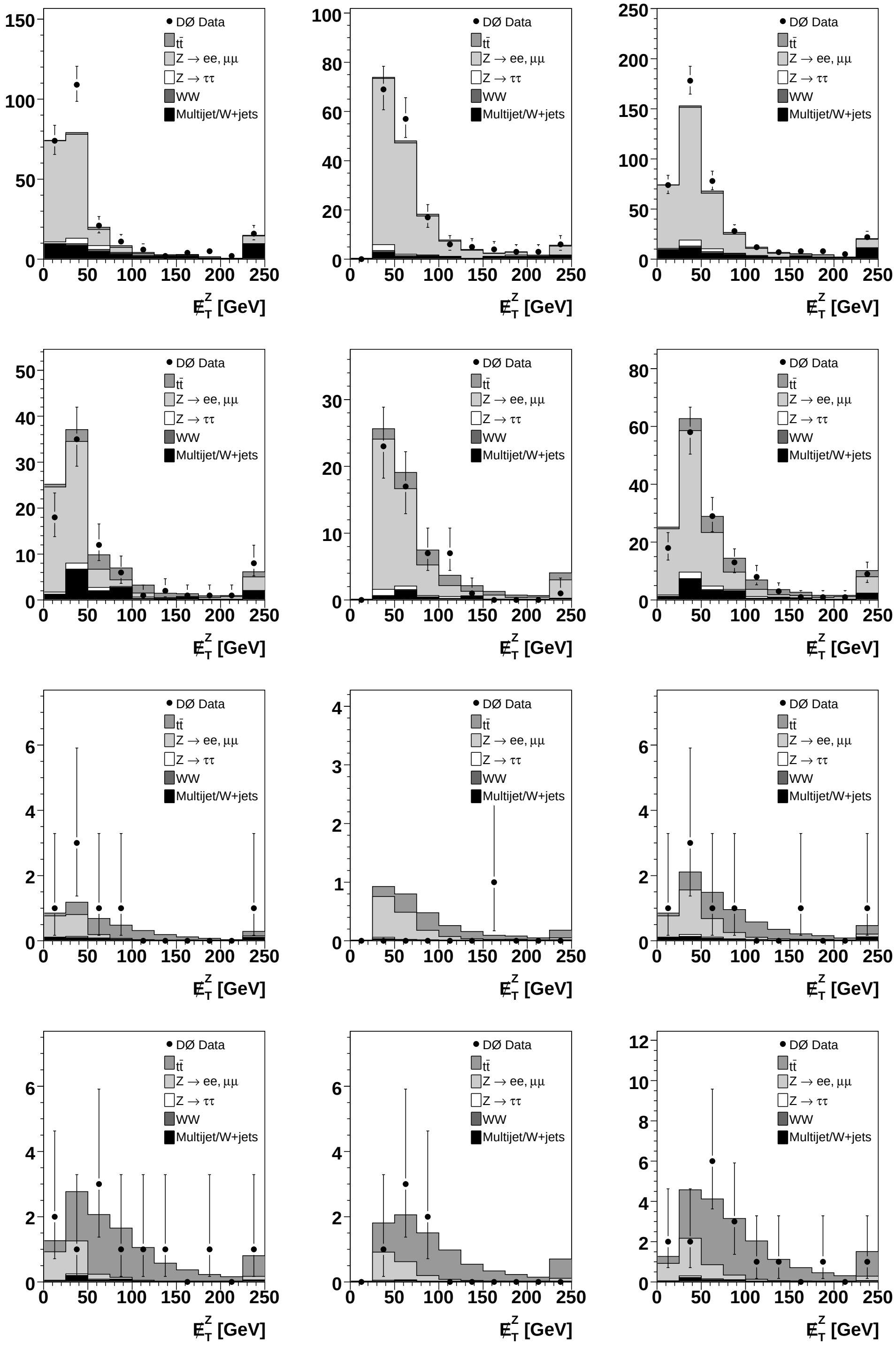

Figure B.3: Observed and predicted $\not\!\!E_T^Z$ in the $e+$track (left), $\mu+$track (middle), and $\ell+$track (right) channels. The two top (bottom) rows show the distributions before (after) b-tagging. Rows one and three show events with one jet and rows two and four show events with two or more jets.

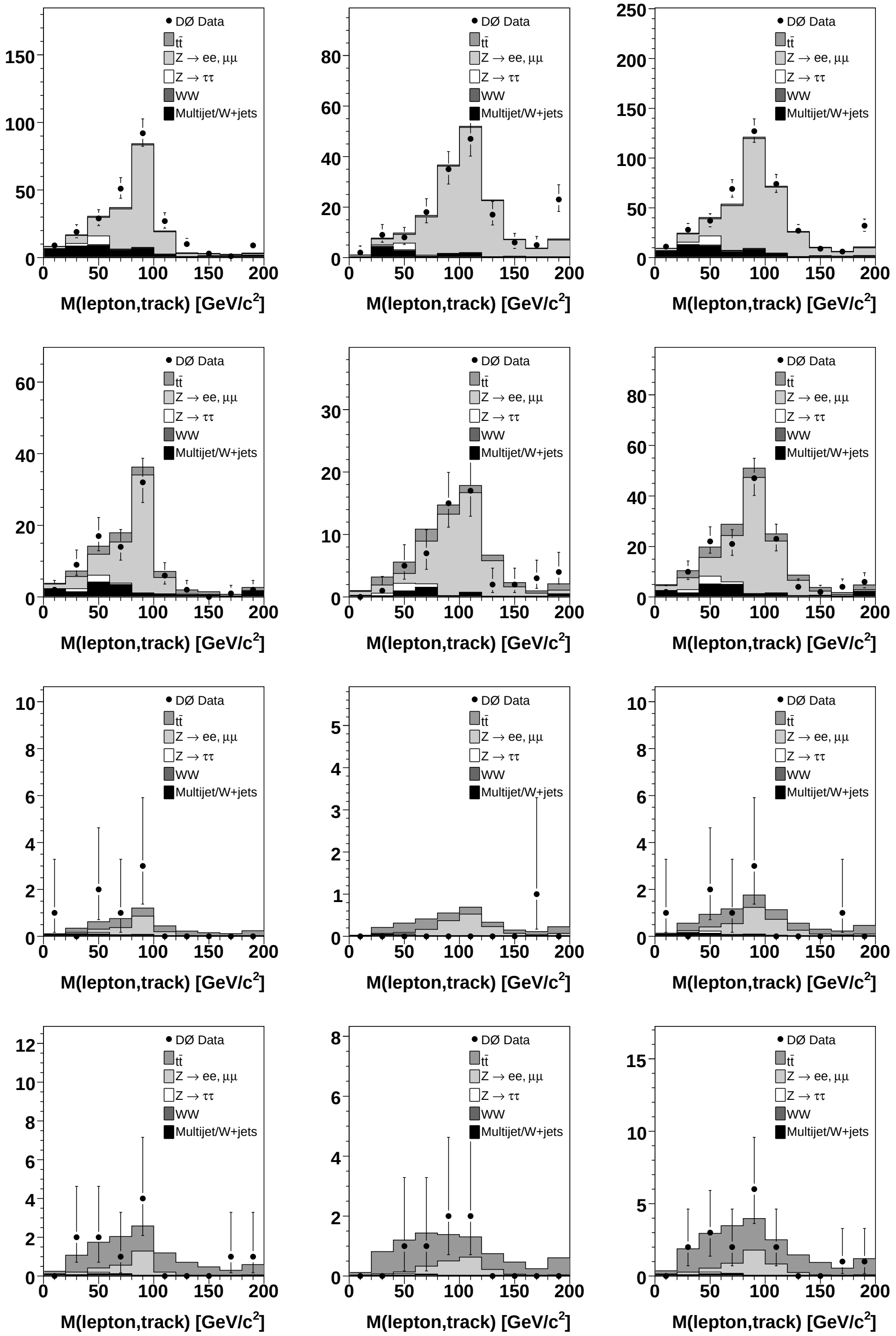

Figure B.4: Observed and predicted invariant mass of the lepton and the track in the $e +$ track (left), $\mu +$ track (middle), and $\ell +$ track (right) channels. The two top (bottom) rows show the distributions before (after) b-tagging. Rows one and three show events with one jet and rows two and four show events with two or more jets.

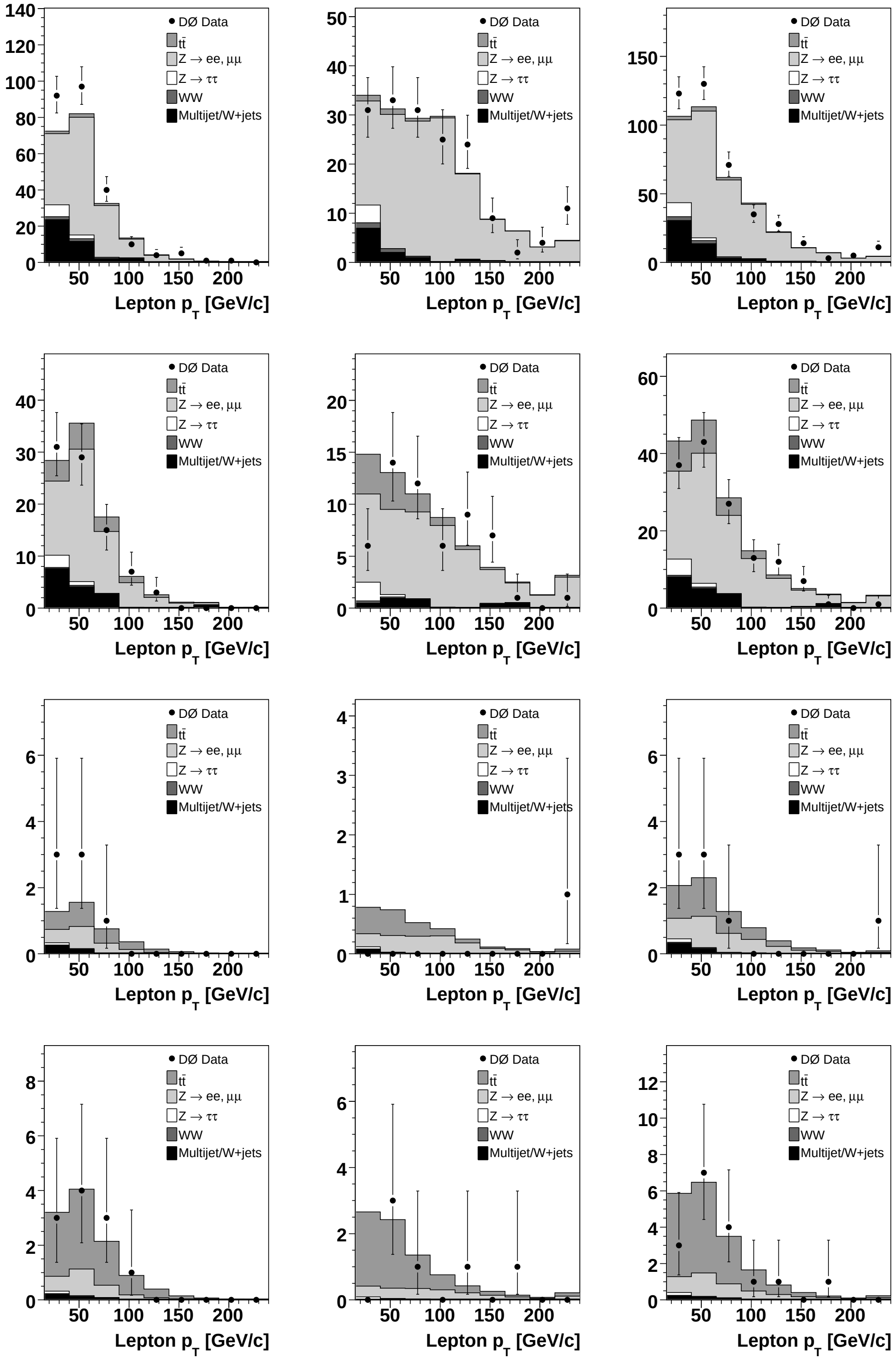

Figure B.5: Observed and predicted lepton p_T in the $e + \text{track}$ (left), $\mu + \text{track}$ (middle), and $\ell + \text{track}$ (right) channels. The two top (bottom) rows show the distributions before (after) b-tagging. Rows one and three show events with one jet and rows two and four show events with two or more jets.

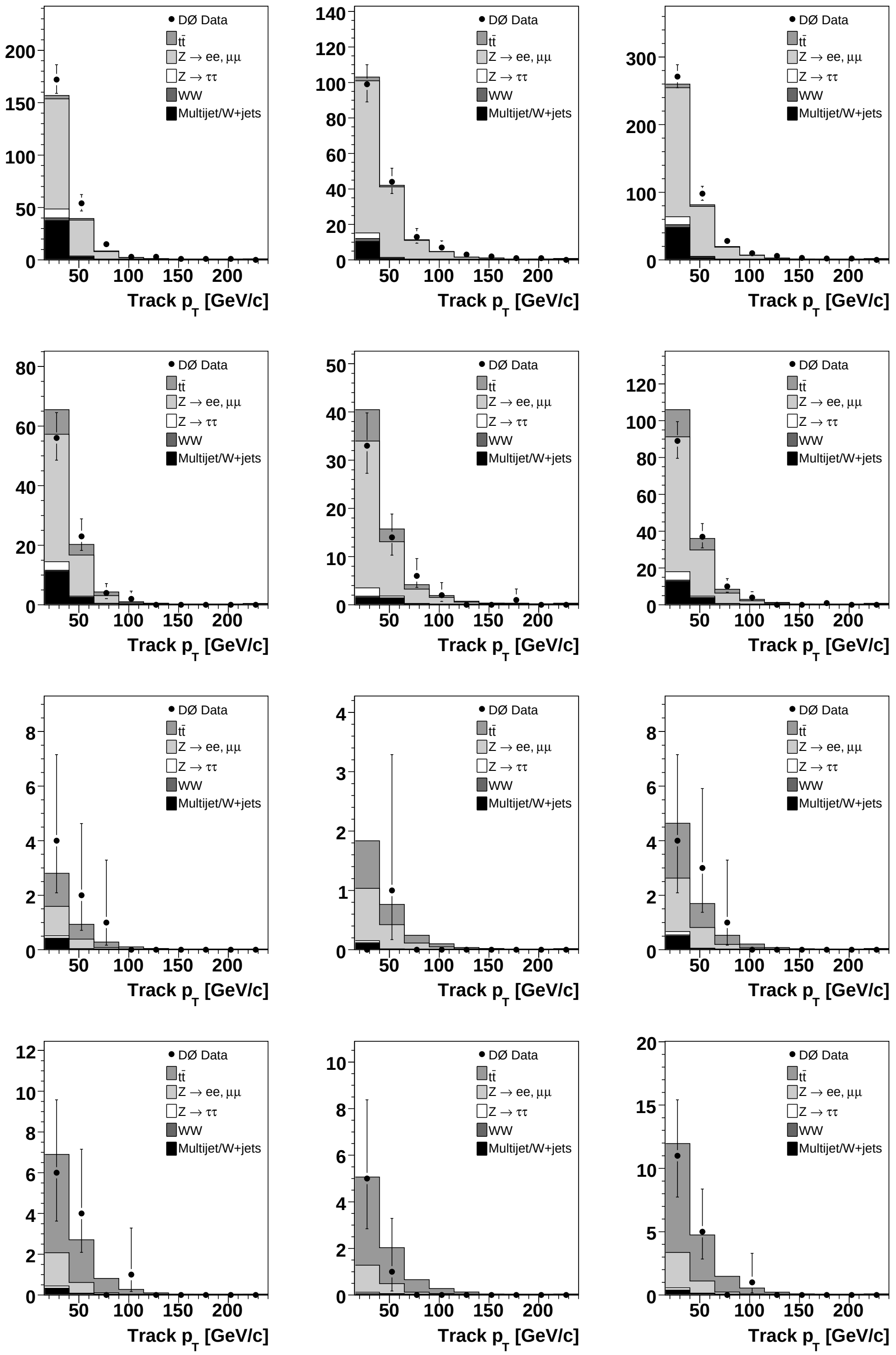

Figure B.6: Observed and predicted track p_T in the $e+$track (left), $\mu+$track (middle), and $\ell+$track (right) channels. The two top (bottom) rows show the distributions before (after) b-tagging. Rows one and three show events with one jet and rows two and four show events with two or more jets.

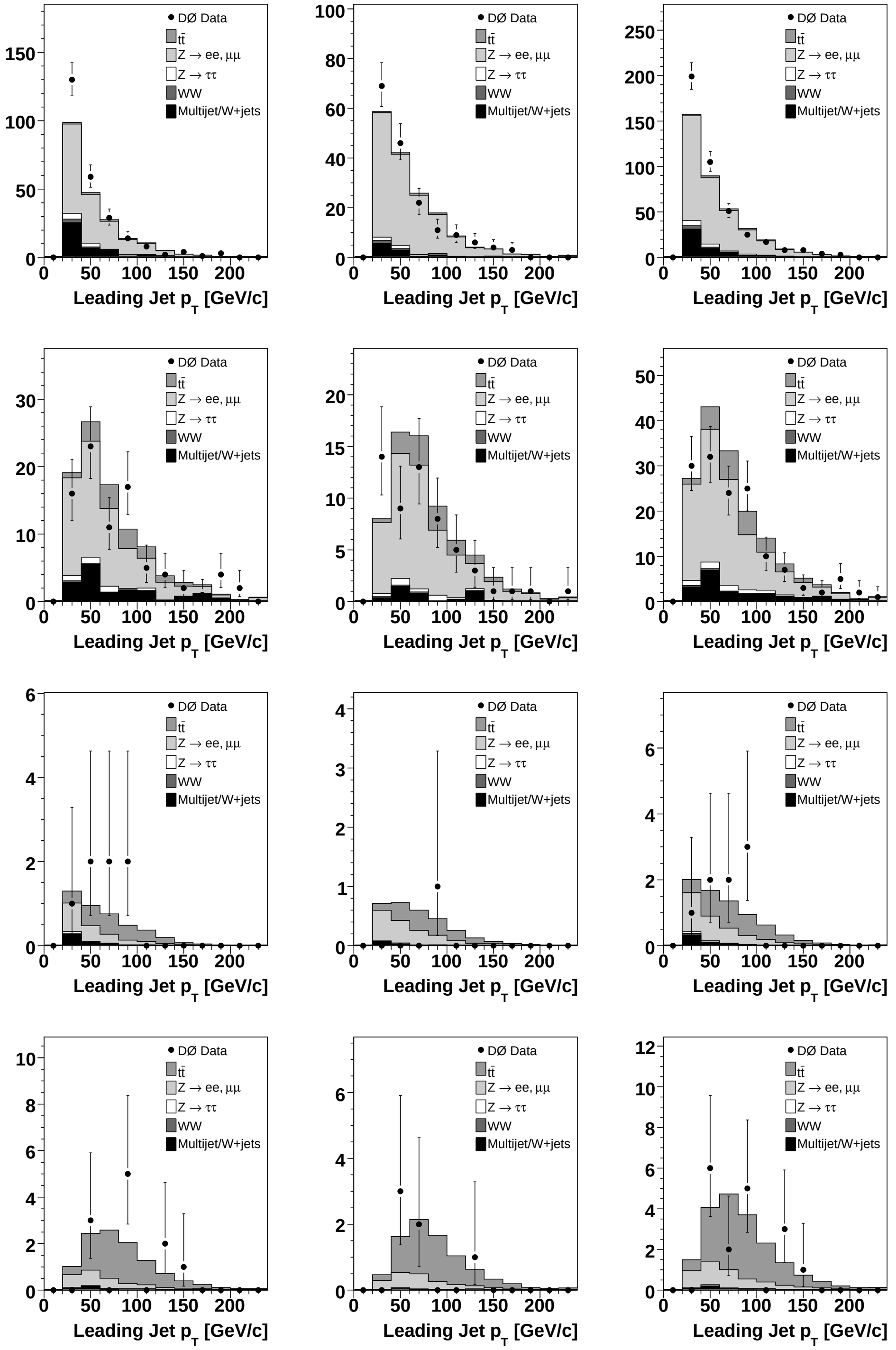

Figure B.7: Observed and predicted leading jet p_T in the $e+$track (left), $\mu+$track (middle), and $\ell+$track (right) channels. The two top (bottom) rows show the distributions before (after) b-tagging. Rows one and three show events with one jet and rows two and four show events with two or more jets.

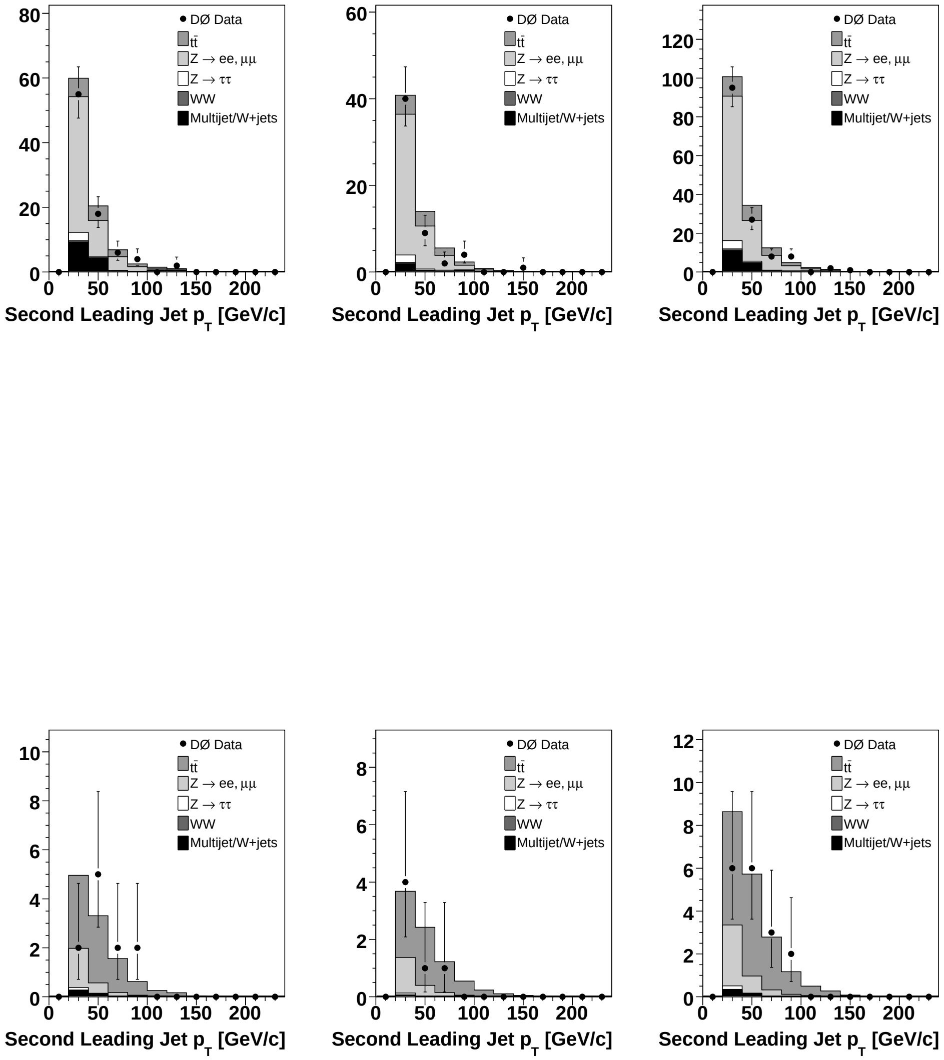

Figure B.8: Observed and predicted second leading jet p_T in the $e +$ track (left), $\mu +$ track (middle), and $\ell +$ track (right) channels. The two top (bottom) rows show the distributions before (after) b-tagging. Rows one and three show events with one jet and rows two and four show events with two or more jets.

Bibliography

[1] L. Christofek et al., FERMILAB-TM-2318-E (2005).

[2] A. Garcia-Bellido et al., DØ Note 4320 (2004).

[3] The CDF Collaboration, Phys. Rev. Lett. **74**, 2626-2631 (1995).

[4] The DØ Collaboration, Phys. Rev. Lett. **74**, 2632-2637 (1995).

[5] M. K. Gaillard, P. D. Grannis and F. J Sciulli, Rev. Mod. Phys. **71**, S96-S111 (1999).

[6] F. Reines and C.L. Cowan, Phys. Rev. **92**, 830-831 (1953).

[7] G. Danby et al., Phys. Rev. Lett. **9**, 36-44 (1962).

[8] The DONUT Collaboration, Phys. Lett. B **504**, 218-224 (2001).

[9] J.J. Thomson (1897).

[10] J. C. Street and E. C. Stevenson, Phys. Rev. **52**, 1003 (1937).

[11] M. L. Perl et al., Phys. Rev. Lett. **35**, 1489-1492 (1975).

[12] M. Gell-Mann, Phys. Lett. **8**, 214-215 (1964).

[13] E598 Collaboration, Phys. Rev. Lett. **33**, 1404-1406 (1974).

[14] SLAC-SP-017 Collaboration, Phys. Rev. Lett. **33**, 1406-1408 (1974).

[15] S. W. Herb et al., Phys. Rev. Lett. **39**, 252 (1977).

[16] M. Planck (1900).

[17] A. Einstein (1905).

[18] The UA1 Collaboration, Phys. Lett. B **122**, 103-116 (1983).

[19] The UA2 Collaboration, Phys. Lett. B **122**, 476-485 (1983).

[20] The UA1 Collaboration, Phys. Lett. B **126**, 398-410 (1983).

[21] The UA2 Collaboration, Phys. Lett. B **129**, 130-140 (1983).

[22] D. P. Barber et al., Phys. Rev. Lett. **43**, 830 (1979).

[23] S. L. Glashow, Nucl. Phys. **22**, 579 (1961).

[24] A. Salam and J. C. Ward, Phys. Lett. **13**, 168-171 (1964).

[25] S. Weinberg, Phys. Rev. Lett. **19**, 1264 (1967).

[26] The SNO Collaboration, Phys. Rev. Lett. **87**, 071301 (2001).

[27] The Super-Kamiokande Collaboration, Phys. Rev. Lett. **93**, 101801 (2004).

[28] The Particle Data Group, J. Phys. G **33**, 1 (2006).

[29] P. W. Higgs, Phys. Lett. **12**, 132-133 (1964).

[30] F. Englert and R. Brout, Phys. Rev. Lett. **13**, 321-322 (1964).

[31] G. S. Guralnik, C. R. Hagen and T. W. B. Kibble, Phys. Rev. Lett. **13**, 585-587 (1964).

[32] D. J. Gross and F. Wilczek, Phys. Rev. D **8**, 3633 (1973).

[33] H. D. Politzer, Phys. Rept. **14**, 129 (1974).

[34] The ALEPH, DELPHI, L3 and OPAL Collaborations and the LEP Working Group for Higgs boson searches, Phys. Lett. B **565**, 61-75 (2003).

[35] S. L. Glashow, J. Iliopoulos and L. Maiani, Phys. Rev. D **2**, 1285 (1970).

[36] G. L. Kane and M. E. Peskin, Nucl. Phys. B **195**, 29 (1982).

[37] The UA1 Collaboration, Phys. Lett. B **256**, 121 (1991), [Erratum-ibid. B **262**, 497 (1991)].

[38] D. Shaile and P. M. Zerwas, Phys. Rev. D **45**, 3262 (1992).

[39] The CDF and DØ Collaborations and the Tevatron Electroweak Working Group, hep-ex/0608032.

[40] J. C. Collins and D. E. Soper, Ann. Rev. Nucl. Part. Sci. **37**, 383 (1987).

[41] The CTEQ Collaboration, Eur. Phys. J. C **12**, 375-392 (2000).

[42] M. Cacciari et al., JHEP **0404**, 068 (2004).

[43] N. Kidonakis and R. Vogt, Phys. Rev. D **68**, 114014 (2003).

[44] N. Kidonakis and R. Vogt, Eur. Phys. J. C **33**, 466 (2004).

[45] B. Harris et al., Phys. Rev. D **66**, 054024 (2002).

[46] T. M. P. Tait, Phys. Rev. D **61**, 34001 (1999).

[47] M. Jeżabek and J. H. Kühn, Nucl. Phys. B **314**, 1 (1989).

[48] The Particle Data Group, Phys. Lett. B **592**, 1 (2004).

[49] S.L. Glashow, E.E. Jenkins, Phys Lett. B **196**, 233 (1987).

[50] C. Hill, S. Parke, Phys. Rev. D **49**, 4454 (1994).

[51] The CDF Collaboration, Phys. Rev. Lett. **80**, 2773 (1998).

[52] The CDF Collaboration, Phys. Rev. Lett. **80**, 2779 (1998).

[53] The CDF Collaboration, Phys. Rev. D **64**, 032002 (2001).

[54] The CDF Collaboration, Phys. Rev. Lett. **93**, 142001 (2004).

[55] The CDF Collaboration, Phys. Rev. D **71**, 052003 (2005).

[56] The CDF Collaboration, Phys. Rev. Lett **97**, 082004 (2006).

[57] The CDF Collaboration, Phys. Rev. D **71**, 072005 (2005).

[58] The CDF Collaboration, Phys. Rev. D **72**, 052003 (2005).

[59] The CDF Collaboration, Phys. Rev. D **72**, 032002 (2005).

[60] The CDF Collaboration, Phys. Rev. Lett. **96**, 202002 (2006).

[61] The DØ Collaboration, Phys. Rev. D **67**, 012004 (2003).

[62] The DØ Collaboration, Phys. Lett. B **626**, 35 (2005).

[63] The DØ Collaboration, Phys. Lett. B **626**, 45 (2005).

[64] The DØ Collaboration, Phys. Lett. B **626**, 55 (2005).

[65] W. Bernreuther, M. Flesch and P. Haberl, Phys. Rev. D **58** 114031 (1998).

[66] C. T. Hill and S. J. Parke, Phys. Rev. D **49**, 4454 (1994).

[67] C. T. Hill, Phys. Lett. B **345**, 483 (1995).

[68] R. M. Harris, C. T. Hill and S. J. Parke, hep-ph/9911288.

[69] The CDF Collaboration, Phys. Rev. Lett. **82**, 2038 (1999).

[70] The CDF Collaboration, Phys. Rev. Lett. **85**, 2062 (2000).

[71] The DØ Collaboration, Phys. Rev. Lett. **92**, 221801 (2004).

[72] The DØ Collaboration, hep-ex/0612052.

[73] The DØ Collaboration, Phys. Lett. B **639**, 616 (2006).

[74] The CDF Collaboration, Phys. Rev. Lett. **86**, 3233 (2001).

[75] The CDF Collaboration, Phys. Rev. Lett. **95**, 102003 (2005).

[76] The CDF Collaboration, Phys. Rev. Lett. **80**, 2525 (1998).

[77] J.F. Gunion et al., *The Higgs Hunters Guide*, Addison–Wesley, Redwood City, California (1990).

[78] The CDF Collaboration, Phys. Rev. Lett. **72**, 1977 (1994).

[79] The CDF Collaboration, Phys. Rev. D **54**, 735 (1996).

[80] The CDF Collaboration, Phys. Rev. Lett. **79**, 357 (1997).

[81] The CDF Collaboration, Phys. Rev. D **62**, 012004 (2000).

[82] The DØ Collaboration, Phys. Rev. Lett. **82**, 4975 (1999).

[83] The DØ Collaboration, Phys. Rev. Lett. **88**, 151803 (2002).

[84] The CDF Collaboration, Phys. Rev. Lett. **84**, 216 (2000).

[85] The CDF Collaboration, Phys. Rev. D **73**, 111103(R) (2006).

[86] The CDF Collaboration, hep-ex/0608062.

[87] The DØ Collaboration, hep-ex/0609045.

[88] The DØ Collaboration, Phys. Rev. D Rap. Comm. **72**, 011104(R) (2005).

[89] The DØ Collaboration, Phys. Lett. B **617**, 1 (2005).

[90] T. Stelzer, S. Willenbrock, Phys. Lett. B **374**, 169 (1996).

[91] The DØ Collaboration, Phys. Rev. Lett. **85**, 256 (2000).

[92] E. Simmon, hep-ph/9908511.

[93] The CDF Collaboration, Phys. Rev. Lett. **80**, 2767 (1998).

[94] The CDF Collaboration, Phys. Rev. Lett. **82**, 271 (1999).

[95] The CDF Collaboration, Phys. Rev. D **63**, 032003 (2001).

[96] The CDF Collaboration, Phys. Rev. Lett. **96**, 152002 (2006).

[97] The CDF Collaboration, Phys. Rev. D **73**, 112006 (2006).

[98] The CDF Collaboration, Phys. Rev. D **74**, 032009 (2006).

[99] The CDF Collaboration, Phys. Rev. Lett. **96**, 022004 (2006).

[100] The CDF Collaboration, Phys. Rev. D. **73**, 032003 (2006).

[101] The CDF Collaboration, Phys. Rev. D. **73**, 092002 (2006).

[102] The DØ Collaboration, Phys. Rev. Lett. **79**, 1197 (1997).

[103] The DØ Collaboration, Phys. Rev. Lett. **80**, 2063 (1998).

[104] The DØ Collaboration, Phys. Rev. D **58**, 052001 (1998).

[105] The DØ Collaboration, Phys. Rev. D **60**, 052001 (1999).

[106] The DØ Collaboration, Nature **429**, 638 (2004).

[107] The DØ Collaboration, Phys. Lett. B **606**, 25 (2005).

[108] The DØ Collaboration, hep-ex/0609053.

[109] The DØ Collaboration, hep-ex/0609056.

[110] S. Willenbrock, hep-ph/0211067.

[111] The LEP Electroweak Working Group, hep-ex/0612034.

[112] D. Chang, W. FG. Chang and E. Ma, Phys. Rev. D **59**, 091503 (1999).

[113] D. Chang, W. FG. Chang and E. Ma, Phys. Rev. D **61**, 037301 (2000).

[114] D. Choudhury, T. M. Tait and C. E. Wagner, Phys. Rev. D**65**, 053002 (2002).

[115] The DØ Collaboration, Phys. Rev. Lett. **98**, 041801 (2007).

[116] J. Thompson, FERMILAB-TM-1909 (1994).

[117] S. D. Holmes, R. E. Gerig and D. E. Johnson, FERMILAB-Conf-89/183 (1989).

[118] J. A. MacLachlan, FERMILAB-Pub-98/338 (1998).

[119] C. D. Curtis, IEEE Trans. Nucl. Sci. **26**, 4120 (1979).

[120] The DØ Collaboration, Nucl. Instrum. Meth. A **338**, 185-253 (1994).

[121] The DØ Collaboration, Nucl. Instrum. Meth. A **565**, 463-537 (2006).

[122] T. Zimmerman et al., IEEE Trans. Nucl. Sci. **42**, 803-807 (1995).

[123] R. J. Yarema et al., Fermilab-TM-1892 (1994).

[124] The E710 Collaboration, Phys. Rev. Lett. **63**, 2784 (1989).

[125] The E811 Collaboration, Phys. Lett. B **445**, 419 (1999).

[126] The CDF Collaboration, Phys. Rev. D **50**, 5550 (1994).

[127] S. Klimenko, J. Konigsberg and T. M. Liss, FERMILAB-FN-0741 (2003).

[128] E. A. Burke et al., IEEE Trans. Nucl. Sci. **34**, 1134 (1987).

[129] E. A. Burke et al., IEEE Trans. Nucl. Sci. **40**, 1372 (1993).

[130] M. Moll, Ph.D. Thesis, University of Hamburg (1999).

[131] L. J. Beattie et al., Nucl. Instr. and Meth. A **412**, 238-246 (1998).

[132] F. Lemeilleur et al., Nucl. Instrum. Meth. A **360**, 438-444 (1995).

[133] T. Kohriki at al., IEEE Trans. Nucl. Sci. **43**, 1200-1202 (1996).

[134] T. Ohsugi et al., Nucl. Instrum. Meth. A **342**, 22-26 (1994).

[135] T. Ohsugi et al., Nucl. Instrum. Meth. A **383**, 116-122 (1996).

[136] T. Ohsugi et al., Nucl. Instrum. Meth. A **383**, 166-173 (1996).

[137] M. Moll, E. Fretwurst and G. Lindström, Nucl. Instrum. Meth. A **426**, 87-93 (1999).

[138] S. M. Sze, *Semiconductor devices*, Physics and Technology. John Wiley & Sons (1985).

[139] G. Casse, Ph.D. Thesis, Universite Joseph Fourier - Grenoble (1998).

[140] G. Kramberger et al., Nucl. Instrum. Meth. A **481**, 297-305 (2002).

[141] The Rose Collaboration, Nucl. Instrum. Meth. A **466**, 308-326 (2001).

[142] R. Wunstorf, Ph.D. Thesis, University of Hamburg (1992).

[143] K. Gill et al., Nucl. Instrum. Meth. A **322**, 177-188 (1992).

[144] T. Schulz, Ph.D. Thesis, University of Hamburg (1996).

[145] A. Chilingarov et al., Nucl. Instrum. Meth. A **360**, 432 (1995).

[146] H. Feick, Master's Thesis, University of Hamburg (1993).

[147] H.E. Boesch and F.B. McLean, IEEE Trans. Nucl. Sci. **32**, 3940 (1985).

[148] R. Wunstorf, IEEE Trans. Nucl. Sci. **44**, 806-814 (1997).

[149] The DØ Collaboration, Nucl. Instrum. Meth. A **473**, 49-52 (2001).

[150] The DØ Collaboration, Nucl. Instrum. Meth. A **530**, 105-109 (2004).

[151] The DØ Collaboration, FERMILAB-TM-2345-E (2006).

[152] A. Vasilescu (INPE Bucharest) and G. Lindstroem (University of Hamburg), *Displacement damage in silicon*, on-line compilation.

[153] S. Worm, Nucl. Instr. and Meth. A **418**, 120-127 (1998).

[154] R. E. Kalman, Transactions of the ASME–Journal of Basic Engineering D **82**, 35-45 (1960).

[155] R. Frühwirth, Nucl.Instrum. Meth. A **262**, 444 (1987).

[156] P. V. C. Hough, International Conference on High Energy Accelerators and Instrumentation, CERN (1959).

[157] P. Billoir, Nucl. Instrum. Meth. A **225**, 352 (1984).

[158] P. Billoir and S. Qian, Nucl. Instrum. Meth. A **294**, 219 (1990).

[159] E. J. Wolin and L. L. Ho, Nucl. Instrum. Meth. A **329**, 493 (1993).

[160] U. Baur (ed.), R. K. Ellis (ed.) and D. Zeppenfeld (ed.), FERMILAB-PUB-00-297.

[161] B. Clément et al., DØ Note 4159 (2003).

[162] M. L. Mangano et al. JHEP 0307:001 (2003), hep-ph/0206293.

[163] M. L. Mangano, M. Moretti and R. Pittau, Nucl. Phys. B **632**, 343-362 (2002).

[164] F. Caravaglios et al., Nucl. Phys. B **539**, 215-232 (1999).

[165] T. Sjöstrand et al., Comput. Phys. Commun. **135**, 238 (2001).

[166] R. Brun and F. Carminati, CERN Program Library Long Writeup W5013 (1993).

[167] R. Fields, *Min-Bias and the Underlying Event at the Tevatron and the LHC*, talk presented at the Fermilab ME/MC Tuning Workshop, Fermilab, Oct. 4, 2002.

[168] The CDF Collaboration, Phys. Rev. D **65**, 092002 (2002).

[169] D. Lange, A. Ryd et al., *The EvtGen Event Generator Package*, in Proceedings of CHEP (1998).

[170] S. Jadach et al., Comput. Phys. Commun. **76**, 361 (1993).

[171] J.M. Campbell and R. K. Ellis, Phys Rev D **60**, 113006 (1999).

[172] T. Wyatt, Int. J. Mod. Phys. A **19**, 794-807 (2004).

[173] J. Strandberg, Ph.D. Thesis, Stockholm University (2006).

[174] The CDF Collaboration, CDF Note 8148 (2006).

[175] The DØ Collaboration, hep-ex/0611002.

[176] The ATLAS Collaboration, CERN/LHCC/99-15 (1999).

[177] I. Borjanovic et al., Eur. Phys. J. **C39S2**, 63-90 (2005).